UNIVERSITY OF PADUA

DEPARTMENT OF CIVIL, ENVIRONMENTAL AND ARCHITECTURAL ENGINEERING

Master's Degree in Water and Geological Risk Engineering

MASTER THESIS

Simulation of large-scale experimental failure of flood defence systems

Supervisor:

Chiar.ma Prof.ssa Francesca Ceccato

Graduate: Abdul Rahim Naqib

matr. 2039985

ACADEMIC YEAR 2022-2023

ABSTRACT

Embankments or otherwise known as levees or dikes are typical flood defence structures. Levees have allowed people to settle along rivers and low-lying countries where the risk of flooding is high. Although levees provide protection against floods, they are not exempt from being prone to failure. The risks posed by levee failure can be catastrophic. This makes it crucial to assess the consequences of levee failures. The limit equilibrium method (LEM) and finite element method (FEM) are two techniques capable of simulating levee failure. However, the former does not allow for a progressive simulation of the complete failure process, while the latter encounters convergence issues and cannot simulate large displacements. To overcome these issues, the material point method (MPM) is introduced. In this study, two numerical simulations are conducted to replicate an experimental slope failure of a full-scale earthen levee known as IJkDijk South Dike that took place in the Netherlands in 2012. The first simulation employed FEM for pre-failure analysis, while the second employed MPM for the post-failure analysis where large deformations are present. Before simulating the experiment, a basic slope was modelled as a benchmark to ensure consistency between the two different methods for simulating the same problem. This helped to validate post-failure analysis results which involved mapping of stresses from the onset of failure. Furthermore, sensitivity analysis was performed for the strength and consolidation parameters in the pre-failure analysis, as well as for the stiffness and assignment of the number of material points per element in the post-failure analysis. Overall, the models managed to capture the deep sliding failure mechanism reported in the experiment, with the MPM model permitting the evolution of the failure over time.

ACKNOWLEDGEMENTS

First and foremost, I would like to thank God for all His blessings and for giving me the opportunity to pursue my master's degree in Italy. I am forever indebted to the University of Padua for providing me with a fully funded scholarship, which greatly helped cover my expenses and alleviate any worries. I am also grateful to my supervisor, Professor Francesca Ceccato, for patiently and expertly guiding me at every step of the way to complete my master's thesis. Moreover, I would like to express my gratitude to all the Professors involved in the 'Water and Geological Risk Engineering' master's program for making the past two years an enjoyable learning experience. Their dedication extended beyond the classroom, encompassing outdoor activities as well. Furthermore, I am thankful for the staff at 'Consorzio Università Rovigo' for their invaluable assistance whenever it was needed. Lastly, I would like to thank my family for their continuous prayers and encouragement.

TABLE OF CONTENT

ABSTRACT 1
ACKNOWLEDGEMENTS 2
LIST OF TABLES 5
LIST OF FIGURES 7
1 INTRODUCTION 11
1.1 LEVEE OVERVIEW 11
1.2 PROBLEM STATEMENT 12
1.3 OBJECTIVES 13
2 THE IJkDijk TRIAL EMBANKMENT EXPERIMENT 14
2.1 SITE 14
2.2 LEVEE GEOMETRY 16
2.2.1 Levee construction material 16
2.2.2 Monitoring devices 16
2.2.3 South Dike geometry 18
2.3 STRATIGRAPHY 19
2.4 GEOTECHNICAL PARAMETERS 20
2.5 LOAD SEQUENCE 22
2.6 FAILURE DESCRIPTION 24
3 METHODOLOGY 26
3.1 COMPUTATIONAL TOOLS 26
3.1.1 Finite element method 26
3.1.2 Material point method 28
3.2 CONSTITUTIVE MODELS 33
3.2.1 Mohr-Coulomb 33
3.2.2 Drucker-Prager 35
3.2.3 Soft Soil 35
4 BENCHMARK SLOPE 37
4.1 FEM MODEL 37
4.1.1 Geometry and Discretization 37
4.1.2 Material 38
4.1.3 Analysis type 39
4.1.4 Results 40

4.2 MPM MODEL 42
4.2.1 Geometry and Discretization 42
4.2.2 Material 44
4.2.3 Analysis type 45
4.2.4 Results 46
4.3 FEM+MPM MODEL 51
5 NUMERICAL MODELLING OF PRE-FAILURE 53
5.1 FEM MODEL 53
5.1.1 Geometry and Discretization 53
5.1.2 Material 55
5.1.3 Analysis type 56
5.2 RESULTS 58
6 NUMERICAL MODELLING OF POST-FAILURE 65
6.1 MPM MODEL 65
6.1.1 Geometry and Discretization 65
6.1.2 Material 68
6.1.3 Analysis type 69
6.2 RESULTS 70
7 COMPARISON WITH EXPERIMENT 85
7.1 DISCUSSION 85
8 CONCLUSION 91
APPENDIX A 93
APPENDIX B 98
APPENDIX C 112
APPENDIX D 118
APPENDIX E 169
APPENDIX F 174
APPENDIX G 180
9 BIBLIOGRAPHY 182

LIST OF TABLES

Table 2. 1. GeoBeads sensors elevation with respect to m NAP. 17
Table 2. 2. Soil stratigraphy depth and thickness of the levee test site. 19
Table 2. 3. Summary of the geotechnical parameters. 21

Table 4. 1. Material properties and mechanical properties of the benchmark slope. 38
Table 4. 2. Construction stages of the benchmark slope. 39
Table 4. 3. Safety factors at load application of 5kN/m^2, 10kN/m^2 and 15kN/m^2. 40
Table 4. 4. Total displacement (m) for (a) stress initialization, (b) load application of 5kN/m^2, (c) load application of 10kN/m^2 and (d) load application of 15kN 41
Table 4. 5. MPM material properties and mechanical properties of the benchmark slope. 44
Table 4. 6. MPM loading stages of the benchmark slope. 45
Table 4. 7. MPM 5% damping quasi-static analysis total displacement (m) distribution. 48
Table 4. 8. MPM 70% damping quasi-static analysis total displacement (m) distribution. 49
Table 4. 9. MPM dynamic analysis total displacement (m) distribution. 50
Table 4. 10. Total displacement (m) distribution for the case of stresses transferred from load = 15kN/m^2. 52
Table 4. 11. Total displacement (m) distribution for the case of stresses transferred from load = 10kN/m^2. 52

Table 5. 1. Material properties and mechanical properties of the South Dike simulation. 56
Table 5. 2. Construction stages of the South Dike. 57
Table 5. 3. Safety factors at stage 23, 25 and 26 59

Table 6. 1. MPM material properties and mechanical properties of the South dike. 68
Table 6. 2. South Dike post-failure deviatoric strain evolution (0.0s to 12.5s). 74
Table 6. 3. South Dike post-failure total displacement evolution (0.0s to 12.5s). 75
Table 6. 4. Mechanical and numerical properties modified for each post-failure analysis run. 77
Table 6. 5. Final load step of each post-failure analysis run. 77
Table 6. 6. Second run South Dike post-failure deviatoric strain evolution (0.0s to 0.6957E-03s) 80
Table 6. 7. Second run South Dike post-failure total displacement evolution (0.0s to 0.6957E-03s). 80
Table 6. 8. Third run South Dike post-failure deviatoric strain evolution (0.0s to 0.9s). 81
Table 6. 9. Third run South Dike post-failure total displacement evolution (0.0s to 0.9s). 82
Table 6. 10. Fourth run South Dike post-failure deviatoric strain evolution (0.0s to 1.2s). 83
Table 6. 11. Fourth run South Dike post-failure total displacement evolution (0.0s to 1.2s). 84

Table 7. 1. Horizontal displacements measured by the inclinometers, extracted from Koelewijn (2012). 86

Table A. 1. Total stress in x-direction for (a) stress initialization, (b) load application of 5kN/m^2, (c) load application of 10kN/m^2 and (d) load application of 15kN/m^2..... 94
Table A. 2. Total stress in y-direction for (a) stress initialization, (b) load application of 5kN/m^2, (c) load application of 10kN/m^2 and (d) load application of 15kN/m^2..... 95
Table A. 3. Shear stress for (a) stress initialization, (b) load application of 5kN/m^2, (c) load application of 10kN/m^2 and (d) load application of 15kN/m^2. 96
Table A. 4. Pore stress for (a) stress initialization, (b) load application of 5kN/m^2, (c) load application of 10kN/m^2 and (d) load application of 15kN/m^2. 97

Table B. 1. MPM 5% damping quasi-static analysis total stress in the x-direction distribution. 100
Table B. 2. MPM 5% damping quasi-static analysis total stress in the y-direction distribution. 101
Table B. 3. MPM 5% damping quasi-static analysis shear stress distribution..... 102
Table B. 4. MPM 5% damping quasi-static analysis pressure evolution. 103
Table B. 5. MPM 70% damping quasi-static analysis total stress in the x-direction distribution. 104
Table B. 6. MPM 70% damping quasi-static analysis total displacement in the y-direction distribution. 105
Table B. 7. MPM 70% damping quasi-static analysis shear stress distribution..... 106
Table B. 8. MPM 70% damping quasi-static analysis pressure evolution. 107
Table B. 9. MPM dynamic analysis total stress in the x-direction distribution. 108
Table B. 10. MPM dynamic analysis total stress in the y-direction distribution. 109
Table B. 11. MPM dynamic analysis shear stress distribution. 110
Table B. 12. MPM dynamic analysis pressure evolution..... 111

Table C. 1. Horizontal stress (kN/m^2) distributions for the case of stresses transferred from load = 15kN/m^2. 114
Table C. 2. Vertical stress (kN/m^2) distributions for the case of stresses transferred from load = 15kN/m^2. 114
Table C. 3. Shear stress (kN/m^2) distributions for the case of stresses transferred from load = 15kN/m^2. 115
Table C. 4. Pressure (kN/m^2) distributions for the case of stresses transferred from load = 15kN/m^2. 115
Table C. 5. Horizontal stress (kN/m^2) distributions for the case of stresses transferred from load = 10kN/m^2. 116
Table C. 6. Vertical stress (kN/m^2) distributions for the case of stresses transferred from load = 10kN/m^2. 116
Table C. 7. Shear stress (kN/m^2) distributions for the case of stresses transferred from load = 10kN/m^2. 117
Table C. 8. Pressure (kN/m^2) distributions for the case of stresses transferred from load = 10kN/m^2. 117

Table E. 1. Modified base peat properties and their respective simulation runs..... 169
Table E. 2. Factor of safety of each run and their respective final simulation stages. 169

Table F. 1. South dike post-failure vertical stress evolution (0.0s to 12.5s). 176
Table F. 2. South dike post-failure pressure evolution (0.0s to 12.5s). 177

LIST OF FIGURES

Figure 2. 1. Aerial view of the position of the East, West and South Dike in Booneschans (Koelewijn & Peters, 2012). 15
Figure 2. 2. Levee transversal cross section (a) with 1m grid intervals and longitudinal cross section (b) with dimensions in m. 17
Figure 2. 3. 2D schematization of the entire model during the final construction stage (dimensions in m). 18
Figure 2. 4. An aerial photograph of the South Dike failure by Boertjens Chose (Zomer, 2012). 24
Figure 2. 5. Middle section of the South dike, indication of failure after forensic investigation (Koelewijn, 2012). 25

Figure 3. 1. Severe mesh distortion example when simulating a large deformation problem using the standard Lagrangian FEM (Rohe & Vermeer, 2014)..... 28
Figure 3. 2. MPM calculation steps (Ceccato, 2015). 30
Figure 3. 3. Stress-strain relationship of an elasto-perfect plastic material, obtained from Midas FEA NX (2023) tutorial manual..... 33
Figure 3. 4. Mohr-Coulomb failure envelope for drained (a) and undrained (b) soil conditions, retrieved from Midas FEA NX (2023) tutorial manual..... 34
Figure 3. 5. Mohr-coulomb and Drucker-Prager yield surfaces on the principle effective stress space (a) and on the deviatoric plane (b) (Kim et al., 2012). 35
Figure 3. 6. Normal consolidation and overconsolidation line, obtained from the tutorial manual of (Midas FEA NX (2023)..... 36

Figure 4. 1. Benchmark slope FEM model geometry, discretization, and boundary conditions. 38
Figure 4. 2. Benchmark slope MPM model geometry and discretization. 42
Figure 4. 3. MPM boundary conditions: (a) solid traction (loading) and (b) solid fixities. 43

Figure 5. 1. Discretization and boundary conditions. 54
Figure 5. 2. Total stresses and shear stress (kN/m^2) at the time of filling of containers. 61
Figure 5. 3. Pore stress (kN/m^2) at the time of filling of containers. 62
Figure 5. 4. Displacements (m) at the time of filling of containers. 63
Figure 5. 5. Pore stress (kN/m^2) from transient seepage analysis at the time of sand core filled to the crest. 64

Figure 6. 1. South Dike MPM model geometry and discretization (red =active elements, blue = inactive elements). 66
Figure 6. 2. South Dike MPM boundary conditions: (a) solid traction (load) and (b) solid fixities. 67
Figure 6. 3. Transferred plane strain total horizontal stress (a), total vertical stress (b), and shear stress (c) (kN/m^2). 72
Figure 6. 4. Transferred transient-seepage analysis pore stress (kN/m^2). 73
Figure 6. 5. Total displacement (a), horizontal displacement (b), and vertical displacement (c) (m) at the end of the simulation (load step:125). 76
Figure 6. 6. Number of MPs per element assigned to the South Dike mesh (a: run 1,2,3 and b: run 4) 78

Figure 7. 1. Initial (black line) and final (red line) slope configuration of the South Dike's west-cross section (Koelewijn, 2012) (a) and simulated final total displacement contour (b). 88
Figure 7. 2. Initial (black line) and final (red line) slope configuration of the South Dike's middle-cross section (Koelewijn, 2012) (a) and simulated final total displacement contour (b). 89
Figure 7. 3. Indication of sliding plane depth in the middle cross section (a) and MPM final displacement imposed on the material ID contour (b). 90

Figure B. 1. 2D stress tensor components in Paraview. 98
Figure B. 2. Selected MP position (a) and displacement comparison (b). 99

Figure C. 1. Selected MP position (a) and displacement (m) comparison (b). 113

Figure D. 1. Pore stress (kN/m^2) from steady state seepage analysis at pre-levee stage. 118
Figure D. 2. Total stresses and shear stress (kN/m^2) at pre-levee stage. 119
Figure D. 3. Pore stress (kN/m^2) at pre-levee stage. 120
Figure D. 4. Total stresses and shear stress (kN/m^2) at levee construction step 1. 121
Figure D. 5. Pore stress (kN/m^2) at levee construction step 1 122
Figure D. 6. Displacements (m) at levee construction step 1 122
Figure D. 7. Total stresses and shear stress (kN/m^2) at levee construction step 2. 123
Figure D. 8. Pore stress (kN/m^2) at levee construction step 2 124
Figure D. 9. Displacements (m) at levee construction step 2 125
Figure D. 10. Total stresses and shear stress (kN/m^2) at levee construction step 3. 126
Figure D. 11. Pore stress (kN/m^2) at levee construction step 3 127
Figure D. 12. Displacements (m) at levee construction step 3 128
Figure D. 13. Total stress and shear stress (kN/m^2) at levee construction step 4 129
Figure D. 14. Pore stress (kN/m^2) at levee construction step 4 130
Figure D. 15. Displacements (m) at levee construction step 4 131
Figure D. 16. Total stresses and shear stress (kN/m^2) at levee construction step 5. 132
Figure D. 17. Pore stress (kN/m^2) at levee construction step 5 133
Figure D. 18. Displacements (m) at levee construction step 5 134
Figure D. 19. Total stresses and shear stress (kN/m^2) at container weight stage. 135
Figure D. 20. Pore stress (kN/m^2) at container weight stage. 136
Figure D. 21. Pore stress (kN/m^2) from transient seepage analysis at first filling of sand core stage. 137

Figure D. 22. Total stresses and shear stress (kN/m^2) at first filling of sand core stage. 138
Figure D. 23. Pore stress (kN/m^2) at first filling of sand core stage. 139
Figure D. 24. Displacements (m) at first filling of sand core stage. 140
Figure D. 25. Pore stress from transient seepage analysis when basin is filled. 141
Figure D. 26. Total stresses and shear stress (kN/m^2) when basin is filled. 142
Figure D. 27. Pore stress (kN/m^2) when basin is filled. 143
Figure D. 28. Displacements (m) when basin is filled. 144
Figure D. 29. Pore stress (kN/m^2) from transient seepage analysis at first excavation stage. 145
Figure D. 30. Total stresses and shear stress (kN/m^2) at first excavation stage. 146
Figure D. 31. Pore stress (kN/m^2) at first excavation stage. 147
Figure D. 32. Displacements (m) at first excavation stage. 148
Figure D. 33. Pore stress (kN/m^2) from transient seepage analysis at second excavation stage. 149
Figure D. 34. Total stresses and shear stress (kN/m^2) at second excavation stage. 150
Figure D. 35. Pore stress (kN/m^2) at second excavation stage. 151
Figure D. 36. Displacements (m) at second excavation stage. 152
Figure D. 37. Pore stress (kN/m^2) from transient seepage analysis at third excavation stage. 153
Figure D. 38. Total stresses and shear stress (kN/m^2) at third excavation stage. 154
Figure D. 39. Pore stress (kN/m^2) at third excavation stage. 155
Figure D. 40. Displacements (m) at third excavation stage. 156
Figure D. 41. Pore stress (kN/m^2) from consolidation analysis at third excavation stage. 157
Figure D. 42. Pore stress (kN/m^2) from transient seepage analysis at fourth excavation stage. 157
Figure D. 43. Total stresses and shear stress (kN/m^2) at fourth excavation stage. 158
Figure D. 44. Pore stress (kN/m^2) at fourth excavation stage. 159
Figure D. 45. Displacements (m) at fourth excavation stage. 160
Figure D. 46. Pore stress (kN/m^2) from transient seepage analysis at fifth excavation stage. 161
Figure D. 47. Total stresses and shear stress (kN/m^2) at fifth excavation stage. 162
Figure D. 48. Pore stress (kN/m^2) at fifth excavation stage. 163
Figure D. 49. Displacements (m) at fifth excavation stage. 164
Figure D. 50. Pore stress (kN/m^2) from transient seepage analysis at second filling of sand core. 165
Figure D. 51. Total stresses and shear stress (kN/m^2) at second filling of sand core (scaled for better visualization). 166
Figure D. 52. Pore stress (kN/m^2) at second filling of sand core (scaled for better visualization). 167
Figure D. 53. Displacements (m) at second filling of sand core. 168

Figure E. 1. Total displacement (m) contour of the first run at its final stage (Containers filled). 170
Figure E. 2. Total displacement (m) contour of the second run at its final stage (Containers filled). 170
Figure E. 3. Total displacement (m) contour of the third run at its final stage (Excavation 5)..... 171
Figure E. 4. Total displacement (m) contour of the fourth run at its final stage (Excavation 5). 171
Figure E. 5. Total displacement (m) contour of the fifth run at its final stage (Containes filled)..... 172
Figure E. 6. Total displacement (m) contour of the sixth run at its final stage (Containers filled)..... 172
Figure E. 7. Settlement (m) results of the reference run, run 5 and run 6. 173

Figure F. 1. Location of MPs (a) and their respective displacements in m (b). 178
Figure F. 2. South Dike kinetic energy (kJ) plot. 179

Figure G. 1. Final MP distribution of the first run. 180
Figure G. 2. Final MP distribution of the second run. 180
Figure G. 3. Final MP distribution of the third run. 181
Figure G. 4. Final MP distribution of the fourth run. 181

1 INTRODUCTION

1.1 LEVEE OVERVIEW

One typical engineering solution to protect an area adjacent to a body of water or with an elevation below the sea level from the risk of flooding is building levees. These are embankments which act as a defence system against floodwaters.

Levees have made it possible for people to settle and build towns or cities along rivers. A prime example is the Mississippi River and Tributaries levees, which now provide protection against catastrophic floods for over 4 million citizens, 1.5 million homes, 33,000 farms and numerous important transportation routes (Mississippi Valley Division, U.S. Army corps of Engineers, n.d.).

In lowland countries, flood risk is high. For instance, most of the Netherlands lies below sea level, hence making it prone to flood risk. To mitigate this, levees have been built. Levees along the coasts of highly populated and heavily industrialized regions of the Netherlands are required to be designed to withstand a storm event that has a return period of 10,000 years (Silva et al., 2004).

Despite the effectiveness of levees in combating flood-related disasters, it can still be subject to failure. Owing to climate change, weather patterns become more unpredictable and extreme events such as intense precipitation and floods become more frequent. As a result, sea-level rises and water levels in rivers or other water bodies fluctuate more often.

Fluctuations in rivers lead to rapid filling and drawdown conditions. Hence, this causes geotechnical problems to occur which may potentially cause levees to fail. In 2007, flooding in the Grijalva watershed in Tabasco State, Mexico, highlighted the susceptibility of levees by showing that their stability was undermined due to hydraulic gradients (seepage forces) generated by rapid filling and drawdown conditions as well rain infiltration in their crests (López-Acosta & Tarantino, 2018).

Moreover, the risks associated with levee failure, especially during an extreme event, should not be taken lightly and must be assessed by relevant authorities of places where they are built. This is because their breach and destruction not only cause huge economic losses but loss of human and animal lives as well.

1.2 PROBLEM STATEMENT

The simulation of failure of levees can be conducted through the limit equilibrium method (LEM) and finite element method (FEM). The failure criterion which is used by LEM does not consider the stress path to failure. It identifies failure from the stress state only and the failure surface must be determined a-priori. Hence, levee failure cannot be simulated progressively and failure modes due to high seepage forces such as uplift at the landside of levees cannot be appropriately captured. On the other hand, stress-strain behaviour of soil is considered by FEM which implies that the model generates the failure surface and there is no need for it to be pre-defined (Griffth & Lane, 1999). Therefore, an accurate slope stability analysis is achieved, and progressive simulation of failure permitted. However, to evaluate the impact of levee failures and perform risk assessment, it is vital to understand the failure from initiation to the entire collapse mechanism which includes the post-failure displacement. This cannot be conducted with LEM and FEM but can be done with the material point method (MPM). Large displacement beyond the onset of failure is capable of being simulated by MPM as it does not suffer from elements distorting and solutions diverging which is typical of FEM. This report presents two numerical models (FEM and MPM) that simulate an experimental slope failure of a full-scale earthen levee. The experiment was carried out in September 2012 in Bad Nieuweschans, Groningen province, the Netherlands, by a Dutch research program known as the IJkdijk (‘calibration levee’).

1.3 OBJECTIVES

The following are the objectives of this research:

1. To simulate the failure of the experimental levee from start to the onset of failure using FEM including all experimental loading stages.
2. To simulate the post-failure large displacements of the experimental levee occurring beyond the onset of failure using MPM.
3. To compare the results obtained from FEM, MPM, and the experiment.

Although an attempt has been made by Melnikova et al. (2015) to numerically simulate the levee failure, this attempt involved simplifications, such as reducing the total number of simulation stages compared to the actual number of experimental stages. Additionally, the investigation was solely on the pre-failure, with no post-failure analysis of the levee conducted, a step crucial for risk assessment. Hence, the primary aim of this study is to include all the experimental stages in the simulation and to perform not only pre-failure analysis but also post-failure analysis.

2 THE IJkDijk TRIAL EMBANKMENT EXPERIMENT

2.1 SITE

The Dutch research program, 'IJkdijk', which refers to 'calibration levee', has built multiple levees starting from 2007 for experimental purposes. The two specific goals of this research program are to test different types of sensors for levee monitoring under field conditions and to better understand the mechanisms involved in levee failures.

A three million Euro fund had been awarded to the IJkdijk foundation in 2011 by the Dutch Department of Economic Affairs, Agriculture and Innovation to conduct tests which include an All-in-One Sensor Validation Test (AIO-SVT). This test was carried out in August and September 2012 (Koelewijn, 2012). The following are the aims of the test:

1. To test sensor-systems installed in and on levees along with data processing and an information system capable of providing an alert in the event of failure.
2. To acquire further knowledge on failure mechanisms of levees and their prevention methods.

Three separate dikes (levees) were built to undertake the AIO-SVT. These levees are called the West Dike, East Dike and South Dike, which reflect their relative position on the test site at Booneschans, in the North-East of the Netherlands. In this study, only the South Dike was replicated to perform the numerical simulations. Figure 2.1 shows an aerial view of the position of the levees.

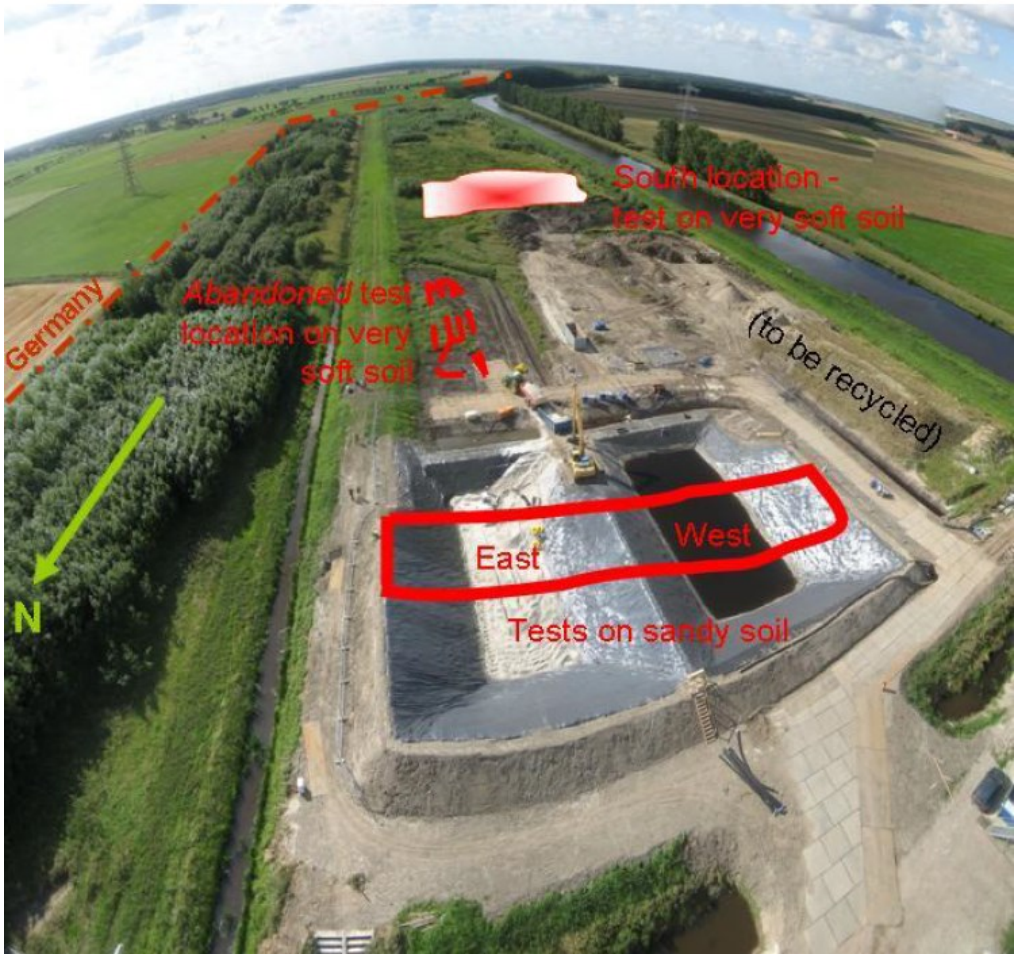

Figure 2. 1. Aerial view of the position of the East, West and South Dike in Booneschans (Koelewijn & Peters, 2012).

2.2 LEVEE GEOMETRY

2.2.1 Levee construction material

The core of the levee is made of sand. It is covered by a layer of clay with a thickness of 0.5m on both sides of the levee slope, making it impermeable. On the left side of the levee, a small embankment is built from soil on the surrounding test site to mimic sea-side conditions by forming a basin of 1m depth. In the numerical models, this embankment is modelled as the same material as the base clay upon which the levee is built.

2.2.2 Monitoring devices

The levee had been installed with sensors supplied by companies which participated in the experiment. These are piezometers, inclinometers, strain and temperature meters as well as settlement gauges. 'GeoBeads' sensors which measure both the pore water pressure and inclination are provided by 'Alert Solutions' while other installed inclinometers are provided by 'SAAF' and 'StabiAlert'. Moreover, the strain measurements are recorded with fibre-optic cables provided by 'Koenders'. Figure 2.2 displays the cross-section of the levee and the position of the sensors while the elevation of the GeoBeads sensors with respect to the 'Amsterdam Ordnance Datum' or 'Normaal Amsterdams Peil' (NAP) is presented in Table 2.1 (Melnikova et al., 2015).

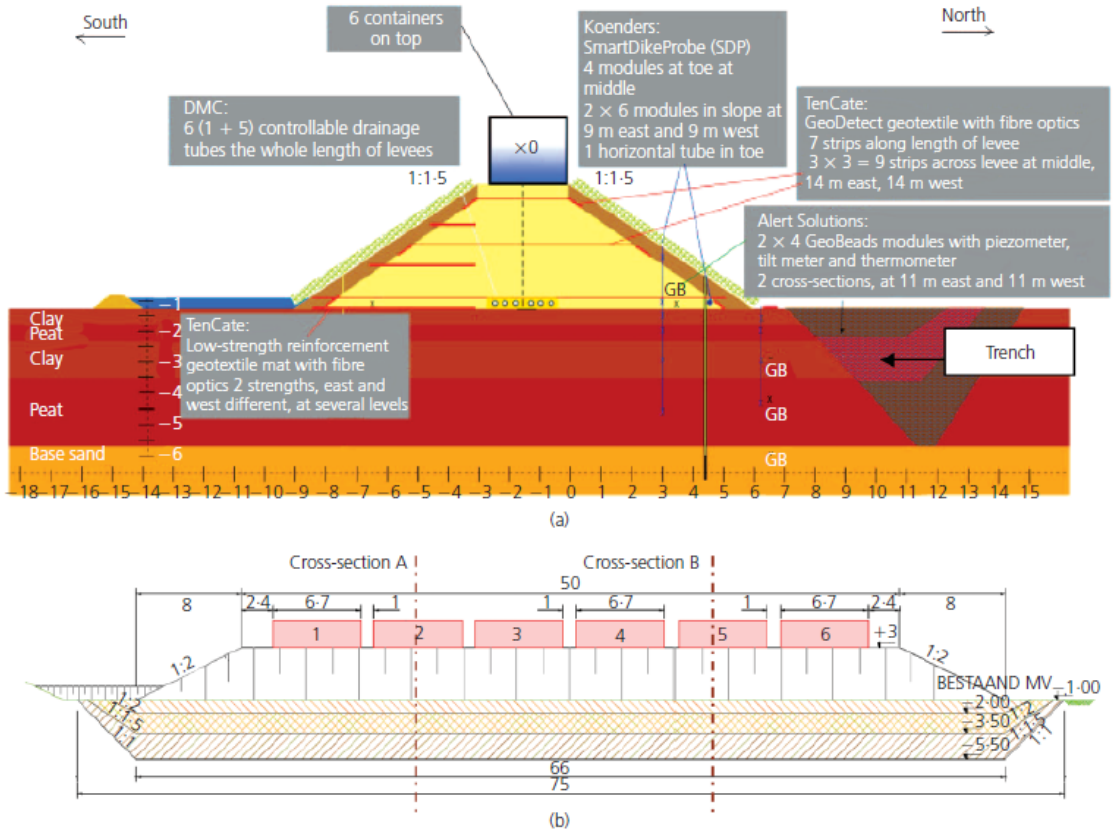

Figure 2. 2. Levee transversal cross section (a) with 1m grid intervals and longitudinal cross section (b) with dimensions in m.

Table 2. 1. GeoBeads sensors elevation with respect to m NAP.

Cross-section	GeoBeads sensor	Depth: m NAP
A	GB-AG-1 (sand core)	-1.52
	GB-AG-2 (thick peat layer)	-3.00
	GB-AG-3 (thick clay layer)	-4.30
	GB-AG-4 (base sand layer)	-5.62
B	GB-AG-5 (sand core)	-1.70
	GB-AG-6 (thick peat layer)	-2.97
	GB-AG-7 (thick clay layer)	-4.30
	GB-AG-8 (base sand layer)	-6.02

2.2.3 South Dike geometry

At the end of the construction stage, the geometry of the levee according to the report of (Koelewijn, 2012) are as follows:

- Height of levee: 4m above the ground.
- Side slopes of the levee: 1:1.5 (V:H)
- Thickness of clay layer: 0.5m
- Excavation of ditch 1.5m from the toe of the levee on the North side.
- Depth of ditch: 2m below the ground level.
- Bottom width of ditch: 4m
- Slope of ditch: 1:1 on the left side (levee side) and 1:2 on the right side.

A schematization of the levee geometry along with the small embankment and ditch during the final stage of the construction used in the numerical simulations is presented in Figure 2.3.

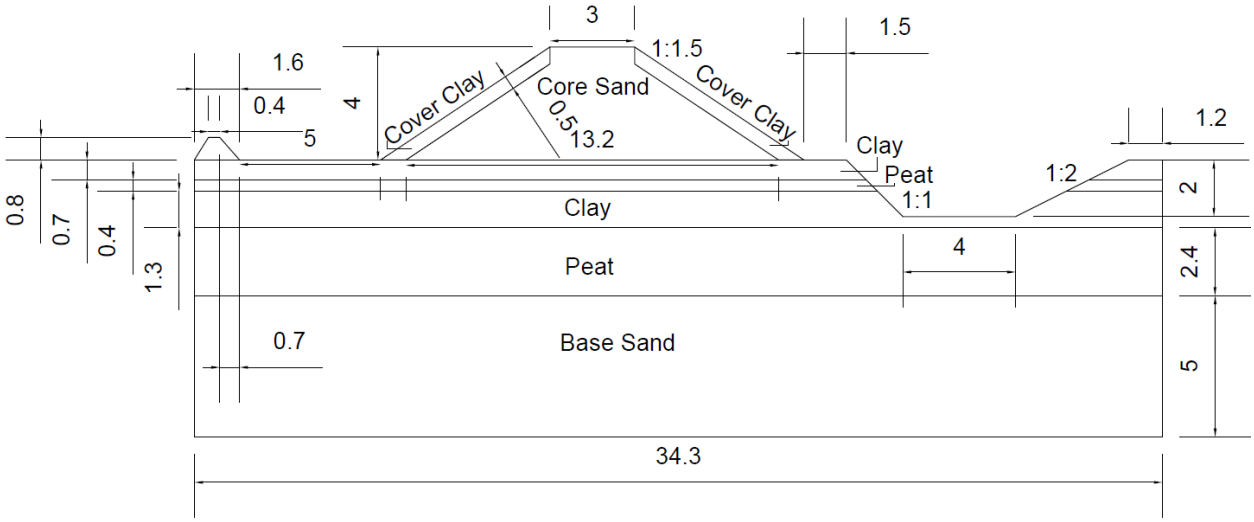

Figure 2. 3. 2D schematization of the entire model during the final construction stage (dimensions in m).

2.3 STRATIGRAPHY

It is stated in the report by Koelewijn (2012) that the levee is constructed on alternating layers of clay and peat with a total thickness of 4.5m. Moreover, in the article authored by Melnikova et al. (2015), it is mentioned that approximately 4m below the ground surface, a stiff sand layer is present upon which the clay and peat composition is situated. The article also reports that the groundwater elevation is the same as the ground level as obtained from the groundwater level map of the Netherlands. The soil stratigraphy depth with respect to NAP determined by 4 manual drillings along with the thickness of each soil layer is provided in Table 2.2 (Koelewijn & Peters, 2012).

Table 2. 2. Soil stratigraphy depth and thickness of the levee test site.

Soil material	Depth: m NAP	Thickness (m)
Clay	-1.1	0.7
Peat	-1.8	0.4
Clay	-2.2	1.3
Peat	-3.5	2.4
Sand	-5.9	5

2.4 GEOTECHNICAL PARAMETERS

It is reported by Koelewijn & Peters (2012) that the geotechnical parameters used to estimate initial settlement due to construction of the levee are determined through back analysis of the levee's collapse. It is also noted that some of these parameters are obtained from laboratory tests, which may be less reliable because of the small sample size of the soil and measurements not being conducted in-situ. In addition, it is crucial to acknowledge that the slope instability design calculations performed using Bishop's method are based on similar calculations conducted prior to and following the September 2008 slope stability test and that certain parameters provided in the report, specifically those related to settlement have been adjusted to fit this test at the IJKdijk site.

Moreover, in the numerical simulation of the 2012 South Dike experiment initial settlement resulting from construction carried out by Melnikova et al. (2015), it is informed that drained soil properties, particularly the effective cohesion and friction angle for peat and clay, are derived through the consolidated drained triaxial tests. As for the numerical simulation of the levee failure, an average undrained shear strength is utilized which is obtained from cone penetration tests (CPT) for clay and peat conducted prior to construction. The value for both is assumed to be the same. Then, the undrained Young's modulus for clay and peat are estimated from the average undrained shear strength. This has been done by obtaining the modulus at 50% of failure strain for clay and peat through laboratory triaxial tests and plotted against the undrained shear strength to deduce a relationship between the two parameters for each soil.

Furthermore, Table 2.3 presents a summary of the initial settlement and stability analysis parameters reported in Koelewijn & Peters (2012) [1] as well as those utilized by Melnikova et al. (2015) [2].

Table 2. 3. Summary of the geotechnical parameters.

Material	Dry unit weight, γ_{dry} [kN/m^3]	Saturated unit weight, γ_{sat} [kN/m^3]	Young's Modulus [MPa]	Poisson's Ratio	Effective Friction angle, φ [°]	Effective Cohesion, c [kPa]	Undrained cohesion, c_u [kPa]	Over-consolidation Ratio, OCR	Consolidation Coefficient, Cv (m^2/s)
Core sand	15.11[1] 18[2]	19.41[1] 20[2]	30[2]	0.3[2]	35[1] 30[2]	0[2]	-	-	-
Cover clay	18[1,2]	18[1,2]	37.5[2]	0.3[2]	32[2]	75[2]	30[1]		-
Clay	15.93[1] 14[2]	15.93[1] 14[2]	1.16 [2] (gravity settlement) 11.6[2] (reloading)	0.3[2] (gravity settlement) 0.49[2] (reloading)	31.92[1] 29.4[2]	6.3[1] 4[2]	20[2]	2.3[1]	6.7E-06[1]
Peat	10.09[1] 10[2]	10.09[1] 10[2]	0.16[2] (gravity settlement) 1.6[2] (reloading)	0.3[2] (gravity settlement) 0.49[2] (reloading)	33.87[1] 27.5[2]	0[1] 9.7[2]	20[2]	2.3[1]	8.3E-06[1]
Sand	18[1] 19[2]	20[1] 19[2]	150[2]	0.3[2]	35[1] 31.1[2]	0[1,2]	-	-	Drained[1]

2.5 LOAD SEQUENCE

Construction of the South Dike commenced on June 13, 2012, and reached completion approximately two weeks later, on June 26, 2012 (Koelewijn, 2012). This is three months ahead of the start of the experiment, allowing for soil consolidation to take place through the dissipation of excess pore pressure (Melnikova et al., 2015).

According to the report by Koelewijn (2012), the levee experiment followed the loading sequence outlined below, along with their corresponding time (chronology):

1. **First day of the test, 12:12pm, September 3rd, 2012 (t=0hrs):** The sand core of the levee is gradually infiltrated with water until a phreatic level of 0.5m above the Northern toe level is attained.
2. **From t=1.90 to t=9.55hrs:** The basin at the South side of the levee is filled (1m).
3. **Second day:** At the Northern side of the levee, a ditch is excavated 1.5m from the toe in multiple stages.
4. **From t=23.17 to t=24.05hrs, 1st excavation stage:** Depth of 0.5m and a bottom width of 2m. The left side slope is 1:1 while the right-side slope is 1:1.5.
5. **From t=24.88 to t=26.30hrs, 2nd excavation stage:** Depth of 1m and the bottom width remains as 2m. Slopes are maintained as well.
6. **From t=26.80 to t=28.30hrs, 3rd excavation stage:** Bottom width widened to 4m while depth of 1m is maintained.
7. **Third day of the test:** Excavation is continued.
8. **From t=45.80 to t=47.30hrs, 4th excavation stage:** Depth of ditch is now 1.5m with a bottom width of 4m as the previous stage. Left side slope is 1:1 and right-side slope is 1:2.
9. **From t=49.80 to t=52.55hrs, 5th excavation stage:** This is the final stage where the depth is now 2m below ground surface. The bottom width and sides slopes are as before.
10. **Fourth day of the test, from t=67.63hrs:** Sand core of the levee is infiltrated with water again.
11. **At t=67.97hrs:** Infiltration is stopped as settlement and horizontal deformation is observed.
12. **At t=69.83hrs:** Infiltration is resumed.

13. **From t= 76.85hrs:** The six tanks on top of the levee are filled with water starting with an initial level of 0.25m which is completed within 30 minutes. Typically, every seven hours, another round of filling takes place.
14. **At t=117.65hrs:** A water level of about 1.75m in the tanks is reached.
15. **Sixth day of the test, Saturday September the 8th:** This is the final day of the test. The levee sand core is completely infiltrated with water. In addition, water is pumped out of the ditch.

The numerical simulations conducted in this study tries as much as possible to replicate these load sequences. There are some differences. For instance, the water level in the container is set at 1.4m. This value is derived from the information reported in Melnikova et al. (2015) which states that the volume of each container is 28m^3. Therefore, considering its placement on top of the levee with a crest width of 3m and a container length of 6.7m, the resulting height amounts to about 1.4m. Moreover, some simplifications have been made such as omitting the inclusion of water in the ditch. The numerical models will be further explained in Chapters 5 and 6 of this thesis.

2.6 FAILURE DESCRIPTION

It has been anticipated before the start of the levee experiment aimed at examining macro-instability failure mechanisms that two potential modes of failure were possible. The first involved the uplift or rupture of the clay cover due to the generation of high pore pressures resulting from water infiltration into the levee core. The second mode entailed the occurrence of slope instability, caused by a deep sliding plane within the original subsoil on which the levee is constructed. Ultimately, the cause of the levee failure was the second mode (Koelewijn, 2012).

On the sixth day of the test after 122.26 hrs, at 2.27pm on Saturday September the 8th, the collapse occurred (Koelewijn, 2012). This happened after the sand core was forcefully saturated with water. The slope of the ditch that was near to containers 4 and 5 fragmented (containers position in Figure 2.2). Subsequently, another sliding movement was observed but on a less deep plane, and there was a rapid reduction in pore pressure within the sand core. Due to insufficient time for the pore pressures to dissipate, the failure of the levee occurred in predominantly undrained conditions (Melnikova et al., 2015). An aerial view of the collapsed levee is shown in Figure 2.4.

Figure 2. 4. An aerial photograph of the South Dike failure by Boertjens Chose (Zomer, 2012).

The criterion for the deformation of the levee is that a minimum deformation of at least 20 cm is required. This was met as measured by the inclinometer in the middle section of the levee, right in front of the toe at 2:13pm on the failure day (Koelewijn, 2012). The post-failure cross-section of this part of the levee along with the indication of the shear planes, deformation and skewed peat layer is presented in Figure 2.5.

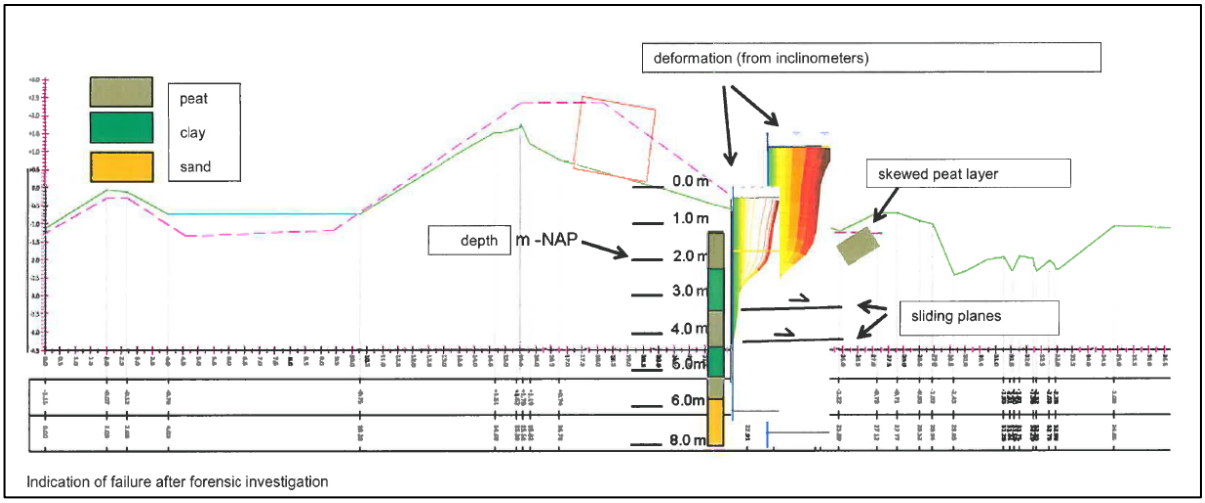

Figure 2. 5. Middle section of the South dike, indication of failure after forensic investigation (Koelewijn, 2012).

Moreover, it is reported in Koelewijn (2012) that slope stability analysis has been carried out using Bishop (1955) and Van (2001) methods. It is estimated that after the last excavation stage, the factor of safety is 1.05 using Van's method and 1.08 using Bishop's method. Both methods yield similar results which are close to 1, indicating a situation close to failure. At the failure stage of the experiment, the calculated safety factor is 0.94 and 0.98, using Van's and Bishop's methods respectively. Again, similar results are provided by both methods. The safety factor is below 1 which means that the levee has failed. These values will serve as a reference for the numerical modelling of this experiment.

3 METHODOLOGY

In this chapter, the numerical tools used to simulate the IJkdijk South Dike experiment will be explained, specifically the finite element method (FEM) and the material point method (MPM). Additionally, the constitutive models employed to represent the soil behaviour will be explained.

3.1 COMPUTATIONAL TOOLS

To simulate the levee up to the onset of failure, FEM is utilized. Conversely, for analysis beyond the onset of failure, in other words, for large displacement analysis, MPM is employed. Girardi et al. (2022) have suggested utilizing a combination of FEM and MPM to simulate slope instability. FEM permits the investigation of pre-failure due to its computational efficiency. However, standard Lagrangian FEM will not converge past the onset of failure because of extreme element deformation. Hence, subsequently, MPM can be applied to describe the complete failure mechanism, including post-failure.

3.1.1 Finite element method

The FEM software used is Midas FEA NX (2023). This software allows for the execution of construction stage analysis. Therefore, the simulation can be performed in stages to replicate loading stages conducted in the experiment. Each construction stage is not analysed independently, which implies that structural changes and loading history from the preceding stage impact the results of the following stage analysis. The analysis features used to carry out the construction stage analysis in this study include stress analysis and sequential-stress-seepage-slope analysis.

In stress analysis, time is not considered within its domain, therefore, it is not possible to specify the duration for applying the boundary condition such as the infiltration of water into the levee core over a specific time.

The stress-seepage analysis is a one-way coupled approach, where the pressure distribution obtained from the seepage analysis is used in the subsequent stress analysis to revise the stress state and soil displacements. This method is not fully coupled, which means that changes in soil effective stresses do not affect the water pressures. Only the water pressure distribution influences the effective stresses of the soil.

There are two types of seepage analysis that are governed by Darcy's law: steady state and transient analysis. The difference between the two lies in the boundary conditions at the interface of the ground or levee. In steady state flow, the boundary conditions remain constant over time without any changes. For example, this occurs when there is a constant river level behind a levee. On the other hand, transient analysis takes into account the influence of time. For instance, it considers variations in river level, such as a rise or fall, behind a levee.

Furthermore, slope stability is analysed using the strength reduction method (SRM). Midas FEA NX allows to conduct slope stability analysis using SRM in every stress analysis performed in the construction stage analysis. The failure point of the slope is determined using this method when the calculation no longer converges. This is achieved when the calculation stops converging through the gradual reduction in the soil shear strength and friction angle. The minimum factor of safety of the slope is then calculated using highest strength reduction ratio at the failure point.

Additionally, it is possible to allow an undrained material behaviour to be considered in any stress construction stage or for the entire simulation. When stress is analysed under drained condition, the software assumes that the dissipation of water has occurred over an extended period. Conversely, when accounting for undrained soil behaviour, failure triggered by loading occurs rapidly, allowing no time for water dissipation.

3.1.2 Material point method

Simulations carried out by FEM are analysed under quasi-static conditions. Its objective is to seek for an equilibrium condition. In doing so, the computational mesh formed by discretizing the continuum into discrete elements becomes distorted. This is typical in problems that involve a large displacement. Elements are entangled because of mesh distortion, and this exerts a significant impact on the solution for large deformation problems (Sulsky et al., 1994). For this reason, results are not accurate and ultimately, the solution does not converge. Figure 3.1 illustrates a case of severe mesh distortion when simulating a large deformation problem using the standard Lagrangian FEM. Hence, MPM is introduced to overcome the problems arising from large deformations.

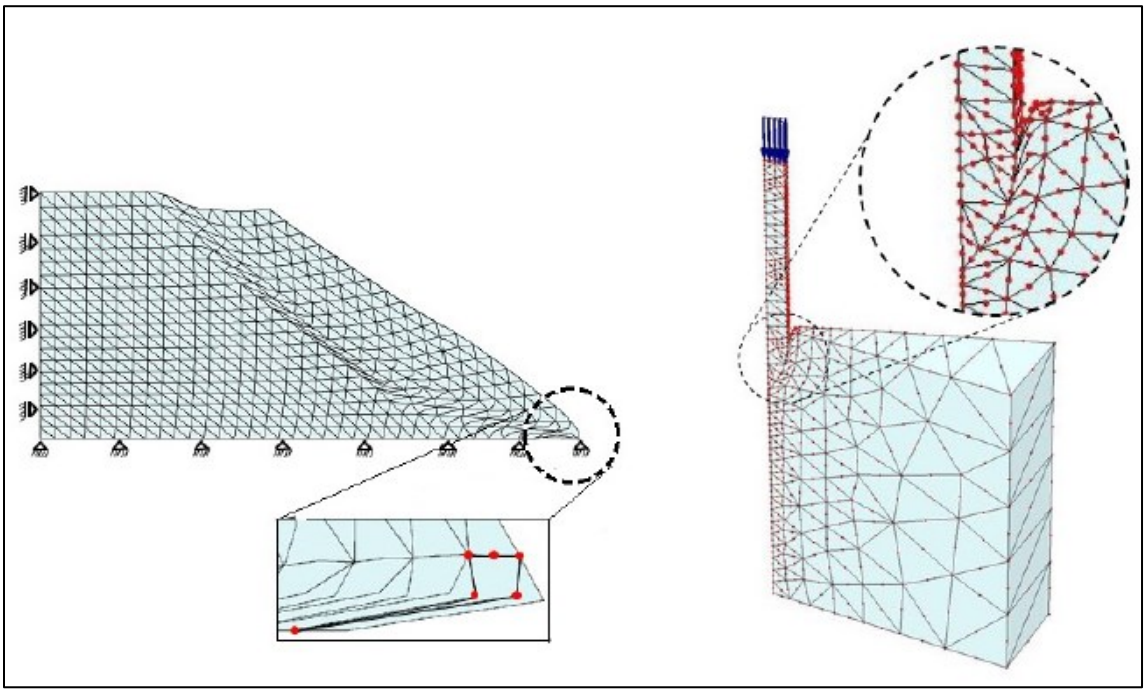

Figure 3. 1. Severe mesh distortion example when simulating a large deformation problem using the standard Lagrangian FEM (Rohe & Vermeer, 2014).

While there exist alternative numerical formulations to resolve distortion issues, such as the arbitrary Lagrangian-Eulerian FEM (ALE FEM) that allows for changes to the computational mesh, it can be computationally expensive in certain cases. Moreover, the accuracy of results obtained from remeshing techniques and ALE FEM may be uncertain because challenges are encountered with history-dependent materials during the remapping of state variables. In a study by Girardi et al. (2021), similar results were obtained with FEM

and limit equilibrium method (LEM) at small strains when MPM was used to simulate an experimental large-scale slope stability problem and it had the advantage of simulating large strains.

The spatial discretization of the computational domain in MPM consists of two frameworks which are the material points (MPs) and the computational mesh. The MPs are considered to represent the continuum body as a set of Lagrangian points. The initialization and storage of all physical properties of the continuum such as velocities, stresses and strains are held by the MPs during an analysis. Moreover, the equations that are solved at the MPs are the mass conservation and that of the constitutive models adopted to describe the behaviour of the soil materials.

With regards to the computational mesh, it is comparable to the mesh of conventional FEM. At the nodes of the mesh, the discretized momentum balance equations are solved. During computation, the MPs can move throughout the mesh, which is referred to as Eulerian mesh, hence, providing the Lagrangian description of the continuum. It is to be noted that the mesh covers the entire domain and those without MPs are labelled as inactive.

The existence of MPs and their movement throughout the mesh during an analysis is what differs MPM from FEM significantly. It is basically an advanced formulation of FEM. Thus, within the finite element framework, it is categorized under an ALE formulation (Beuth et al., 2010).

Figure 3.2 demonstrates the MPM algorithm for a single calculation step of a time increment in four stages. At the start of the time step, all the relevant quantities required to define the momentum balance equations are mapped from the MPs to the computational mesh (Fig. 3.2(a)). Next, the equations of motion are solved at the nodes of the mesh to determine the incremental primary unknown variables (Fig. 3.2(b)). Then, the mapping of the nodal solution back to the MPs takes place to calculate the stresses and strains along with updating their positions, velocities, and accelerations (Fig. 3.2(c)). Thereafter, since the mesh does not store any permanent information, it can be reset freely or kept fixed.

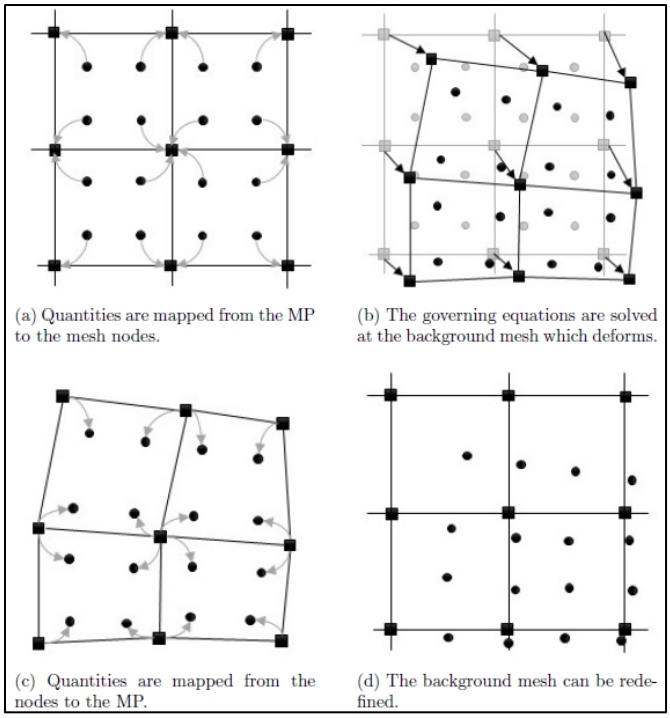

Figure 3. 2. MPM calculation steps (Ceccato, 2015).

Currently, there are four formulations of the MPM which are one-phase single point, two-phase single point, two-phase double point, and three-phase single point approach. Single point refers to one MP carrying all phases involved and double point refers to two MPs carrying a different phase each. The formulation to be adopted depends on the specific field of application. This simplifies the problem and reduces the computational time since it is not required to consider all interactions between the solid, liquid and gas phases that make up a soil mixture for every geomechanical problem.

Fully saturated drained or undrained soil condition can be modelled by the one-phase single point formulation. This simplification is possible because, in the drained condition, excess pore pressure is 0, and in the undrained condition, the relative movement between solid and liquid phase is set to 0. Therefore, only the solid velocity field is considered and there is no excess pore pressure generation. As for the two-phase single point formulation, it is typically applied when simulating consolidation or problems where generation or dissipation of excess pore pressure are present. Thus, both the solid and liquid movements are accounted for. Furthermore, the two-phase double point formulation should be applied for cases in which there is a phase transition, or a role is played by the entry and exit of groundwater and free surface water. Moreover, in unsaturated soil conditions, all three constituents of the soil are

found and hence, the three-phase single point formulation should be utilized to take into consideration the acceleration of the gas phase. Such applications are rainfall infiltration and effects of drought in slope failure.

As reported earlier, the failure of the IJkDijk levee occurred under undrained conditions when the core was saturated with water. Therefore, the one-phase single point formulation of MPM would be used for the post-failure analysis. The general form of the governing equations are as follows:

1. Mass conservation

The differential equation (Eq.3.1) describes the conservation of mass.

$$\frac{d\rho}{dt} + \rho\, div(\vec{v}) = 0 \tag{3.1}$$

The total time derivative is denoted by d/dt, ρ is the mass density of the material and $\vec{v}$ is the velocity vector. This relation implies that the mass of each MP remains constant during deformation.

2. Momentum balance

The conservation of momentum equation is presented in equation 3.2.

$$\rho \frac{d\vec{v}}{dt} = div(\sigma^T) + \rho\vec{g} \tag{3.2}$$

The acceleration vector is denoted by d$\vec{v}$/dt, σ is the stress matric and $\vec{g}$ is the gravity vector. In contrast to FEM, the acceleration term is considered by MPM, enabling it to perform dynamic simulations.

3. Conservation of energy

Equation 3.3 represents the energy conservation equation. It implies that only mechanical work is considered as the source of energy while heat or any thermal energy sources are neglected.

$$\rho \frac{dE}{dt} = \dot{\varepsilon}^T \sigma \tag{3.3}$$

The internal energy per unit mass denoted by E and $\dot{\varepsilon}^T$ is the deformation rate matrix.

There are two boundary condition (BC) types that can be applied to the formulation. Firstly, the essential BCs or Dirichlet BCs which correspond to prescribed displacements. These are defined by equation 3.4.

$$\vec{u}(\vec{x}, t) = \vec{U}(t) \tag{3.4}$$

The prescribed surface displacement vector is denoted by $\vec{U}(t)$.

Secondly, the traction BCs, also known as the natural BCs or Neuman BCs which correspond to prescribed boundary stresses. These are defined by equation 3.5.

$$\sigma(\vec{x}, t)\, \vec{n} = \vec{\tau}(t) \tag{3.5}$$

The outward unit normal vector of the traction boundary surface on which the stress is applied is represented by $\vec{n}$ and the prescribed surface traction vector is $\vec{\tau}(t)$.

Moreover, the post-failure analysis of the levee simulated in this study is performed using Anura3D (2023), an open-source code developed by the Anura3D MPM Research Community. The computational cycle for the one-phase single point MPM formulation for each timestep, as summarized from the Anura3D Scientific Manual (Anura3D MPM Research Community, 2022) is as follows:

1. Nodal mass is calculated using shape functions to form a lumped mass matrix.
2. Internal and external forces at nodes are evaluated.
3. Momentum balance equation is solved, and nodal accelerations are determined.
4. Velocity at MPs are updated.
5. Nodal momentum is updated.
6. Nodal velocities are updated.
7. Incremental nodal displacement is computed.
8. Strain increment is computed.
9. Stresses are updated using material constitutive model.
10. Volume and mass densities of MPs are updated.
11. MP displacements and positions are updated.
12. As MPs now contain updated information, nodal values are discarded, and computational mesh is initialized for the next step.

It should be emphasized that that while MPM has the advantage of simulating large deformations, which FEM struggles with due to element distortion issues, it is not without drawbacks. Numerical instabilities can arise stemming from MPs crossing element boundaries, and computational time can be expensive, especially when performing a coupled analysis for problems involving a low permeability soil.

3.2 CONSTITUTIVE MODELS

The mathematical idealizations of material behaviour are constitutive models. These models characterize the stress-strain relationship of a material as well as defining its stiffness. The model should be selected depending on how well it can simulate the characteristics and behaviour of the soil. Besides, the availability of data that is used to calculate the model parameters influences the choice. There are several models available in literature; however, this thesis focuses on elaborating on only three elastoplastic models used, where the material behaviour is assumed to be elastic up to the yield stress, after which deformation becomes plastic.

3.2.1 Mohr-Coulomb

The material behaviour property which defines the Mohr-Coulomb constitutive model is an elasto-perfect plastic type. This is illustrated in Figure 3.3. The stress (σ')- strain (ε) relationship demonstrates that the deformation is elastic (ε^e) below the yield stress. Upon exceeding the yield stress, the material undergoes permanent plastic deformation (ε^p) without any further increase in stress.

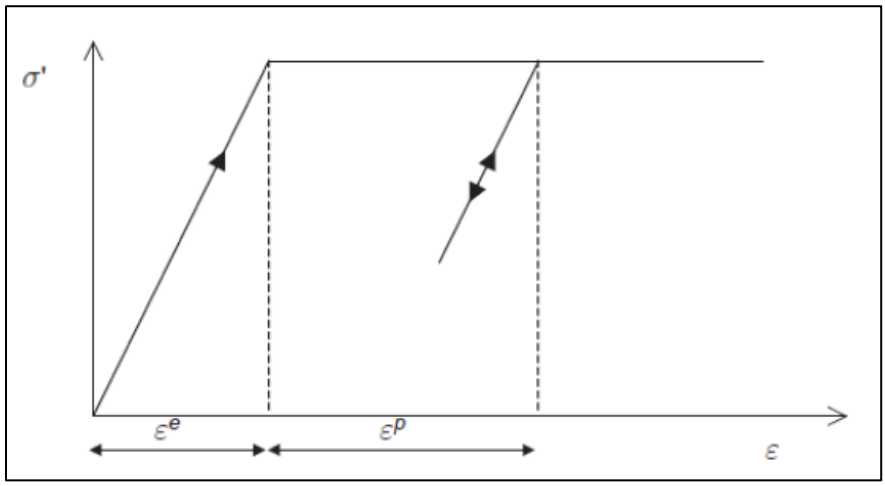

Figure 3. 3. Stress-strain relationship of an elasto-perfect plastic material, obtained from Midas FEA NX (2023) tutorial manual.

Coulomb states that the shear strength of soil is comprised of two components which are cohesion (c) and friction angle (φ). Equation 3.6 linearly expresses its relationship with the two components and normal stress (σ).

$$\tau = c + \sigma tan\varphi \tag{3.6}$$

Mohr-Coulomb's failure criterion is stress-path independent. In other words, the yield behaviour is not influenced by the material's stress history and is determined solely by its present stress state. Also, because the original model does not capture a material's hardening or softening behaviour, this means that the yield function is fixed in the stress space without considering a hardening rule. Although these assumptions may not precisely simulate actual soil behaviour, the analysis is simplified.

Figure 3.4 presents the failure envelope for drained (a) and undrained (b) soil condition. In drained condition, c is the intercept of linear relationship between shear stress and normal stress while the friction angle is the slope. As for undrained condition, c is equal to the undrained shear strength (s_u) and friction angle is 0.

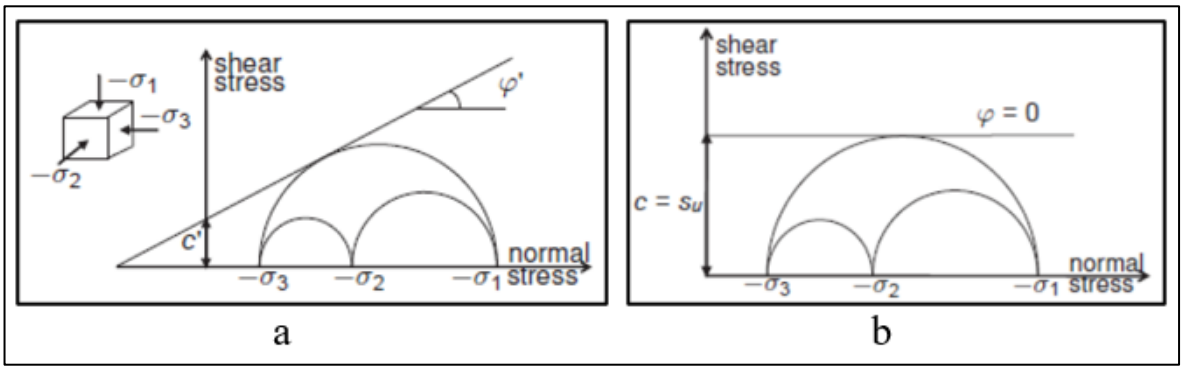

Figure 3. 4. Mohr-Coulomb failure envelope for drained (a) and undrained (b) soil conditions, retrieved from Midas FEA NX (2023) tutorial manual.

Furthermore, other parameters that are included in the model are dilatancy angle and tensile strength. The dilatancy angle is a strength parameter for roughness. With regards to tensile strength, it is generally ignored for geo-materials as it is significantly lower than compressive or shear strength.

3.2.2 Drucker-Prager

Like the Mohr-Coulomb model, the strength of soil is derived from cohesion and friction in the Drucker-Prager model. Both models are defined in a very similar manner. However, the Drucker-Prager model solves the numerical issues that happen on the corners of the yield shape of the Mohr-Coulomb model. The yield surfaces of both models on the principle effective stress space and deviatoric plane are shown in Figure 3.5(a) and (b) respectively.

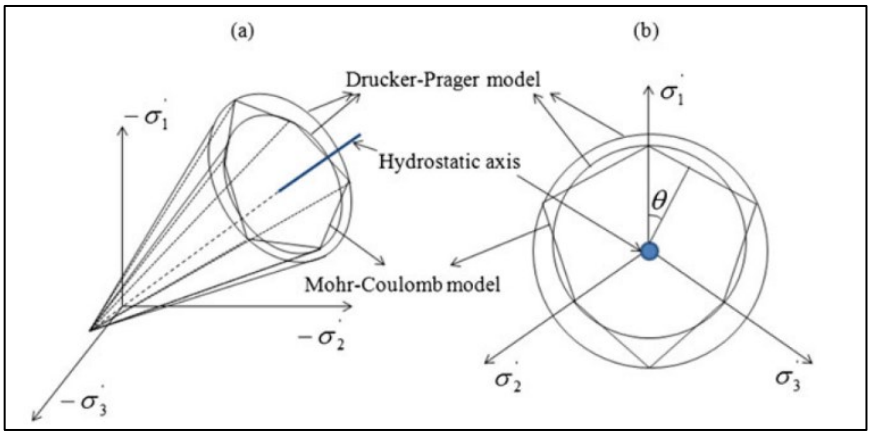

Figure 3. 5. Mohr-coulomb and Drucker-Prager yield surfaces on the principle effective stress space (a) and on the deviatoric plane (b) (Kim et al., 2012).

It can be observed that, as opposed to the Drucker-Prager model, there are six corners and a common vertex on the tension side of the hydrostatic axis included in the yield function of the Mohr-Coulomb model. Numerical instabilities in return mapping can emerge from the discontinuous corners (Borja et al., 2003; Wang et al., 2004). Return mapping is a numerical method employed to determine stress and strain states during plastic deformation.

3.2.3 Soft Soil

Unlike the Mohr-Coulomb and Drucker-Prager models, the soft soil model is stress-path dependent. Thus, the stress history of the material is taken into consideration, allowing a more realistic representation of the soil's behaviour. This model is well-suited for simulating materials that have a high degree of compressibility like normally consolidated clay and peat, etc. Commonly, it is used for the analysis of settlement.

The main nonlinear parameters for the estimation of the soil strength are the compression index (C_c), swelling index (C_s), cohesion, friction angle and the dilatancy angle.

The C_c and C_s accounts for the stress-history of the soil and are derived from the plot of void ratio-effective stress on a logarithmic scale for the material under study. These indexes are used to calculate the slope normal consolidation line (λ) and the slope of the overconsolidation line (κ). Their relationship with the slopes in Midas FEA NX (2023) are the following:

$$\lambda = \frac{C_c}{2.303} \tag{3.7}$$

$$\kappa = \frac{C_s}{2.303} \tag{3.8}$$

Both lines are shown on a plot of volume change versus pressure in Figure 3.6.

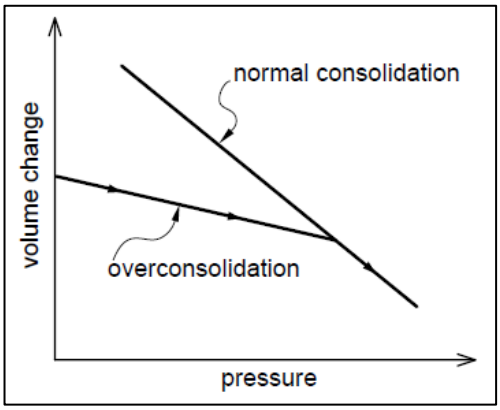

Figure 3. 6. Normal consolidation and overconsolidation line, obtained from the tutorial manual of (Midas FEA NX (2023).

Moreover, the cohesion and friction angle are the same failure parameters as used to define the shear strength in Mohr-Coulomb's model. As for the dilatancy angle, the recommended value by Midas FEA NX (2023) is zero. This is because soft soils such as clay and peat experience negligible dilation when subjected to shear stress. Regardless of the overconsolidation degree, clays have a very low dilation angle (Hong, 2020).

Furthermore, another important parameter in the soft soil model, but in general for constitutive models that consider a soil's stress history is the overconsolidation ratio (OCR). The influence of past loading and unloading cycles on the mechanical response of the soil is simulated through the OCR. The OCR value is the ratio of the pre-consolidation stress to the present stress endured by the soil. Hence, stress distribution of a soil's in-situ state can be determined from the current loaded stress distribution through the OCR.

4 BENCHMARK SLOPE

Prior to simulating the pre- and post-failure of the IJkdijk experimental levee, a simple 2D slope is modelled as a benchmark. The slope is analysed up to the failure point using both FEM and MPM, and a comparison is made in terms of stresses and displacement. Next, the total stresses and pore pressures from the pre-failure analysis, simulated by FEM, are transferred to MPM for the post-failure analysis. The goal is to ensure consistency between the two different techniques in simulating the same problem.

4.1 FEM MODEL

This subsection presents the numerical model setup, analysis type and outcomes of the 2D plane strain FEM model benchmark slope.

4.1.1 Geometry and Discretization

The benchmark slope has a cross-section of 2.2 m x 1 m, with a slope angle of 20.56°. The depth of the base clay is 0.4 m, while the height of the levee composed of sand is 0.6m from the top of the base. The crest width measures 0.6 m, and the distance in front of the toe 0.6m. The water level is at the same elevation as the toe. As for the size of the mesh, it is set to 0.05m and the element type is a combination of triangles and quadrilaterals. The total number of nodes is 708 and for the elements, it is 618. Furthermore, the boundary conditions imposed are the loads on the crest and the solid fixities at the base, left and right sides of the model. The load is applied in 5 stages from 5kN/m^2 up to 25kN/m^2 in increments of 5kN/m^2. The base is fully fixed while the sides are fixed normally. Figure 4.1 illustrates the model geometry, discretization, and boundary conditions.

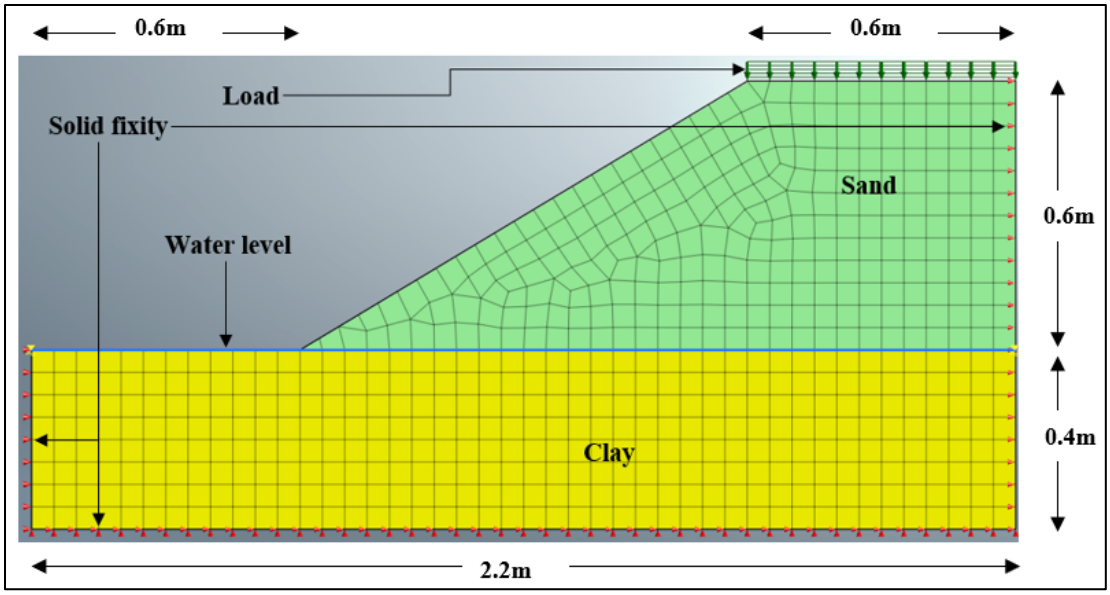

Figure 4. 1. Benchmark slope FEM model geometry, discretization, and boundary conditions.

4.1.2 Material

The levee is constructed of sand, whereas the base is made from clay. The constitutive model selected to describe both materials is the elasto-plastic Mohr-Coulomb failure criterion. The sand behaviour is drained while for clay, undrained. The effective stiffness and strength parameters of the material are utilized. To improve convergence, cohesion of the sand is set to 1kN/m^2. Further material properties and mechanical parameters are provided in Table 4.1.

Table 4. 1. Material properties and mechanical properties of the benchmark slope.

Material property	**Levee sand**	**Base clay**
Saturated unit weight [kN/m^3]	20	16
Unit weight [kN/ m^3]	18	16
Initial void ratio [-]	0.5	0.5
Permeability coefficient [m/s]	10^{-4}	10^{-8}
Elastic modulus [kN/m^2]	$30x10^3$	$11.6x10^3$
Undrained Poisson's ratio [-]	-	0.495
Effective Poisson's ratio [-]	0.3	0.3
Effective friction angle [°]	30	30
Effective cohesion [kN/m^2]	1	6

4.1.3 Analysis type

A quasi-static stress analysis considering undrained material behaviour is performed. The maximum negative pore pressure is set to 0 which implies that suction is not considered. Hence, friction and cohesion are not suction-dependent, and a conservative assumption is made.

The analysis is performed in six construction stages. Stage 1 is the stress initialization stage in which stress distribution is established from the self-weight of the levee, in other words, gravity loading phase. From stage 2 onwards to stage 6, a load of 5kN/m^2 is progressively applied, increasing by 5kN/m^2 in each subsequent stage, with the final stage applying a load of 25kN/m^2. The stages are summarized in Table 4.2.

Table 4. 2. Construction stages of the benchmark slope.

Stage	**Load applied**
1	Self-weight/gravity
2	5kN/m^2
3	10kN/m^2
4	15kN/m^2
5	20kN/m^2
6	25kN/m^2

Furthermore, a slope stability analysis using the strength reduction method is also performed. This is applied from stage 2 onwards.

4.1.4 Results

The contour plots of the total stress distribution in the x (*S-XX*) and y (*S-YY*) directions, along with the shear stress (*S-XY*) in the x-y plane and pore pressure distributions, are presented in Appendix A.

In the first stage, the initial stress distribution of the benchmark slope is produced by the application of gravity load. The pore pressure follows a hydrostatic distribution, and the displacement starts from 0. The total displacement plot is provided in Table 4.4.

As load is applied to the crest starting from the second stage, it can be observed that the total stresses begin to increase. A sliding slip surface is developed and clearly shown when a load of 15kN/m^2 is applied in stage 4.

Furthermore, pore pressure develops when the loads are applied. As expected, the pressure distribution is 0 for the slope primarily because it is composed of sand, which has a high permeability and drains water immediately. Also, since suction is not considered in the analysis, the pressure is limited to 0. Positive values represent suction. Conversely, for the base clay, it behaves in an undrained condition and a maximum pressure of -27.24kN/m^2 is generated at a load application of 15kN/m^2.

Moreover, the highest total displacement is about 25mm at the upper portion of the slope where it is concentrated when a load of 15kN/m^2 is applied. This is illustrated in Table 4.4(d). Like in the contour plots of the total stresses and shear stress, the slip surface is evident at this stage.

With regards to the factor of safety (FS), its values are recorded in Table 4.3 for stages 2 to 4. As the load increases to 15kN/m^2, the FS approaches a value of 1, indicating that failure is imminent. However, in stages 5 and 6, where the load application is 20kN/m^2 and 25kN/m^2, respectively, convergence cannot be achieved. Hence, post-failure analysis using FEM cannot be conducted, and all the results are only provided up to stage 4.

Table 4. 3. Safety factors at load application of 5kN/m^2, 10kN/m^2 and 15kN/m^2.

Stage	Load applied (kN/m^2)	Factor of Safety
2	5	1.68
3	10	1.19
4	15	1.00

Table 4. 4. Total displacement (m) for (a) stress initialization, (b) load application of 5kN/m^2, (c) load application of 10kN/m^2 and (d) load application of 15kN

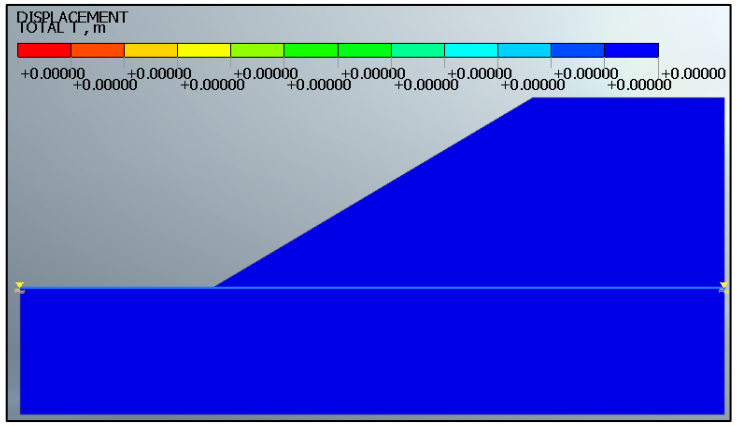

(a) Stress initialization

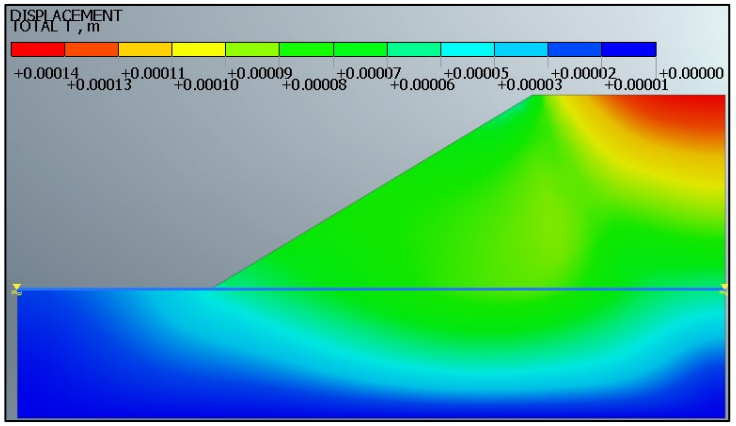

(b) Load applied = 5kN/m^2

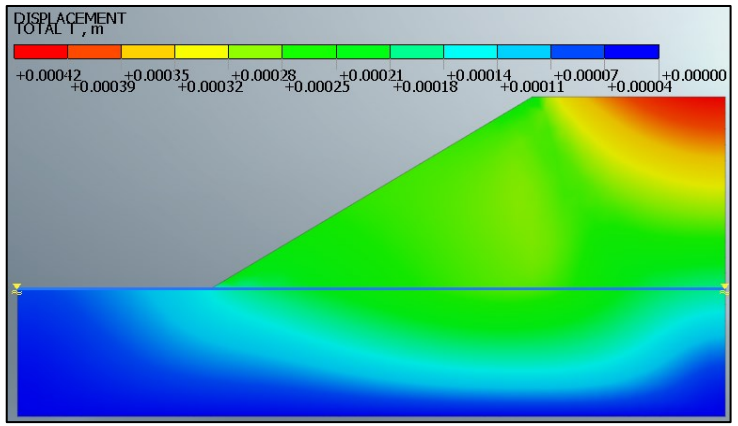

(c) Load applied = 10kN/m^2

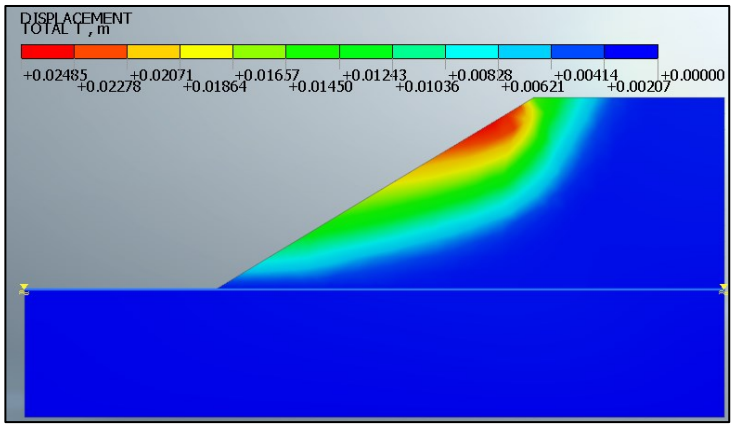

(d) Load applied = 15kN/m^2

4.2 MPM MODEL

This subsection presents the numerical model setup, analysis type and outcomes of the 2D plane strain MPM model benchmark slope.

4.2.1 Geometry and Discretization

The geometry of the MPM model benchmark slope is the same as that of the FEM model, as is the position of the phreatic line (water level). A single point formulation is adopted, and the mesh size is set to 0.05m, like the FEM model. The model consists of 2320 triangular elements and 1229 nodes. As opposed to Lagrangian FEM models, empty areas (inactive blue elements) are required to be defined so that MPs (in active red elements – sand and clay areas) can move into, thus it is also included in the mesh discretization. The number of MPs per element is 3. The model geometry and discretization are displayed in Figure 4.2.

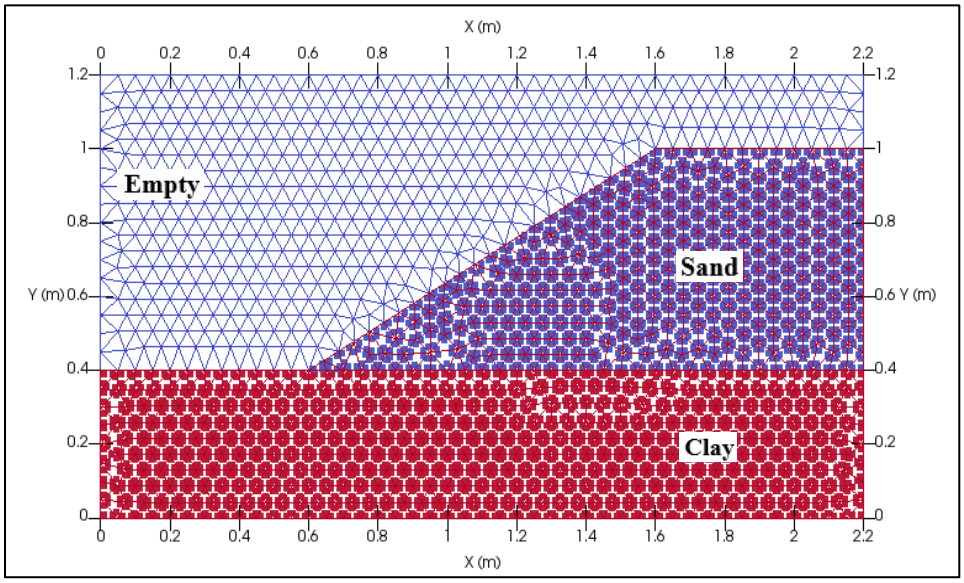

Figure 4. 2. Benchmark slope MPM model geometry and discretization.

Moreover, the boundary conditions include the loads applied on the crest, as well as solid fixities. The load on the crest is applied in stages using the stepwise method, divided into 6 steps. The first step has a multiplier of 0, and the last step has a multiplier of 1. Thus, in the final step, the load reaches 25kN/m^2. It should be noted that the load is applied to the MPs because, in large deformation problems, external loads must be assembled in the MPs to move along with the deforming material. Regarding the fixities, solid fixity is applied in the

horizontal x-direction on the left and right side of the model, in the vertical y-direction at the top, and fully fixed at the base. Figure 4.3 presents the boundary conditions.

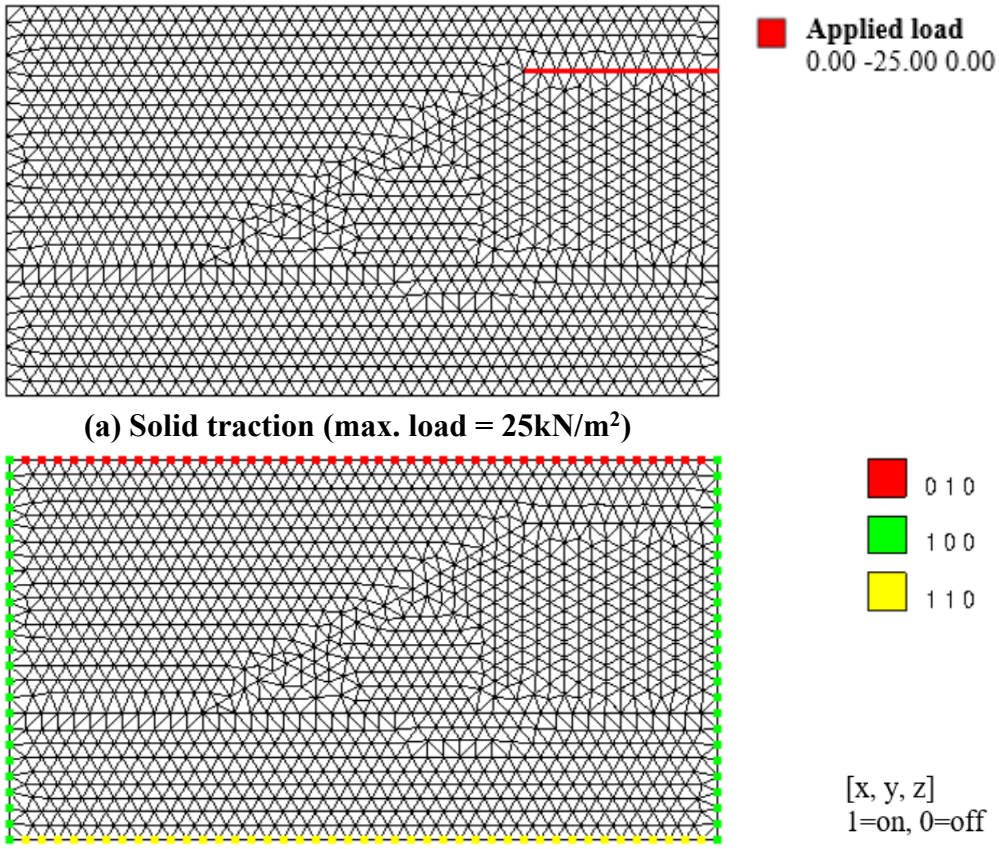

Figure 4. 3. MPM boundary conditions: (a) solid traction (loading) and (b) solid fixities.

4.2.2 Material

As in the FEM model, both the drained levee sand material and the undrained base clay are described using the Mohr-Coulomb failure criterion. The material type for the sand is set as 'dry' and for the base clay as 'saturated-undrained effective stress'. Anura3D requires the solid grains and liquid density to be provided separately, instead of the unit weight of the material. The initial porosities are obtained from their initial void ratios, and the liquid density is assumed to be 1000kg/m^3. Hence, the solid grains density of the materials was then calculated from their unit weights, initial porosity, and the liquid density. Their values are provided in Table 4.5 along with the rest of the material and mechanical parameters that are identical to ones in the FEM model.

Table 4. 5. MPM material properties and mechanical properties of the benchmark slope.

Material property	**Levee sand**	**Base clay**
Material type	Dry	Saturated – undrained effective stress
Initial porosity [-]	0.33	0.33
Density solid [kg/m^3]	2247.01	1942.61
Density liquid [kg/m^3]	-	1000
Effective Young modulus [kN/m^2]	30x10^3	11.6x10^3
Effective poisson's ratio [-]	0.3	0.3
Undrained Poisson's ratio [-]	-	0.495
Effective friction angle [°]	30	30
Effective cohesion [kN/m^2]	1	6

4.2.3 Analysis type

Apart from conducting a dynamic simulation and mapping the results of the onset of failure from the FEM model, two quasi-static stress analysis of the benchmark slope are also performed with different homogeneous local damping conditions (5% and 70%) using the single point MPM formulation.

The analyses are performed in seven loading stages. Stage 0 is the stress initialization stage in which stress distribution is generated from the self-weight of the levee (through the effect of gravity loading). Additionally, the K0-procedure is activated as well as the soil (the slope, crest, and toe 2D-line) and phreatic surface (phreatic line at 0.4m) specified to initialize the stresses considering the initial position of the water level. From stage 1 onwards to stage 6, utilizing the load step (stage) multiplier permitted by Anura 3D, the load is gradually applied until 25kN/m^2 is reached in stage 6. The stages are summarized in Table 4.6.

Table 4. 6. MPM loading stages of the benchmark slope.

Stage	Load multiplier	Load applied
0	0	Gravity
1	0	Gravity + 0kN/m^2
2	0.2	Gravity +5kN/m^2
3	0.4	Gravity +10kN/m^2
4	0.6	Gravity +15kN/m^2
5	0.8	Gravity +20kN/m^2
6	1.0	Gravity +25kN/m^2

It should be noted that in the dynamic analysis, quasi-static convergence with a damping of 70% is implemented only during the stress initialization stage. For the remaining stages, it is not used, and damping is set to 5%.

Moreover, the time per load step (stage) is set to 0.5 seconds which is only considered in the dynamic analysis. The quasi-static simulations run based on the convergence criteria which are the tolerated error of the kinetic energy, the tolerated error of the out-of-balance force, or the maximum number of time steps. To reduce the computational time, a kinetic error and a force error of 0.04 for both the liquid and solid have been set. As for the maximum number of time steps, it is set to 10,000.

In addition, a courant number of 0.98 is used to ensure the stability of the solution, and the strain smoothing feature is applied to minimize kinematic locking.

4.2.4 Results

The MPM simulation results, which cover the evolution of the total stresses normal to the x and y direction of the benchmark slope plane strain model, the evolution of the shear stresses in the x-y plane, and the evolution of the pressure distribution, can be found in Appendix B.

As expected, MPM is able to simulate the entire loading stages to which the slope is subjected to, as opposed to FEM, which stopped when a load of 15kN/m^2 was applied on the crest (close to failure point with FS= 1).

In terms of stresses and pressure distributions during the pre-failure analysis of the slope, among the three MPM analyses, the case of the quasi-static simulation with 5% damping coefficient shows the best agreement with the results of the FEM analysis.

As for the comparison among the MPM analyses, while the quasi-static simulation with a damping of 5% and the dynamic simulation did yield similar stress and pressure distributions throughout all stages, the quasi-static simulation with 70% damping coefficient only did so up to a load of 20kN/m^2 applied. It is well known in literature that high values of damping can alter the failure mechanism. This becomes evident as the collapse of the slope is not captured by the simulation with 70% damping coefficient during the final stage when a load of 25kN/m^2 was applied. For instance, the total stresses in the y-direction ranged between 0kN/m^2 and -48kN/m^2 for the quasi-static simulation with 5% damping coefficient, while for the quasi-static simulation with 70% damping coefficient, the range is substantially lower, between 0.27kN/m^2 and -37kN/m^2.

With regards to the total displacement, at the verge of the slope failure (load application of 15kN/m^2), the maximum value estimated by the quasi-static simulation with 5% damping coefficient, as illustrated in Table 4.7(e) is about 0.70mm. This value is significantly lower than the displacement (around 25 mm) calculated by the FEM simulation (see Table 4.4(d)). The reason for this large difference is the convergence issues faced by FEM at the failure point, making it less reliable in terms of displacement.

Furthermore, increasing the damping coefficient to 70% results in considerably lower total displacements. This can be observed in Table 4.8(g) during the final loading stage, where the highest displacement is just over 1.50mm, in contrast to the 131.9mm measured when the damping coefficient was set to 5%, as presented in Table 4.7(g). In addition, the slip

surface and collapse of the slope is not evident in the quasi-static simulation with a 70% damping coefficient.

Moreover, the dynamic case provides similar total displacement results to the quasi-static simulation with a damping coefficient of 5% up to the stage where a load of 15kN/m^2 was applied, as displayed in Table 4.9. However, during the final stage, it can be observed in Table 4.9(g) that although the result seems similar to the quasi-static simulation with 5% damping coefficient, there is a difference that should be considered. In the dynamic case, the displacement is slightly greater. This disparity is attributed to the fact that they relate to different time periods. The dynamic simulation lasts nearly twice as long (2.5s) compared to the quasi-static simulation, and as the slope is in motion, the displacements are larger in the dynamic case.

Table 4. 7. MPM 5% damping quasi-static analysis total displacement (m) distribution.

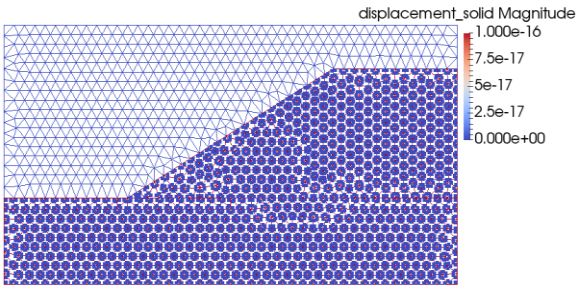

(a) Stress initialization

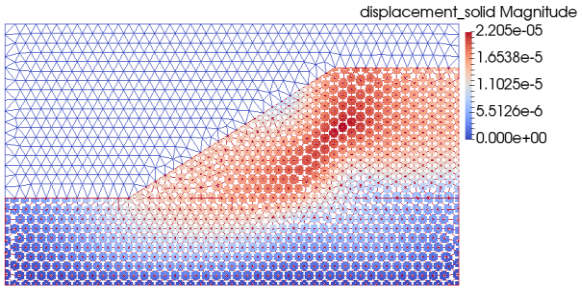

(b) Load stage 1= 0kN/m^2

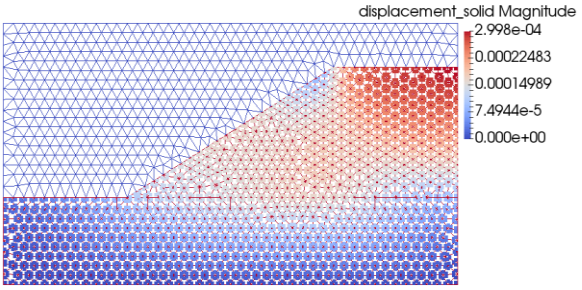

(c) Load stage 2= 5kN/m^2

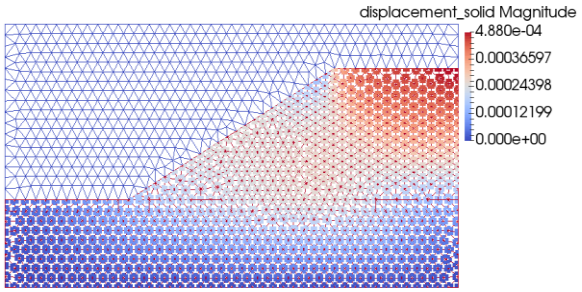

(d) Load stage 3= 10kN/m^2

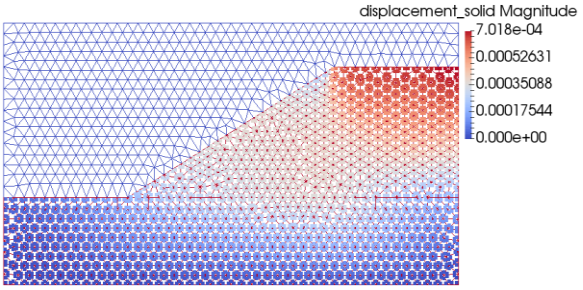

(e) Load stage 4 =15kN/m^2

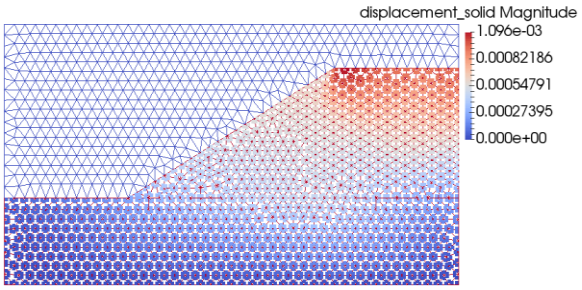

(f) Load stage 5 =20kN/m^2

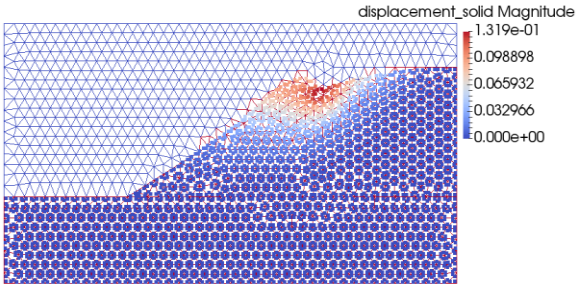

(g) Load stage 6 =25kN/m^2

Table 4. 8. MPM 70% damping quasi-static analysis total displacement (m) distribution.

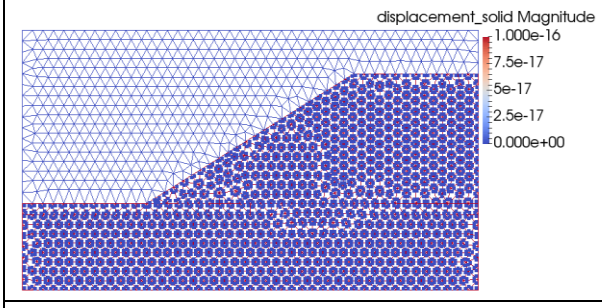

(a) Stress initialization

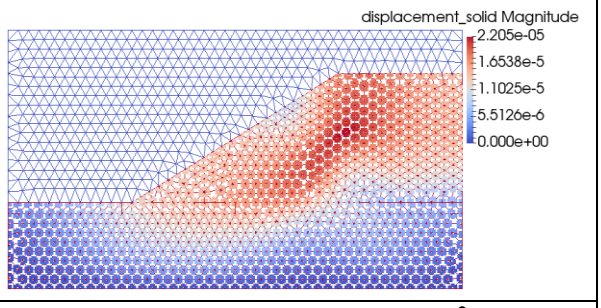

(b) Load stage 1= 0kN/m^2

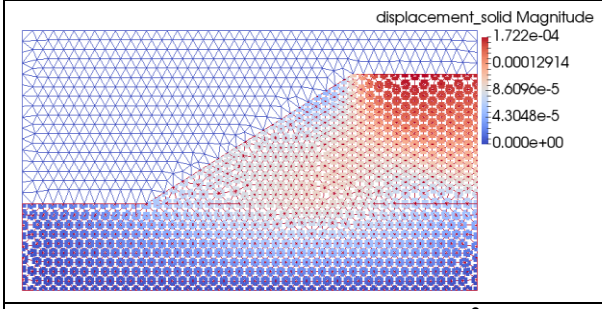

(c) Load stage 2= 5kN/m^2

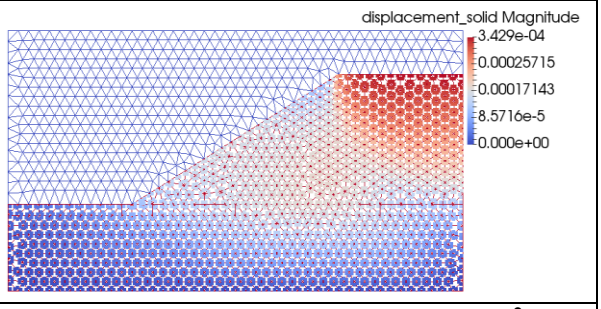

(d) Load stage 3= 10kN/m^2

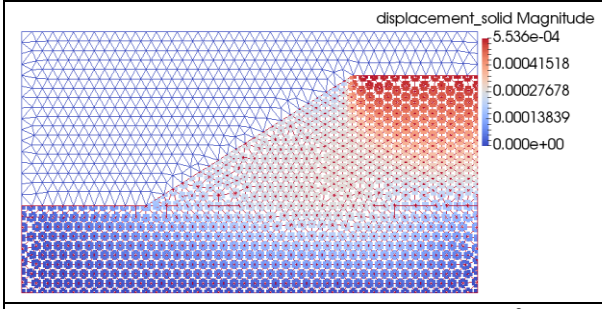

(e) Load stage 4 =15kN/m^2

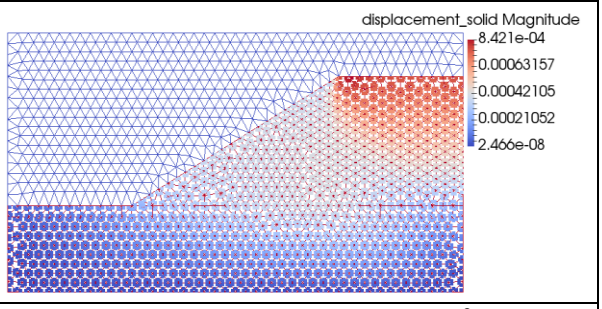

(f) Load stage 5 =20kN/m^2

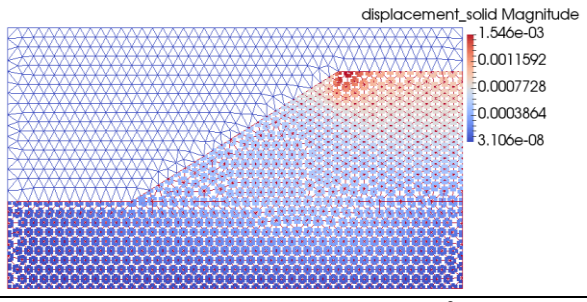

(g) Load stage 6 =25kN/m^2

Table 4. 9. MPM dynamic analysis total displacement (m) distribution.

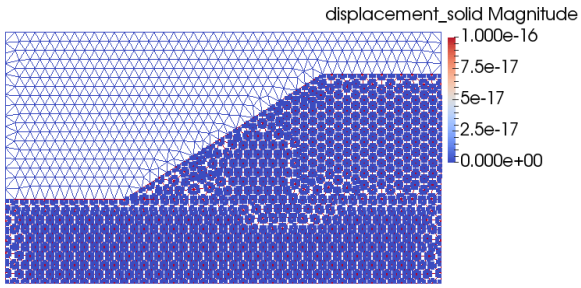	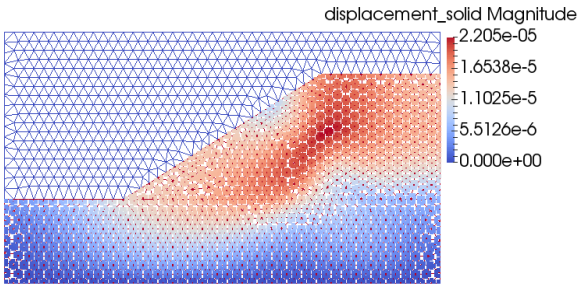
(a) Stress initialization	**(b) Load stage 1= 0kN/m^2**
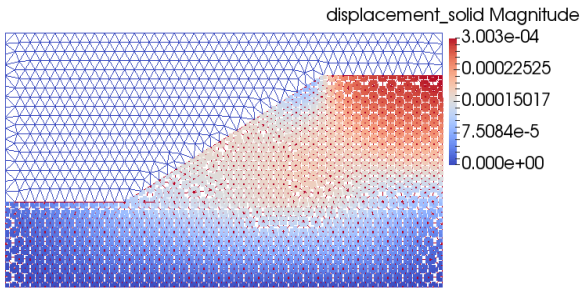	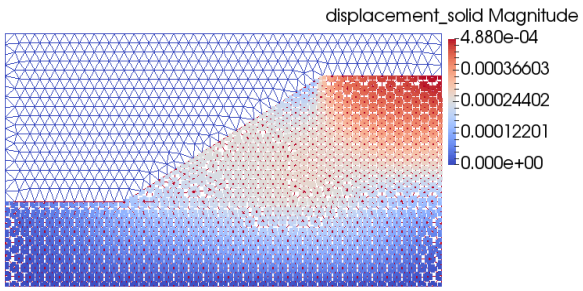
(c) Load stage 2= 5kN/m^2	**(d) Load stage 3= 10kN/m^2**
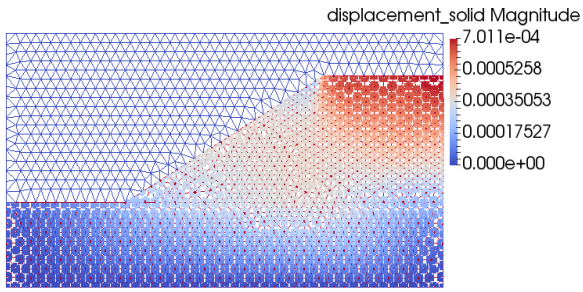	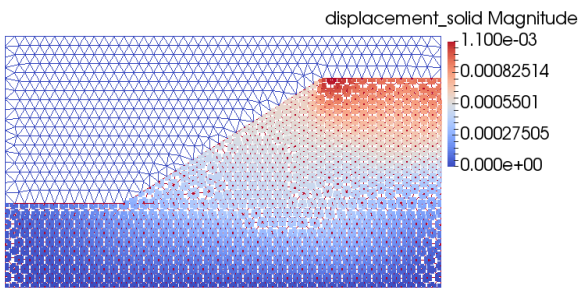
(e) Load stage 4 =15kN/m^2	**(f) Load stage 5 =20kN/m^2**
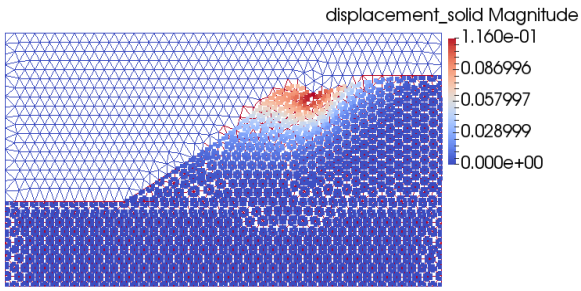	
(g) Load stage 6 =25kN/m^2	

4.3 FEM+MPM MODEL

As seen earlier, FEM analysis could only simulate the loading stages prior to failure of the benchmark slope. Therefore, it is necessary to transfer the total stresses in the x and y directions, including shear stress in the x-y plane, along with the pore stresses, to Anura3D for dynamic post-failure analysis using the MPM. Two simulations were run: the first involved transferring the FEM results produced using Midas FEA NX when a load of 15kN/m^2 was applied, with failure imminent; the second simulation involved transferring the results from an earlier stage where the load application was 10kN/m^2.

Both simulations were run with a damping coefficient of 5% since they are dynamic problems. The stress distributions (normal, shear and pore) from the two simulations are presented in Appendix C. These stress distributions are similar to those generated by the dynamic simulation that was run without involving transfer of stresses from FEM (see Appendix B).

Furthermore, in terms of the total displacement, the results obtained are essentially the same, having a value of 120 mm at the final loading stage. The displacements during the final stage are illustrated in Table 4.10(c) for the case where transfer occurred from a load application of 15kN/m^2, and in Table 4.11(d) from a load application of 10kN/m^2. Both figures display the same slip surface, and their displacement values are also comparable to those generated by the dynamic simulation that was run without involving transfer of stresses from FEM (see Table 4.9(g) in the previous section).

It can now be concluded that mapping stresses produced at the onset of failure or an earlier stage using FEM for the purpose of post-failure analysis using MPM on Anura3D has been validated. Therefore, the simulation of the post-failure analysis of the IJkDijk South Dike using the same procedure can now proceed.

Table 4. 10. Total displacement (m) distribution for the case of stresses transferred from load = 15kN/m^2.

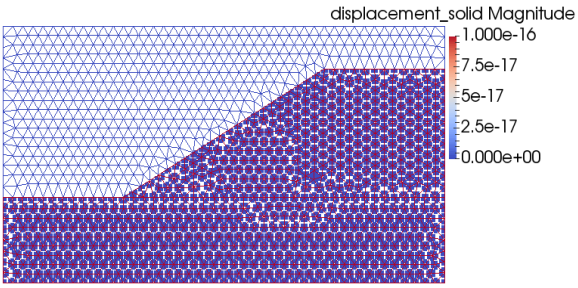

(a) Load transferred (stage 4) = 15kN/m^2

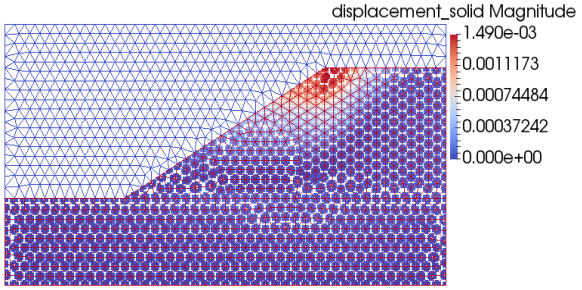

(b) Load stage 5 = 20kN/m^2

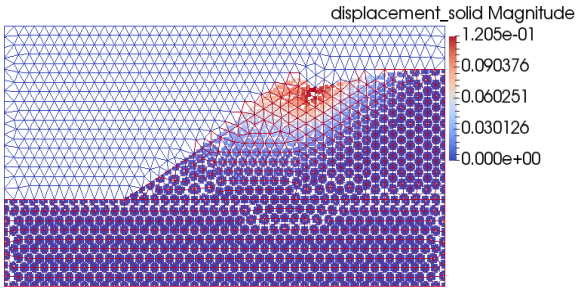

(c) Load stage 6 = 25kN/m^2

Table 4. 11. Total displacement (m) distribution for the case of stresses transferred from load = 10kN/m^2.

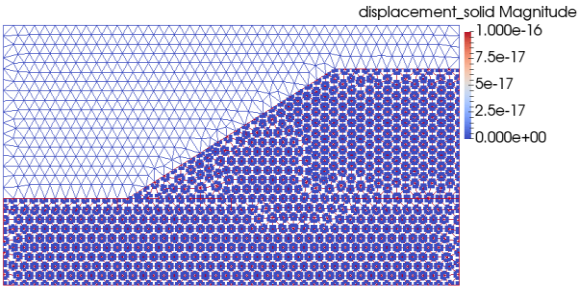

(a) Load transferred (stage 3) = 10kN/m^2

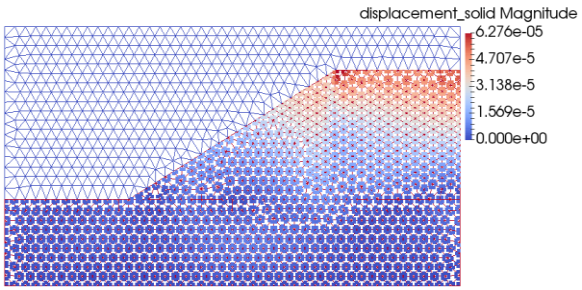

(b) Load stage 4 = 15kN/m^2

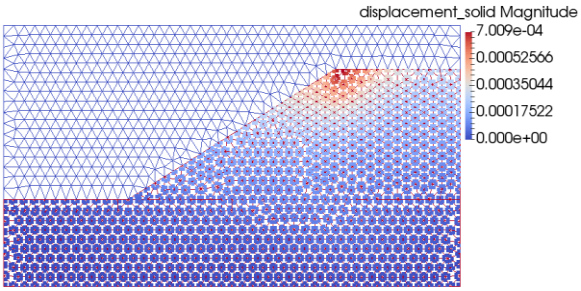

(c) Load stage 5 = 20kN/m^2

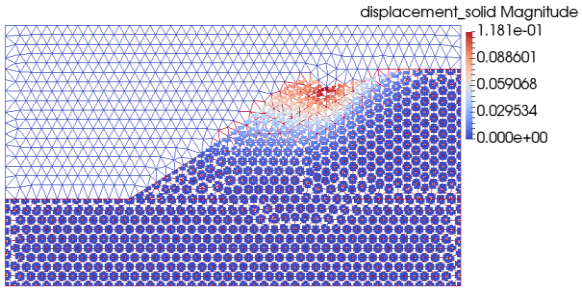

(d) Load stage 6 = 25kN/m^2

5 NUMERICAL MODELLING OF PRE-FAILURE

The numerical model adopting FEM to simulate the pre-failure of the IJkdijk South Dike experiment is described in this chapter. The simulation replicates the load sequence described in section 2.5 chapter 2. The numerical model setup, analysis type, and outcomes of the 2D plane strain model are presented.

5.1 FEM MODEL

5.1.1 Geometry and Discretization

The geometry of the levee is described in detail in section 2.2.3 of chapter 2. The ground water level is set to the same elevation as the toe and follows the ditch line when excavations are made. With regards to the size of the mesh, coarse elements (1m) are used for the base sand layer, less coarse elements (0.5m) for the peat and clay layer just above the base sand, while finer elements (0.2m) are used for the critical zone. These critical zones include the location where excavation is to take place, the first three inter-layers of clay and peat, as well as the levee core and cover. The types of elements used are triangles and quadrilaterals. The total number of nodes is 9181, and the total number of elements is 3030. In addition, to improve the accuracy and numerical simulation of the slope stability analysis, higher order elements are used. The 2D plane-strain FEM model is displayed in Figure 5.1.

Moreover, the boundary conditions include solid fixities at the base and sides of the model, the load of the container filled with water applied on the crest, and the total head for both the basin and the levee core. The base is fully fixed while the sides are fixed normally. The container exerts a pressure of 1.49kN/m^2, and the water inside applies an additional water pressure with a height of 1.4m. The total heads are utilized during the seepage analysis stage, which include steady-state or transient conditions. Initially, both the basin and levee core have a head of 0m. In the subsequent stages, the basin is filled to 1m in a steady state. As for the levee core, it is first filled to a height of 0.5m over a period of about 75.5 minutes, then to 2.5 m in approximately 20.4 minutes, and finally, it is completely filled within a time span of just over 20 minutes. The periods are estimated from the experiment conducted. Additionally, a ‘Review’ boundary condition is applied to the right side of the slope including the ditches.

The Review function is used in Midas FEA NX when it is difficult to locate the exact seepage line. Iterative calculations are made at the selected nodes, and the seepage surface is determined based on the pore pressure value being 0. If the pressure is greater than 0, it is considered as 0, and the node is omitted when it is less than 0. Furthermore, the boundary conditions and the applied positions are illustrated in Figure 5.1.

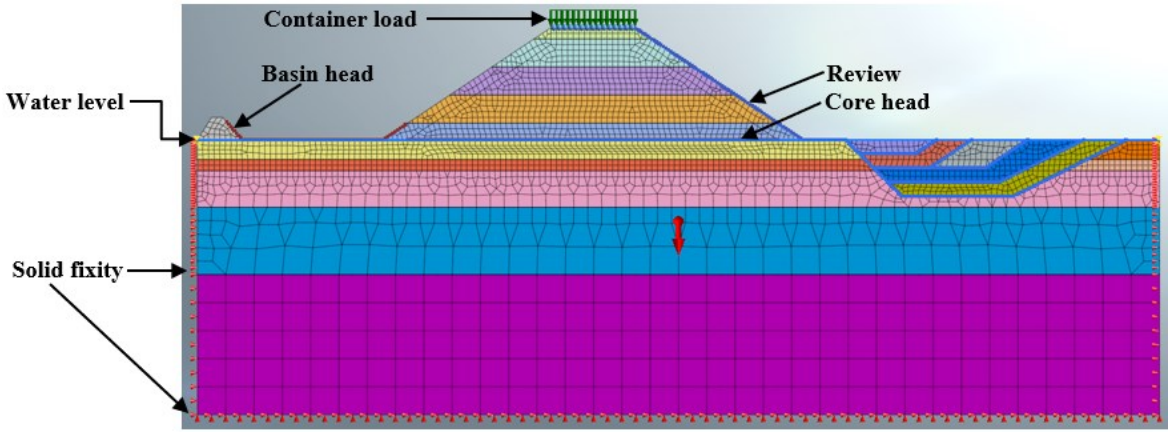

Figure 5. 1. Discretization and boundary conditions.

5.1.2 Material

The core of the South Dike is constructed of sand, whereas the cover is made from low permeable clay. It rests on a foundation composed of interlayers of soft clay and peat, which in turn lie on a thick layer of sand. This arrangement is depicted in the 2D schematization of the entire levee, as provided in Figure 2.3, section 2.2.3 of chapter 2. Additionally, the material used for the small embankment on the left side of the levee is the same clay as that used in the base.

Moreover, the constitutive model selected to describe materials are the Drucker-Prager model for both the cover clay and core sand, the Soft-Soil model for the base clay and base peat, and the Mohr-Coulomb model for the base sand. All of these models are isotropic. The behaviour of the sand materials is drained, while that of the clay and peat materials is undrained. The primary parameters utilized are the effective stiffness and strength parameters for cover clay, core sand and base sand. In addition to the stiffness and strength parameters, the base clay and peat utilize the OCR and slopes of the consolidation and overconsolidation lines. The material properties and mechanical parameters are provided in Table 5.1. These were obtained from Koelewijn & Peters (2012) [1] and Melnikova et al. (2015) [2]. The values with no references were chosen based on the simulation results that were the closest to the experiment.

Furthermore, a parametric analysis has been conducted by using various values of cohesion, friction angle, and slope for both consolidation lines of the base peat to study their effects on the levee failure. Further information on this can be found in Appendix E.

Table 5. 1. Material properties and mechanical properties of the South Dike simulation.

Material property	**Cover clay**	**Core sand**	**Base Clay**	**Base Peat**	**Base Sand**
Saturated unit weight [kN/m^3]	20	20[2]	16	10.1[1]	20[1]
Unit weight [kN/ m^3]	18[1,2]	18[2]	16	10[2]	18[1]
Initial void ratio [-]	0.7	0.5	0.5	0.5	0.5
Permeability coefficient [m/s]	10^{-9}	10^{-4}	10^{-8}	6.343×10^{-6}	10^{-4}
Elastic modulus [kN/m^2]	37500[2]	30000[2]	11600[2]	1600[2]	150000[2]
Undrained Poisson's ratio [-]	0.495	-	0.495	0.495	-
Effective poisson's ratio [-]	0.3[2]	0.3[2]	0.3[2]	0.3[2]	0.3[2]
Effective friction angle [°]	32[2]	30[2]	30	27.5[2]	31.1[2]
Effective cohesion [kN/m^2]	75[2]	0[2]	6	9.7[2]	0.5
Over consolidation ratio, OCR	-	-	2.3[1]	2.3[1]	-
Slope of consolidation line, λ	-	-	0.132	0.278	-
Slope of over consolidation line, κ	-	-	0.013	0.03	-
Dilatancy angle, [°]	-	-	0	0	-

5.1.3 Analysis type

The analysis type performed is stress-seepage, which considers undrained material behaviour, but only for specific stages where it is documented in the literature that failure occurred under undrained conditions. It is important to note that the material that behaves in undrained conditions are only the clay and peat, while sand behaves in a drained manner. To neglect suction effects, the maximum negative pore pressure is set to 0. However, an attempt was also made to see the effects of taking suction into account.

Moving on to the construction stages, the stress initialization stage in which the stress distribution is established from the gravity loading phase, is prior to the construction of the levee. The levee is constructed in 5 stages as reported by Koelewijn & Peters (2012). Hence, following the stress initialization stage, the construction of the levee is simulated in 5 stages. It is important to note that during the 5 construction stages of the levee, the 'Estimate Initial Stress of Activated Elements' option is selected to prevent over-estimation of displacement because FEA NX perform Linear Analysis even if non-linear material is assigned to the elements to calculate the initial stress of the ground (Midas FEA, 2023).

Furthermore, the subsequent construction stages are based on the loading sequence described in section 2.5 of chapter 2. These stages are summarized in Table 5.2.

Table 5. 2. Construction stages of the South Dike.

Stage ID	Stage name/load applied	Stage type	Analysis control
1	Pre-levee	Steady-State	-
2	Stress initialization	Stress	-
3	Levee construction step 1	Stress	Estimation of initial stress of activated elements considered.
4	Levee construction step 2	Stress	
5	Levee construction step 3	Stress	
6	Levee construction step 4	Stress	
7	Levee construction step 5	Stress	
8	Container weight	Stress	material undrained
9	First filing of sand core	Transient seepage	-
10	First filing of sand core	Stress	material undrained
11	Filling of basin	Transient seepage	-
12	Filling of basin	Stress	material undrained
13	First excavation	Transient seepage	-
14	First excavation	Stress	material undrained
15	Second excavation	Transient seepage	-
16	Second excavation	Stress	material undrained
17	Third excavation	Transient seepage	-
18	Third excavation	Stress	material undrained
19	Consolidation	Transient seepage	-
20	Fourth excavation	Transient seepage	-
21	Fourth excavation	Stress	material undrained
22	Fifth excavation	Transient seepage	-
23	Fifth excavation	Stress	material undrained
24	Second filing of sand core	Transient seepage	-
25	Second filing of sand core	Stress	material undrained
26	Filling of containers	Stress	material undrained
27	Sand core filled	Transient seepage	-
28	Sand core filled	Stress	material undrained

Furthermore, the analysis of the slope stability using the strength reduction method has been initiated from the final stage of excavation.

5.2 RESULTS

The results of the simulation, starting from the steady-state seepage analysis before the construction of the levee, where the pore stresses distribution is hydrostatic, as well as the stress initialization using gravity, also prior to the levee construction, up to the stress analysis following the seepage analysis of the second filling of the levee's sand core are provided in Appendix D.

The final stress analysis performed by the simulation is the stage (26) in which the containers are filled with water. Figure 5.2 illustrates the total horizontal stress (a), total vertical stresses (b) and shear stresses (c).

At the centre of the levee, the *S-XX* ranges between -133.60kN/m^2 at the bottom of the base sand to 1.19kN/m^2 at the top of the crest. The range is reduced in the section where the ditch is present, with a value of -116.07kN/m^2 at the bottom. A similar trend is seen for *S-YY*, where the stress starts from -196.12kN/m^2 at the bottom to -1.58kN/m^2 at the crest, while at the ditch section, the stress at the bottom is -155.13kN/m^2 and approaching 0kN/m^2 at the ditch level in the lower base clay layer. The reduction in stresses at the ditch section is expected, as this section carries a lower weight. Both contours exhibit significant stress concentration at the toes of the levee (magnified in Figure 5.2(a) and (b)), which is a result of numerical instability.

With regards to the shear stress, a maximum value of 14.40kN/m^2 is observed close to the centre of the base sand layer in the section below the ditch. Shear bands are developed in the cover clays of the levee as a result of the added water load to the container.

As for the pore stress presented in Figure 5.3, it ranges between around 87kN/m^2 to nearly 0kN/m^2 at the water table elevation at the ditch level and in the sand core at the point where the water level reached (2.5m above the toe level) as a result of the second filling, which took place at an earlier stage. The areas where the pore stress is close to zero infer that it is the interface between saturated and unsaturated zones. Like in the total stresses, there are high stress concentrations at the toes of the levee due to numerical instability.

Moreover, the total displacement (a), horizontal (b), and vertical displacement (c) are presented in Figure 5.4. Although some movement can be seen on the left side of the levee,

the majority of the displacements take place on the right side. A deep sliding plane with uplift concentrated at the bottom level of the ditch is generated, as reported in the experiment.

Furthermore, the pore stress distribution extracted from the transient seepage analysis when the sand core is fully infiltrated with water is displayed in Figure 5.5. In contrast to the stress analysis performed, positive values indicate compression, while negative values refer to suction. The maximum pressure developed is close to 90kN/m^2 which is at the bottom of the base sand, while at the surface of the water table elevation (tip of the crest and elevation of the ditch), it is about 0kN/m^2.

Moving on to the results of the safety factors, they are listed in Table 5.3 with their corresponding stages. At the final excavation stage, the FS is well above the failure point, with a value of 1.79. However, after the second infiltration of the sand core, it is substantially reduced to 1.08, and further decreased to 1.05 after the filling of the containers with water, a value closer to the verge of failure. At this point, the stress analysis stopped as the solution fails to achieve convergence. Hence, for the post analysis of large deformation, the plane strain stresses at this stage and the pore pressure result from the transient seepage analysis, when the sand core is fully saturated, are transferred to Anura3D.

In the report of Koelewijn (2012), as mentioned before, the factors of safety after the final excavation stage (Excavation 5) were 1.05 using Van's method and 1.08 using Bishop's method, yielding similar results. These results differ from the FS of 1.79 obtained using the strength reduction method. Nevertheless, because the failure of the levee occurred after the levee core was completely filled with water, a FS value of 1.05 at the stage of filling the containers, which is one stage before the core is fully filled, is in good agreement with the experiment as the onset of failure.

Table 5. 3. Safety factors at stage 23, 25 and 26.

Stage ID	Stage name/load applied	Factor of Safety (FS)
23	Fifth excavation	1.79
25	Second filling of sand core	1.08
26	Filling of containers	1.05

In addition, Table E.1 in Appendix E highlights the parameters of the base peat that were modified for the sensitivity analysis, which are marked in yellow. The first simulation run serves as the reference, and its results have been described. For the final simulation stage

and the corresponding safety factors of each of the six simulation runs, refer to Table E.2 in the Appendix.

Performing the simulation to consider suction in the second run slightly increased the FS to 1.064 from 1.050 during the containers filled stage. Taking suction into account reduces the chances of failure and enhances stability.

In the third run, when the cohesion was decreased by $2kN/m^2$, and in the fourth run, when the friction angle was dropped to 24° from 27.5° the solutions started diverging at an earlier stage and stopped in excavation 5 with FS of 1.138 and 1.739, respectively. This indicates that the reduction in strength has a significant effect on failure, highlighting the greater influence of cohesion in the overall stability.

Overall, all the simulations developed the same failure mechanism - deep sliding plane. This is evident in the total displacement contour of each run, as generated by the slope stability analysis in Figures E.1 to E.6, corresponding to runs 1 through 6 respectively. Despite the same failure mechanism, differences can be observed in the total displacement. When suction was considered in run 3, the maximum displacement dropped to 0.10m from 0.33m (in run 1), which again proves that taking suction into account is less conservative. Reducing the cohesion in run 3 and friction angle in run 4, a maximum displacement of around 0.10m is achieved. This value mainly refers to the uplift produced at the bottom of the ditch, as expected due to the onset of failure being at an earlier stage (5^{th} excavation). In runs 5 and 6, the displacements decreased at the base because lower consolidation coefficients were used.

Regarding the slopes of the normal (run 5) and over-consolidation (run 6) lines, their decreased values had slightly dropped the FS to 1.031 during the filling of containers. While reducing the normal consolidation slowed down settlement at the final step of the levee construction, as illustrated in Figure E.7 (b), the slight decrease of the over-consolidation slope did not have any visible changes in the settlement (Figure E.7 (c)) compared to the reference run in (a) of the same Figure. This is because the over-consolidation slope would have a considerable effect in the reloading stages.

Stage 26:

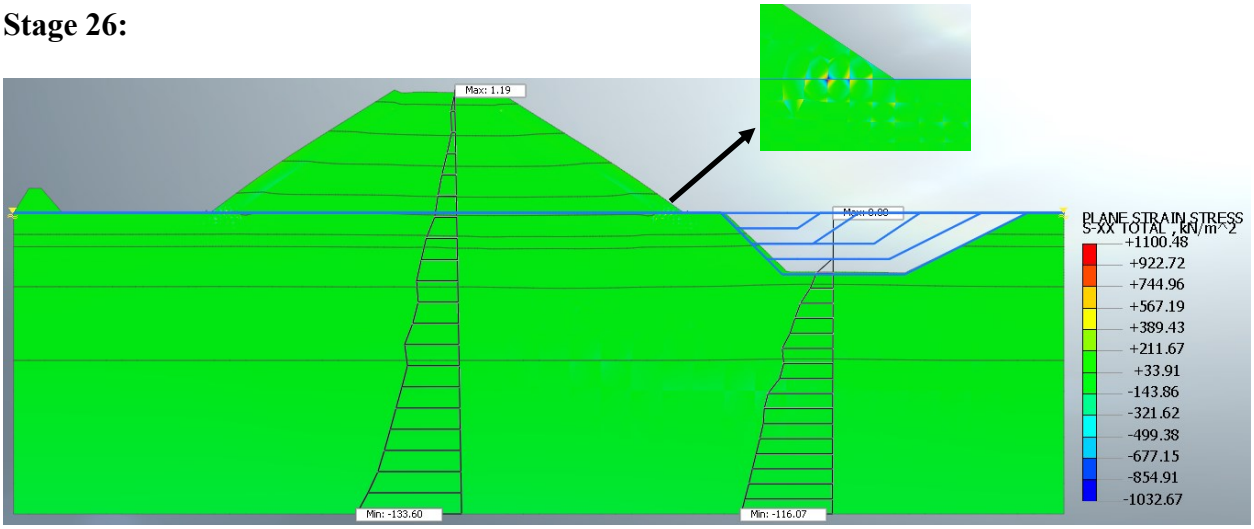

(a) Total horizontal stress, S-XX

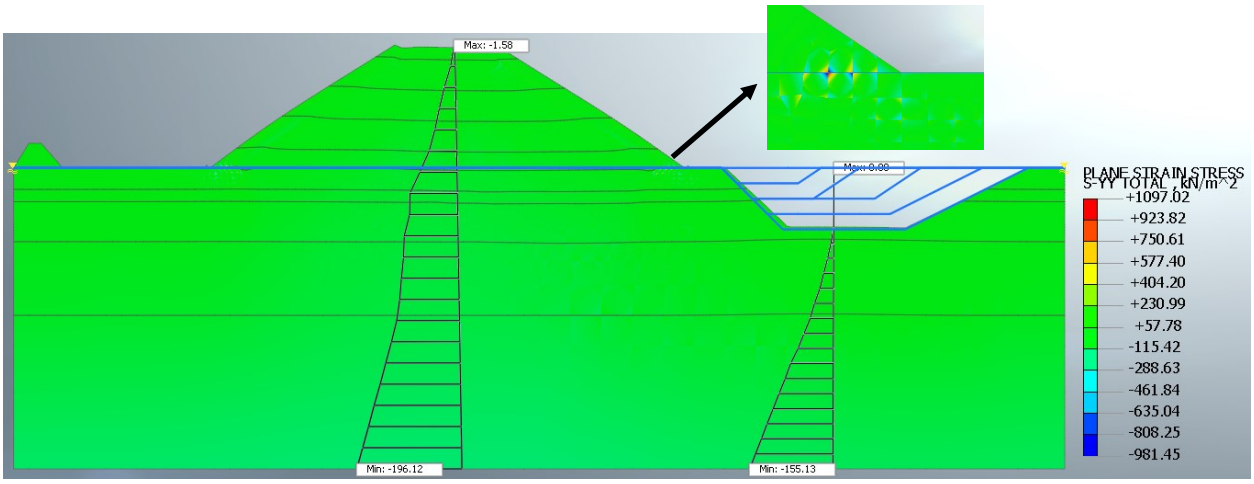

(b) Total vertical stress, S-YY

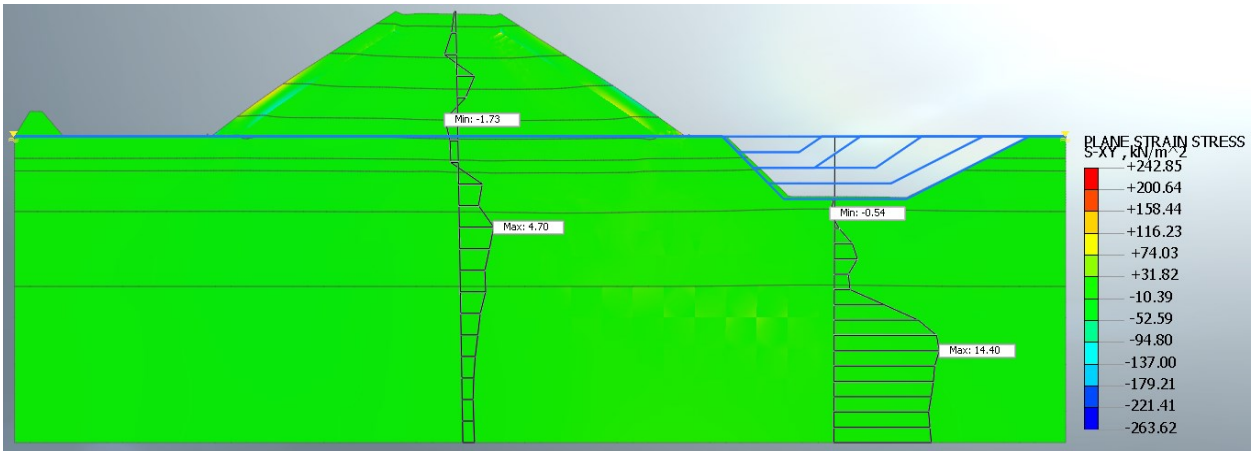

(c) Shear stress, S-XY

Figure 5. 2. Total stresses and shear stress (kN/m^2) at the time of filling of containers.

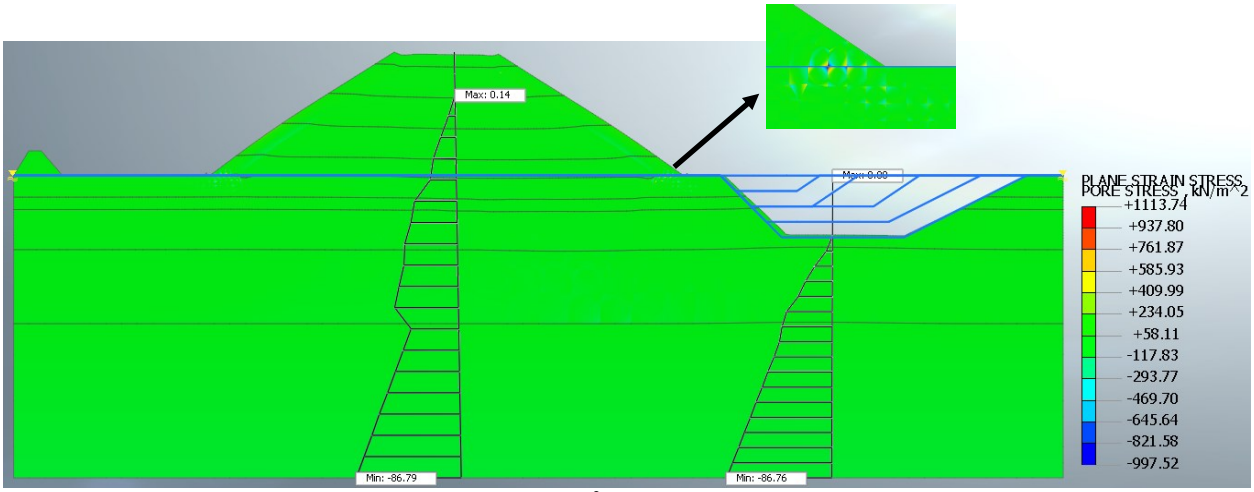

Figure 5. 3. Pore stress (kN/m^2) at the time of filling of containers.

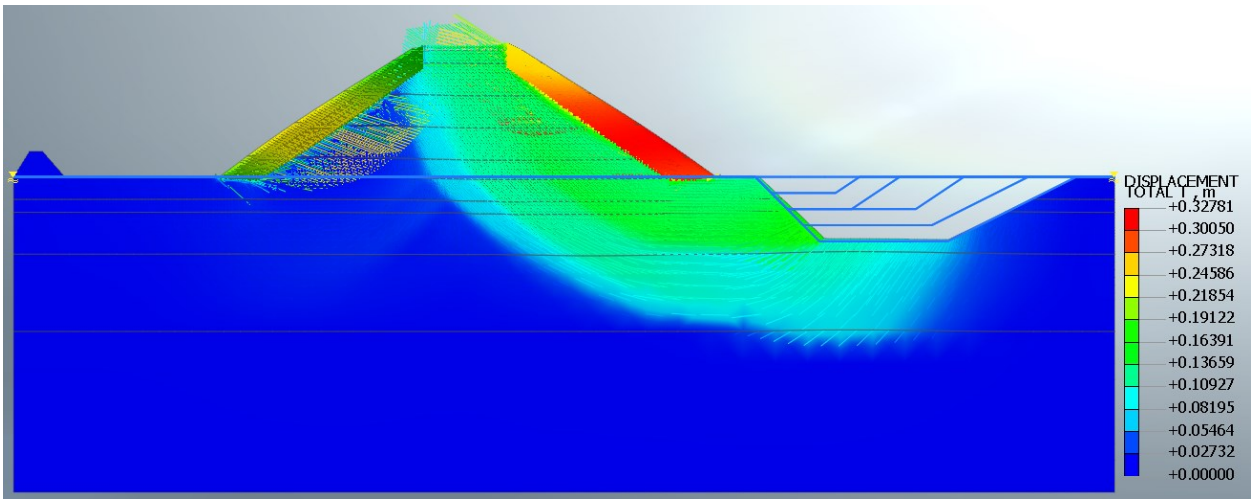

(a) Total displacement, T

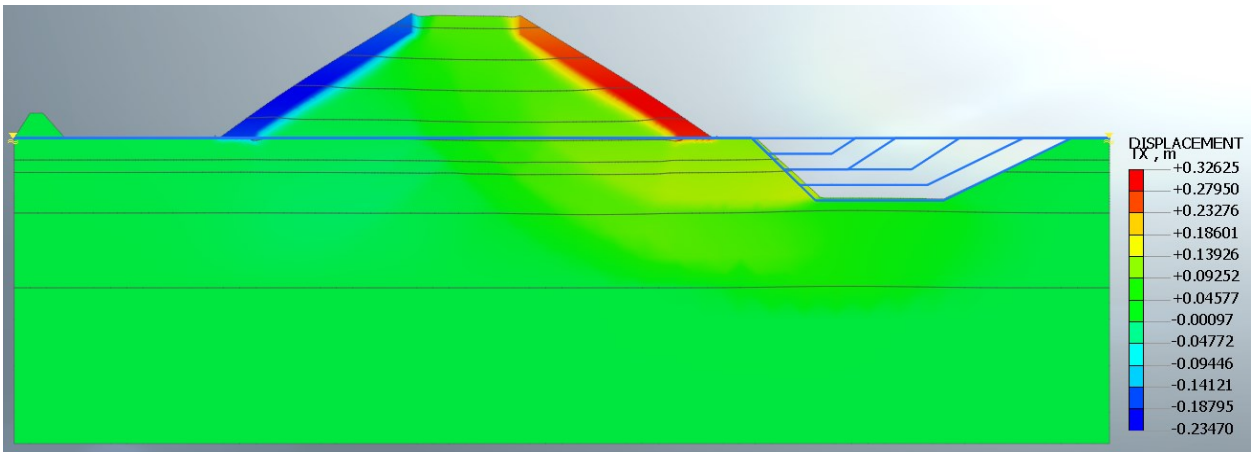

(b) Horizontal displacement, TX

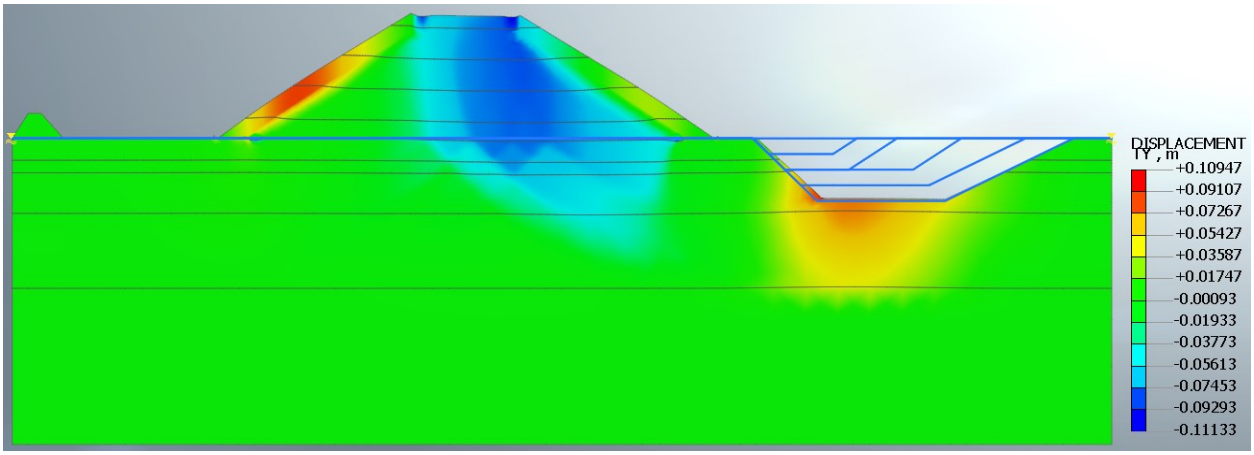

(c) Vertical displacement, TY

Figure 5. 4. Displacements (m) at the time of filling of containers.

Stage 27:

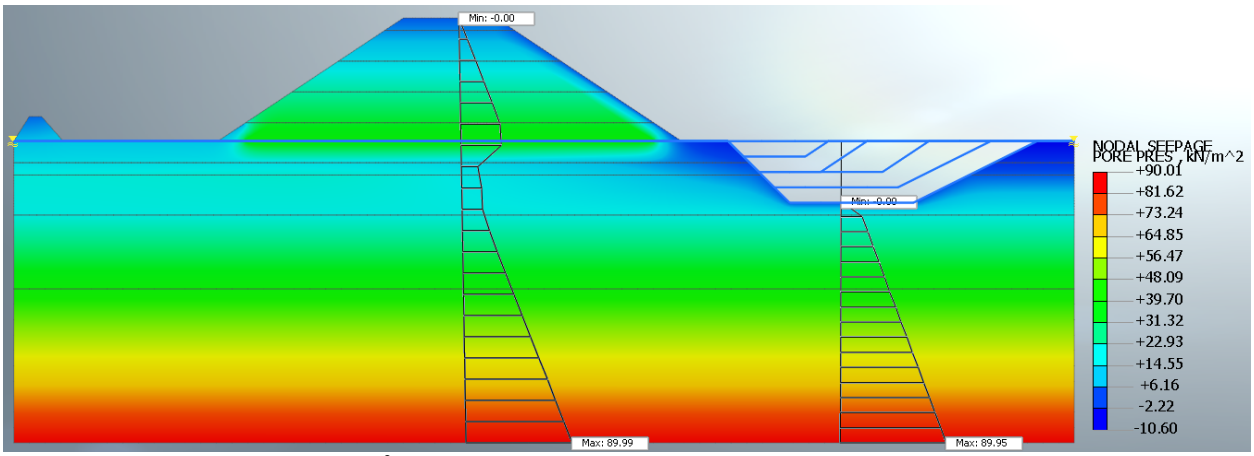

Figure 5. 5. Pore stress (kN/m^2) from transient seepage analysis at the time of sand core filled to the crest.

6 NUMERICAL MODELLING OF POST-FAILURE

In the previous chapter, the FEM model of the South Dike was able to simulate up to the stage where the containers were filled with water for the stress analysis, which is the point of imminent failure. Concerning the seepage analysis, the complete infiltration of the sand core with water was the last stage the model simulated. To investigate the post-failure behavior of the levee, the 2D plane stresses of the containers-filled stage and pore pressures generated from the seepage analysis are transferred to Anura 3D to perform the MPM simulation, which accounts for large displacement.

6.1 MPM MODEL

6.1.1 Geometry and Discretization

The South Dike geometry for the MPM model is akin to the FEM model, including the elevation of the water level. The adopted MPM formulation is a one-phase single point approach, where the behavior of the sand materials is considered to be fully drained, whereas that of the clay and peat is considered undrained. A mesh size of 0.6m for the entire geometry. There are 3228 triangular elements and 1696 nodes. For the movement of MPs into empty elements during the deformation process, an empty area covering the width of the entire levee and a height of one meter just above the crest are defined. Each element covering the levee and its base contains 3 MPs. Figure 6.1 depicts the model geometry and discretization. The red elements represent the active components, indicating they have been assigned with MPs. On the other hand, the blue elements represent inactive components with no assigned MPs. As previously mentioned, inactive elements are required so that the MPs are allowed to move into them when the levee starts to deform.

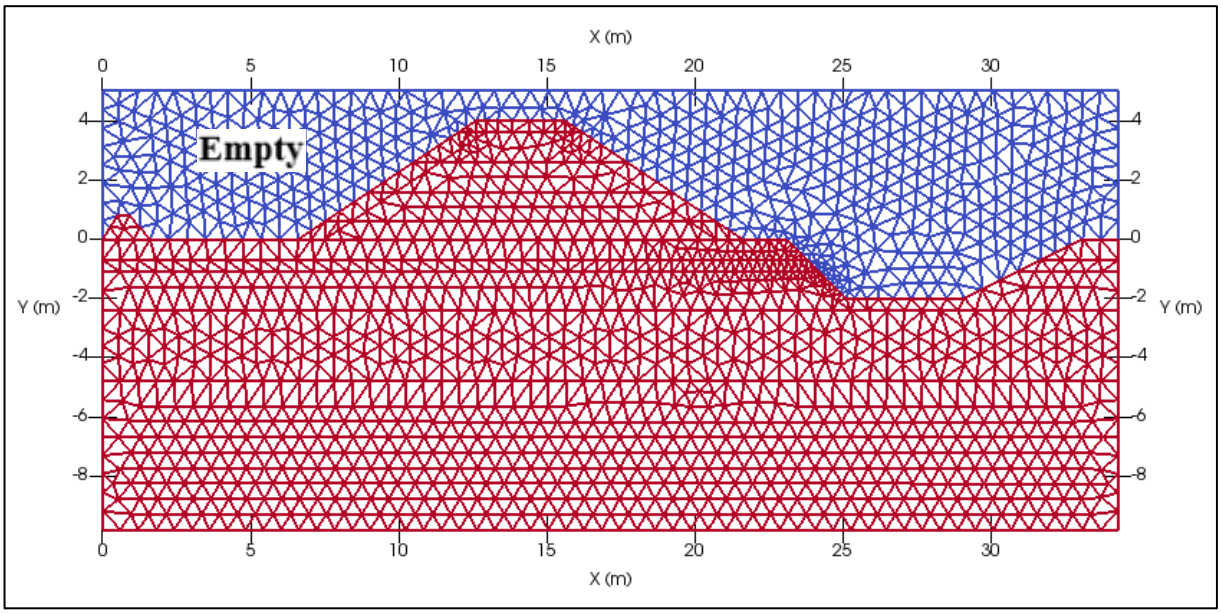

Figure 6. 1. South Dike MPM model geometry and discretization (red =active elements, blue = inactive elements).

Pertaining to the boundary conditions, they consist of the weights of the containers filled with water on the crest, amounting to 15.22kN/m^2, as shown in Figure 6.2(a), as well as solid fixities as illustrated in (b). The load applied to the MPs is maintained throughout the simulation. Furthermore, for the solid fixities, the sides of the model are fixed horizontally, while the top side is fixed vertically, and the base is fully fixed.

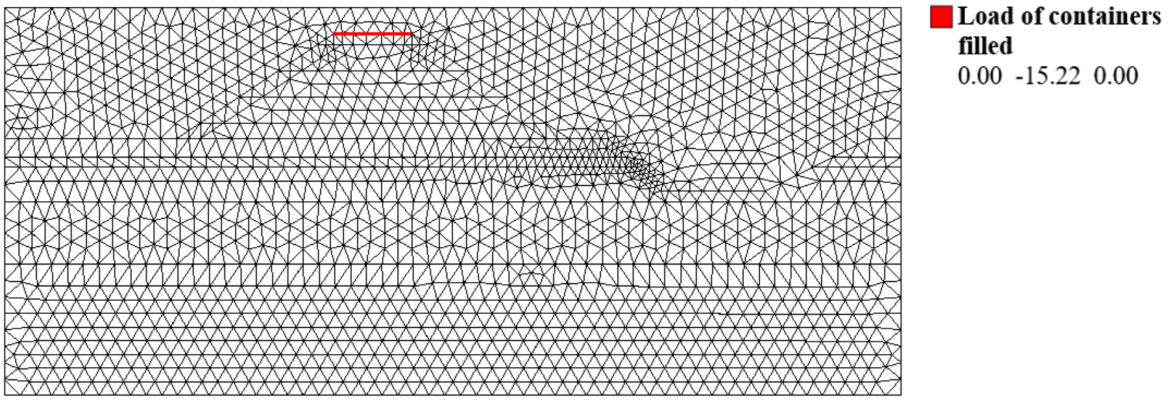

(a) Solid traction (load = 15.22kN/m^2)

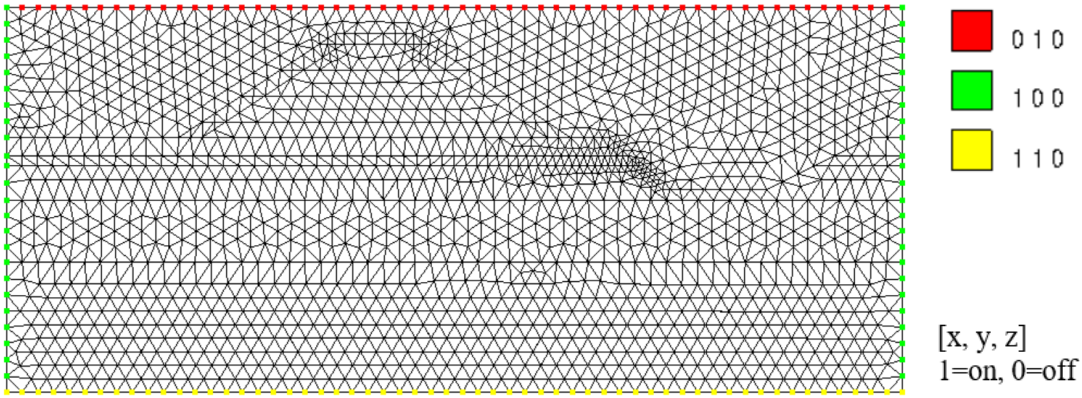

(b) Solid fixities

Figure 6. 2. South Dike MPM boundary conditions: (a) solid traction (load) and (b) solid fixities.

6.1.2 Material

Due to the unavailability of some of the constitutive models in Anura3D that were used in the pre-failure analysis of the levee, only the Mohr-Coulomb failure criterion is utilized to describe the material behaviors for the post-failure analysis. Similar to the FEM model, the material behavior type is set the same, where sand is drained, and base clay and peat are undrained. To ensure numerical stability and to obtain results consistent to the experiment, the Young's modulus of the base clay and core sand has been reduced. Similarly, the effective cohesion of the base clay and peat has been adjusted. The initial porosities used are derived from their initial void ratios, and liquid density is assumed to be 1000kg/m^3. As for the solid grain density of the materials, they were derived from their unit weights used in the FEM model. Table 6.1 summarizes the material and mechanical properties employed.

Table 6. 1. MPM material properties and mechanical properties of the South Dike.

Material property	**Cover clay**	**Core sand**	**Base clay**	**Base Peat**	**Base sand**
Material type	Saturated – undrained effective stress	Dry	Saturated – undrained effective stress	Saturated – undrained effective stress	Saturated - drained
Initial porosity [-]	0.41	0.33	0.33	0.33	0.33
Density solid [kg/m^3]	2761.75	2551.39	1942.61	1044.64	2551.39
Density liquid [kg/m^3]	1000	-	1000	1000	1000
Effective Young modulus [kN/m^2]	37.5x10^3	25x10^3	1.6x10^3	1.6x10^3	150x10^3
Effective poisson's ratio [-]	0.3	0.3	0.3	0.3	0.3
Undrained Poisson's ratio [-]	0.495	-	0.495	0.495	-
Effective friction angle [°]	32	30	30	27.5	31.1
Effective cohesion [kN/m^2]	75	0	2.5	1.8	0.5

6.1.3 Analysis type

The post-failure dynamic simulation of the levee is conducted using the one-phase single point MPM formulation. Since the simulation is dynamic, the homogeneous local damping coefficient is set to 5% in order to improve stability.

As the plane stresses of the containers filled stage and pore stresses from the seepage analysis when the sand core is fully filled are transferred to Anura3D from the FEM model, this essentially constitutes the stress initialization stage. Clearly, gravity load is maintained for the entire simulation. Additionally, the load of the filled containers is activated and kept constant throughout the simulation.

Moreover, the total number of load steps run is 125, with each step lasting 0.1 seconds. Also, for the stability of the numerical simulation, the courant number is set to 0.98, while for the reduction of kinematic locking, the strain smoothing feature is activated.

6.2 RESULTS

The transferred plane strain stresses generated at the onset of failure during the stage when the containers are filled are illustrated in Figure 6.3. The total horizontal stress in Figure 6.3(a) is quite similar to the FEM output in Figure 5.2(a) in section 5.2 of chapter 5. The differences in the overall stress distribution arise due to the extreme stress concentration at the toes of the levee in the pre-failure analysis. This is a typical numerical FEM problem caused by issues in numerical convergence, which the MPM model fortunately does not encounter. Also, the stresses were transferred using an average mesh size of 0.6m, contributing to the observed discrepancies. The same can be said for the total vertical stresses in Figure 6.3(b) when compared to the FEM result in Figure 5.2(b) and the shear stresses in Figure 6.3(c) when compared to the FEM result in Figure 5.2(c).

Regarding the transferred pore stresses generated by the transient-seepage analysis of the levee core being completely saturated with water, as shown in Figure 6.4, the overall stress distribution is similar to the FEM output as provided in Figure 5.5 in section 5.2. It should be noted that in the seepage analysis, negative pore pressures represent suction, while positive compression. Hence, when transferring the results, the signs were changed because in Anura3D, suction is positive while compression is negative.

Moreover, Table 6.2 provides the evolution of the deviatoric strain in the levee over the entire period of the simulation, which lasted 12.5 seconds. The MPM model effectively captures the development of failure over time. The emergence of the sliding plane is evident, with strain primarily occurring at the interface between peat and sand, the left slope of the bottom ditch located within the interlayers of clay and peat, as well as within the levee core. A slight development of a slip surface on the left side of the levee is noticeable, which was not observed in the experiment. This disparity is attributed to the simulation's container being applied uniformly across the MPs, covering the entire width of the crest, whereas in the experiment, the container was placed mostly towards the right side of the levee. Nonetheless, this difference is minor as compared to the significant strain that developed on the right side of the levee. Note that results are scaled for improved visualization.

Furthermore, the corresponding evolution of total displacement throughout the duration is presented in Table 6.3. The magnitude of the displacement, as depicted in Figure 6.5(a), is broken down into its horizontal and vertical component at the end of the simulation, when load step = 125 and time = 12.5 s, shown in (b) and (c), respectively. The sliding plane failure surface and uplift at the bottom of the ditch are observed, analogous to the experiment.

In Appendix F, the vertical stress for the entire duration of the simulation is provided in Table F.1. The stresses start to increase from 2.5s, and at 7.5s, stress rises on both slopes of the levee. From t =10s, a stress increase at the left-side slope of the ditch is noticeable, and stresses on both side slopes of the levee decrease at the end of the simulation when the levee stops moving. As for the pressure evolution, it is presented in Table F.2, where the pressure generally starts to drop (towards suction) from 2.5s and remains somewhat constant for the rest of the period.

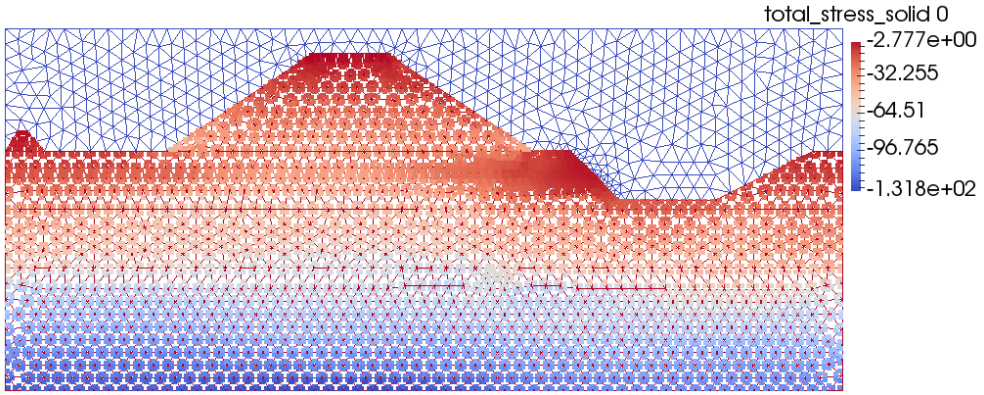

(a) Total horizontal stress

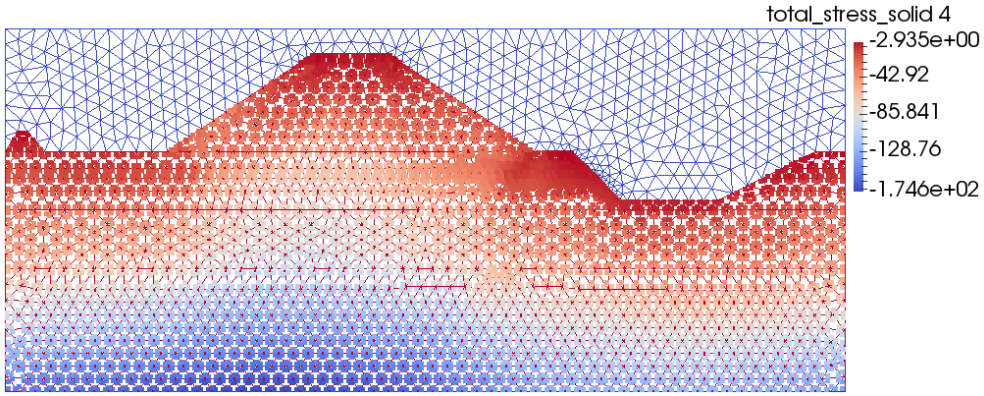

(b) Total vertical stress

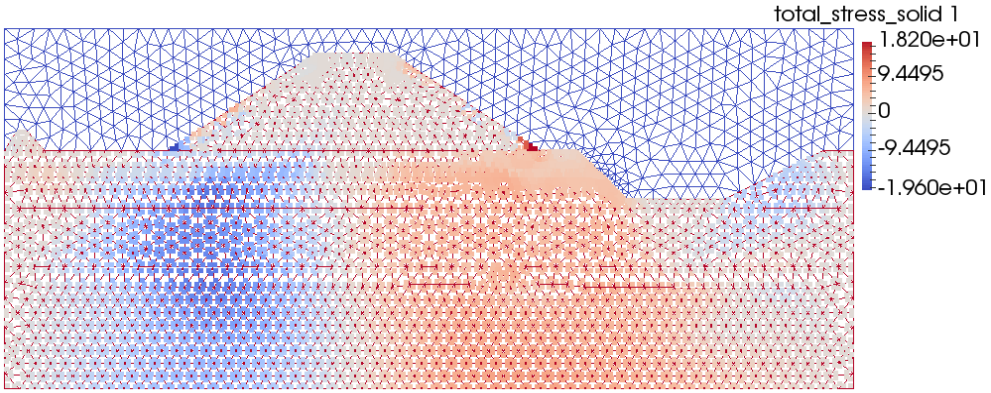

(c) Shear stress

Figure 6. 3. Transferred plane strain total horizontal stress (a), total vertical stress (b), and shear stress (c) (kN/m^2).

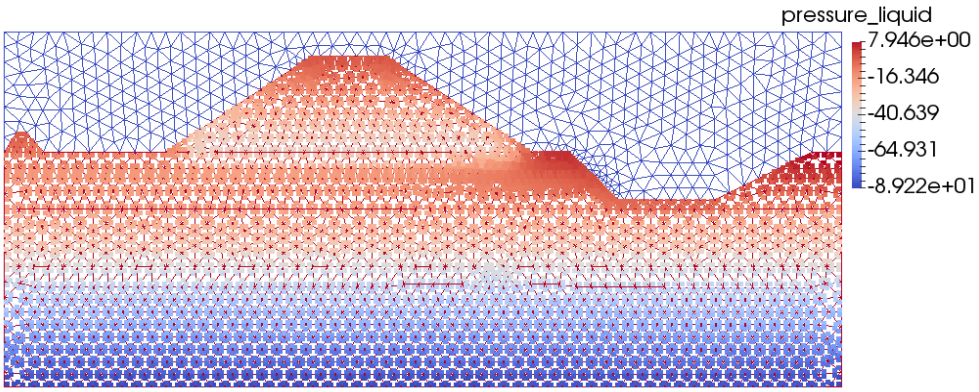

Figure 6. 4. Transferred transient-seepage analysis pore stress (kN/m^2).

Table 6. 2. South Dike post-failure deviatoric strain evolution (0.0s to 12.5s).

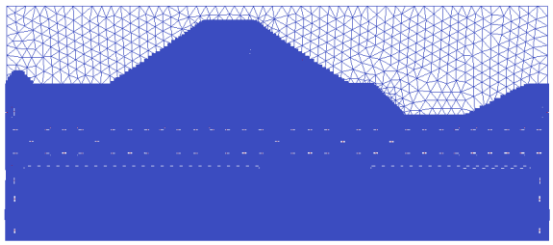	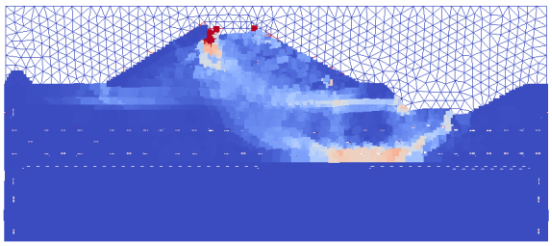
0.0s	2.5s
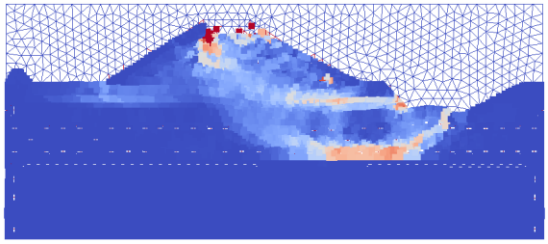	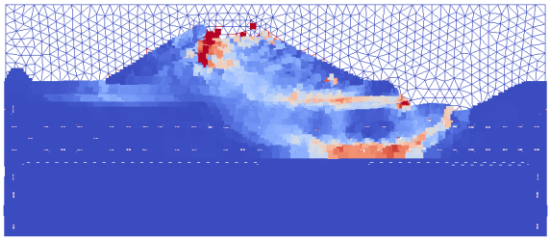
5.0s	7.5s
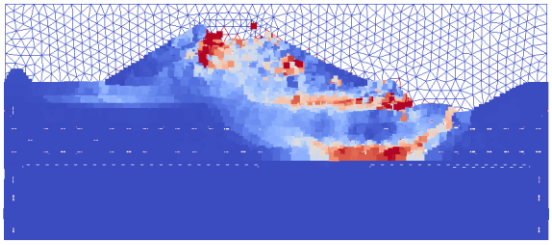	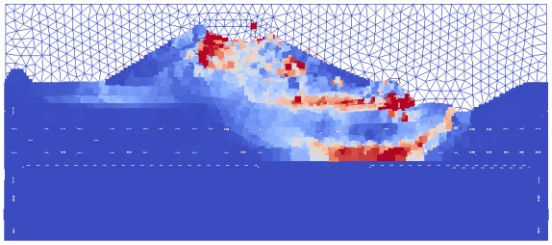
10.0s	12.5s
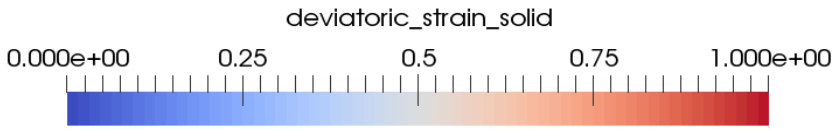	

Table 6. 3. South Dike post-failure total displacement evolution (0.0s to 12.5s).

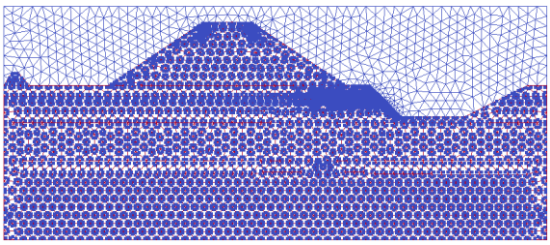	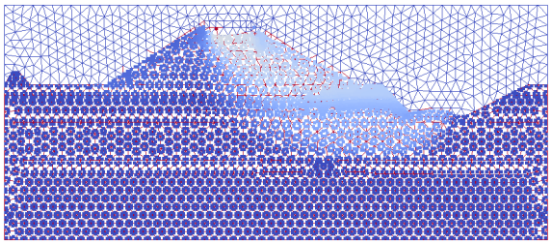
0.0s	2.5s
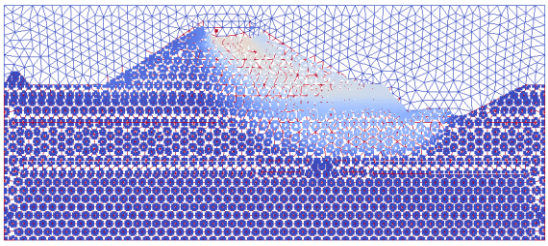	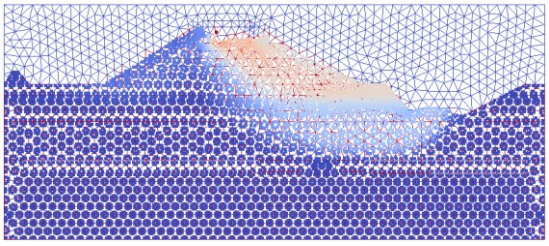
5.0s	7.5s
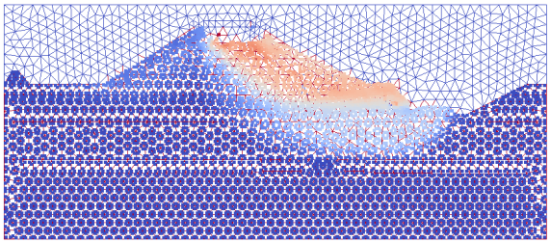	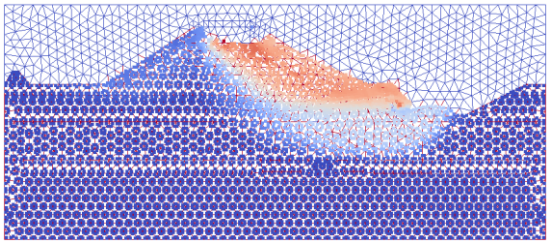
10.0s	12.5s

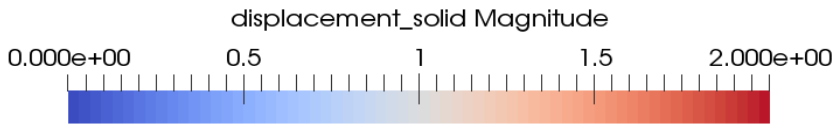

Step 125:

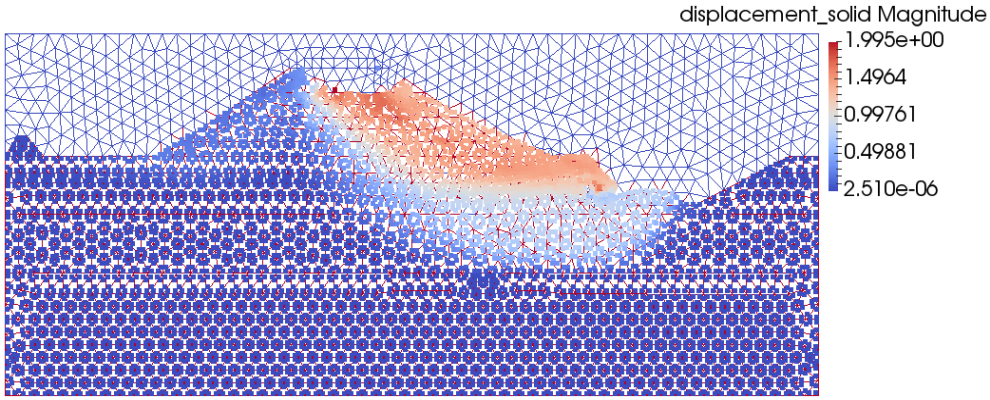

(a) Total displacement

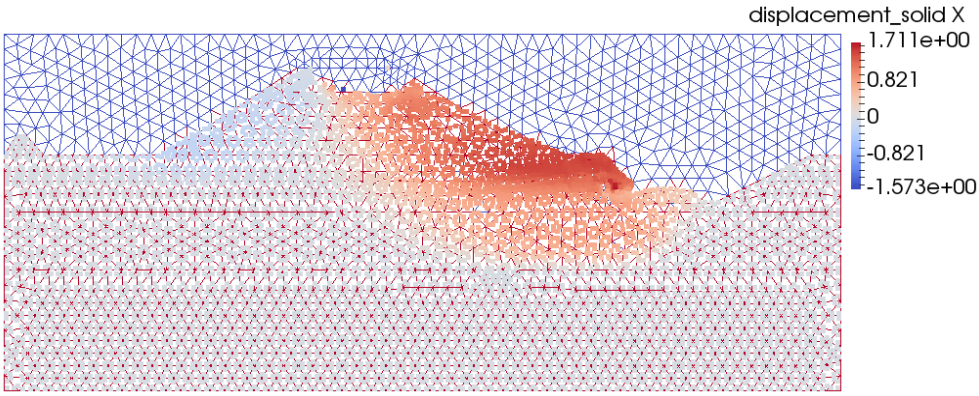

(b) Horizontal displacement

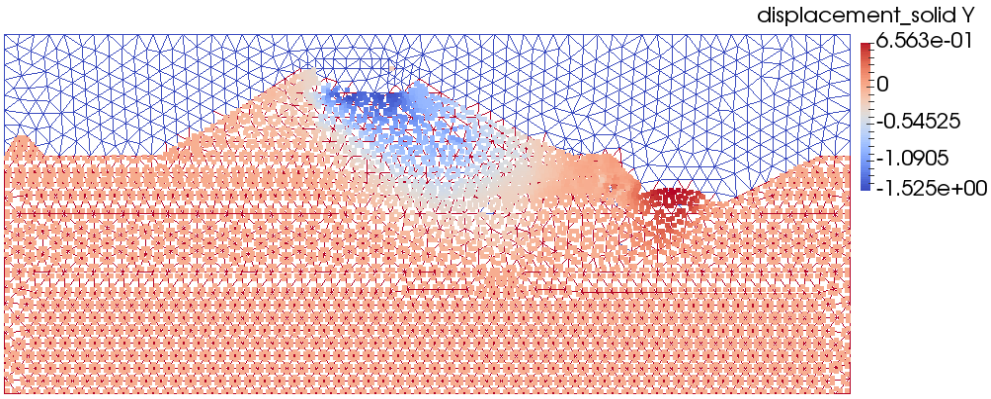

(c) Vertical displacement

Figure 6. 5. Total displacement (a), horizontal displacement (b), and vertical displacement (c) (m) at the end of the simulation (load step:125).

In addition, a parametric analysis has been performed. The modified properties of the four runs are given in Table 6.4. The first run serves as the reference, corresponding to the simulation in which the results have been described. Table 6.5 lists the final load step at which the simulation stopped, along with its corresponding duration. The time per load step for each run is set to 0.1s.

Table 6. 4. Mechanical and numerical properties modified for each post-failure analysis run.

Properties	**First run (reference)**	**Second run**	**Third run**	**Fourth run**
MPs per element	3	3	3	3,12,16
Base clay Young's Modulus, kN/m^2	1600	11600	11600	1600
Base peat Young's Modulus, kN/m^2	1600	11600	1600	1600

Table 6. 5. Final load step of each post-failure analysis run.

Run	**Final load step**	**Duration (s)**
First	125	12.5
Second	1	0
Third	10	0.9
Fourth	13	1.2

For the first three runs, the number of MPs assigned to each element is 3, as depicted in Figure 6.6(a). In the fourth, the distribution is set to 3, 12 and 16, with the highest assigned to the zones that experienced the larges displacements, i.e. the levee itself and the first three layers of the base composed of clay and peat, which are the critical zones, as shown in (b).

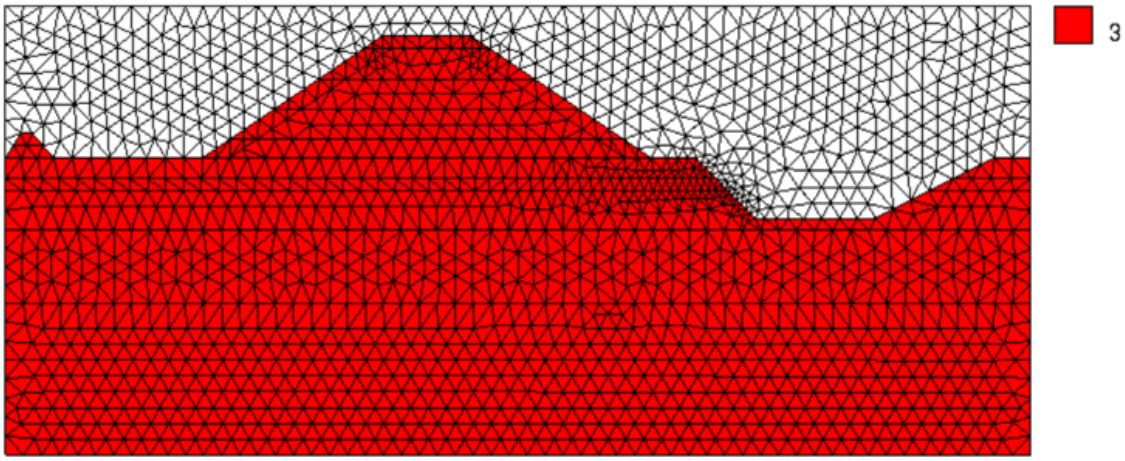

(a) Run 1, 2 and 3

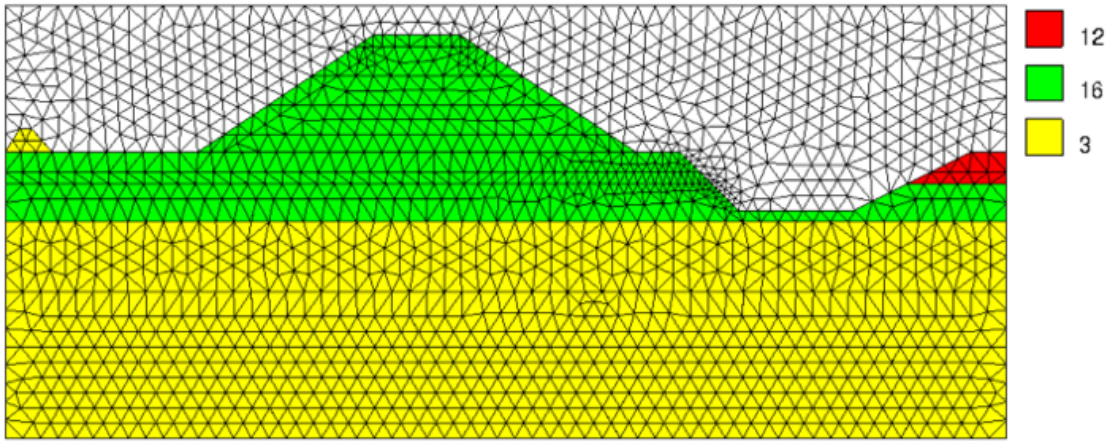

(a) Run 4

Figure 6. 6. Number of MPs per element assigned to the South Dike mesh (a: run 1,2,3 and b: run 4).

The contour results depicting the evolution of the deviatoric strain and the total displacement for the second through fourth runs can be found in Tables 6.6 to 6.11. It can be observed that all simulations, with the exception of the second run, produce the sliding plane failure mechanism. However, due to numerical issues, notably the cell-crossing problem encountered by MPM, the models (run 2,3 and 4) explode and are unable complete the analysis. An in-depth view of the distribution and crossing of the MPs during the final load step of each run is provided in Appendix G.

In run 1 (reference run), where both the base clay and peat had a stiffness value of 1600kN/m^2, the simulation managed to complete the 125 load steps with minimum MPs cross cell issue close to the ditch as depicted in Figure G.1.

When the stiffness was increased to 11,600kN/m^2 for both materials in run 2, crossing of MPs is observed at the base sand and near the ditch, as depicted in Figure G.2. This caused the simulation to stop at the end of the first load step.

Next, in run 3, assigning 11,600kN/m^2 of stiffness value to the base clay and 1600kN/m^2 to the peat causes the simulation to explode mostly near the interface between the clay and peat below the ditch by the 10th load step, as depicted in Figure G.3. This can be attributed to the large difference in stiffness values, which causes numerical instability when an averaging of the material values is performed by the model.

Finally, in the fourth run, when higher MPs per element is assigned, the simulation lasts only till the 13th load step because of the intense MP cross-cell issue close to the left slope of the ditch, as depicted in Figure G.4. A higher number of MPs per element increases the chance of crossing of one element's MP to another.

Run 2:

Table 6. 6. Second run South Dike post-failure deviatoric strain evolution (0.0s to 0.6957E-03s).

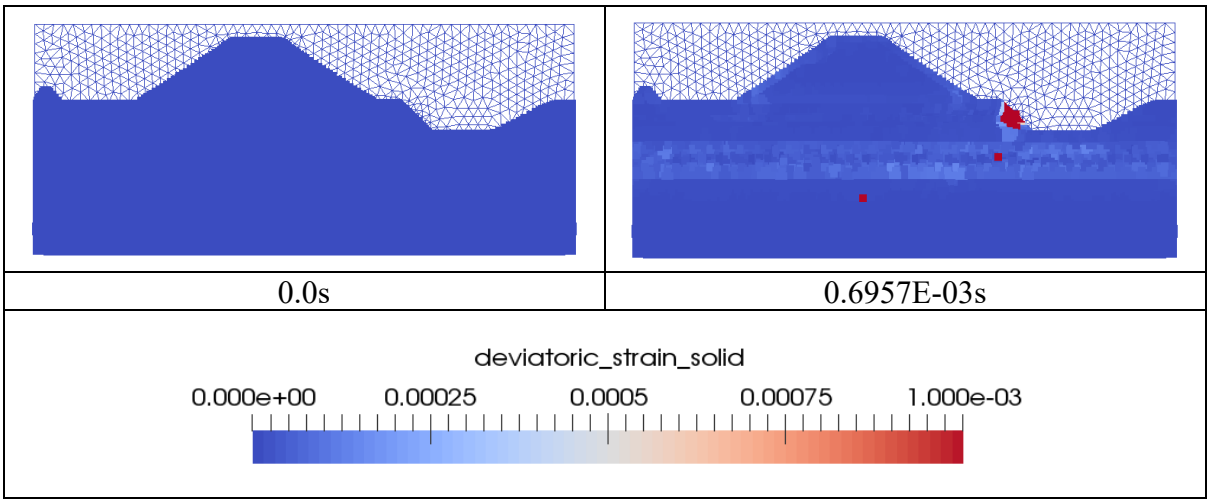

Table 6. 7. Second run South Dike post-failure total displacement evolution (0.0s to 0.6957E-03s).

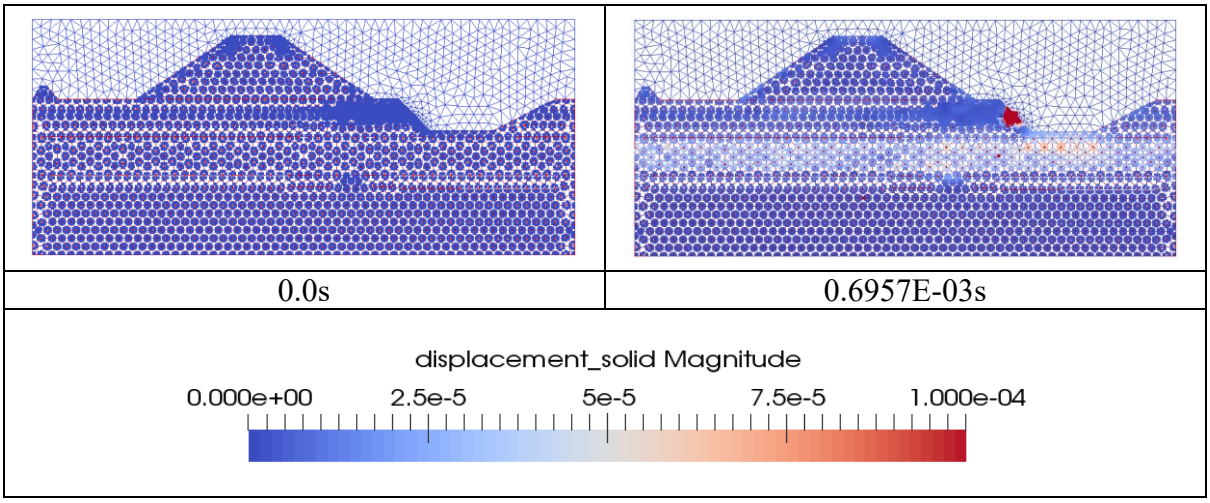

Run 3:

Table 6. 8. Third run South Dike post-failure deviatoric strain evolution (0.0s to 0.9s).

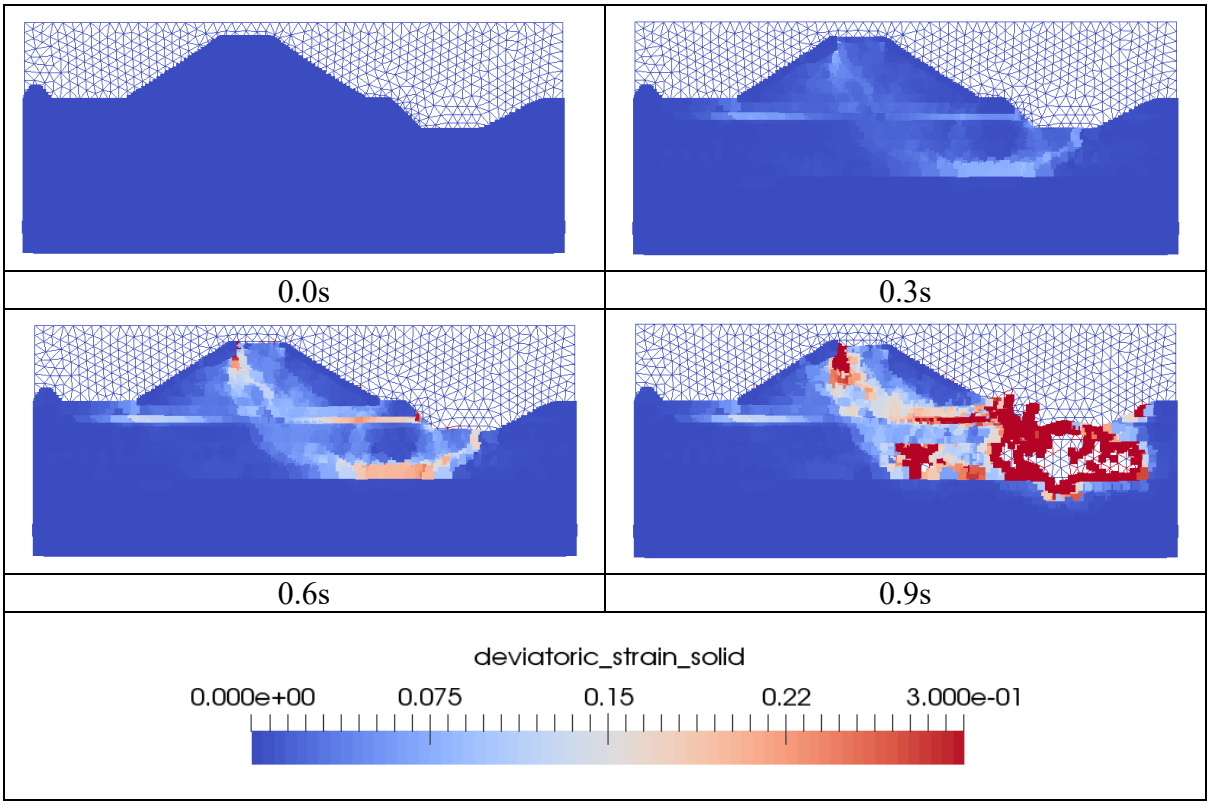

Table 6. 9. Third run South Dike post-failure total displacement evolution (0.0s to 0.9s).

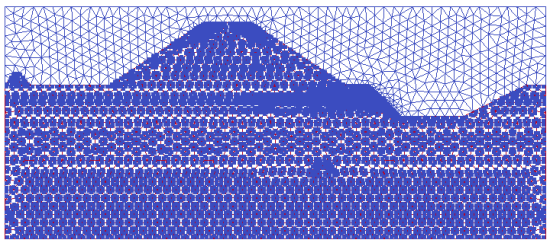	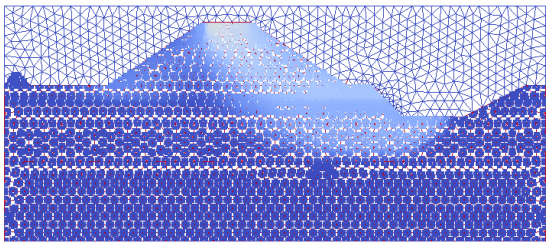
0.0s	0.3s
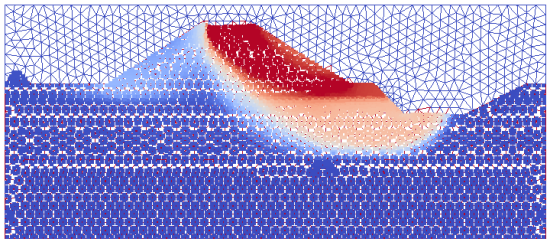	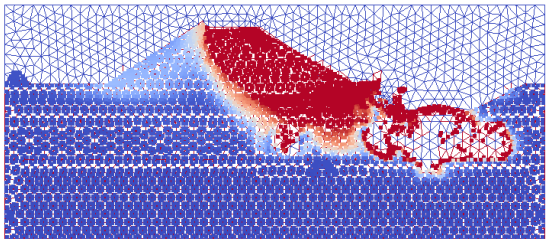
0.6s	0.9s
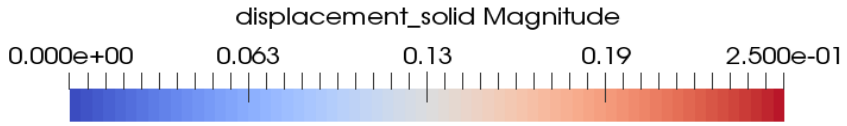	

Run 4:

Table 6. 10. Fourth run South Dike post-failure deviatoric strain evolution (0.0s to 1.2s).

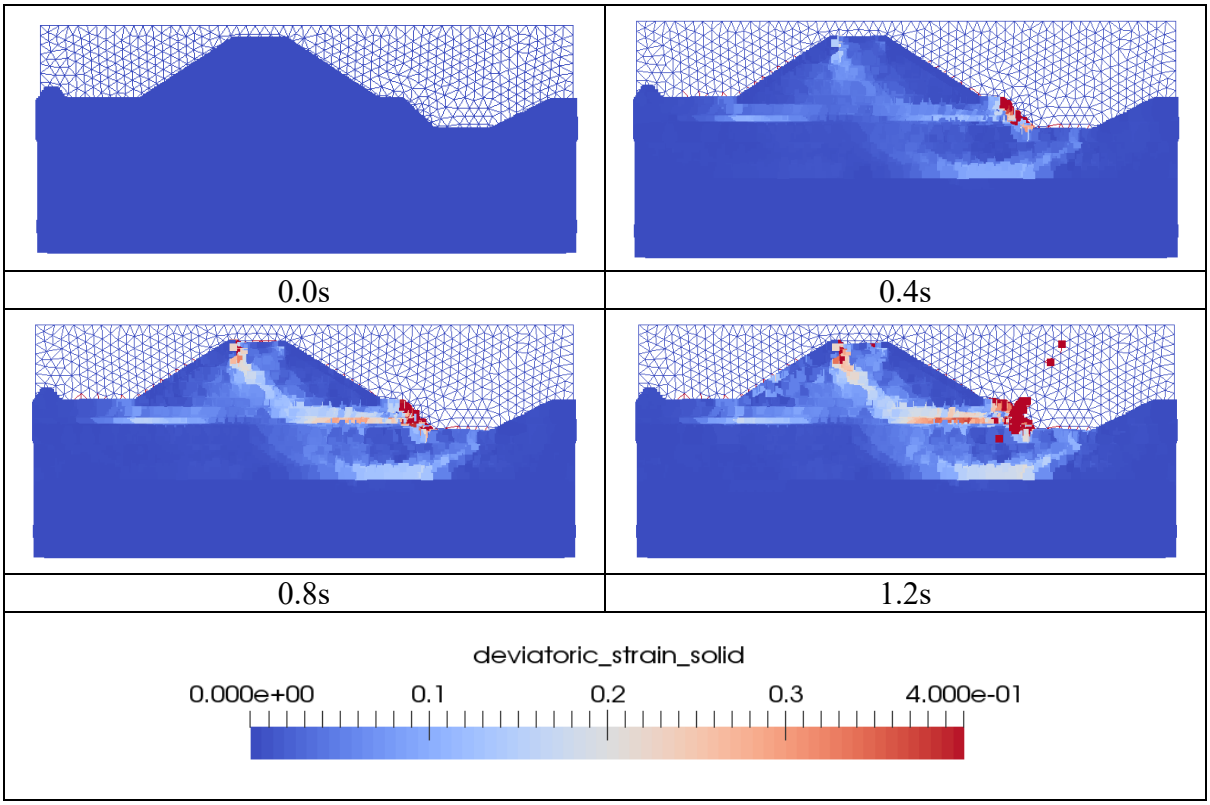

Table 6. 11. Fourth run South Dike post-failure total displacement evolution (0.0s to 1.2s).

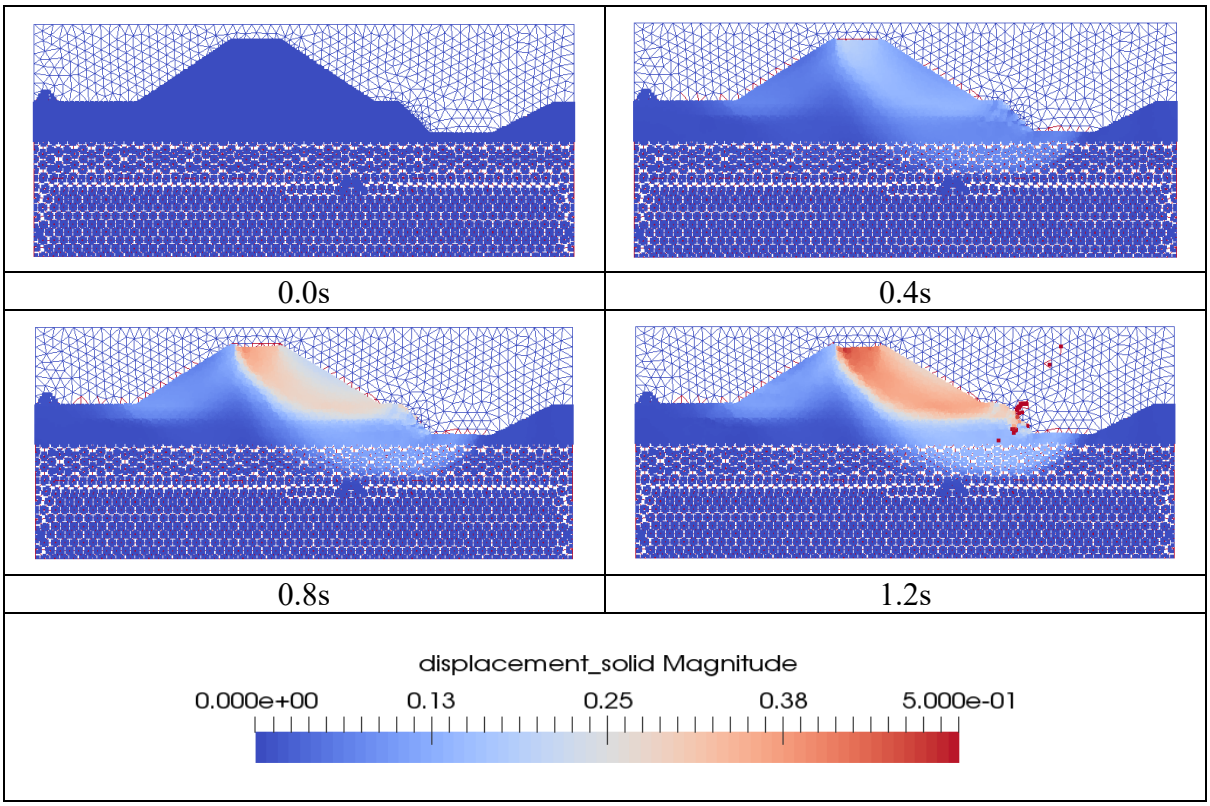

7 COMPARISON WITH EXPERIMENT

Comparing the simulation results of the South Dike before and after failure with the experimental findings is done in this section.

7.1 DISCUSSION

Following the completion of the levee construction, as simulated in stage 7 of the FEM model, the settlement beneath the center of the levee is approximately 0.90m. This is illustrated in Figure D.18(c) in Appendix D. This value falls within the range of 0.85m and 0.99m, as reported in Koelewijn (2012), for the east and west sections of the levee, respectively. Indeed, subsoil characteristics are not uniform; ground conditions exhibit spatially variability (heterogeneity), which contributes to the variation in settlement between the east and west sections of the levee.

Furthermore, the difference in the numerical value of the settlement can be attributed to the lack of provided consolidation parameters. While consolidation parameters such as the OCR (2.3) and consolidation coefficient (6.7E-06m^2/s) were provided by Koelewijn & Peters (2012), these values were insufficient for the soft soil constitutive model used to describe the behaviour of base clay and peat. The determination of the consolidation slopes was set through a trial-and-error process to obtain settlement values closest to the experiment. For base clay, the normal consolidation line slope of 0.132 was used, and for the overconsolidation line slope, it was 0.013. For the peat, 0.238 and 0.03 were determined for the normal consolidation line slope and overconsolidation line slope, respectively.

The FEM model simulated the onset of failure at the stage when the containers were filled with water, attaining a safety factor of 1.05. Subsequently, the simulation that took place before the solution failed to converge was the transient seepage analysis of the complete saturation of the levee core. These results are reasonable because, in the experiment, failure of the levee occurred after the core was forcefully pumped with water. The safety factors calculated using Van's and Bishops's methods, once the maximum pressures were reached at this stage, were 0.92 and 0.95, respectively (Koelewijn, 2012).

Proceeding to the post-failure analysis results, the experimental slope configuration is compared by superimposing its initial and final displacements, marked by black and red lines respectively, onto the magnitude of the final displacement contour generated by Anura3D. This comparison is illustrated in Figure 7.1 for the west cross-section of the South Dike and in Figure 7.2 for the middle cross-section of the South Dike.

As observed, the simulation results generally bear a closer resemblance to the failure in the west cross-section than in the middle cross-section.

The vertical downward displacement at the top of the middle of the crest by the end of the 12.5s simulation period is about 1.4m. This information is derived from the tracking of 'MP 6111' showcased in Figure F.1 in Appendix F. In contrast to the experimental findings, the drop in the crest measures around 0.9m for the west cross-section, whereas for the middle cross-section, this drop is approximately 2m, as indicated in Figures 7.1 and 7.2, respectively.

With regards to the horizontal displacement at the toe, tracked by 'MP 6196' located in the levee toe (refer to Figure F.1 in Appendix F), the simulation yields a value of around 1.45m upon completion. This value is lower compared to the horizontal displacement measured by the inclinometer at the west cross-section's toe on the day of the failure, which was recorded as 0.83m. In the case of the middle cross-section, the horizontal displacement is 1.65m in front of the toe, closer to the simulation results. These measurements were taken on Saturday, September 8th, at 2:30pm. Recorded values at different times of the same day are available in Table 7.1.

Table 7. 1. Horizontal displacements measured by the inclinometers, extracted from Koelewijn (2012).

Time on failure day (8th Saturday 2012)	**East in toe (mm)**	**Middle under crest (mm)**	**Middle in front of toe (mm)**	**West in front of toe (mm)**	**West in toe (mm)**
1:53 PM	115	145	160	140	135
2:13 PM	145	190	200	175	155
2:27 PM	180	430	470	310	320
2:30 PM	225	1450	1650	900	830

Moreover, at the bottom of the ditch, the simulation produces an uplift of approximately 0.70m in magnitude. Although no measurements are available for comparison with the west cross-section, it is evident from the middle cross-section that the uplift occurs to a greater extent.

The disparities in the results of the MPM simulation may stem from the constitutive model used. For all the materials, only the Mohr-Coulomb failure criterion was adopted, owing to its ready availability in Anura3D. As opposed to other more sophisticated models such as soft-soil or modified cam-clay, this does not take into consideration the soil's loading history. It is vital to use models that can appropriately capture the soil's behaviour to prevent any underestimation of deformations.

Another potential explanation can be due to certain differences in replicating the loading stages. For instance, while the model applied the container load to cover the entire width of the crest, in reality, the containers did not extend along the full width (3m). Also, the height of the water in the containers was set to 1.4m in the model. This value was calculated by considering the width of the crest (3m) and container length of 6.7m, and a reported volume of 28m^3 according to Melnikova et al. (2015). However, during the experiment, the height of the water reached in the containers was 1.75m (Koelewijn, 2012).

In addition, the MPM formulation used is the one-phase single point method, which is a simplified approach and does not take into account the unsaturated state of the levee core (before its complete saturation). Provided that more information on the soil properties is available, a more advanced formulation of MPM can be applied, which could potentially better simulate the levee failure to match the experiment.

Nevertheless, the simulation generally is able to reproduce the overall failure mechanism as observed in the experiment. By the end of the dynamic simulation, the deep sliding plane reaches the bottom peat layer located just above the base sand. This aligns with the middle cross-section of the South dike, where the sliding planes are recorded in the interlayers of clay and peat. Figure 7.3(a) depicts the layers in which the sliding plane occurs in the middle cross-section, while (b) illustrates the sliding plane failure mechanism (outlined in the red box) captured by MPM, which is superimposed on the material ID contour.

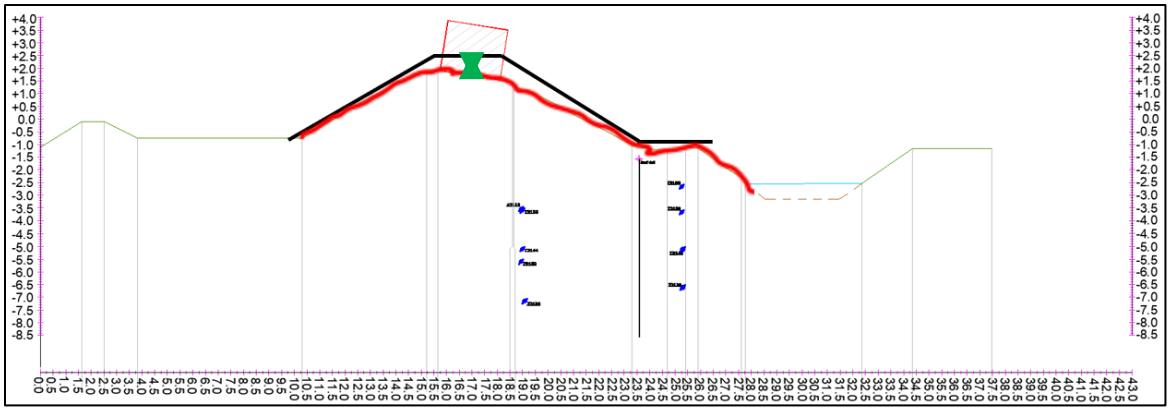

(a) West-cross section

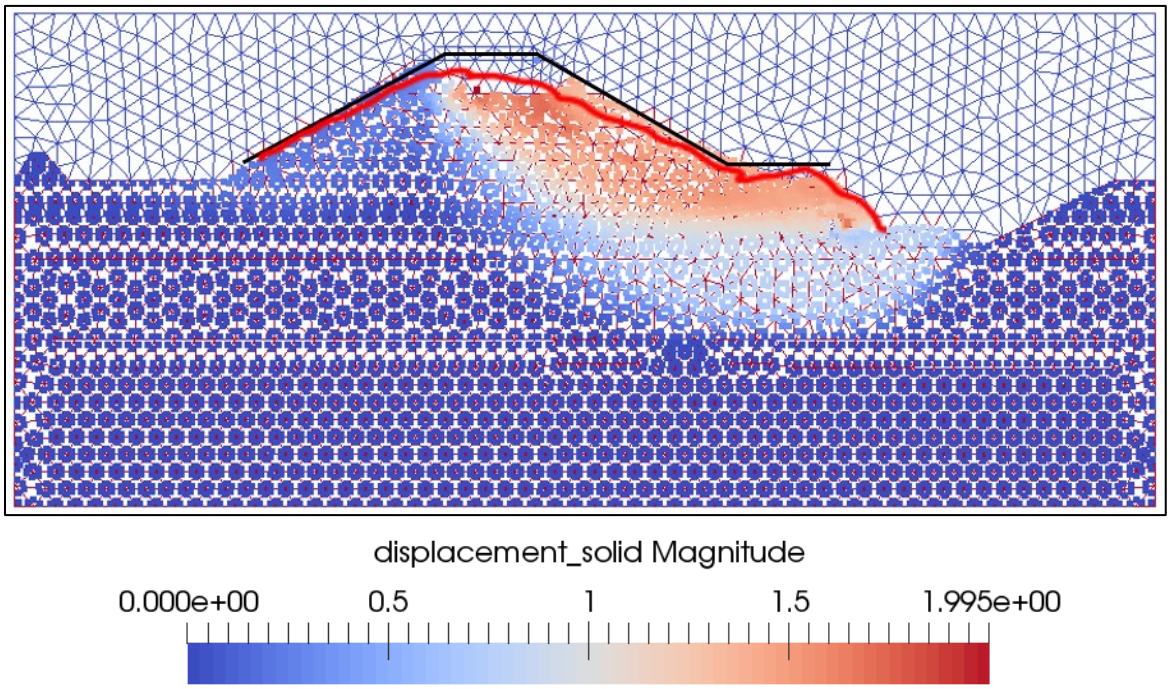

(b) Final total displacement

Figure 7. 1. Initial (black line) and final (red line) slope configuration of the South Dike's west-cross section (Koelewijn, 2012) (a) and simulated final total displacement contour (b).

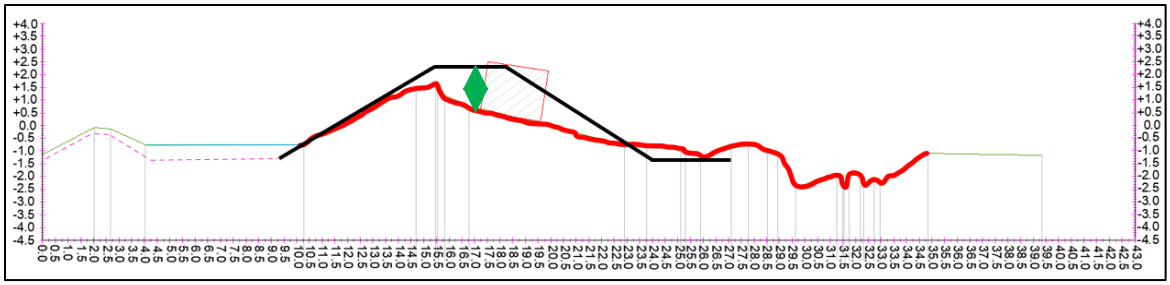

(a) Middle-cross section

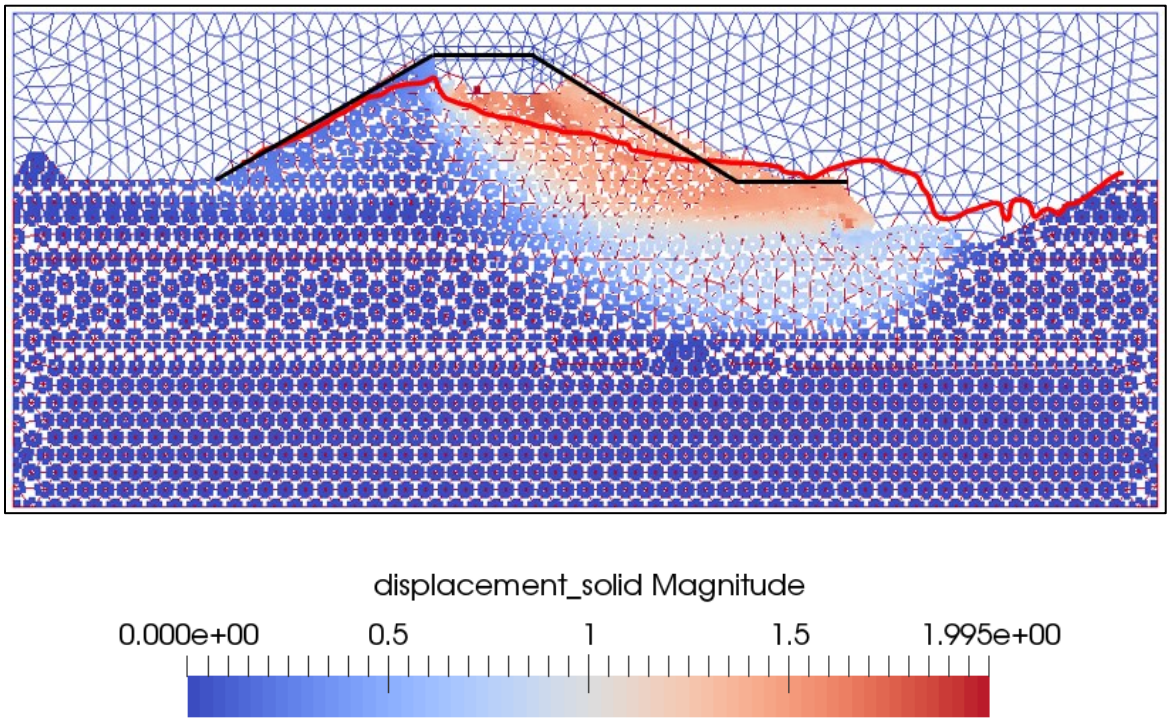

(b) Final total displacement

Figure 7. 2. Initial (black line) and final (red line) slope configuration of the South Dike's middle-cross section (Koelewijn, 2012) (a) and simulated final total displacement contour (b).

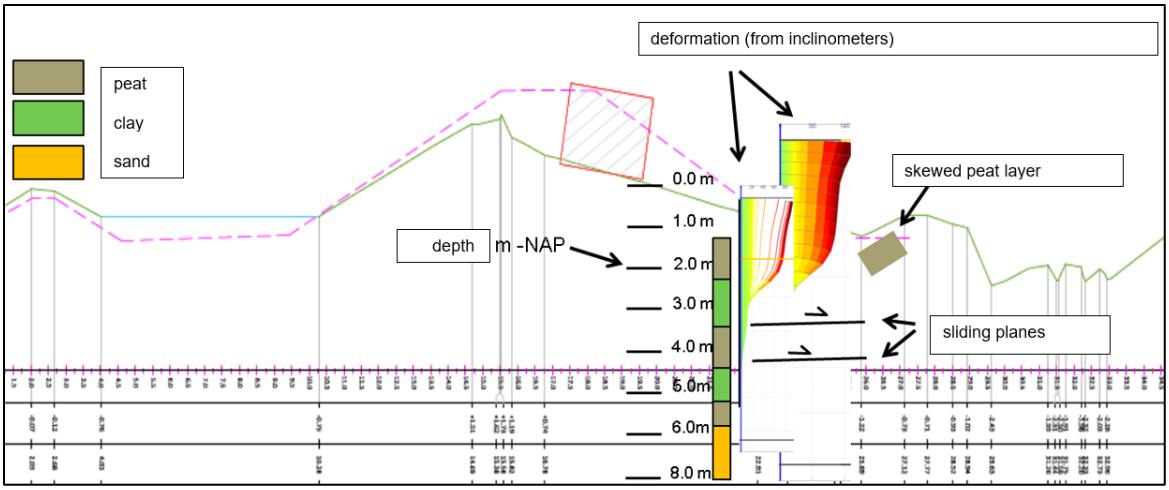

(a) Middle cross-section sliding plane indication

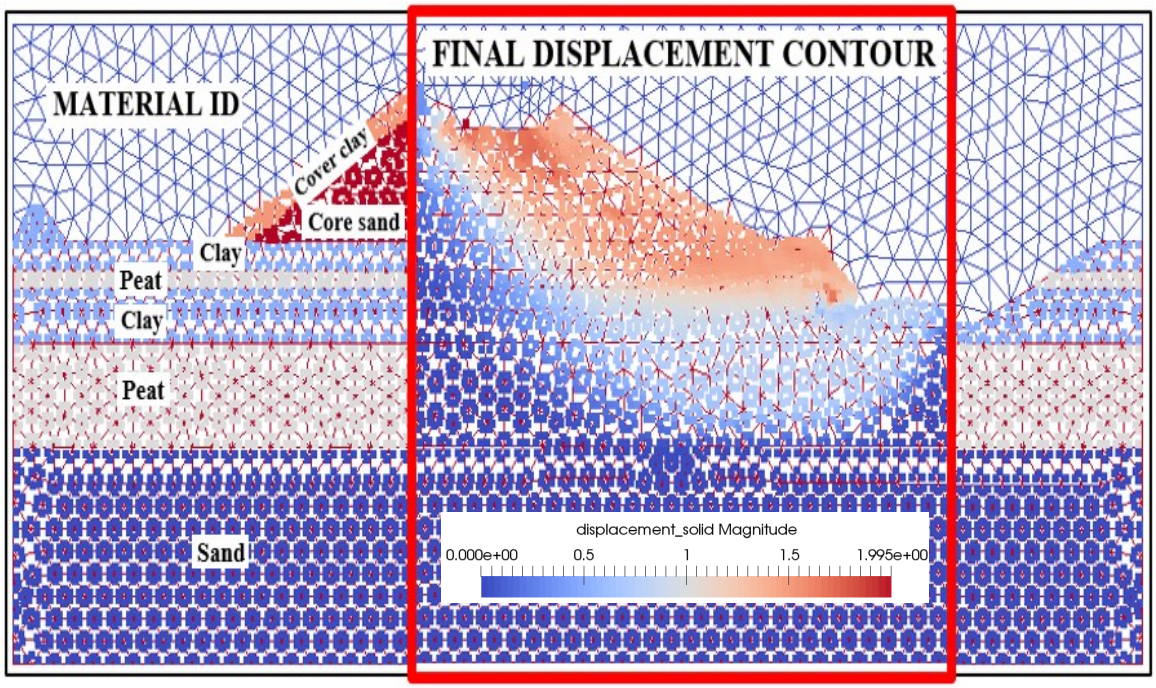

(b) MPM final displacement imposed on material ID contour

Figure 7. 3. Indication of sliding plane depth in the middle cross section (a) and MPM final displacement imposed on the material ID contour (b).

8 CONCLUSION

In this study, two numerical simulations were conducted to replicate an experiment carried out by the Dutch research program, 'IJkdijk'. The experiment involved inducing failure in a full-scale earthen levee named South Dike, located in the North-East of the Netherlands in 2012. The failure was as a result of forcefully infiltrating the levee's core with water.

Before simulating the pre- and post-failure of the levee using FEM and MPM, respectively, a benchmark slope was simulated to ensure consistency of results between the two methods. This step also served as a validation process for when stresses are transferred from the onset of failure in Midas FEA NX to Anura3D for the post-failure analysis. This was successful, demonstrating that simulations involving stress mapping yielded similar results to the MPM simulation that simulated the entire failure mechanism of the benchmark slope.

Moreover, the onset of failure of the South Dike was at the stage in which the containers were filled with water, obtaining a safety factor of 1.05. This safety factor is deemed acceptable, as it occurred before the levee's core was fully infiltrated with water, the stage that led to its failure. Next, the plane stresses at the onset of failure and pore stresses generated by the transient seepage analysis when the core was fully saturated were transferred to Anura3D for post-failure analysis. The evolution of the post-failure deformation was captured over a period of 12.5s, resulting in a maximum horizontal displacement of approximately 1.45m at the toe.

The simulations successfully managed to replicate the overall deep sliding failure mechanism observed in the experiment. The development of the sliding plane was reproduced in both the pre-failure analysis and was also captured in the dynamic simulation for the post-failure analysis, which simulated the large displacement (run-out).

Further improvement in the future can be made by employing constitutive models in the post-failure analysis, especially for the base materials (clay, peat, and sand), which consider the stress path dependency to failure. This is crucial because run-out prediction might be potentially underestimated due to the chosen constitutive model's limitations in best capturing the soil's mechanics.

Another enhancement that can be considered is incorporating the unsaturated soil state and its evolution with suction in the levee's core while it is being infiltrated with water. The soil's water retention curve and hydraulic conductivity curve would be required. This improvement will help in providing a more realistic mimic of the slope behavior when its water table rises, for instance, due to rainfall or by an upstream recharge as done in (Girardi et al., 2023).

Furthermore, the significance of this study lies in its application to risk assessment, which encompasses the evaluation of levee failure run-out. The factor of safety alone cannot fully account for slope movement. This is where MPM proves valuable, facilitating the post-failure-analysis necessary for simulating large displacements and understanding their behavior over time.

APPENDIX A

In this Appendix, the results of the FEM analysis carried out for the benchmark slope are presented. Table A.1(a) depicts the contour plot of *S-XX* for stress initialization, while (b) to (d) of the same figure provide the stress distributions for 5kN/m^2, 10kN/m^2, and 15kN/m^2. Similarly, Table A.2(a) to Table A.2(d) and Table A.3(a) to Table A.3(d) show the contour plots of *S-YY* and *S-XY* for the same load sequence, respectively. Negative values indicate compression, while positive values indicate tension. In addition, the pore pressure evolution is illustrated in Table A.4.

Table A. 1. Total stress in x-direction for (a) stress initialization, (b) load application of 5kN/m^2, (c) load application of 10kN/m^2 and (d) load application of 15kN/m^2.

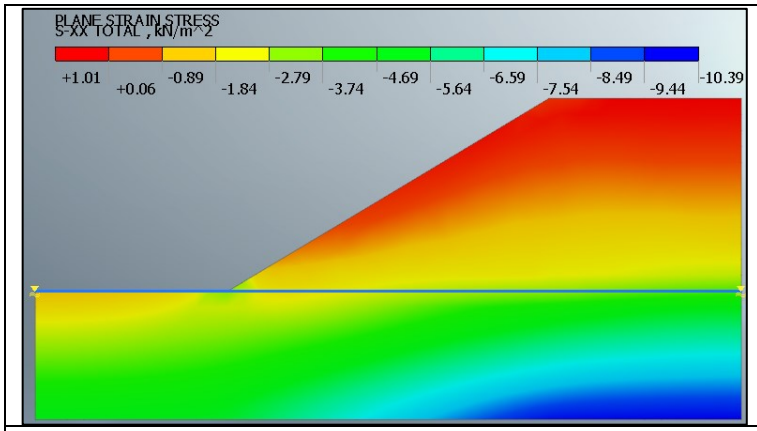

(a) Stress initialization

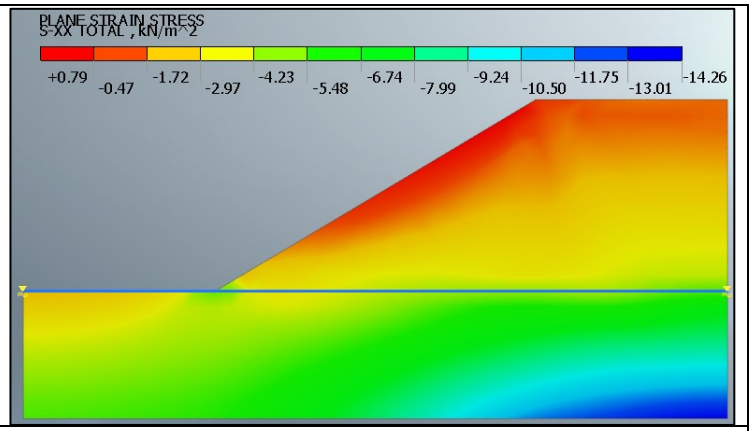

(b) Load applied = 5kN/m^2

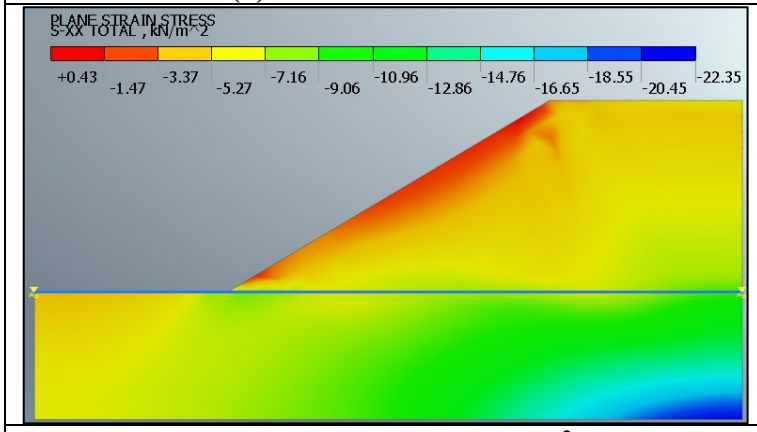

(c) Load applied = 10kN/m^2

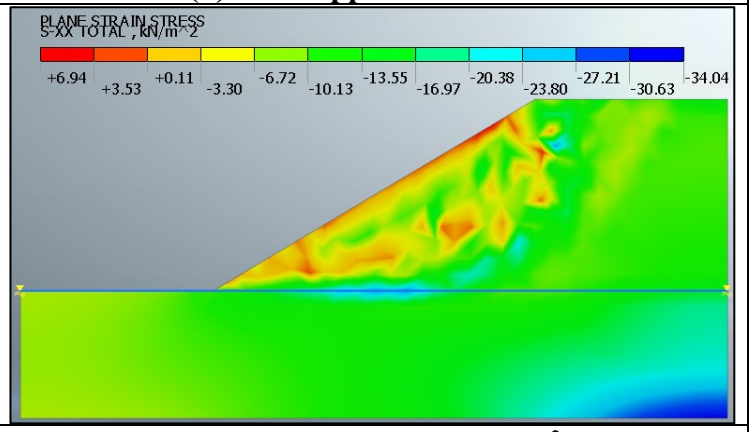

(d) Load applied = 15kN/m^2

Table A. 2. Total stress in y-direction for (a) stress initialization, (b) load application of 5kN/m^2, (c) load application of 10kN/m^2 and (d) load application of 15kN/m^2.

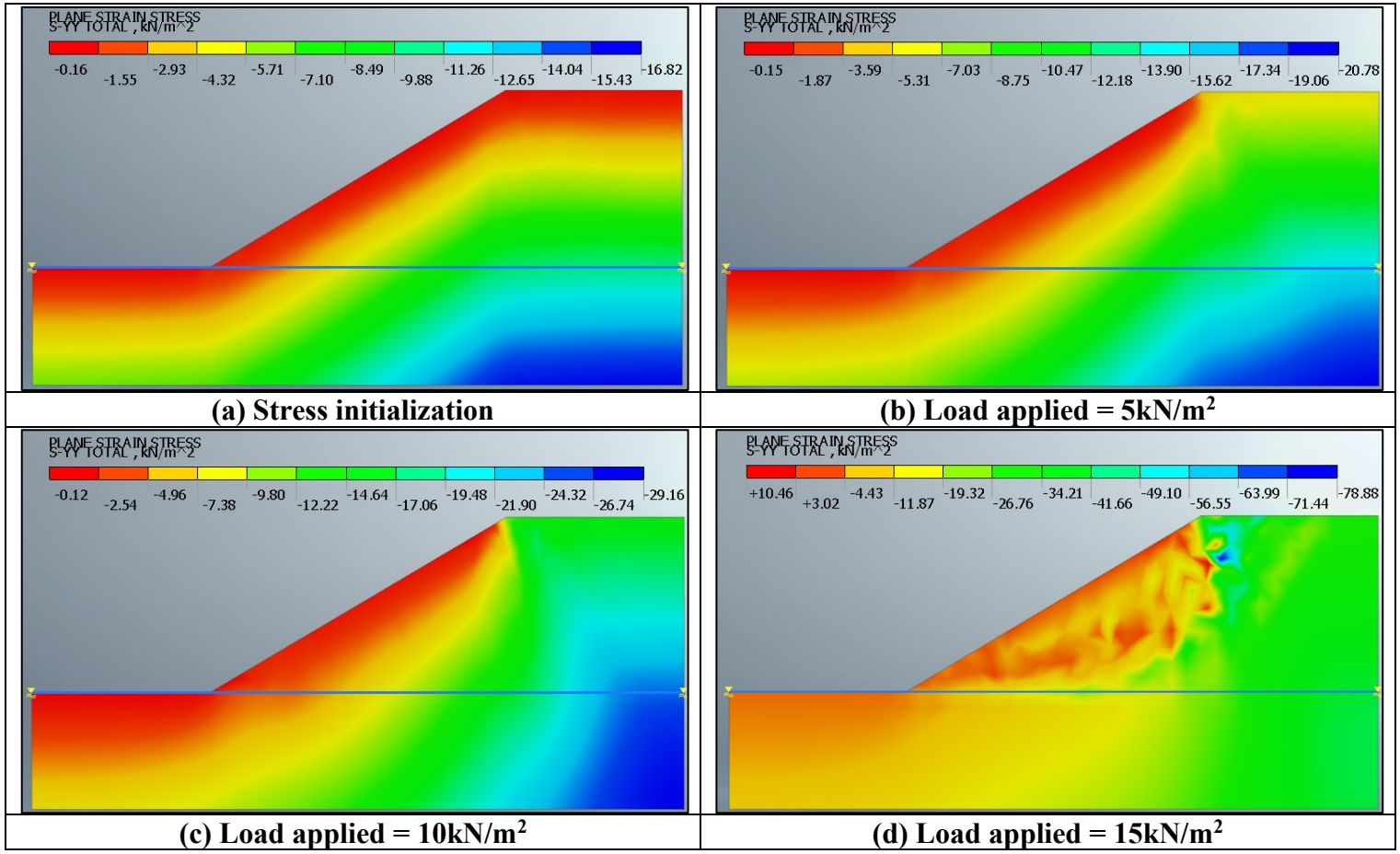

Table A. 3. Shear stress for (a) stress initialization, (b) load application of 5kN/m^2, (c) load application of 10kN/m^2 and (d) load application of 15kN/m^2.

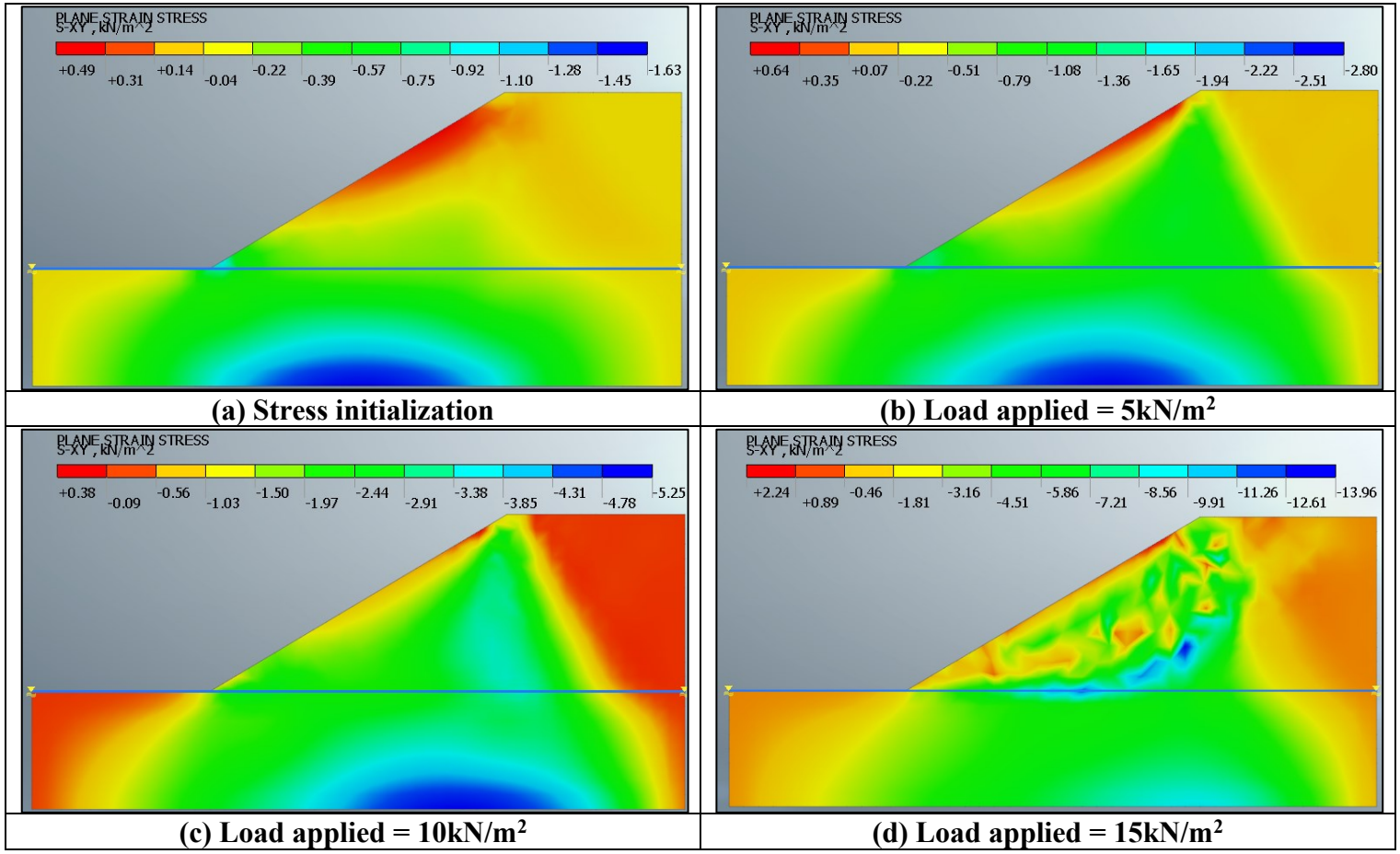

(a) Stress initialization | **(b) Load applied = 5kN/m^2**

(c) Load applied = 10kN/m^2 | **(d) Load applied = 15kN/m^2**

Table A. 4. Pore stress for (a) stress initialization, (b) load application of 5kN/m^2, (c) load application of 10kN/m^2 and (d) load application of 15kN/m^2.

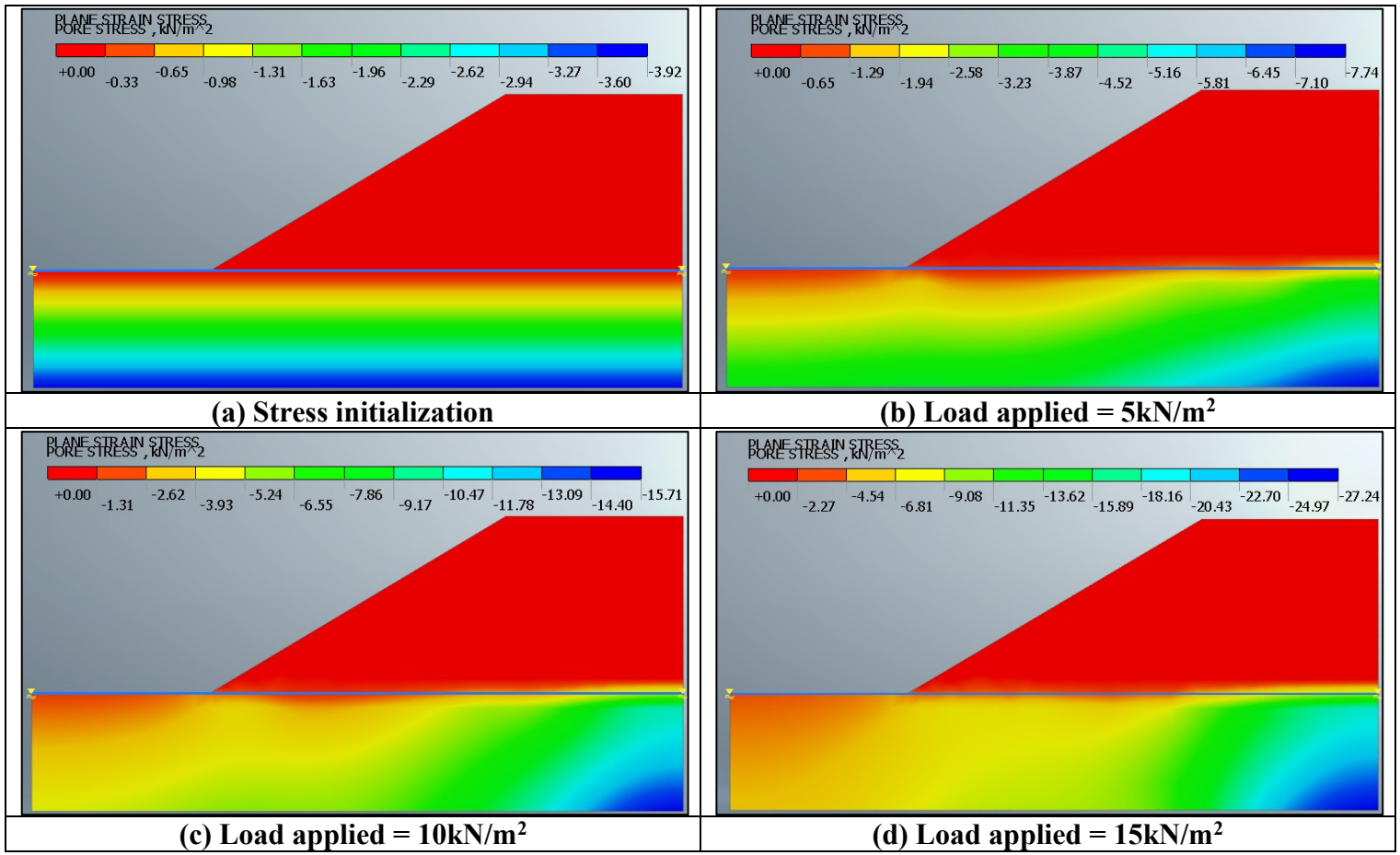

(a) Stress initialization | **(b) Load applied = 5kN/m^2**

(c) Load applied = 10kN/m^2 | **(d) Load applied = 15kN/m^2**

APPENDIX B

This Appendix presents the results of the benchmark slope conducted using MPM. The post-processing software employed to display these results is Paraview.

The components representing the stress tensor in 2D in Paraview are provided in Figure B.1. Horizontal stress is indicated by 0 and vertical stress by 4 while shear stress in the x-y plane by 1.

$$\boldsymbol{\sigma} = \begin{pmatrix} \sigma_{xx} & \tau_{xy} & 0 \\ \tau_{yx} & \sigma_{yy} & 0 \\ 0 & 0 & \sigma_{zz} \end{pmatrix} = \begin{pmatrix} 0 & 1 & 2 \\ 3 & 4 & 5 \\ 6 & 7 & 8 \end{pmatrix} \quad \textit{in 2D}$$

Figure B. 1. 2D stress tensor components in Paraview.

The total number of load steps for both the quasi-static and dynamics simulations is 6. The time per load step set for the dynamic simulation is 0.5s, and it lasted about 2.52s. Figure B.2(a) displays the position of a selected MP, and in (b), its plot of horizontal (Ux) and vertical (Uy) displacement generated by the two quasi-static and one dynamic simulation. As expected, in the highly damped (70%) quasi-static simulation, the displacements are null as compared to the quasi-static simulation damped with a 5% coefficient. The displacements of the dynamic simulation for this selected MP are slightly lower than the quasi-static simulation at the end of the period. It's important to note that time is not considered in the quasi-static analysis, unlike the dynamic case, which explains the difference.

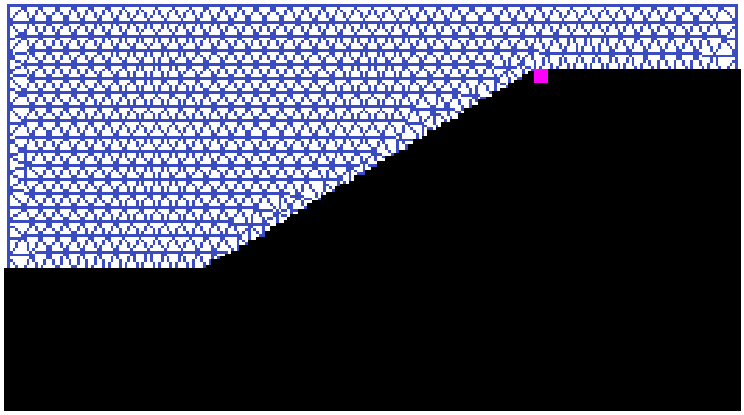

(a) Selected MP (ID = 4061)

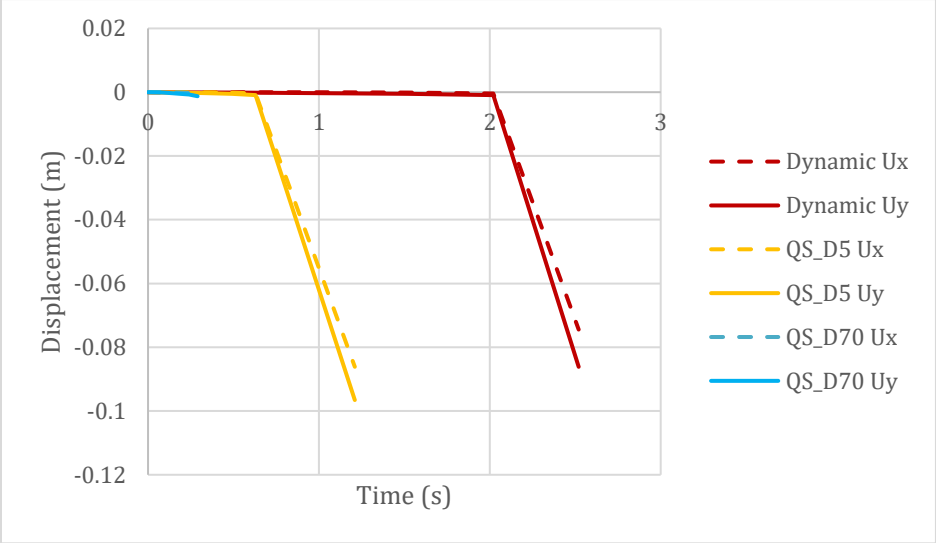

(b) Displacement plot comparison

Figure B. 2. Selected MP position (a) and displacement comparison (b).

Furthermore, Table B.1 to B.4 illustrate the stresses (horizontal, vertical and shear stress), including the pressure distribution, for the entire load stages of the quasi-static MPM simulation with a 5% damping coefficient. Similarly, Table B.5 to B.8 display the results of the quasi-static simulation with a 70% damping coefficient, while Tables B.9 to B.12 present the results of the dynamic MPM simulation.

Damping Coefficient = 5%

Table B. 1. MPM 5% damping quasi-static analysis total stress in the x-direction distribution.

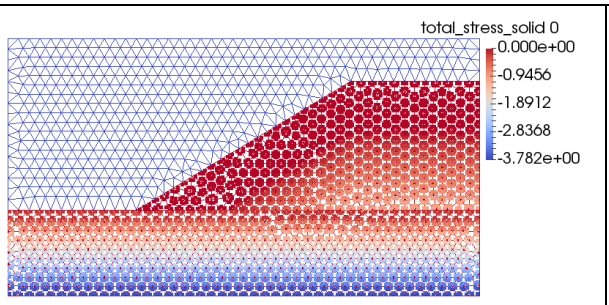

(a) Stress initialization

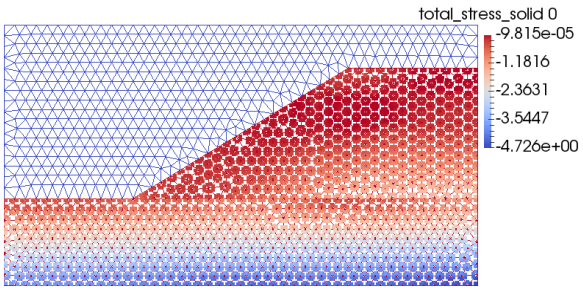

(b) Load stage 1= 0kN/m

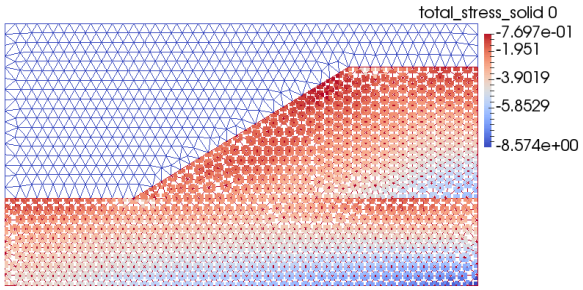

(c) Load stage 2= 5kN/m^2

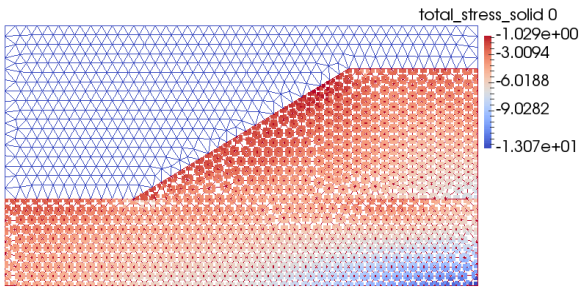

(d) Load stage 3= 10kN/m^2

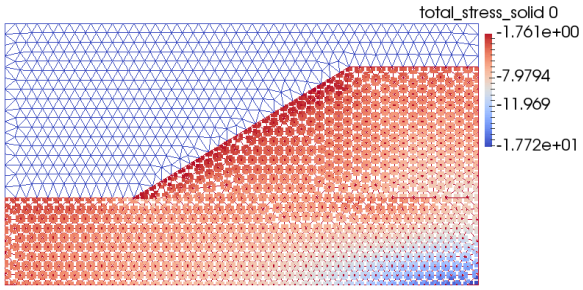

(e) Load stage 4 =15kN/m^2

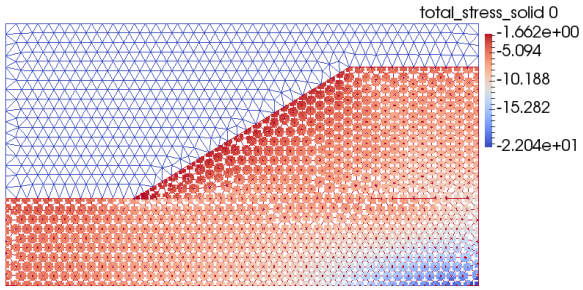

(f) Load stage 5 =20kN/m^2

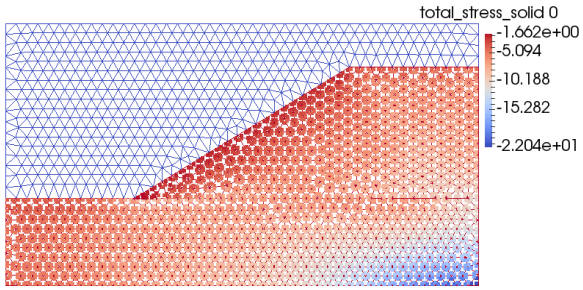

(g) Load stage 6 =25kN/m^2

Table B. 2. MPM 5% damping quasi-static analysis total stress in the y-direction distribution.

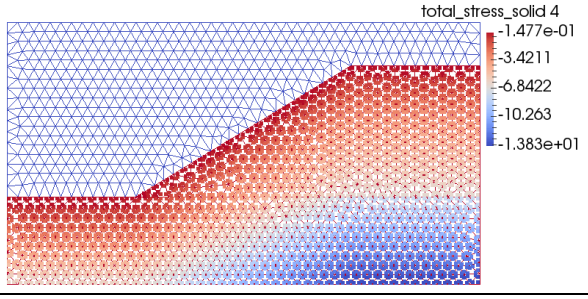

(a) Stress initialization

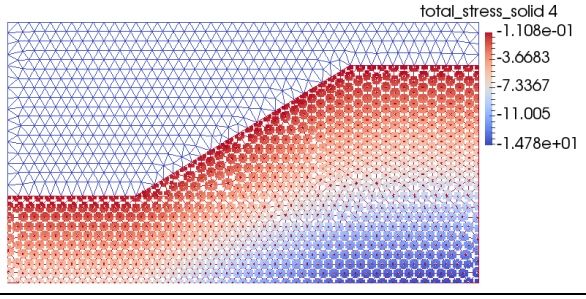

(b) Load stage 1= 0kN/m

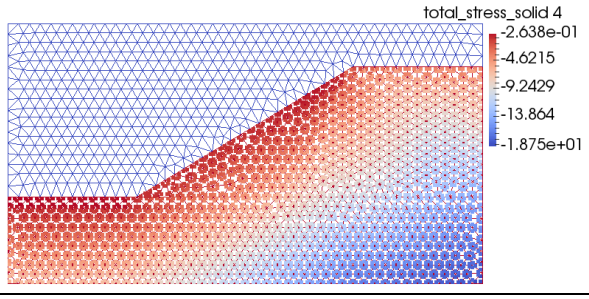

(c) Load stage 2= 5kN/m^2

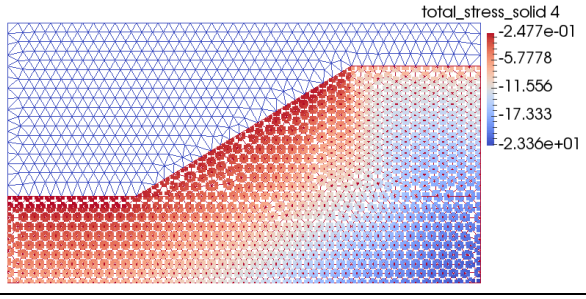

(d) Load stage 3= 10kN/m^2

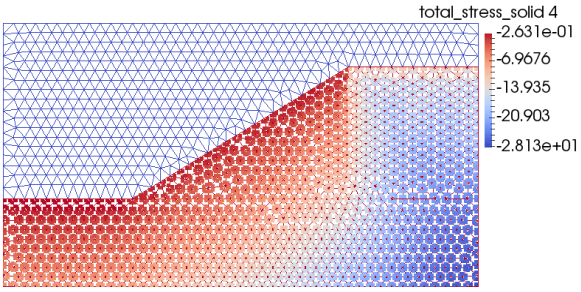

(e) Load stage 4 =15kN/m^2

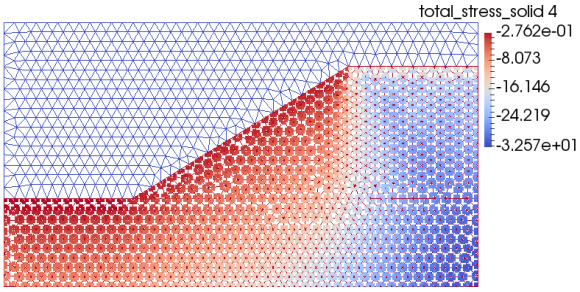

(f) Load stage 5 =20kN/m^2

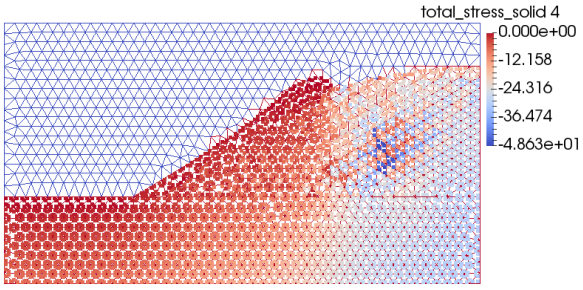

(g) Load stage 6 =25kN/m^2

Table B. 3. MPM 5% damping quasi-static analysis shear stress distribution.

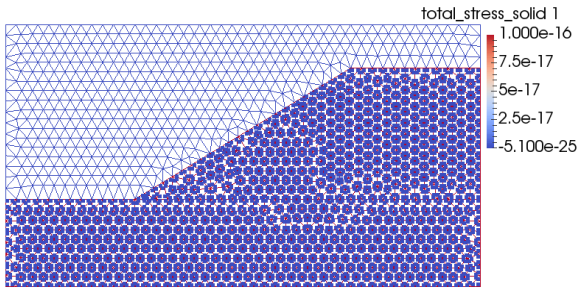

(a) Stress initialization

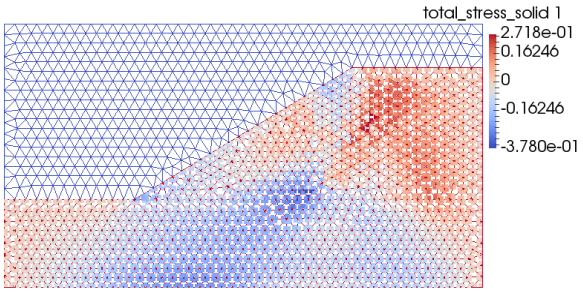

(b) Load stage 1= 0kN/m

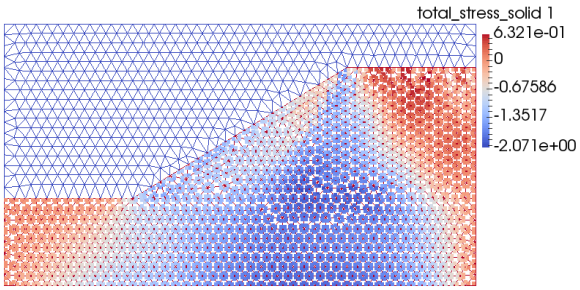

(c) Load stage 2= 5kN/m^2

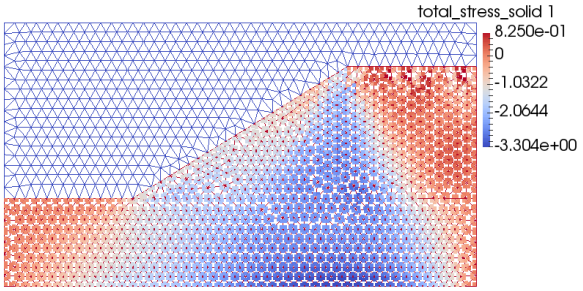

(d) Load stage 3= 10kN/m^2

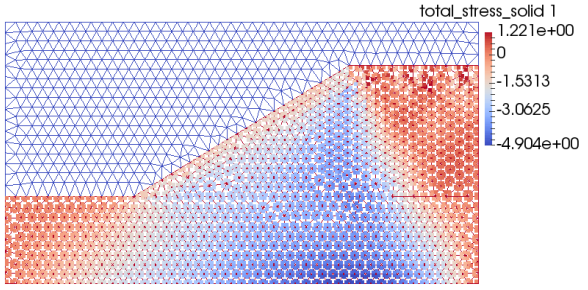

(e) Load stage 4 =15kN/m^2

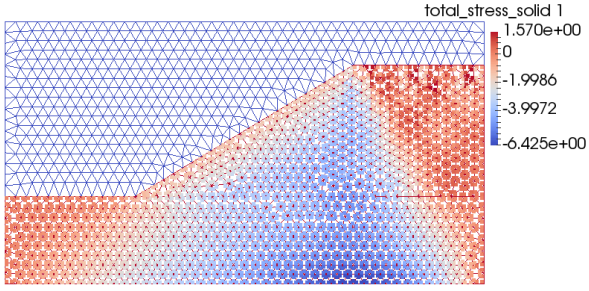

(f) Load stage 5 =20kN/m^2

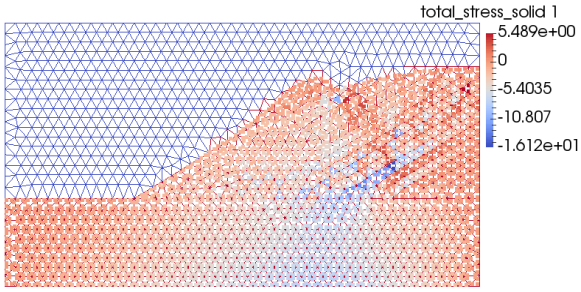

(g) Load stage 6 =25kN/m^2

Table B. 4. MPM 5% damping quasi-static analysis pressure evolution.

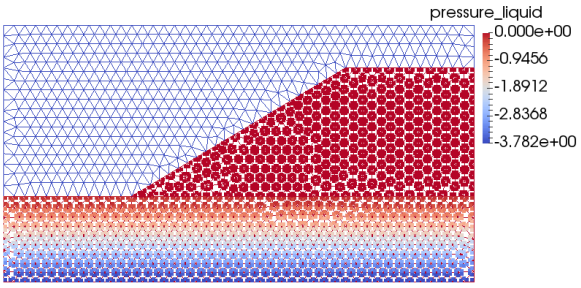

(a) Stress initialization

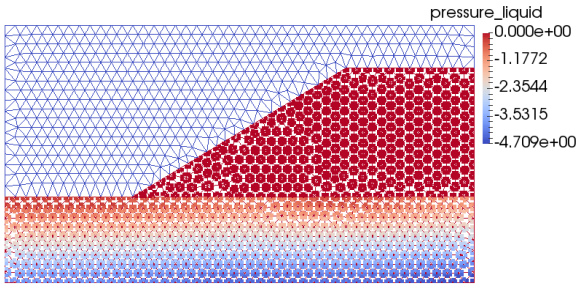

(b) Load stage 1= 0kN/m

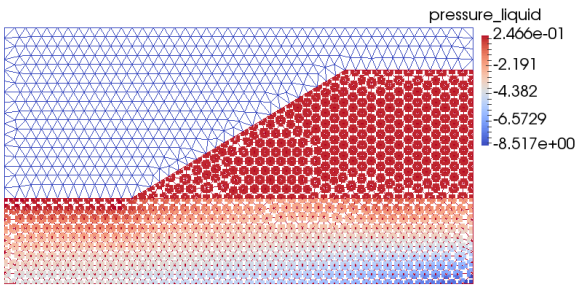

(c) Load stage 2= 5kN/m^2

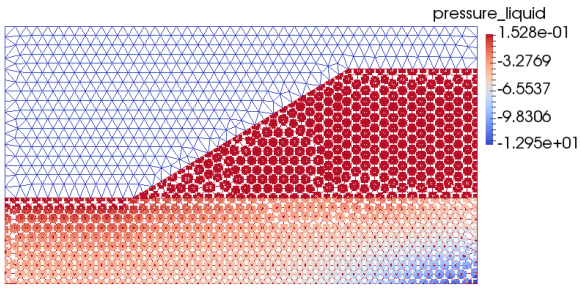

(d) Load stage 3= 10kN/m^2

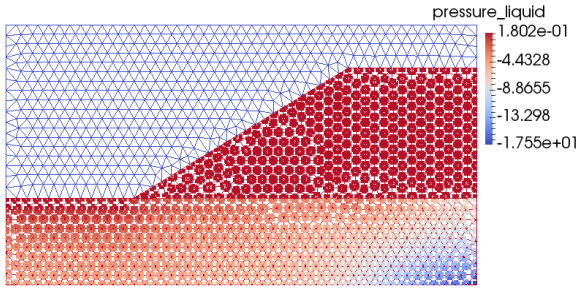

(e) Load stage 4 =15kN/m^2

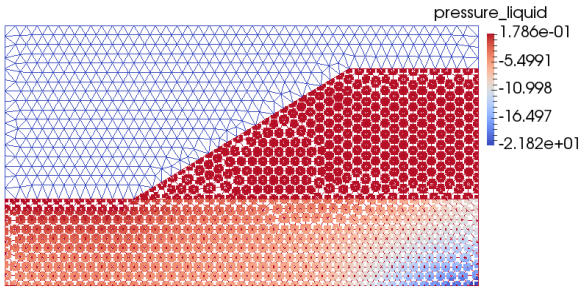

(f) Load stage 5 =20kN/m^2

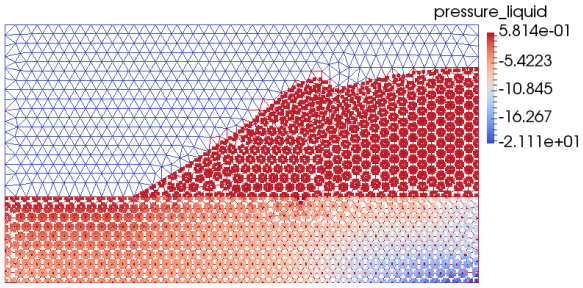

(g) Load stage 6 =25kN/m^2

Damping Coefficient = 70%

Table B. 5. MPM 70% damping quasi-static analysis total stress in the x-direction distribution.

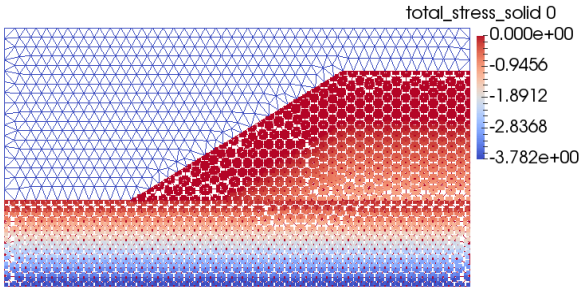

(a) Stress initialization

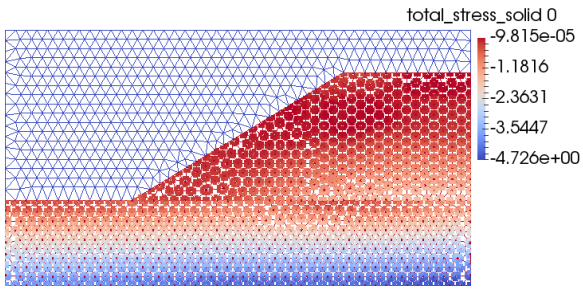

(b) Load stage 1= 0kN/m

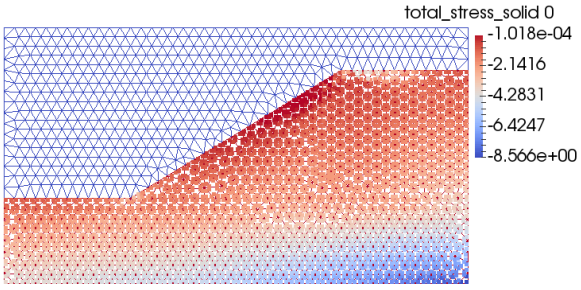

(c) Load stage 2= 5kN/m^2

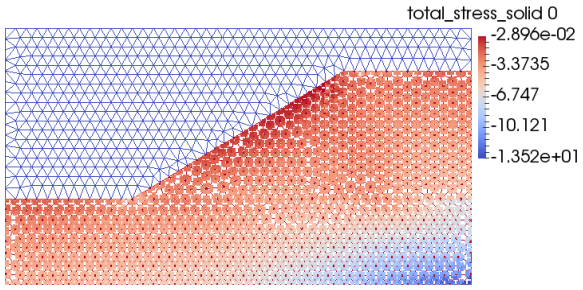

(d) Load stage 3= 10kN/m^2

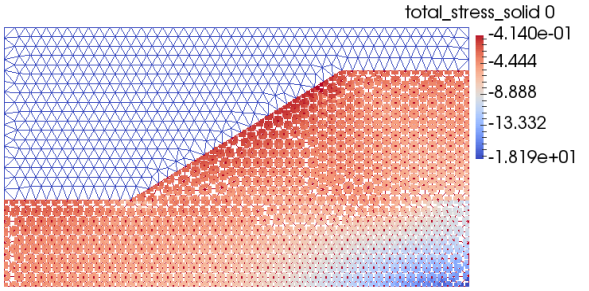

(e) Load stage 4 =15kN/m^2

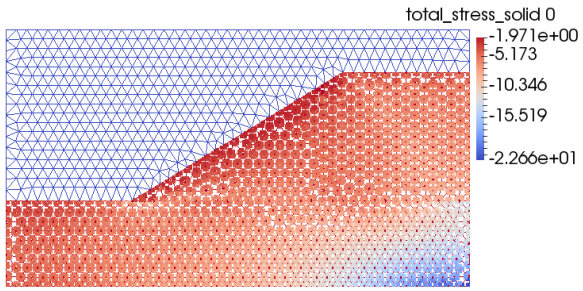

(f) Load stage 5 =20kN/m^2

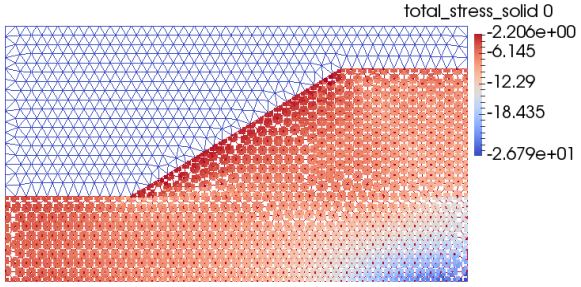

(g) Load stage 6 =25kN/m^2

Table B. 6. MPM 70% damping quasi-static analysis total displacement in the y-direction distribution.

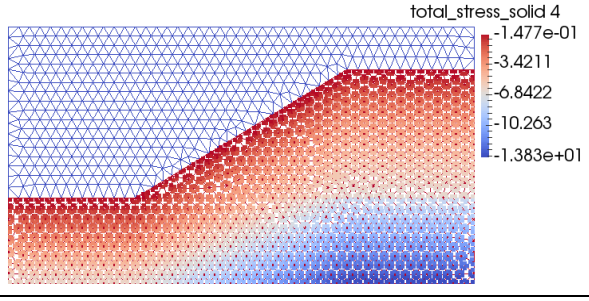

(a) Stress initialization

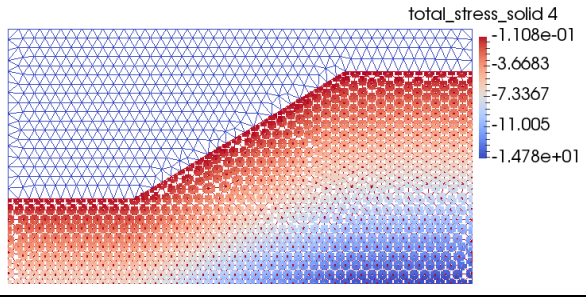

(b) Load stage 1= 0kN/m

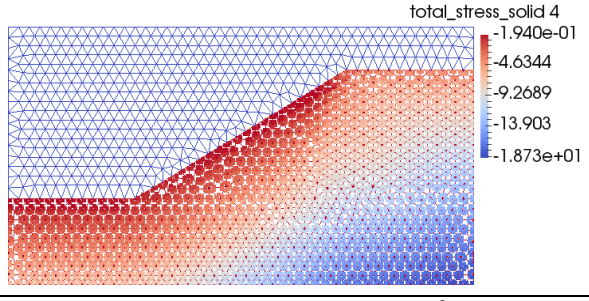

(c) Load stage 2= 5kN/m^2

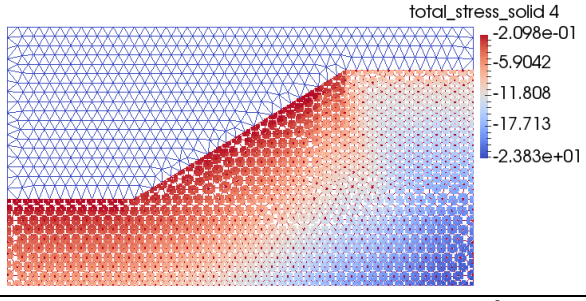

(d) Load stage 3= 10kN/m^2

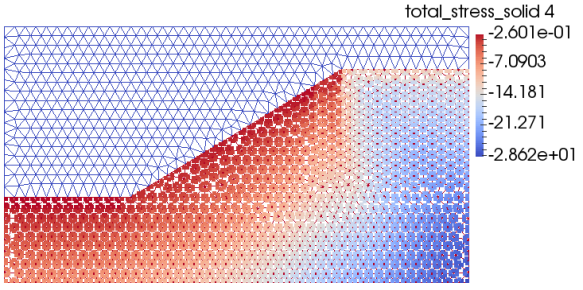

(e) Load stage 4 =15kN/m^2

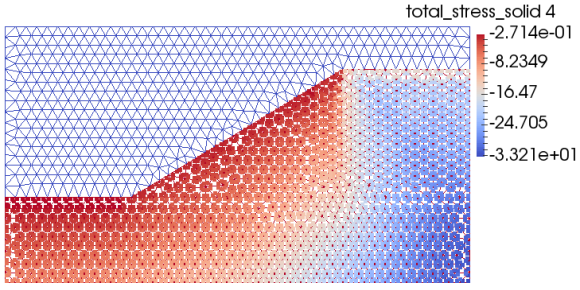

(f) Load stage 5 =20kN/m^2

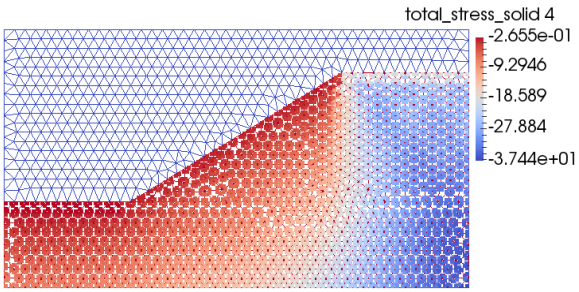

(g) Load stage 6 =25kN/m^2

Table B. 7. MPM 70% damping quasi-static analysis shear stress distribution.

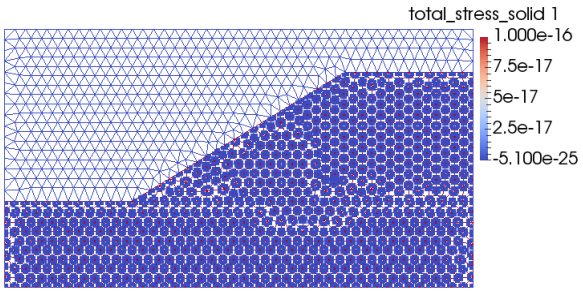

(a) Stress initialization

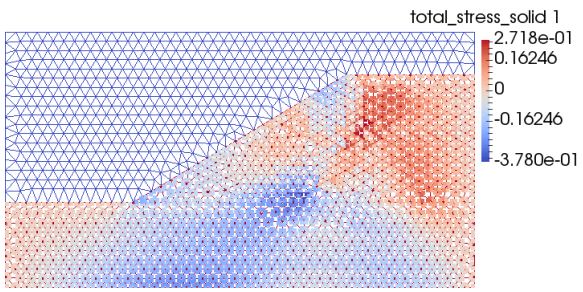

(b) Load stage 1= 0kN/m

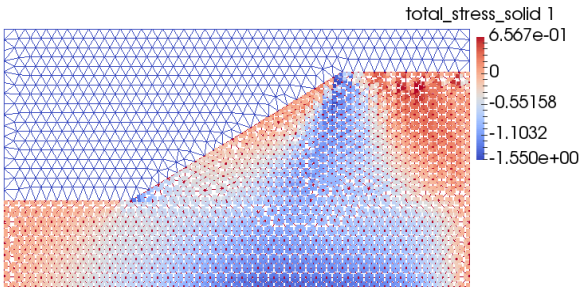

(c) Load stage 2= 5kN/m^2

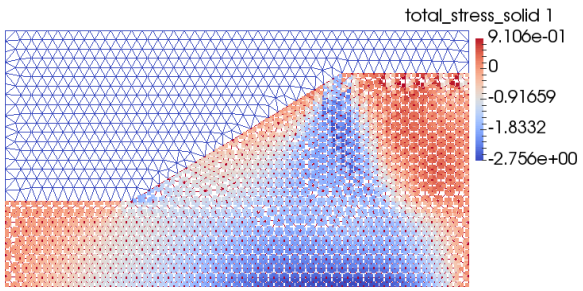

(d) Load stage 3= 10kN/m^2

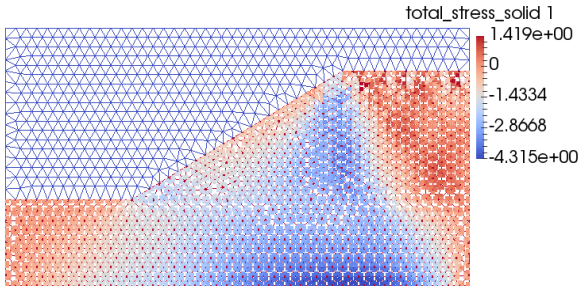

(e) Load stage 4 =15kN/m^2

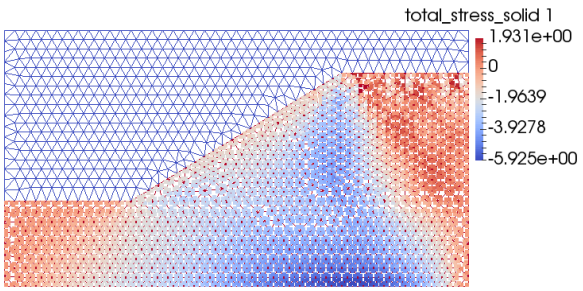

(f) Load stage 5 =20kN/m^2

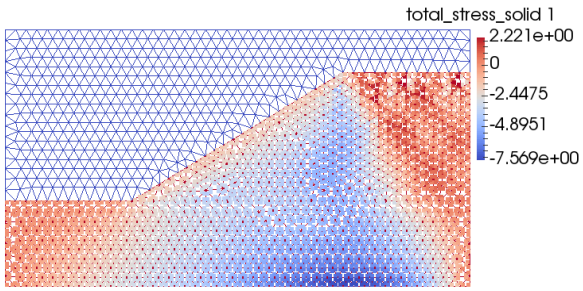

(g) Load stage 6 =25kN/m^2

Table B. 8. MPM 70% damping quasi-static analysis pressure evolution.

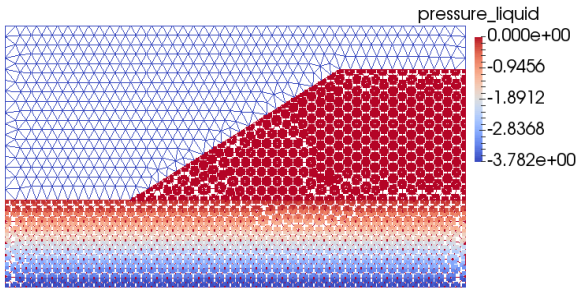

(a) Stress initialization

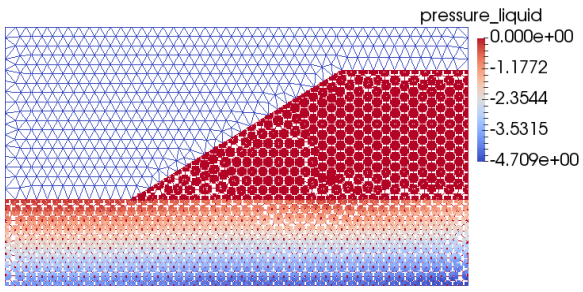

(b) Load stage 1= 0kN/m

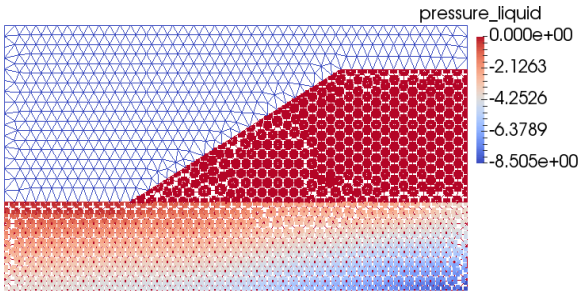

(c) Load stage 2= 5kN/m^2

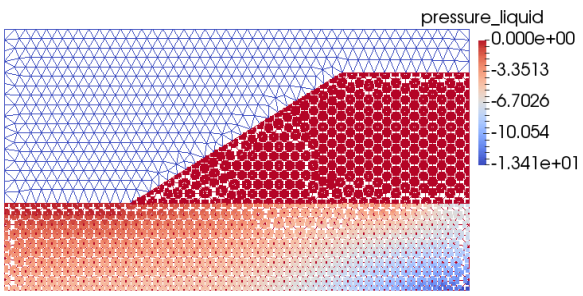

(d) Load stage 3= 10kN/m^2

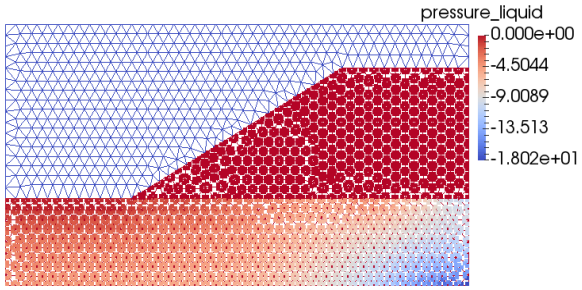

(e) Load stage 4 =15kN/m^2

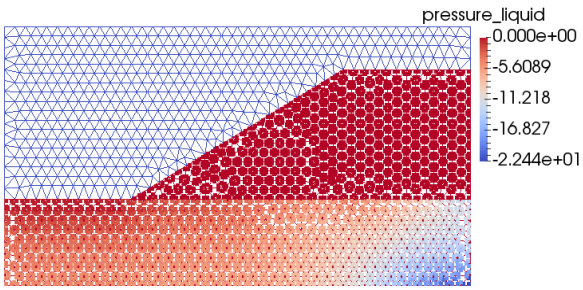

(f) Load stage 5 =20kN/m^2

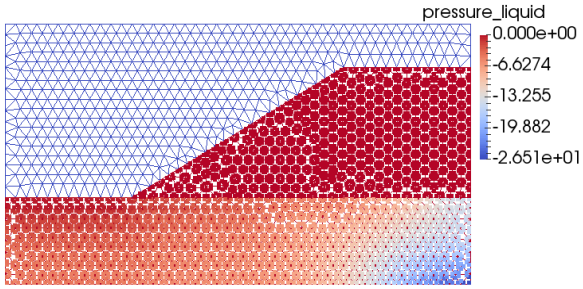

(g) Load stage 6 =25kN/m^2

Dynamic Analysis

Table B. 9. MPM dynamic analysis total stress in the x-direction distribution.

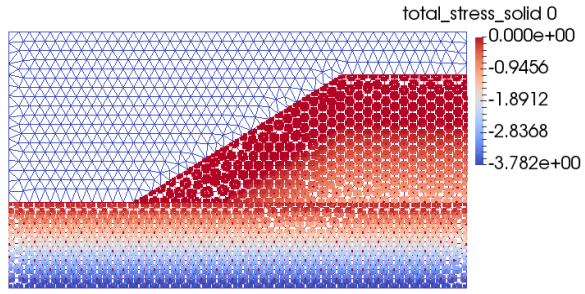

(a) Stress initialization (t= 0s)

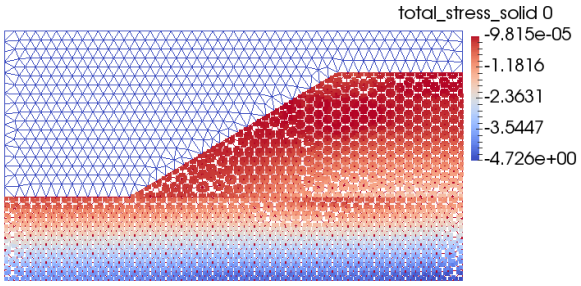

(b) Load stage 1= 0kN/m (t= 0.02s)

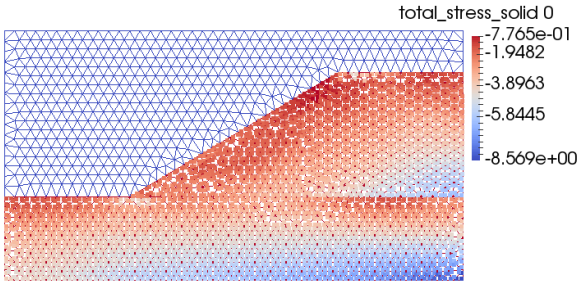

(c) Load stage 2= 5kN/m^2 (t= 0.52s)

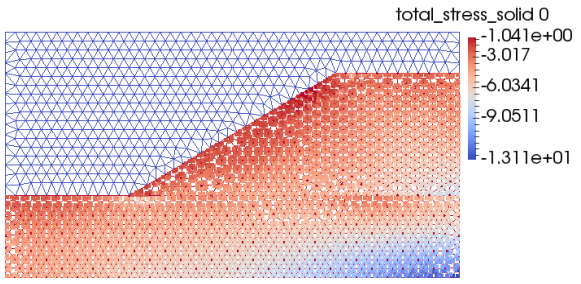

(d) Load stage 3= 10kN/m^2 (t= 1.02s)

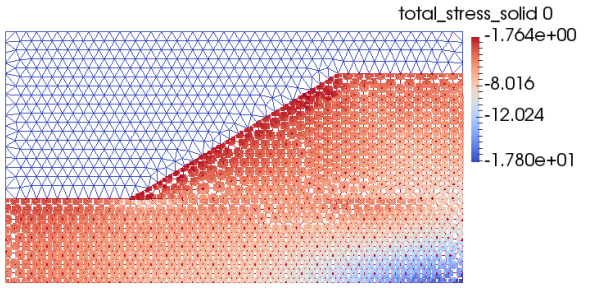

(e) Load stage 4 =15kN/m^2 (t= 1.52s)

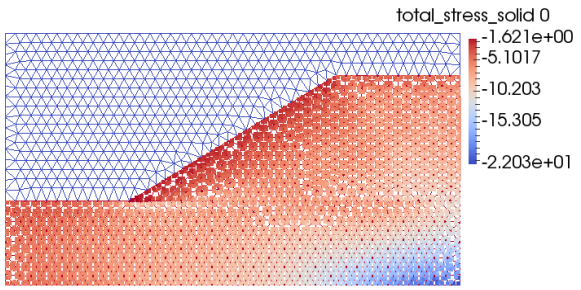

(f) Load stage 5 =20kN/m^2 (t= 2.02s)

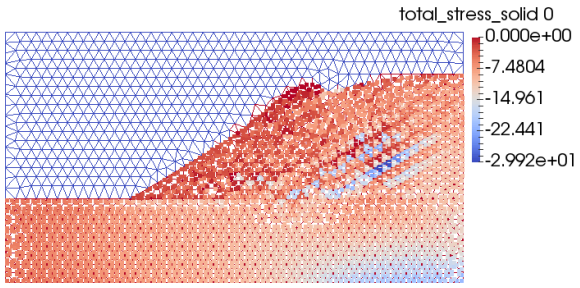

(g) Load stage 6 =25kN/m^2 (t= 2.52s)

Table B. 10. MPM dynamic analysis total stress in the y-direction distribution.

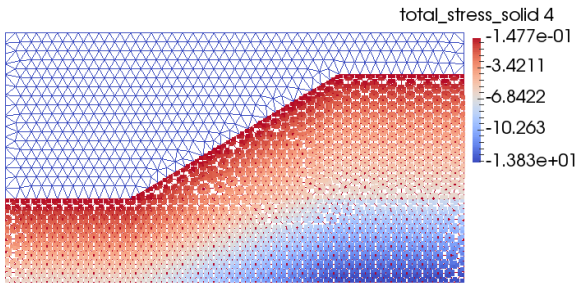	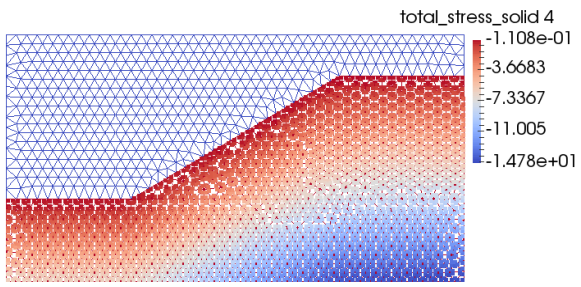
(a) Stress initialization (t= 0s)	**(b) Load stage 1= 0kN/m (t= 0.02s)**
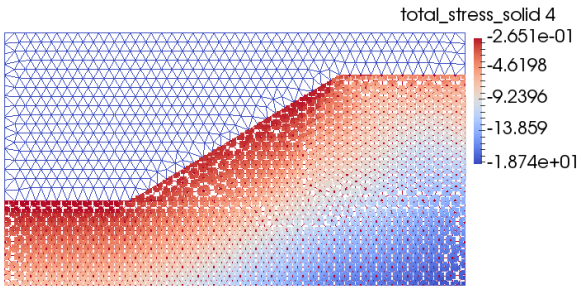	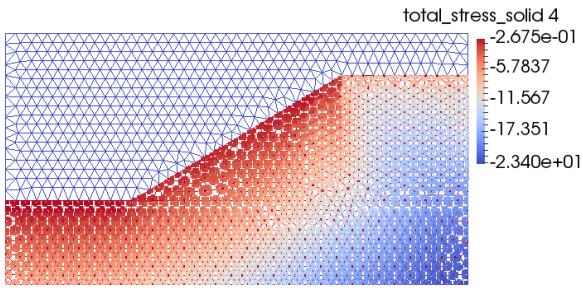
(c) Load stage 2= 5kN/m^2 (t= 0.52s)	**(d) Load stage 3= 10kN/m^2 (t= 1.02s)**
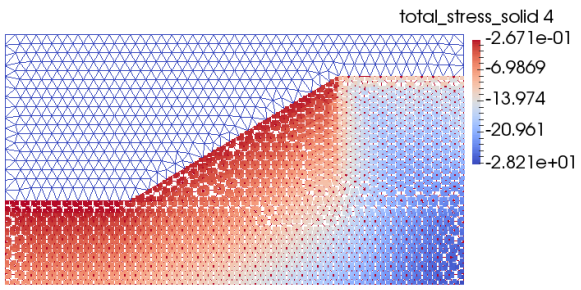	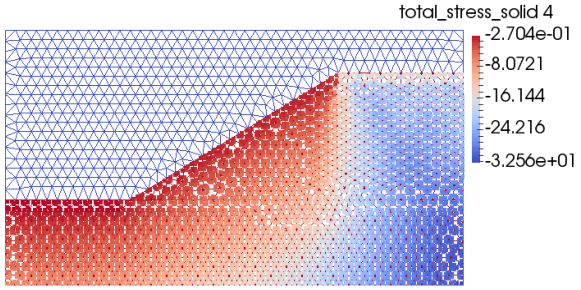
(e) Load stage 4 =15kN/m^2 (t= 1.52s)	**(f) Load stage 5 =20kN/m^2 (t= 2.02s)**
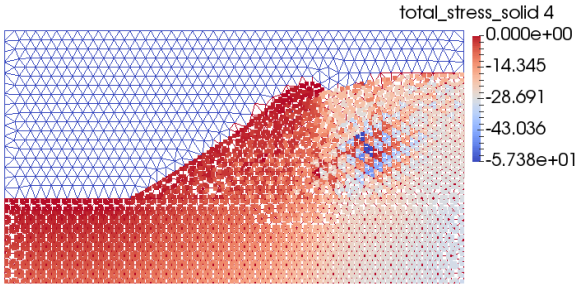	
(g) Load stage 6 =25kN/m^2 (t= 2.52s)	

Table B. 11. MPM dynamic analysis shear stress distribution.

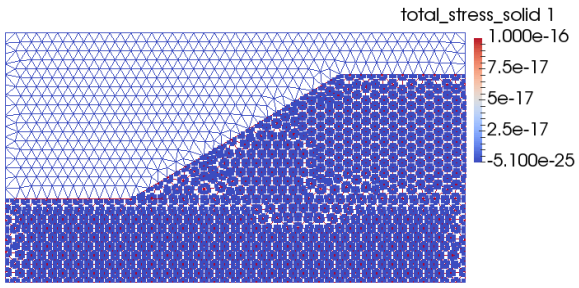

(a) Stress initialization (t= 0s)

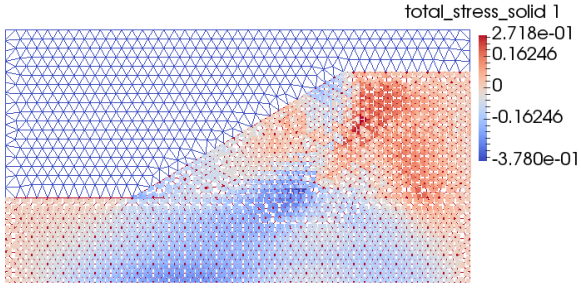

(b) Load stage 1= 0kN/m (t= 0.02s)

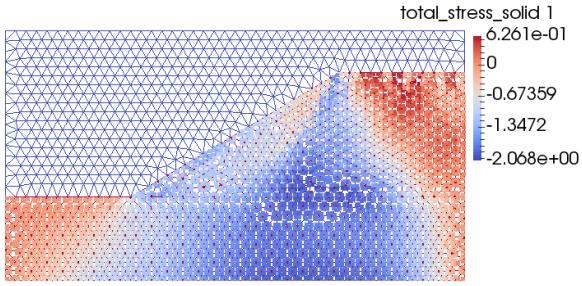

(c) Load stage 2= 5kN/m^2 (t= 0.52s)

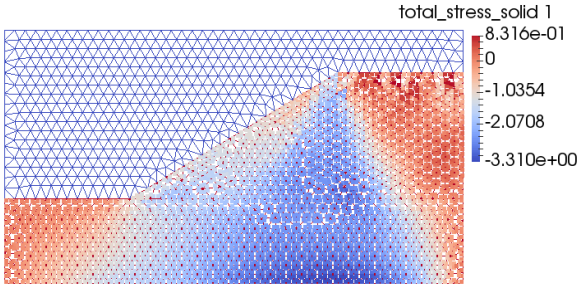

(d) Load stage 3= 10kN/m^2 (t= 1.02s)

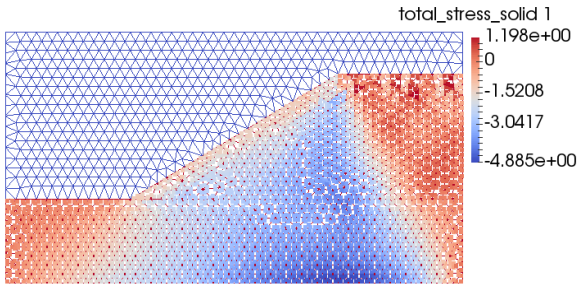

(e) Load stage 4 =15kN/m^2 (t= 1.52s)

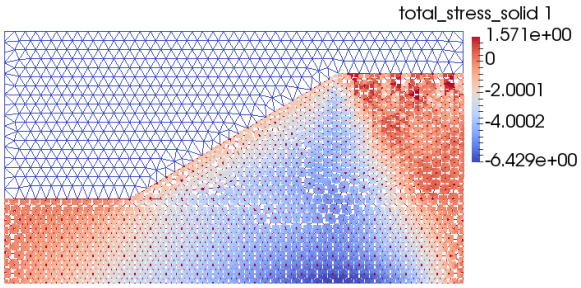

(f) Load stage 5 =20kN/m^2 (t= 2.02s)

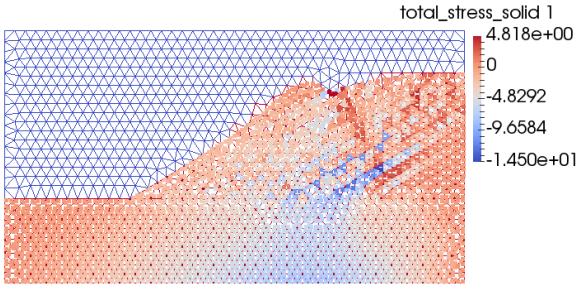

(g) Load stage 6 =25kN/m^2 (t= 2.52s)

Table B. 12. MPM dynamic analysis pressure evolution.

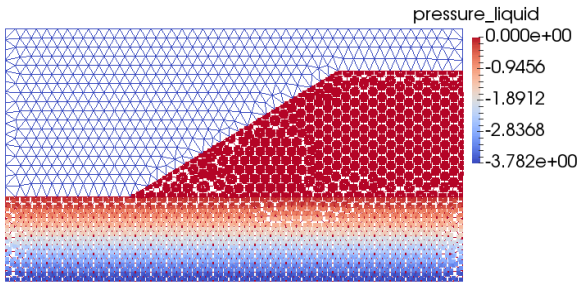

(a) Stress initialization (t= 0s)

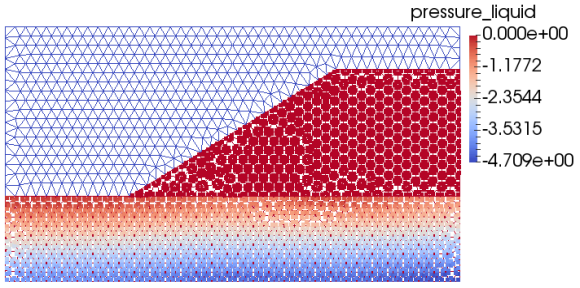

(b) Load stage 1= 0kN/m (t= 0.02s)

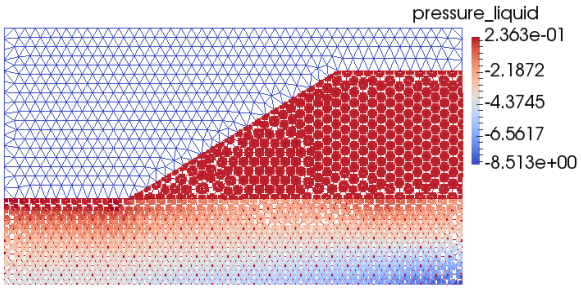

(c) Load stage 2= 5kN/m^2 (t= 0.52s)

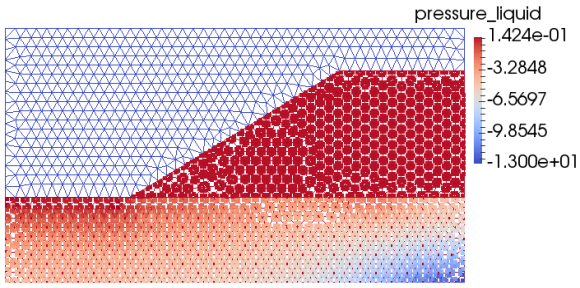

(d) Load stage 3= 10kN/m^2 (t= 1.02s)

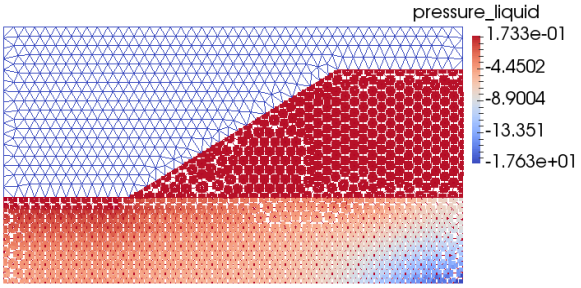

(e) Load stage 4 =15kN/m^2 (t= 1.52s)

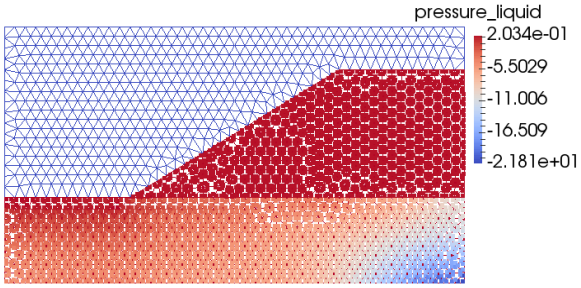

(f) Load stage 5 =20kN/m^2 (t= 2.02s)

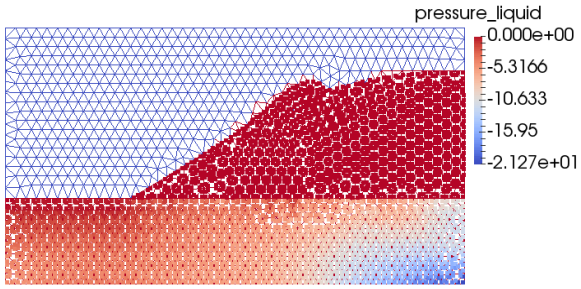

(g) Load stage 6 =25kN/m^2 (t= 2.52s)

APPENDIX C

The post-failure analysis of the benchmark slope results in terms of the stresses (horizontal, vertical and shear) as well as the pressure distributions are provided in this Appendix. These findings are from two dynamic MPM simulations. In the first simulation, stresses calculated using FEM are transferred from the onset of failure (load applied = 15kN/m^2). Conversely, in the second simulation, the stresses are transferred from a load application of 10kN/m^2.

When transferring the plane strain stresses from the FEM model with a load application of 15kN/m^2, the number of load steps set was 2 to reach 25kN/m^2, and it lasted for a duration of 1s. As for the case when transfer occurred from a load application of 10kN/m^2, the total load steps required to reach 25kN/m^2 were 3. This simulation took 1.5s to complete. Time per load step set is 0.5s for both cases.

Furthermore, an MP is selected, as shown in Figure C.1(a), and its horizontal (Ux) and vertical (Uy) displacements over time generated by the simulations involving mapping of stresses from FEM and without mapping are compared (b). As observed, despite the differences in simulation times, the displacement values from all three simulations are nearly identical by the end of their periods. Hence, this benchmark mapping serves as validation for the post-failure analysis of the South dike, involving the mapping of stresses from its onset of failure.

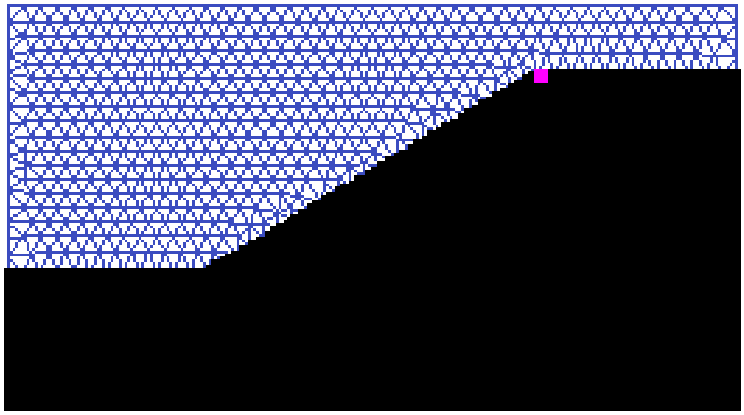

(c) Selected MP (ID = 4061)

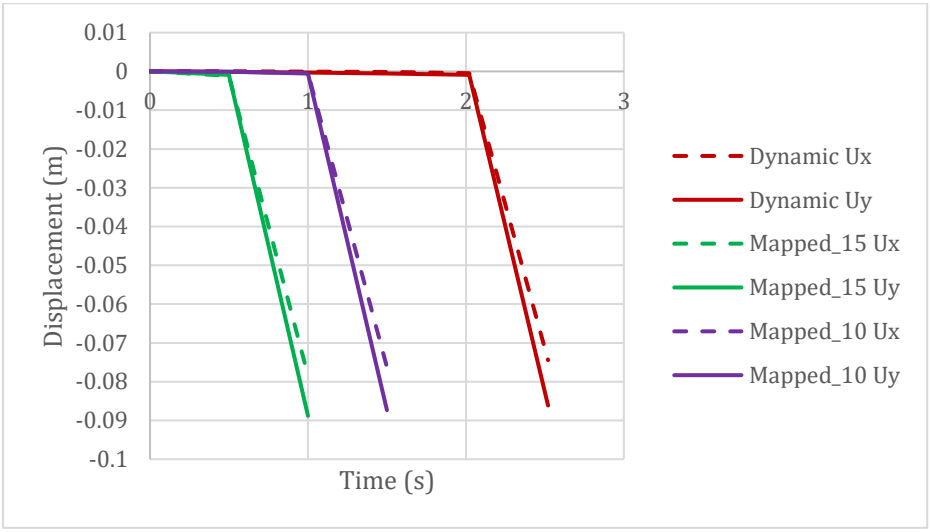

(d) Displacement plot comparison

Figure C. 1. Selected MP position (a) and displacement (m) comparison (b).

Moreover, Tables C.1 to C.4 illustrate the stress and pressure distributions using Paraview for the case where the load is transferred from the onset of failure. On the other hand, Tables C.5 to C.8 depict the stress and pressure distributions for the case of load where the load is transferred from an earlier stage (load applied = 10kN/m^2).

Stresses transferred from load application = 15kN/m^2

Table C. 1. Horizontal stress (kN/m^2) distributions for the case of stresses transferred from load = 15kN/m^2.

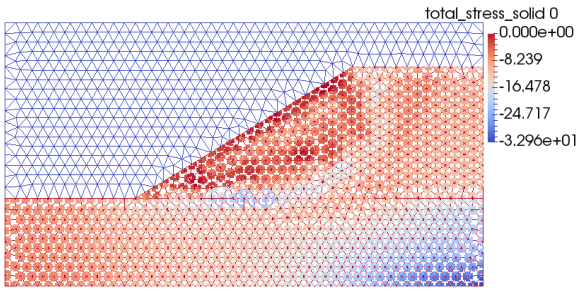

(a) Transfer (stage 4) = 15kN/m^2 (t= 0s)

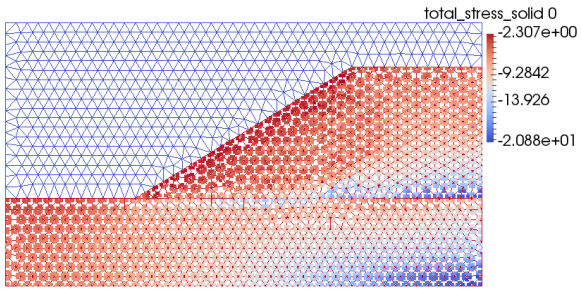

(b) Load stage 5 = 20kN/m^2 (t= 0.5s)

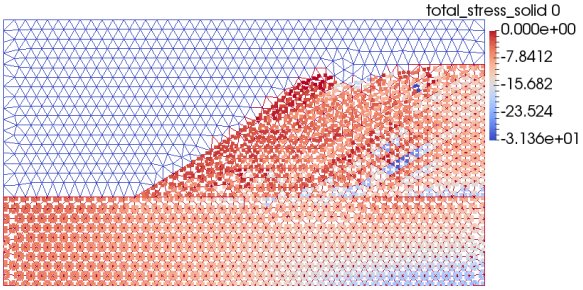

(c) Load stage 6 = 25kN/m^2 (t= 1s)

Table C. 2. Vertical stress (kN/m^2) distributions for the case of stresses transferred from load = 15kN/m^2.

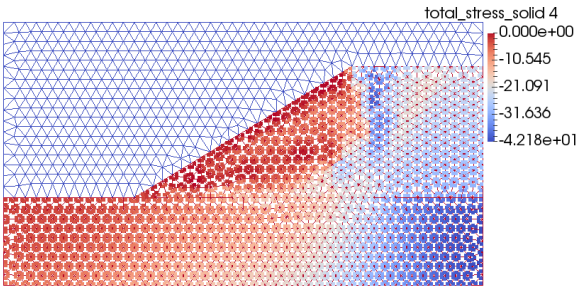

(a) Transfer (stage 4) = 15kN/m^2 (t= 0s)

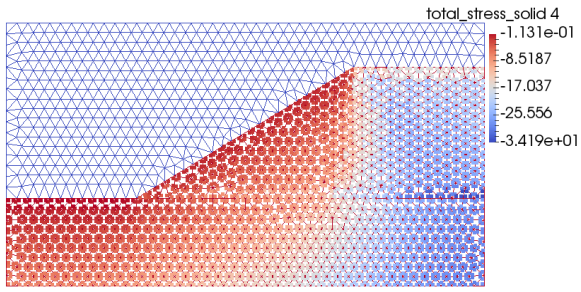

(b) Load stage 5 = 20kN/m^2 (t= 0.5s)

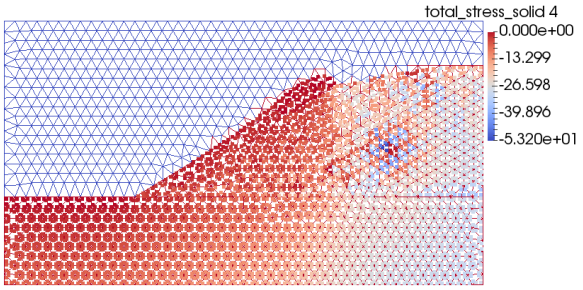

(c) Load stage 6 = 25kN/m^2 (t= 1s)

Table C. 3. Shear stress (kN/m^2) distributions for the case of stresses transferred from load = 15kN/m^2.

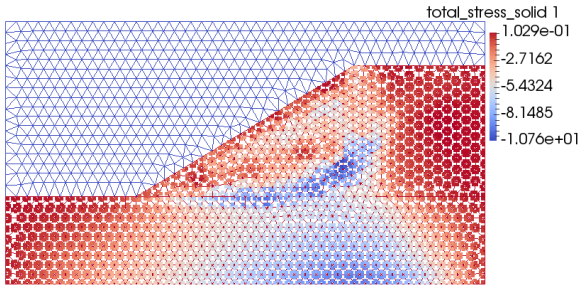

(a) Transfer (stage 4) = 15kN/m^2 (t= 0s)

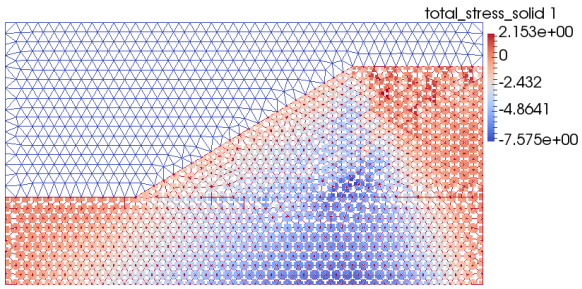

(b) Load stage 5 = 20kN/m^2 (t= 0.5s)

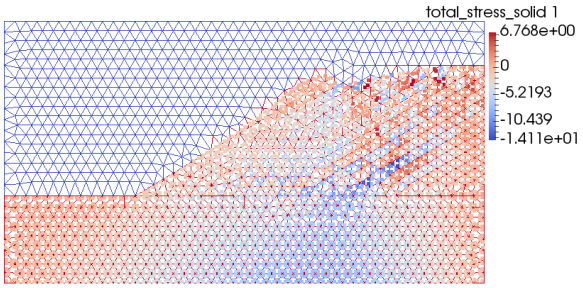

(c) Load stage 6 = 25kN/m^2 (t= 1s)

Table C. 4. Pressure (kN/m^2) distributions for the case of stresses transferred from load = 15kN/m^2.

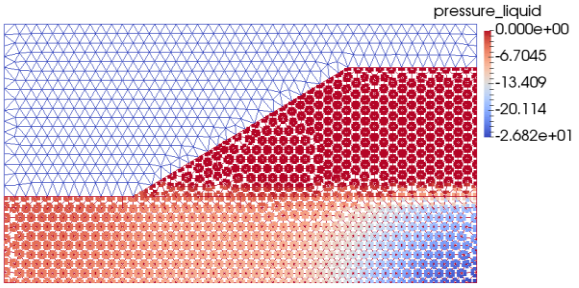

(a) Transfer (stage 4) = 15kN/m^2 (t= 0s)

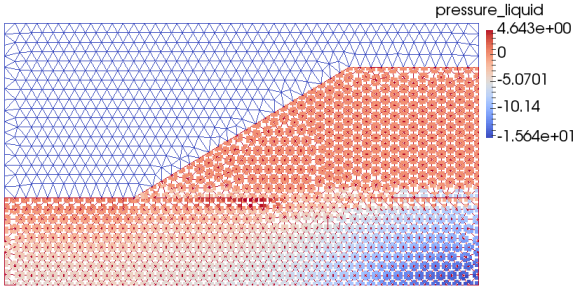

(b) Load stage 5 = 20kN/m^2 (t= 0.5s)

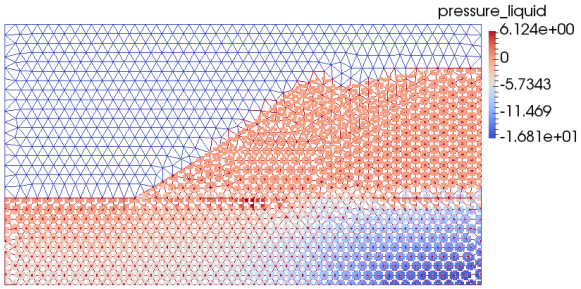

(c) Load stage 6 = 25kN/m^2 (t= 1s)

Stresses transferred from load application = 10kN/m^2

Table C. 5. Horizontal stress (kN/m^2) distributions for the case of stresses transferred from load = 10kN/m^2.

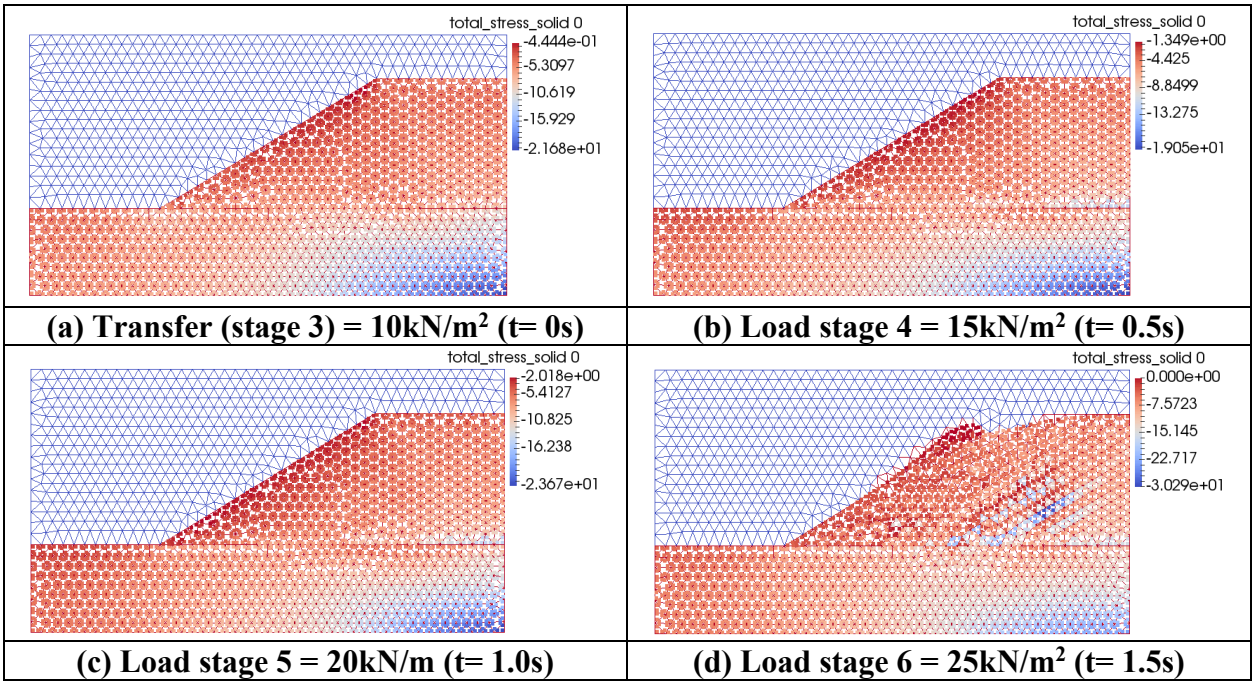

(a) Transfer (stage 3) = 10kN/m^2 (t= 0s) | (b) Load stage 4 = 15kN/m^2 (t= 0.5s)

(c) Load stage 5 = 20kN/m (t= 1.0s) | (d) Load stage 6 = 25kN/m^2 (t= 1.5s)

Table C. 6. Vertical stress (kN/m^2) distributions for the case of stresses transferred from load = 10kN/m^2.

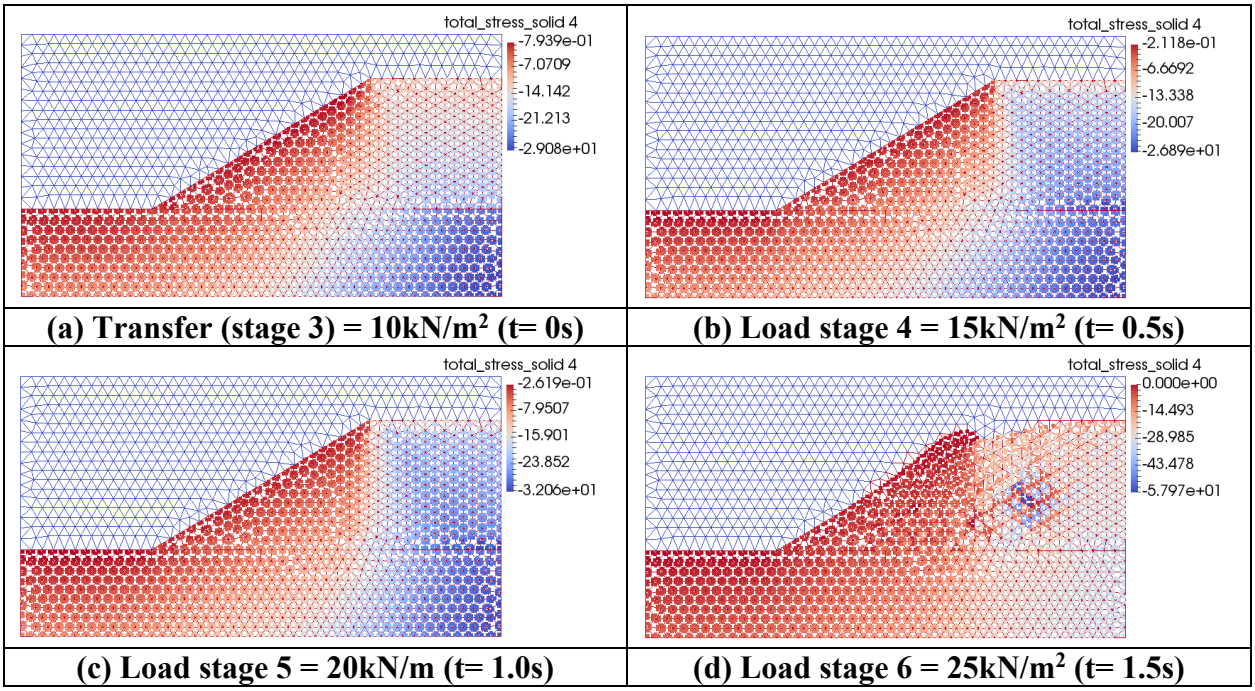

(a) Transfer (stage 3) = 10kN/m^2 (t= 0s) | (b) Load stage 4 = 15kN/m^2 (t= 0.5s)

(c) Load stage 5 = 20kN/m (t= 1.0s) | (d) Load stage 6 = 25kN/m^2 (t= 1.5s)

Table C. 7. Shear stress (kN/m^2) distributions for the case of stresses transferred from load = 10kN/m^2.

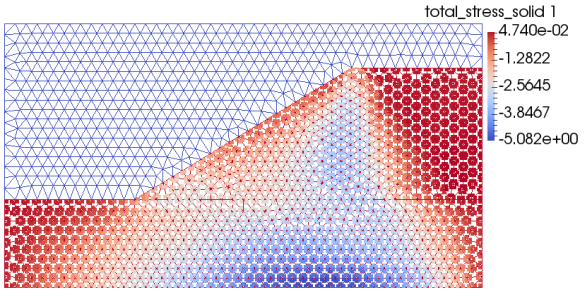

(a) Transfer (stage 3) = 10kN/m^2 (t= 0s)

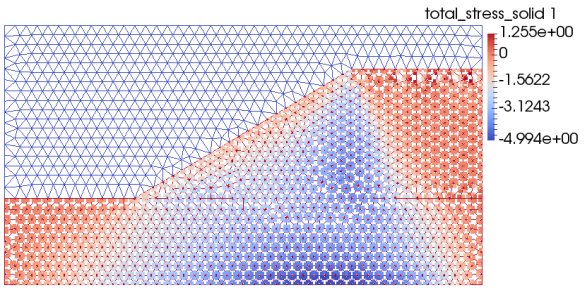

(b) Load stage 4 = 15kN/m^2 (t= 0.5s)

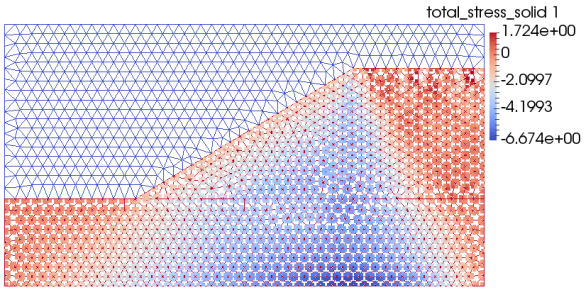

(c) Load stage 5 = 20kN/m (t= 1.0s)

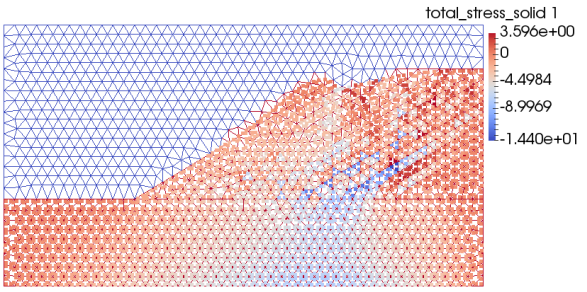

(d) Load stage 6 = 25kN/m^2 (t= 1.5s)

Table C. 8. Pressure (kN/m^2) distributions for the case of stresses transferred from load = 10kN/m^2.

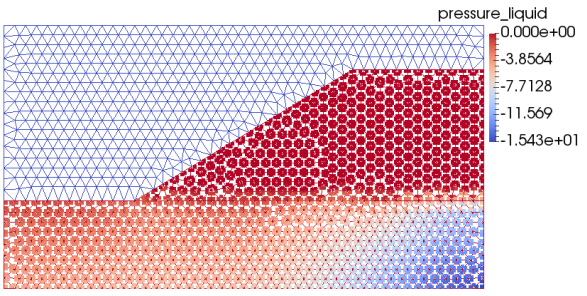

(a) Transfer (stage 3) = 10kN/m^2 (t= 0s)

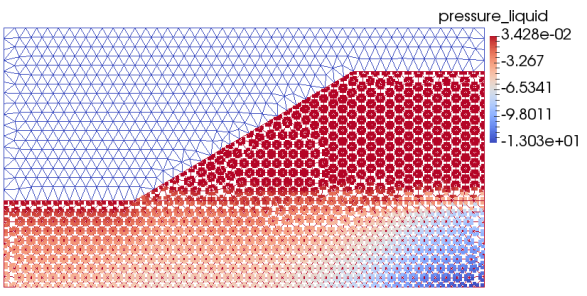

(b) Load stage 4 = 15kN/m^2 (t= 0.5s)

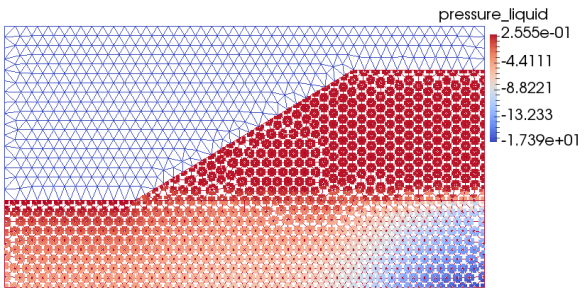

(c) Load stage 5 = 20kN/m (t= 1.0s)

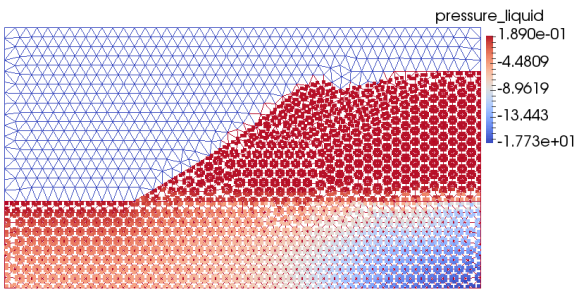

(d) Load stage 6 = 25kN/m^2 (t= 1.5s)

APPENDIX D

The seepage and stress analysis results of the pre-failure analysis of the South Dike, consisting of 25 out of the 27 stages (from Stage 1: steady-state seepage analysis to Stage 25: stress analysis of the second filling of the sand core), are illustrated in Figure D.1 to D.53.

Stage 1: Pre-levee steady-state seepage analysis

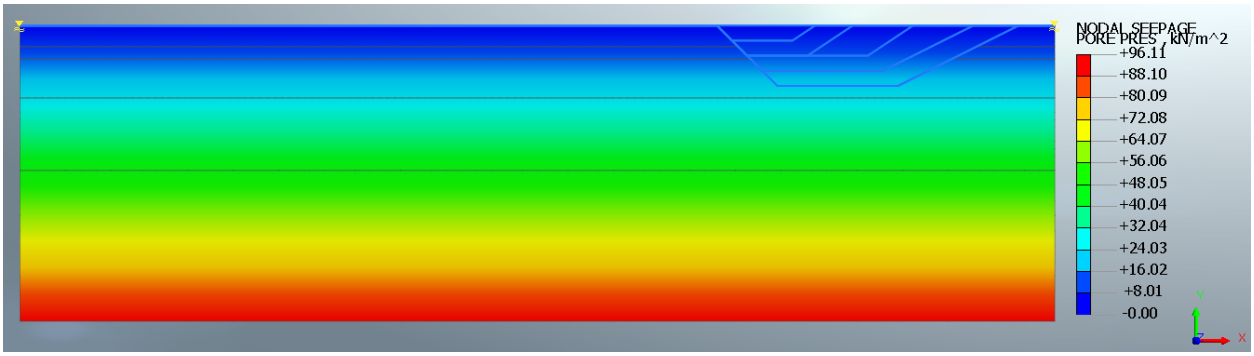

Figure D. 1. Pore stress (kN/m^2) from steady state seepage analysis at pre-levee stage.

Stage 2: Pre-levee stress initialization

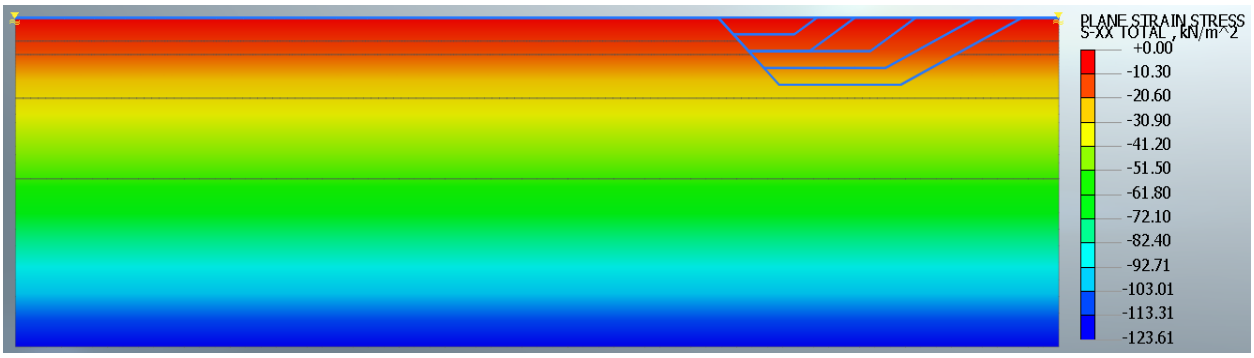

(a) Total horizontal stress, S-XX

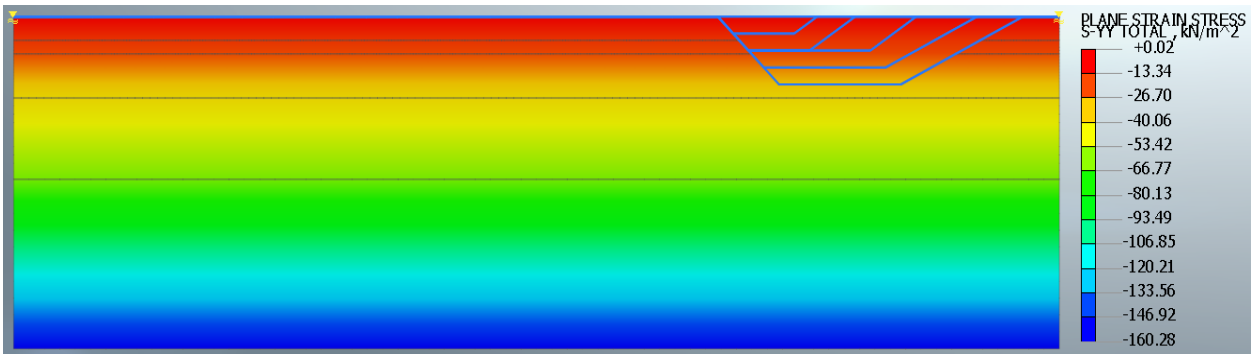

(b) Total vertical stress, S-YY

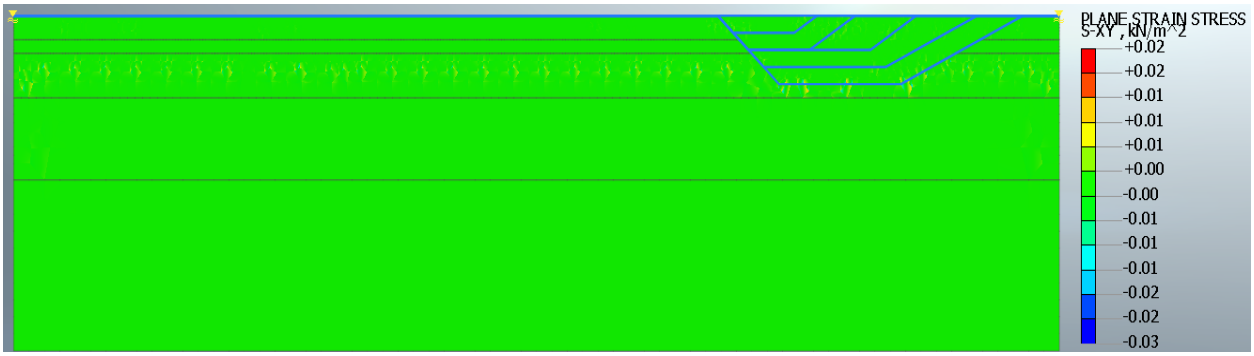

(c) Shear stress, S-XY

Figure D. 2. Total stresses and shear stress (kN/m^2) at pre-levee stage.

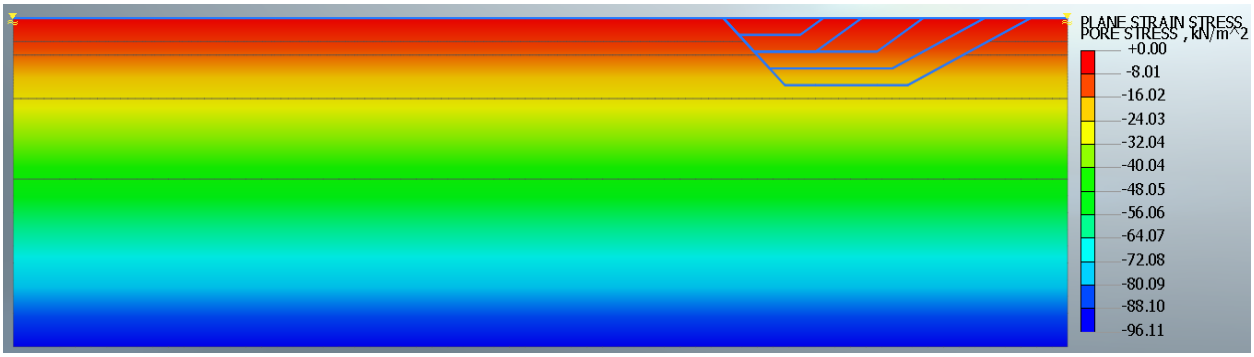

Figure D. 3. Pore stress (kN/m^2) at pre-levee stage.

Stage 3: Levee construction step 1 stress analysis

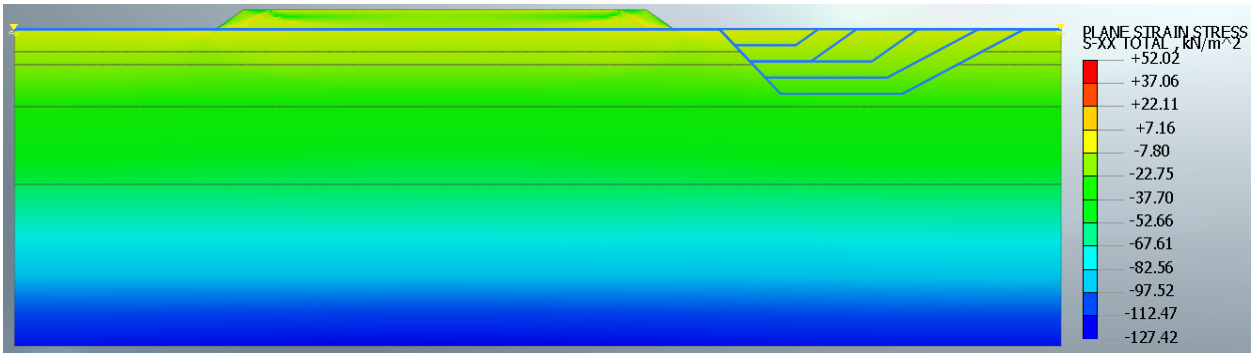

(a) Total horizontal stress, S-XX

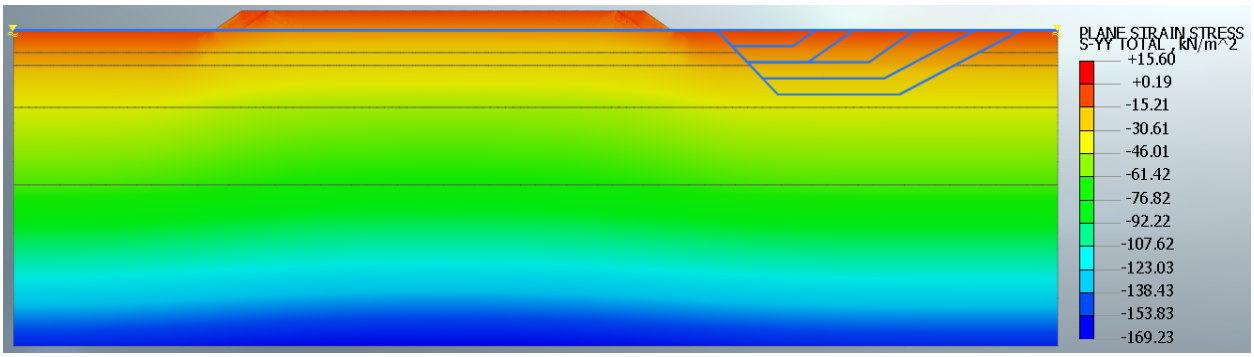

(b) Total vertical stress, S-YY

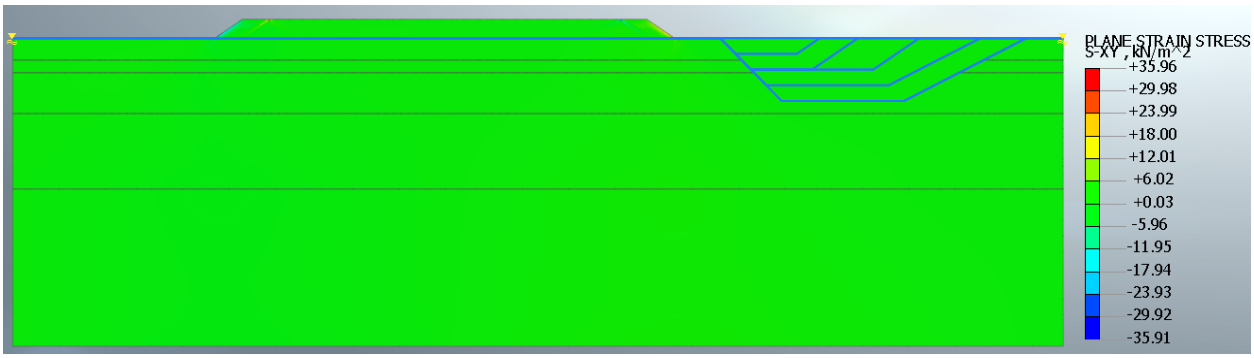

(c) Shear stress, S-XY

Figure D. 4. Total stresses and shear stress (kN/m^2) at levee construction step 1.

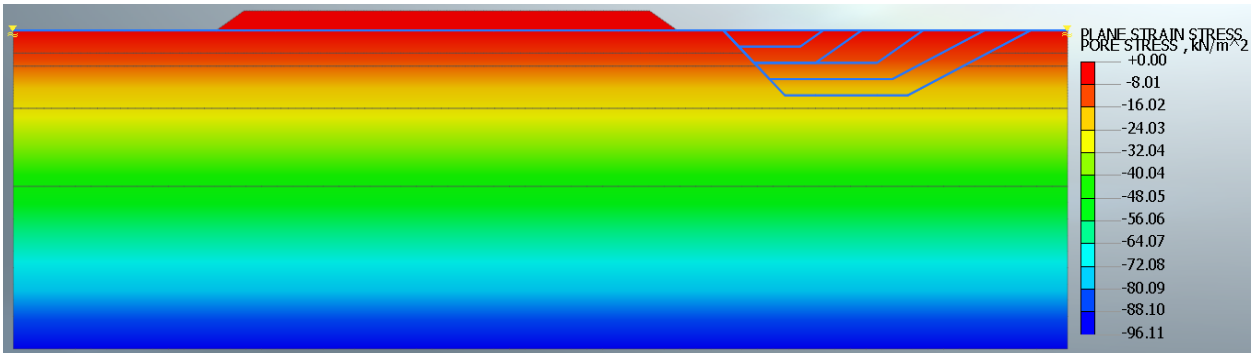

Figure D. 5. Pore stress (kN/m^2) at levee construction step 1.

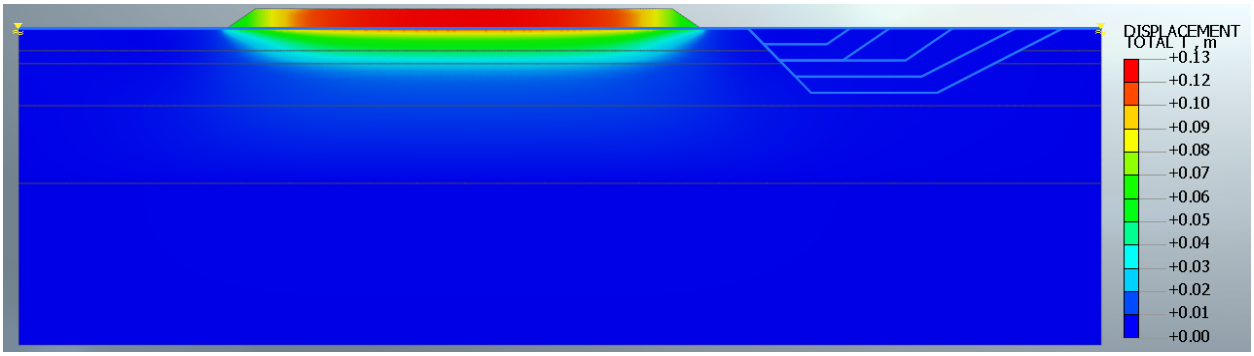

(a) Total displacement, T

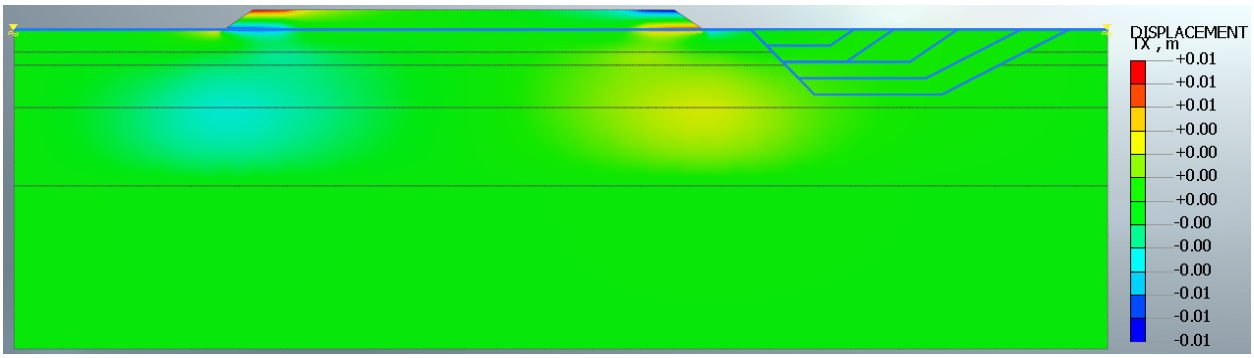

(b) Horizontal displacement, TX

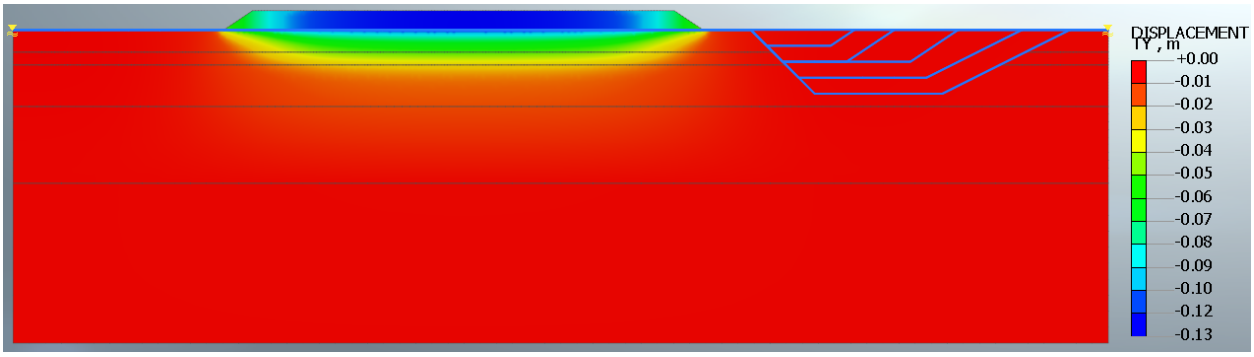

(c) Vertical displacement, TY

Figure D. 6. Displacements (m) at levee construction step 1.

Stage 4: Levee construction step 2 stress analysis

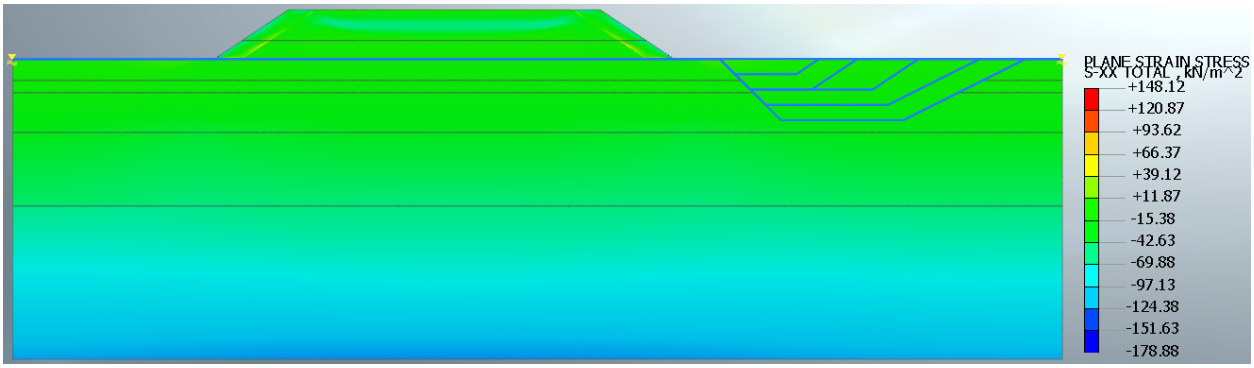

(a) Horizontal stress, S-XX

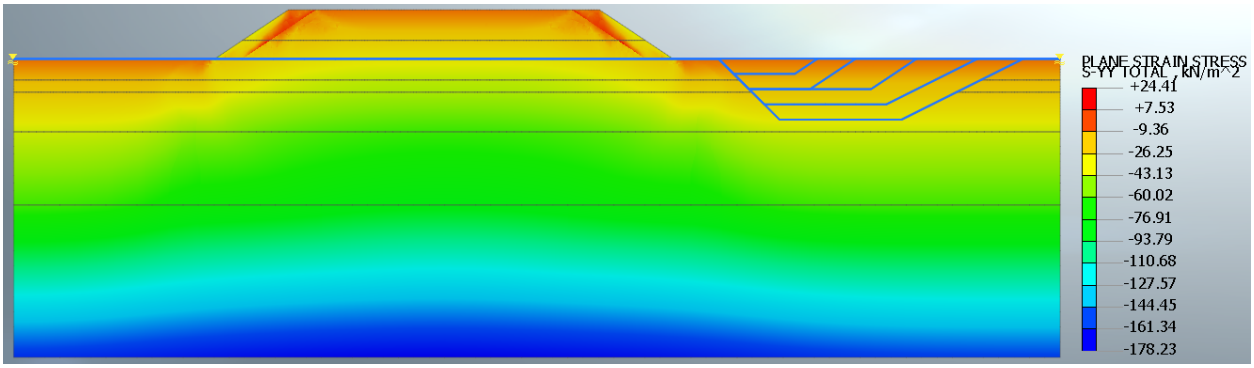

(b) Vertical stress, S-YY

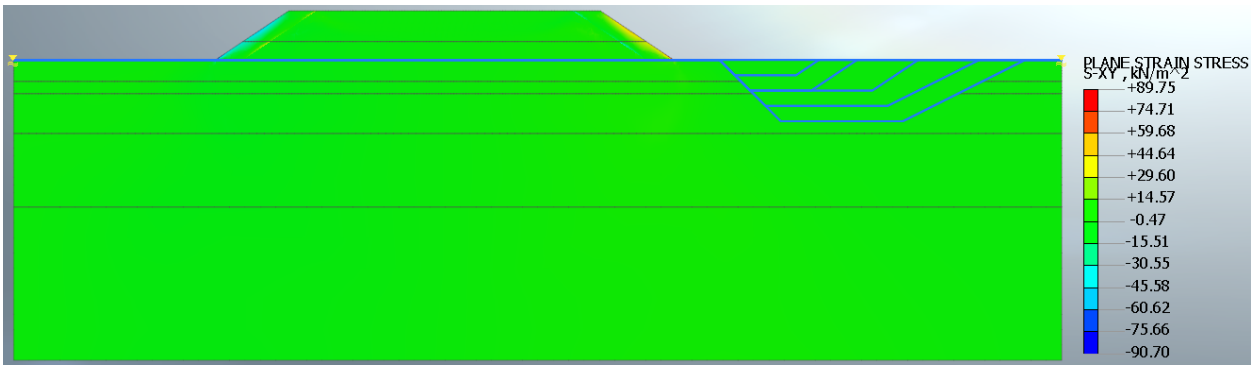

(c) Shear stress, S-XY

Figure D. 7. Total stresses and shear stress (kN/m^2) at levee construction step 2.

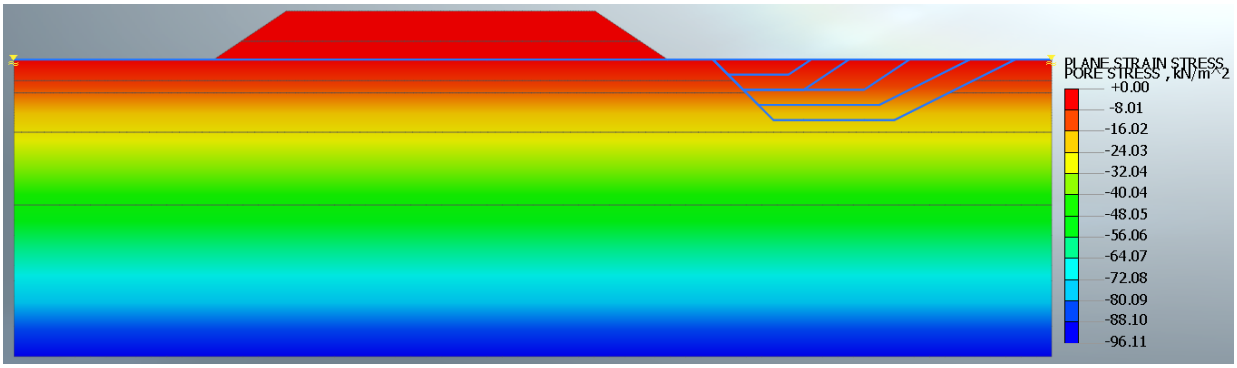

Figure D. 8. Pore stress (kN/m^2) at levee construction step 2.

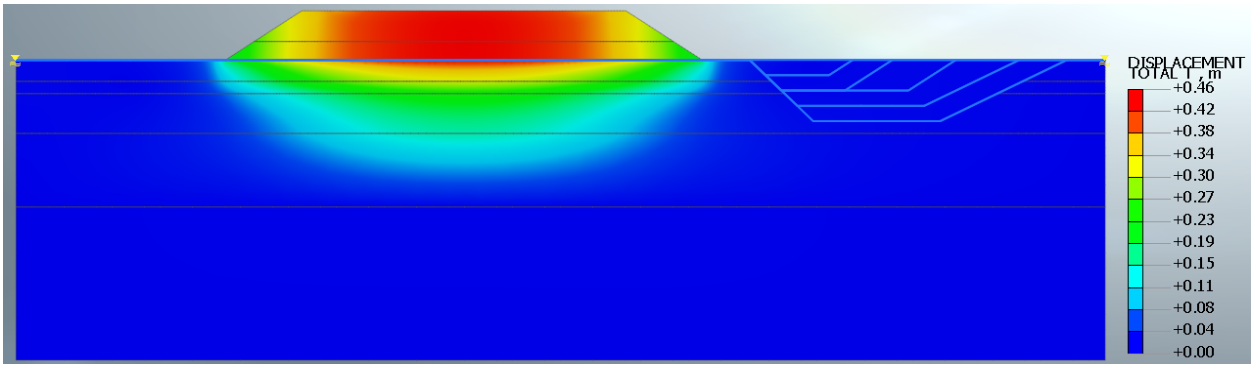

(a) Total displacement, T

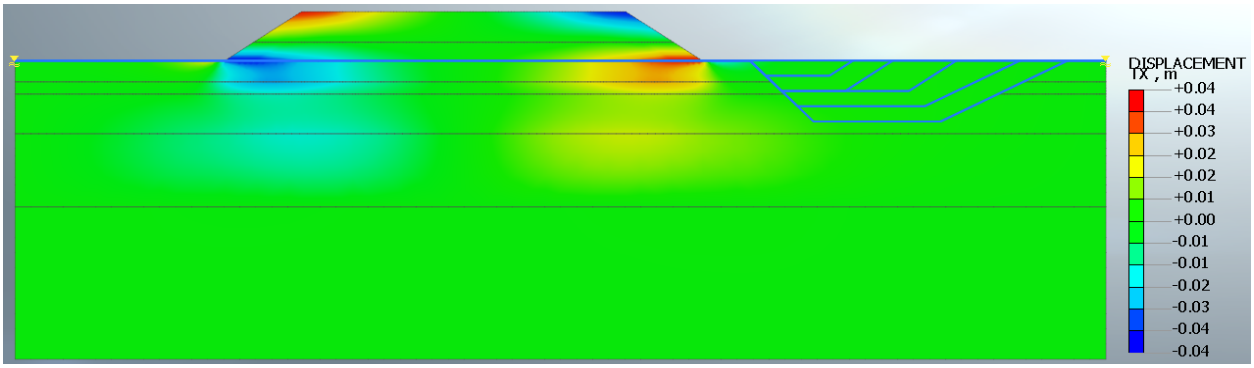

(b) Horizontal displacement, TX

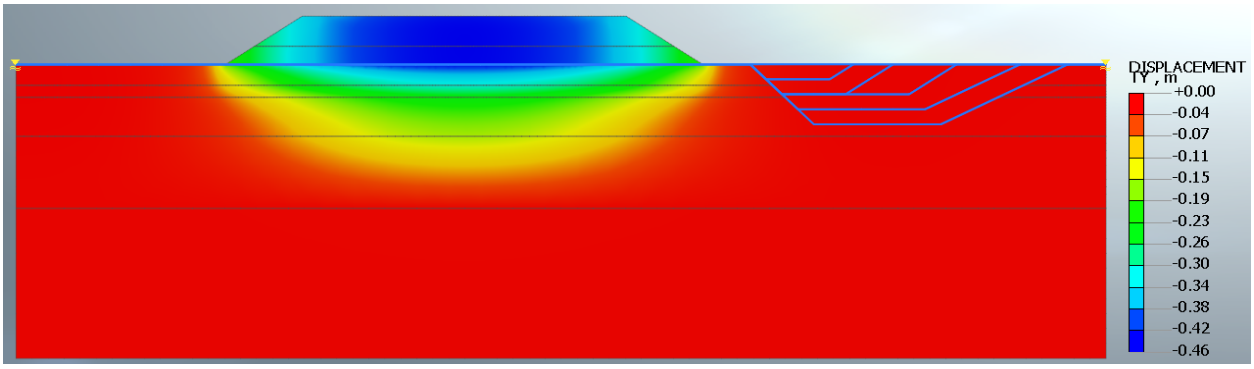

(c) Vertical displacement, TY

Figure D. 9. Displacements (m) at levee construction step 2.

Stage 5: Levee construction step 3 stress analysis

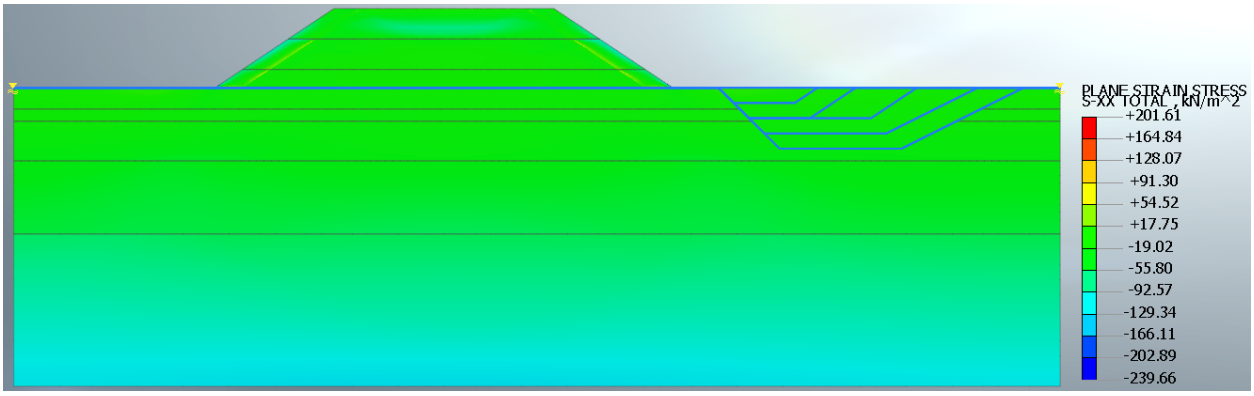

(a) Horizontal stress, S-XX

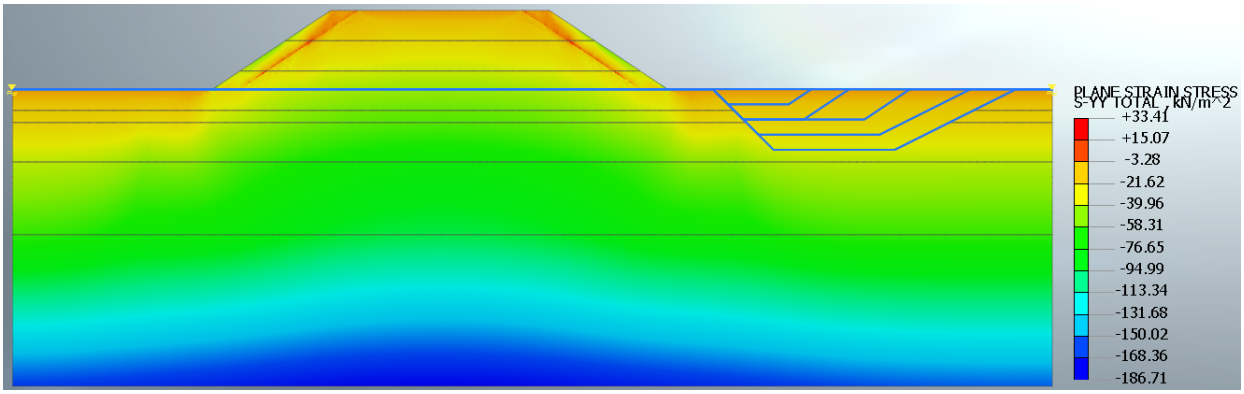

(b) Vertical stress, S-YY

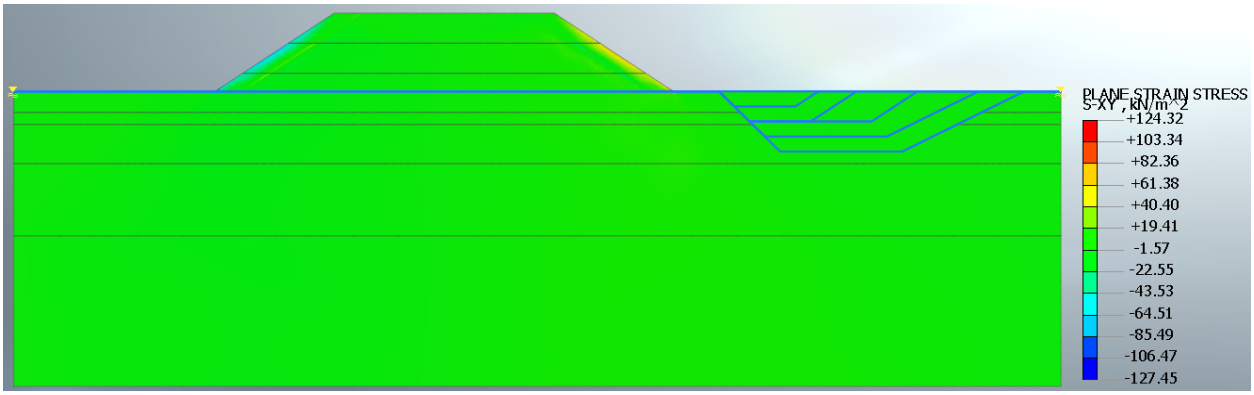

(c) Shear stress, S-XY

Figure D. 10. Total stresses and shear stress (kN/m^2) at levee construction step 3.

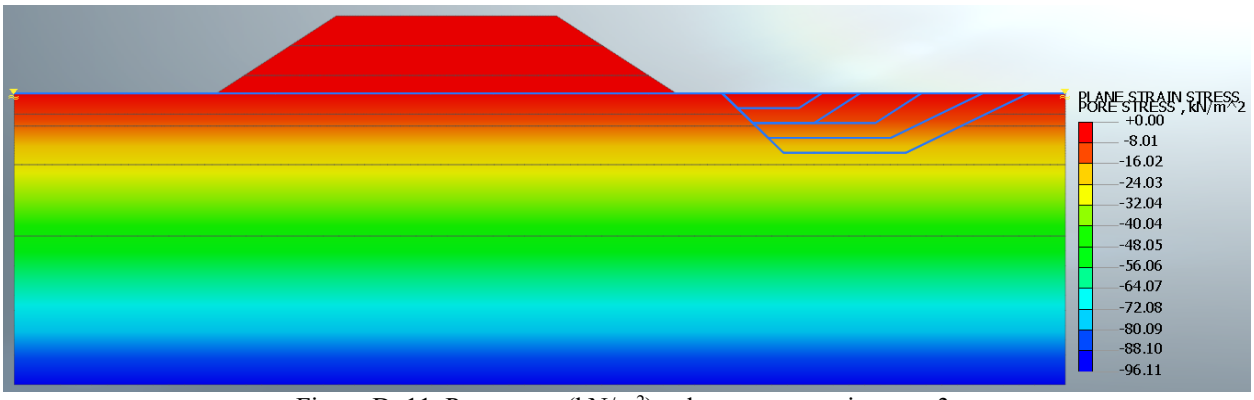

Figure D. 11. Pore stress (kN/m^2) at levee construction step 3.

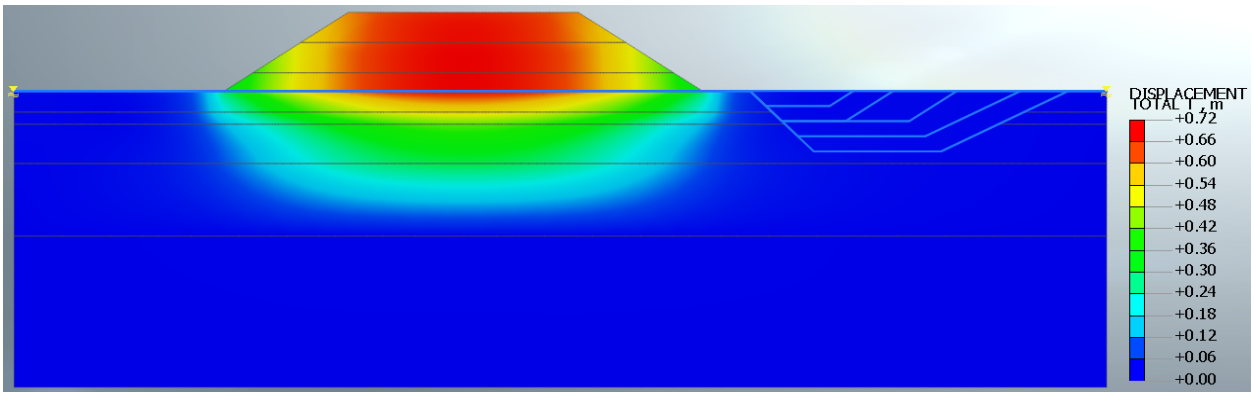

(a) Total displacement, T

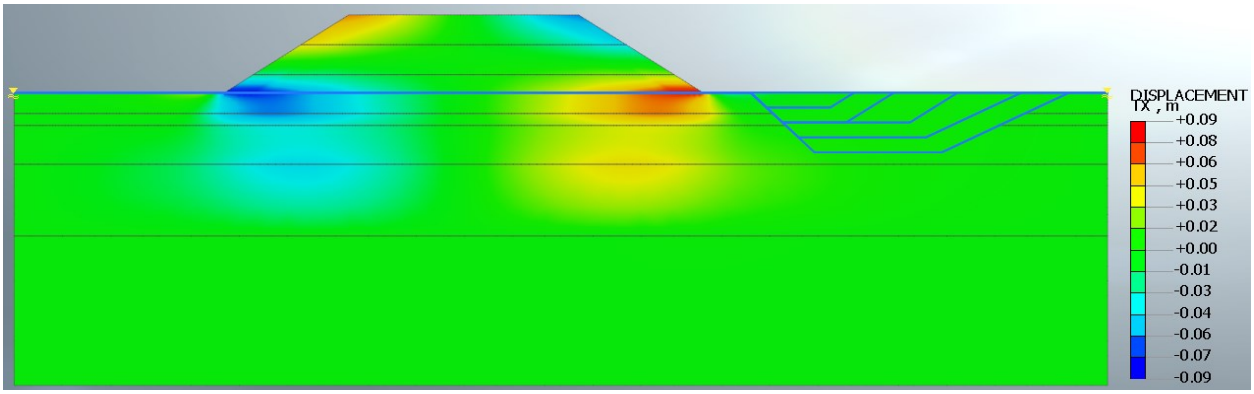

(b) Horizontal displacement, TX

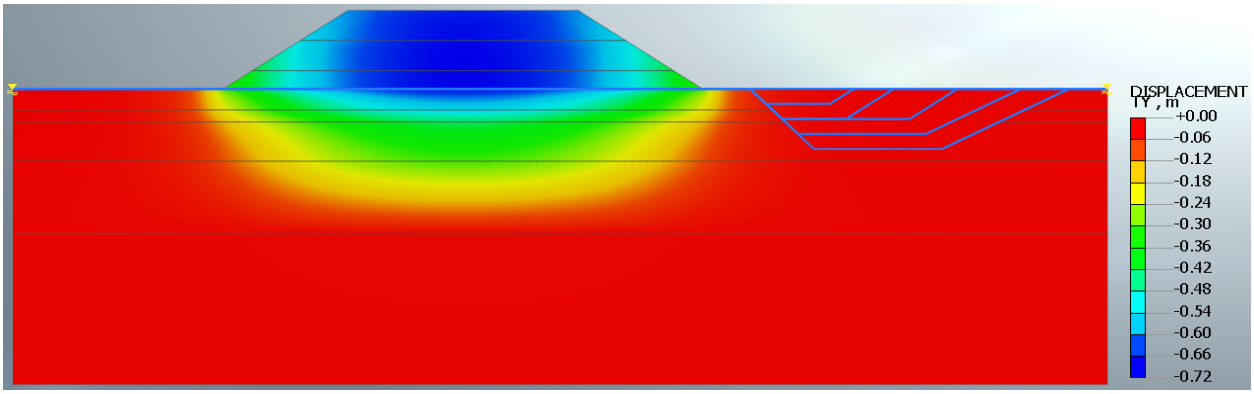

(c) Vertical displacement, TY

Figure D. 12. Displacements (m) at levee construction step 3.

Stage 6: Levee construction step 4 stress analysis

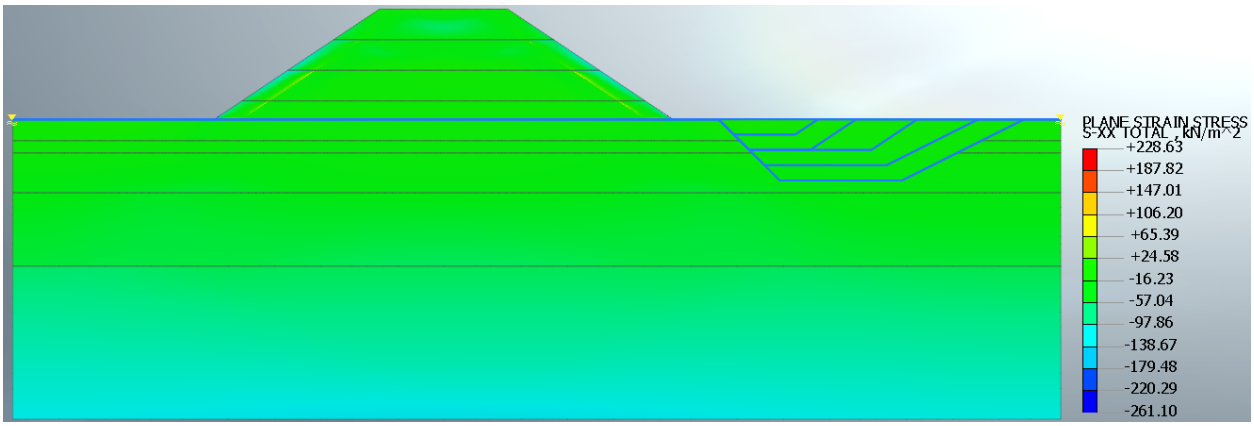

(a) Horizontal stress, S-XX

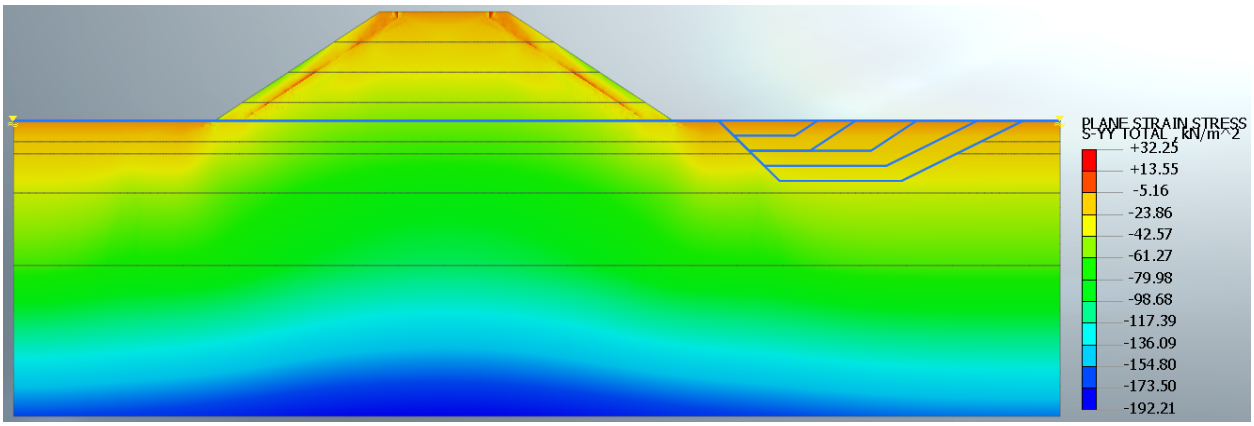

(b) Vertical stress, S-YY

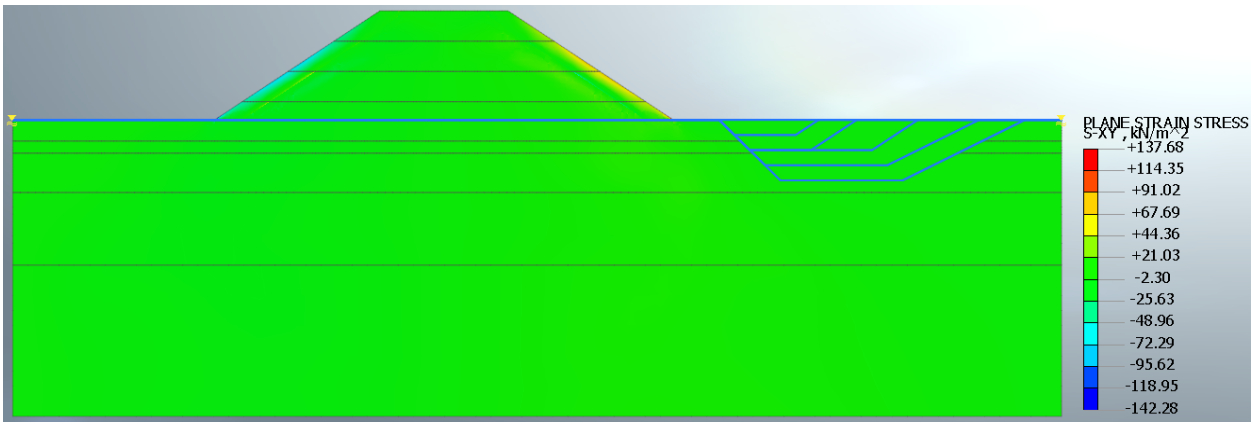

(c) Shear stress, S-XY

Figure D. 13. Total stress and shear stress (kN/m^2) at levee construction step 4.

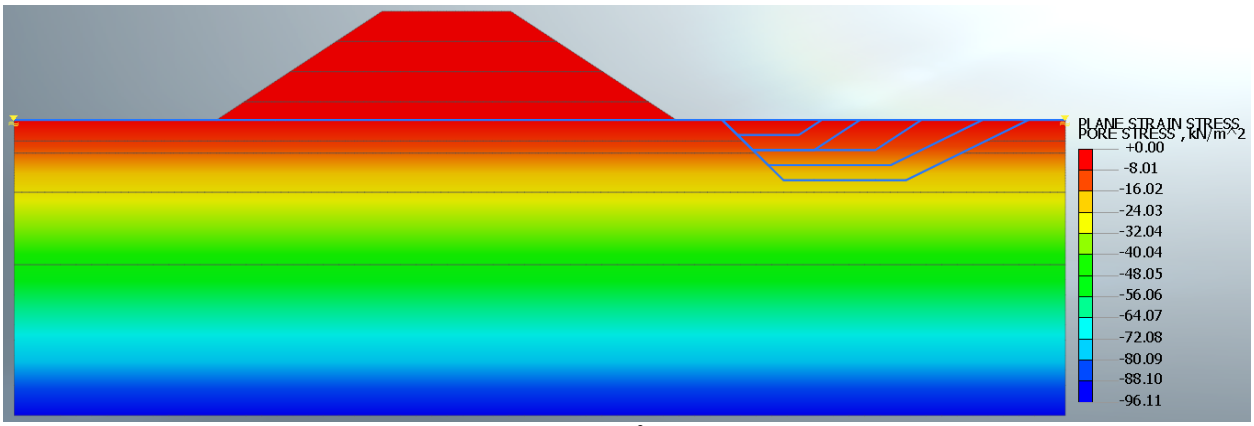

Figure D. 14. Pore stress (kN/m^2) at levee construction step 4.

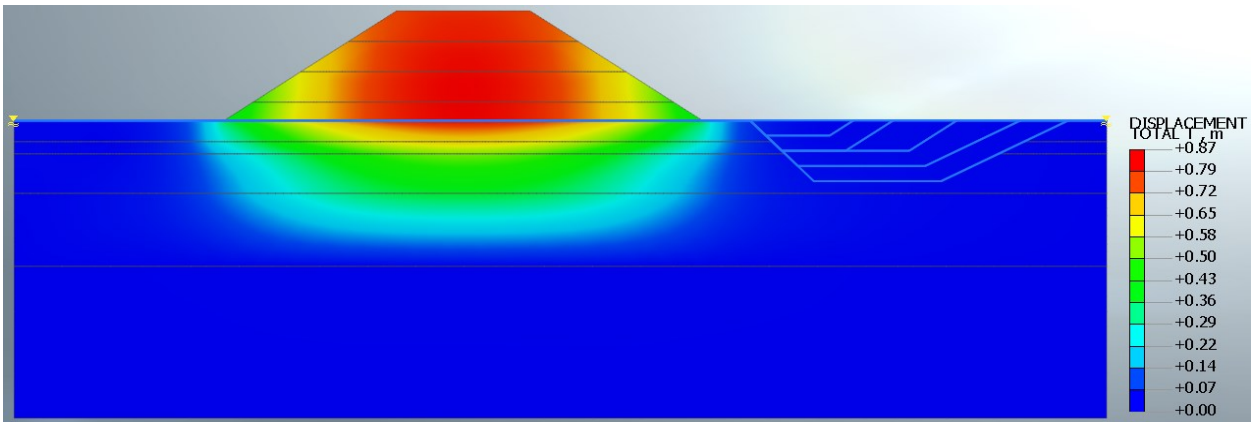

(a) Total displacement, T

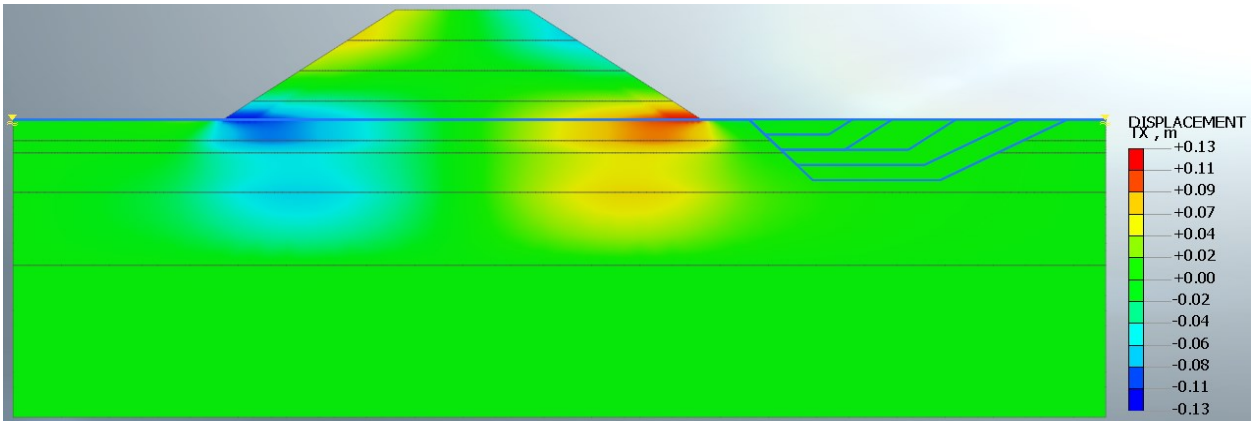

(b) Horizontal displacement, TX

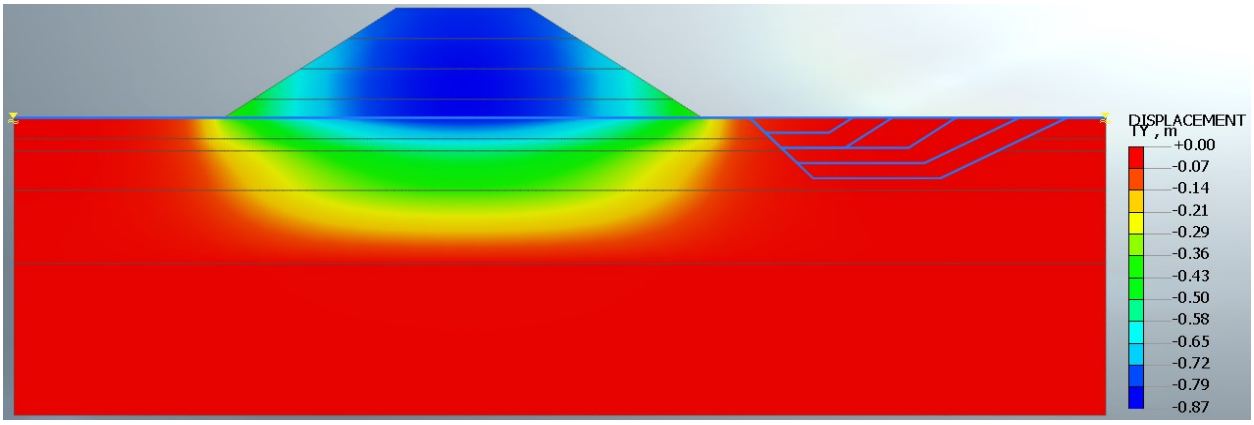

(c) Vertical displacement, TY

Figure D. 15. Displacements (m) at levee construction step 4.

Stage 7: Levee construction step 5 stress analysis

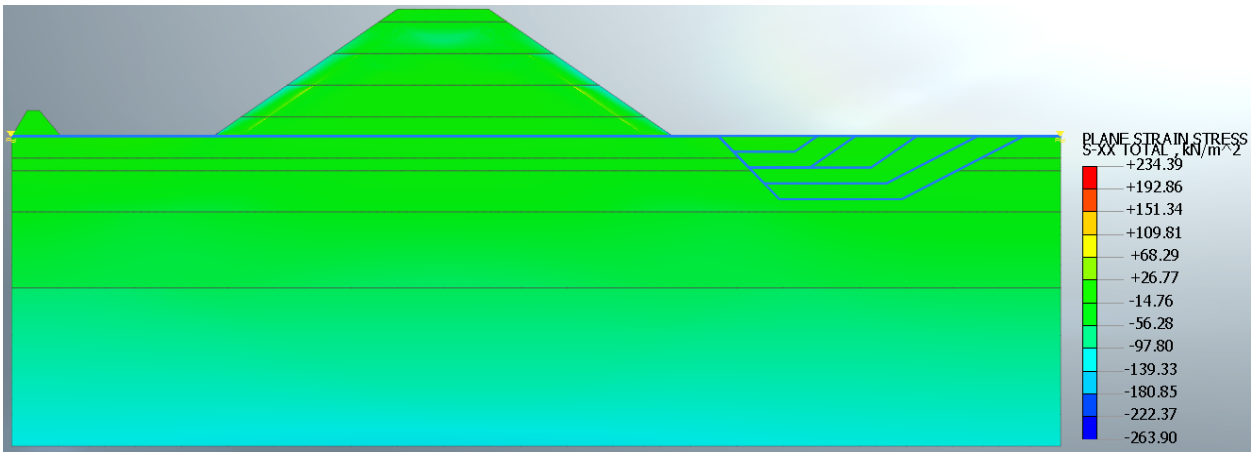

(a) Horizontal stress, S-XX

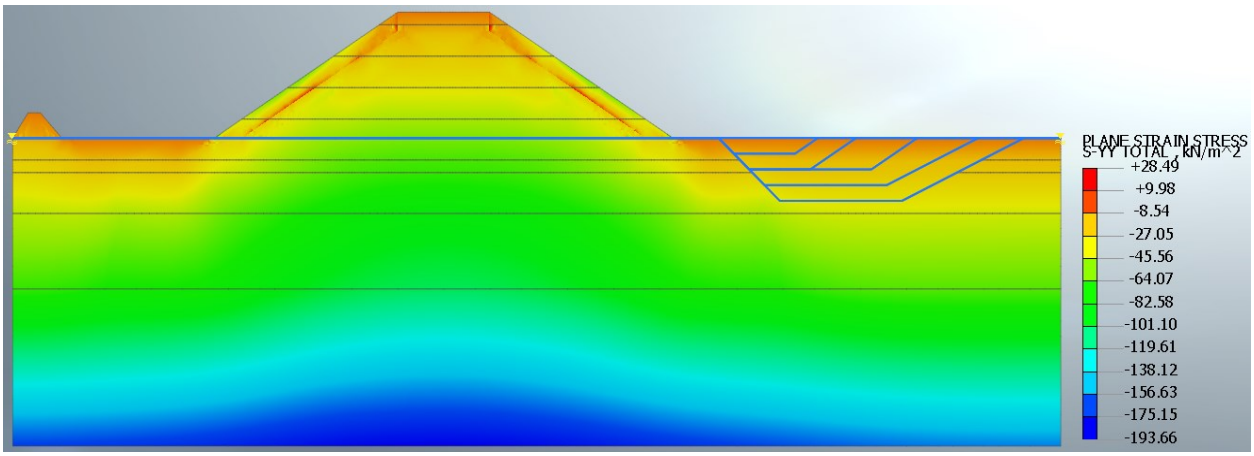

(b) Vertical stress, S-YY

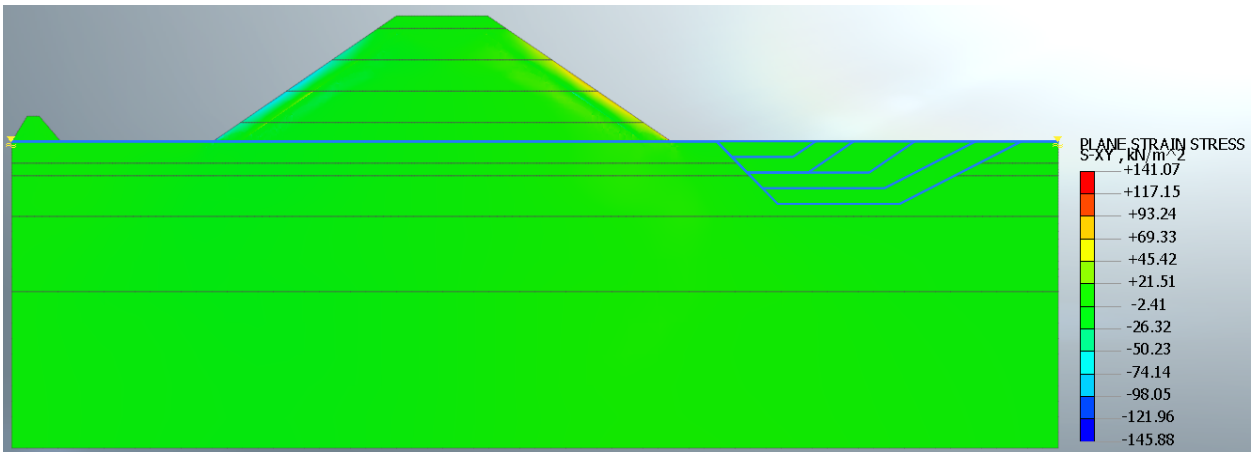

(c) Shear stress, S-XY

Figure D. 16. Total stresses and shear stress (kN/m^2) at levee construction step 5.

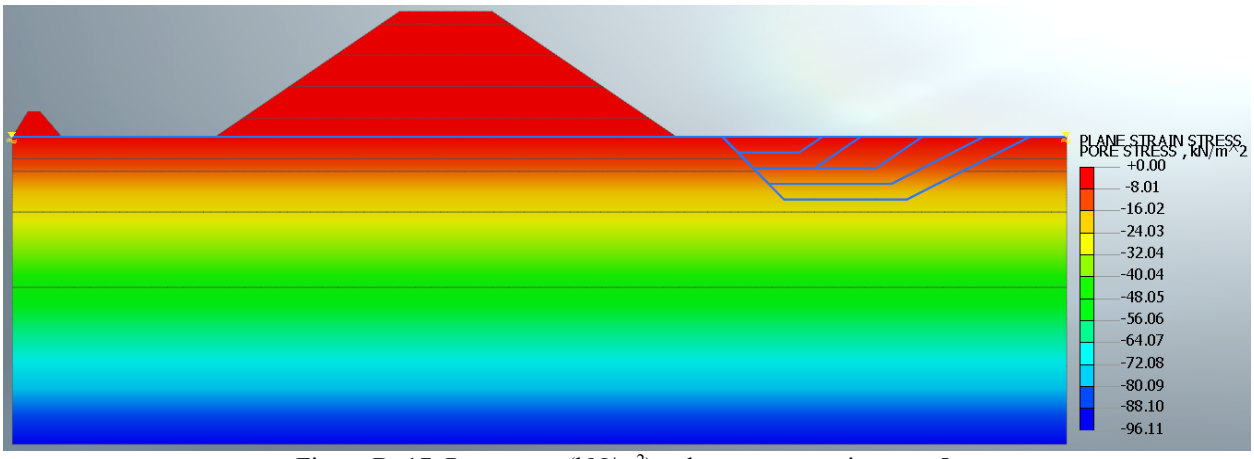

Figure D. 17. Pore stress (kN/m^2) at levee construction step 5.

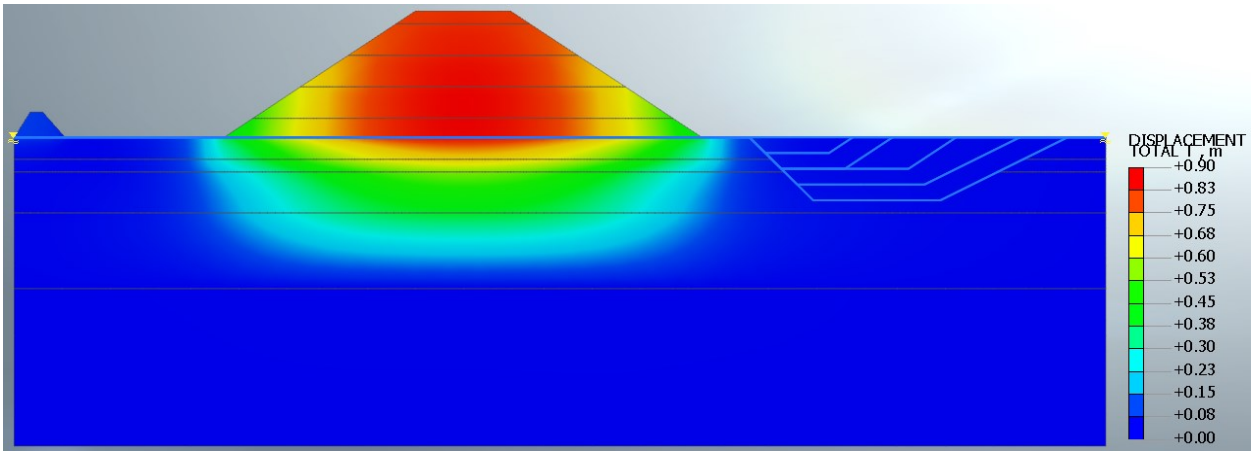

(a) Total displacement, T

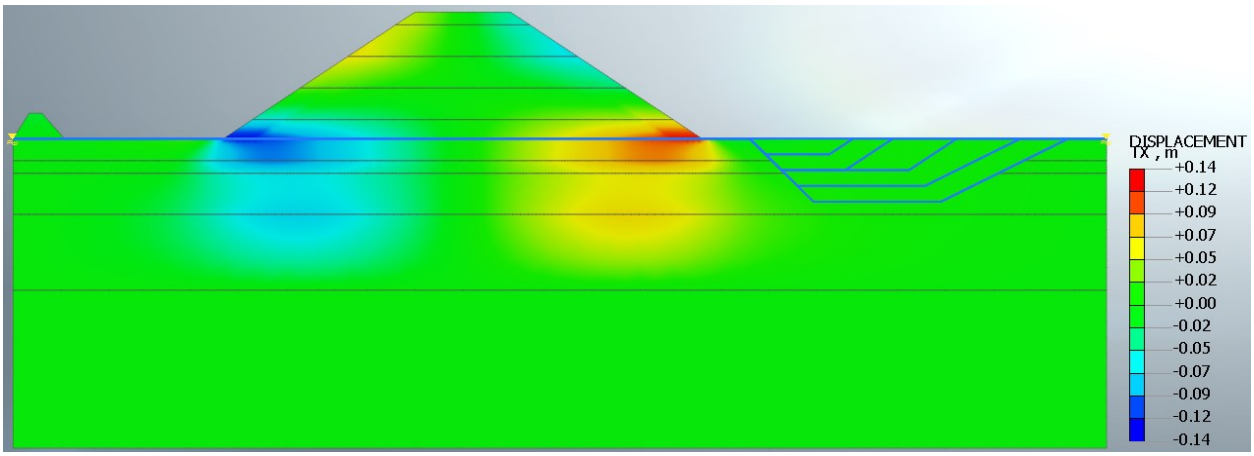

(b) Horizontal displacement, TX

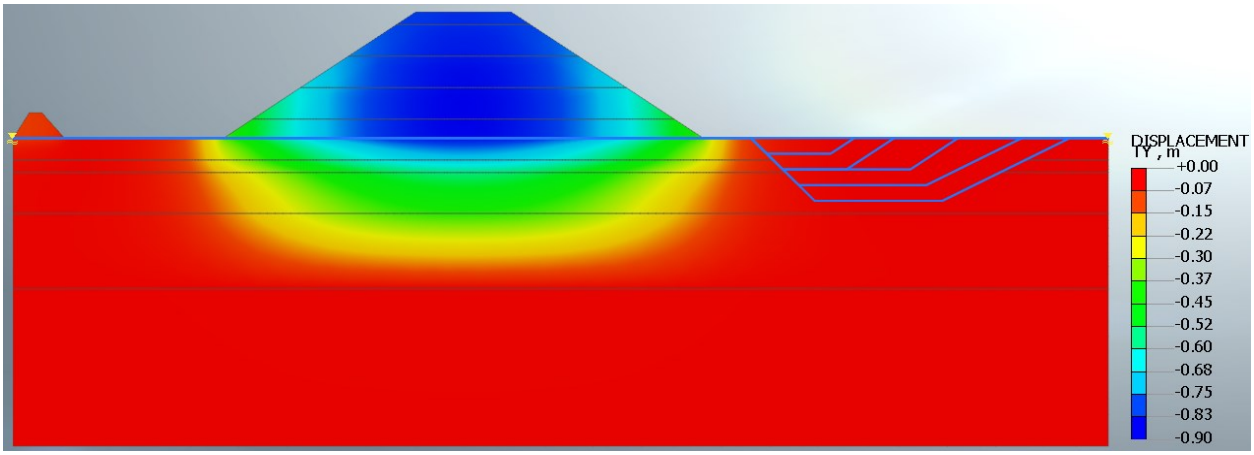

(c) Vertical displacement, TY

Figure D. 18. Displacements (m) at levee construction step 5.

Stage 8: Container weight stress analysis

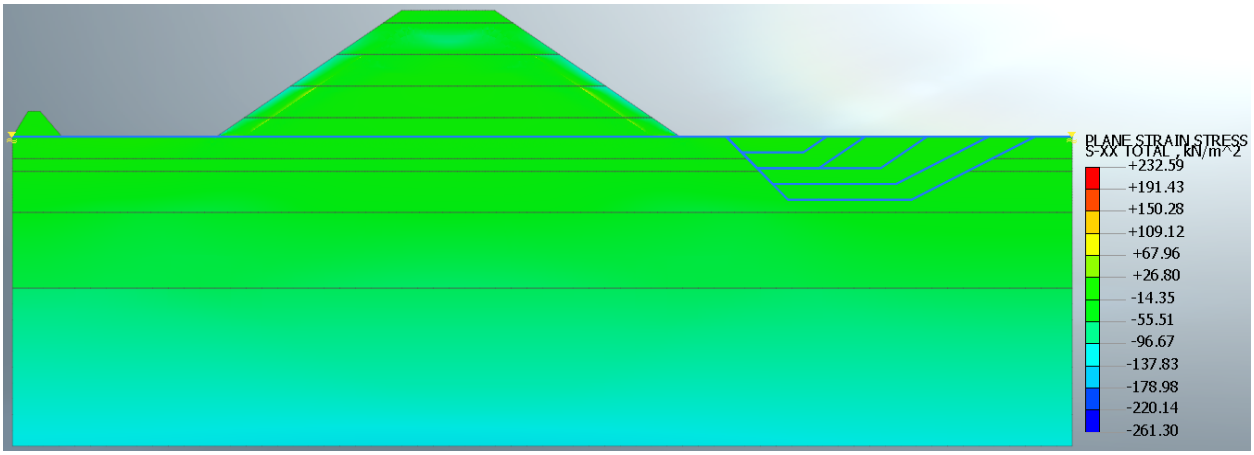

(a) Horizontal stress, S-XX

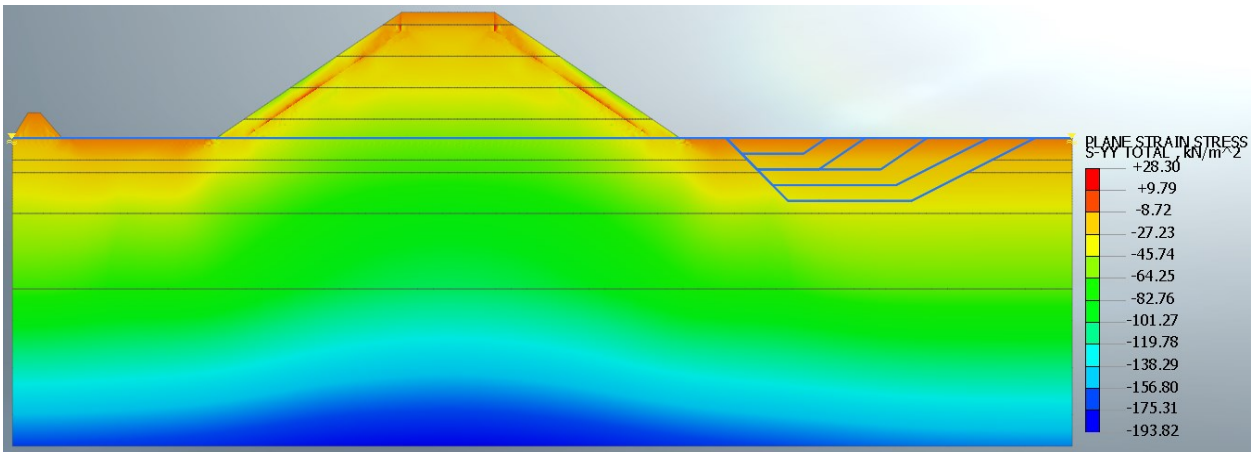

(b) Vertical stress, S-YY

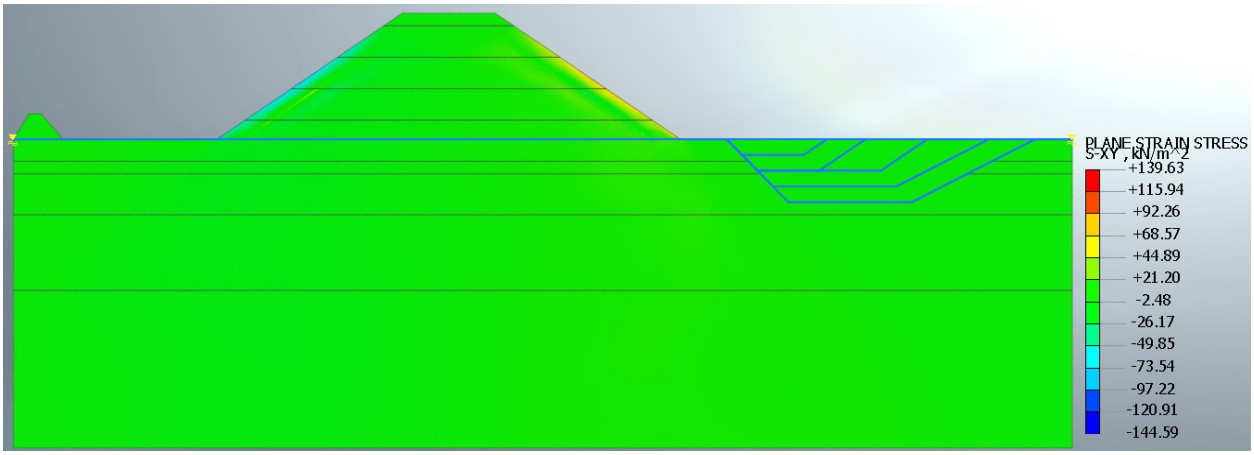

(c) Shear stress, S-XY

Figure D. 19. Total stresses and shear stress (kN/m^2) at container weight stage.

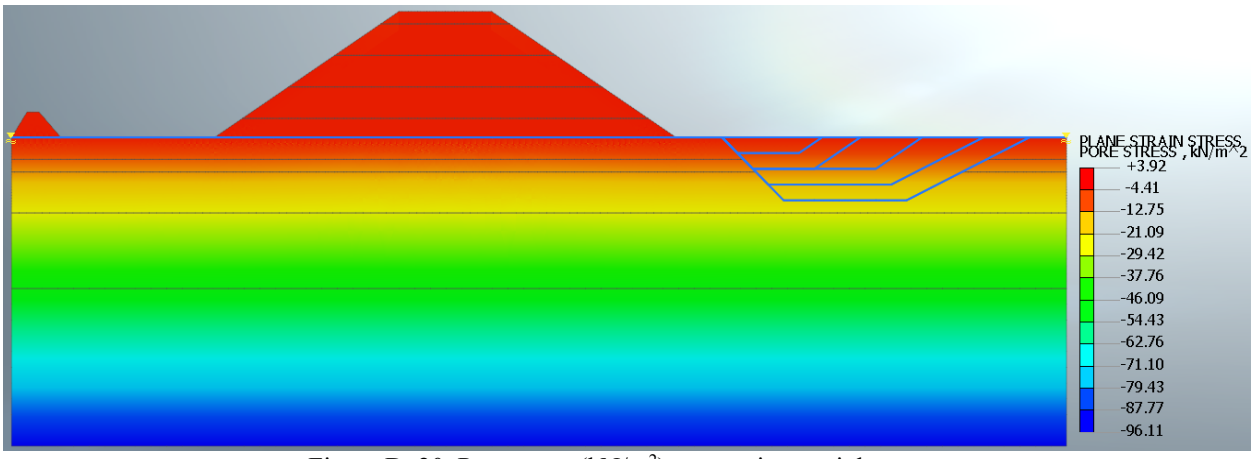

Figure D. 20. Pore stress (kN/m^2) at container weight stage.

Stage 9: First filling of sand core transient seepage analysis

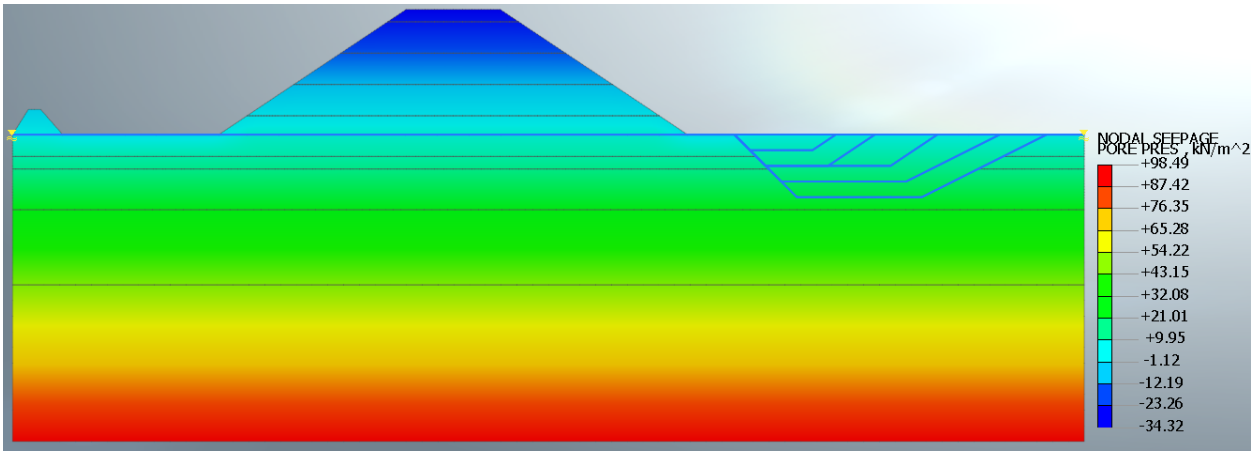

Figure D. 21. Pore stress (kN/m^2) from transient seepage analysis at first filling of sand core stage.

Stage 10: First filling of sand core stress analysis

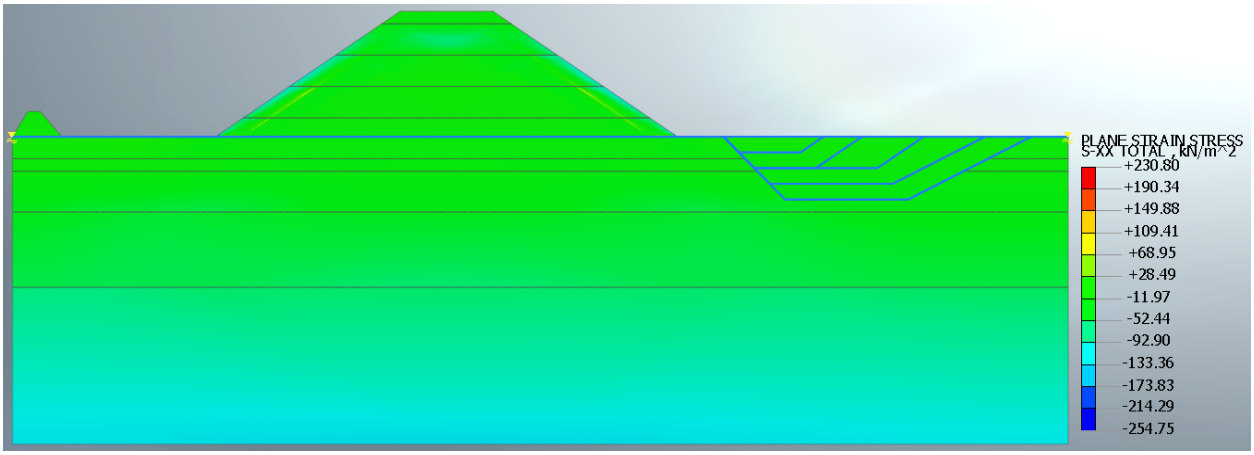

(a) Horizontal stress, S-XX

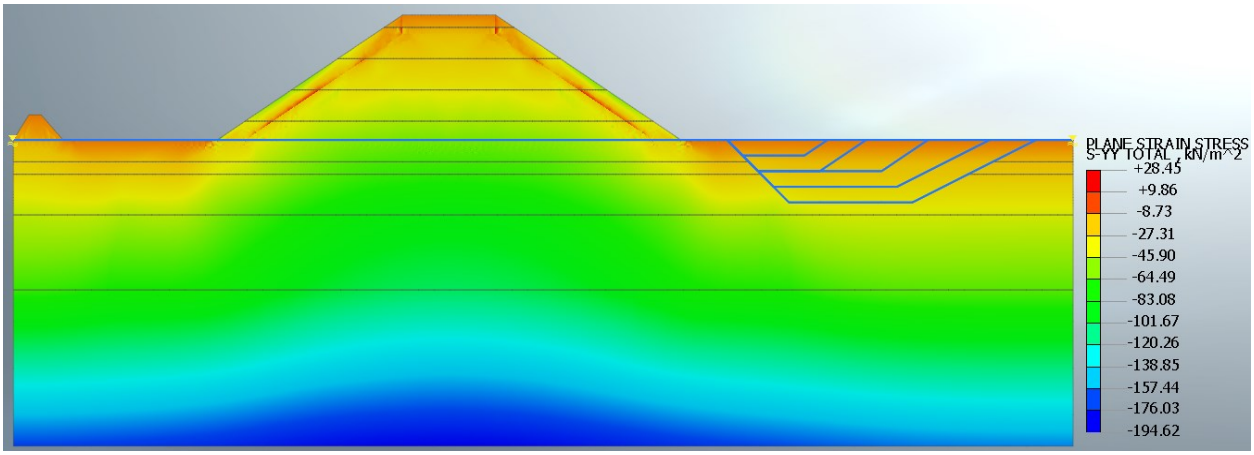

(b) Vertical stress, S-YY

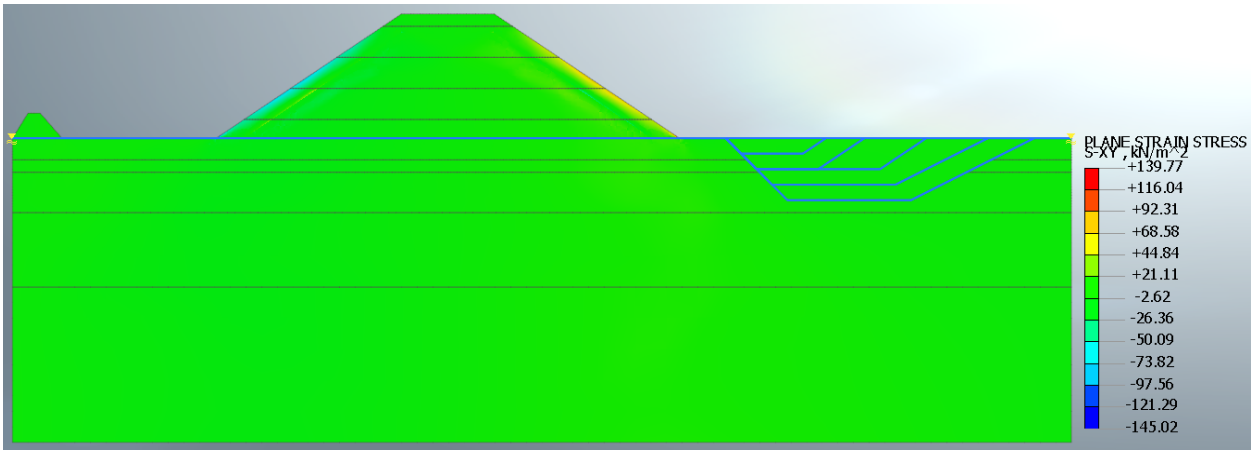

(c) Shear stress, S-XY

Figure D. 22. Total stresses and shear stress (kN/m^2) at first filling of sand core stage.

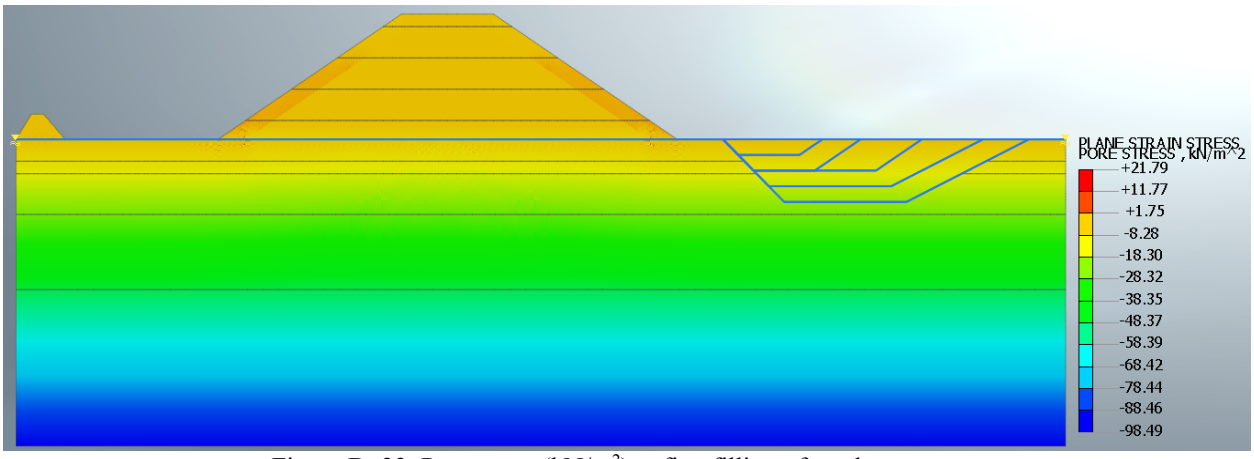

Figure D. 23. Pore stress (kN/m^2) at first filling of sand core stage.

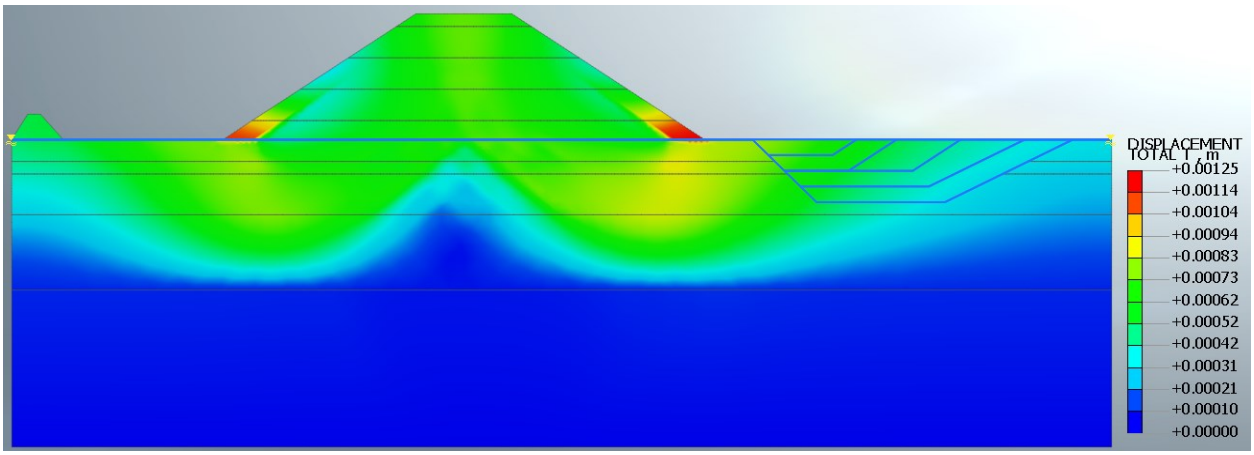

(a) Total displacement, T

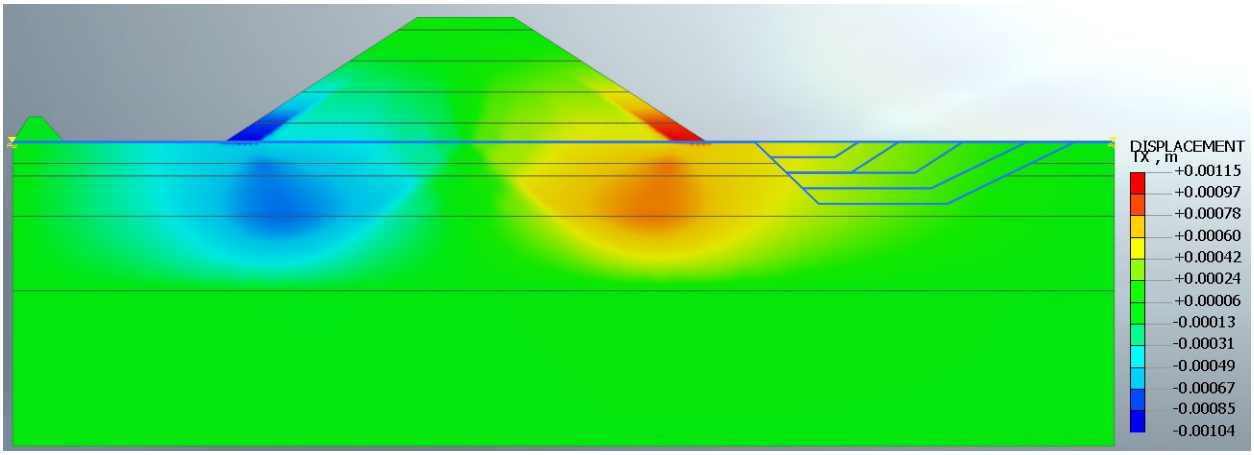

(b) Horizontal displacement, TX

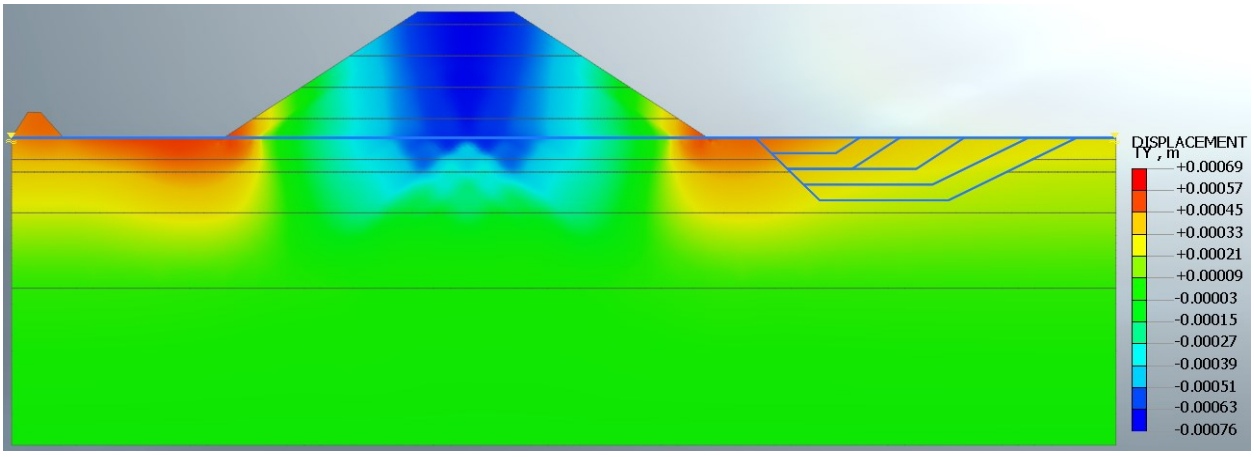

(c) Vertical displacement, TY

Figure D. 24. Displacements (m) at first filling of sand core stage.

Stage 11: Filling of basin transient seepage analysis

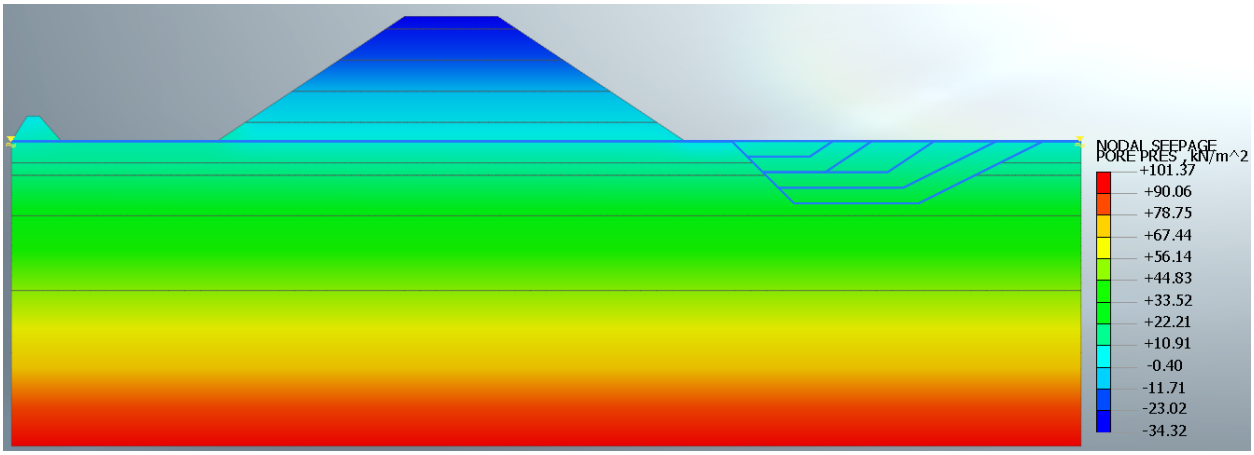

Figure D. 25. Pore stress from transient seepage analysis when basin is filled.

Stage 12: Filling of basin stress analysis

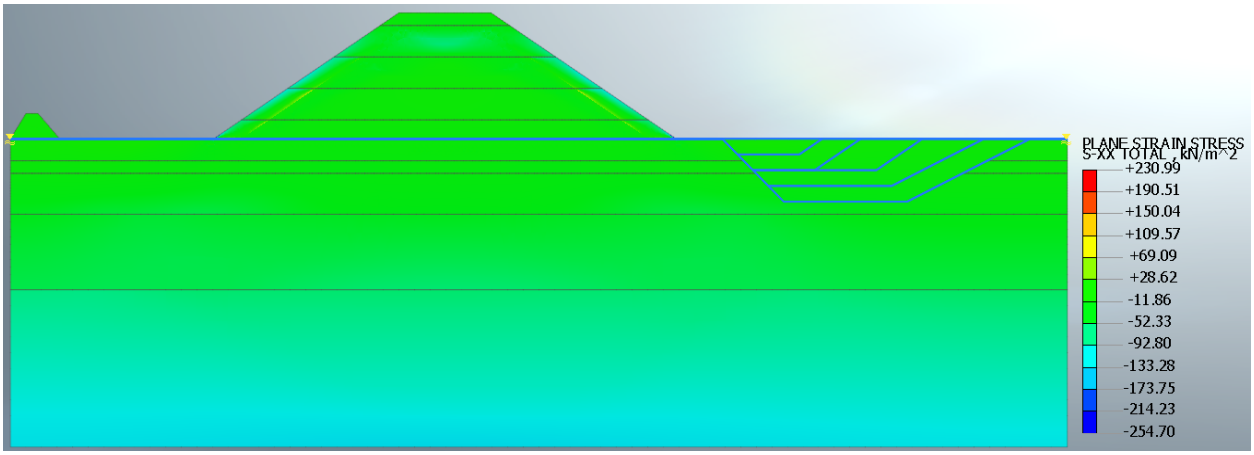

(a) Horizontal stress, S-XX

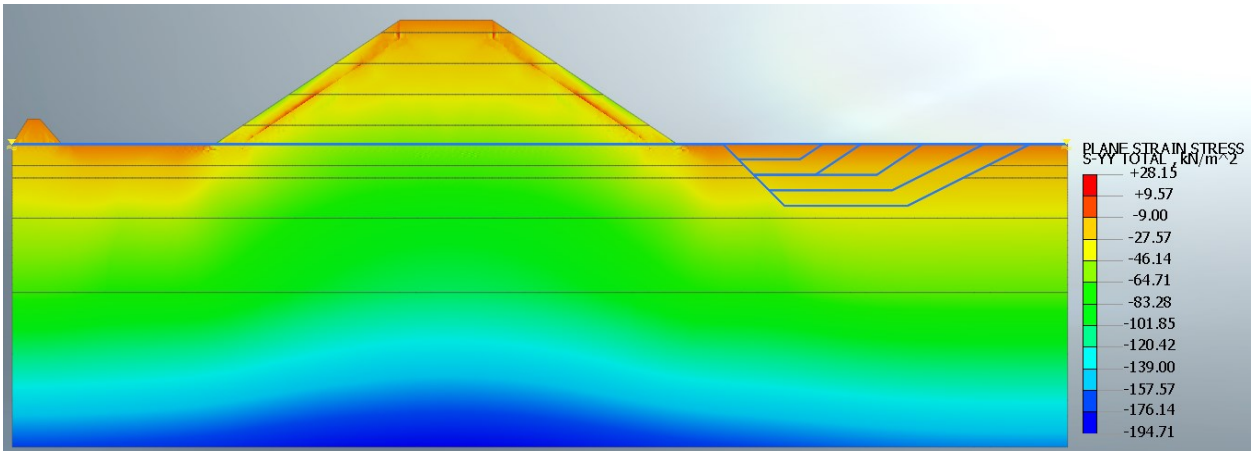

(b) Vertical stress, S-YY

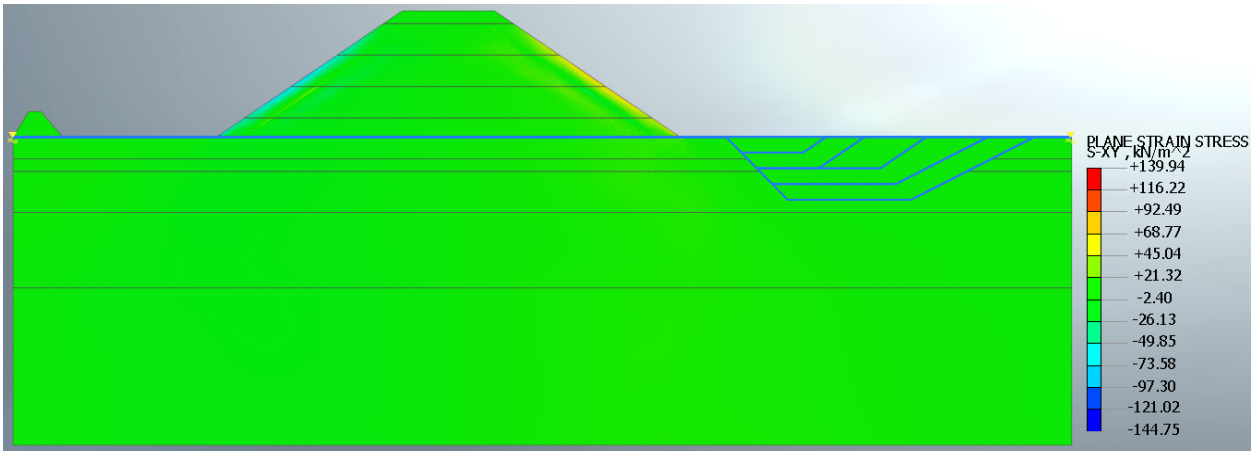

(c) Shear stress, S-XY

Figure D. 26. Total stresses and shear stress (kN/m^2) when basin is filled.

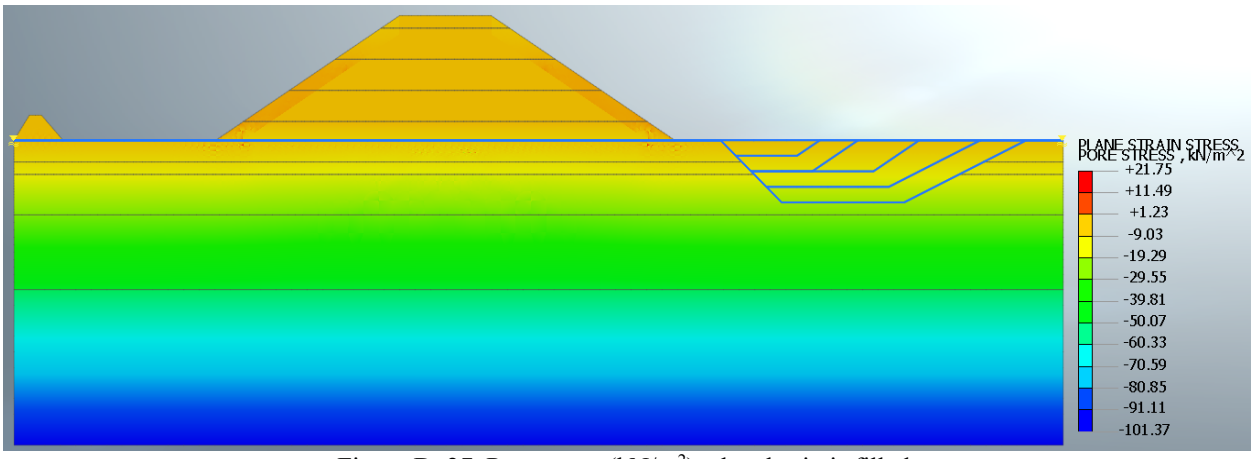

Figure D. 27. Pore stress (kN/m^2) when basin is filled.

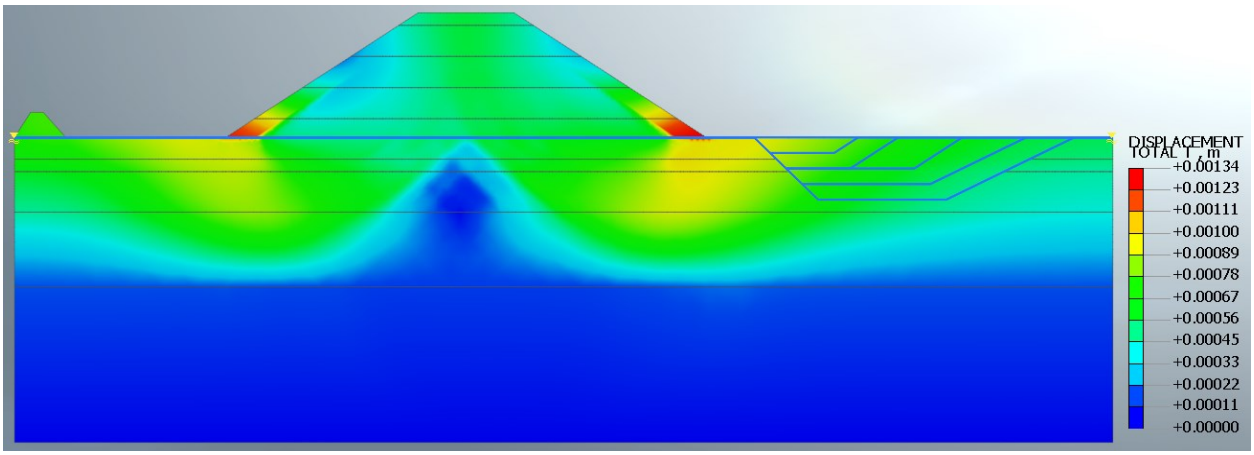

(a) Total displacement, T

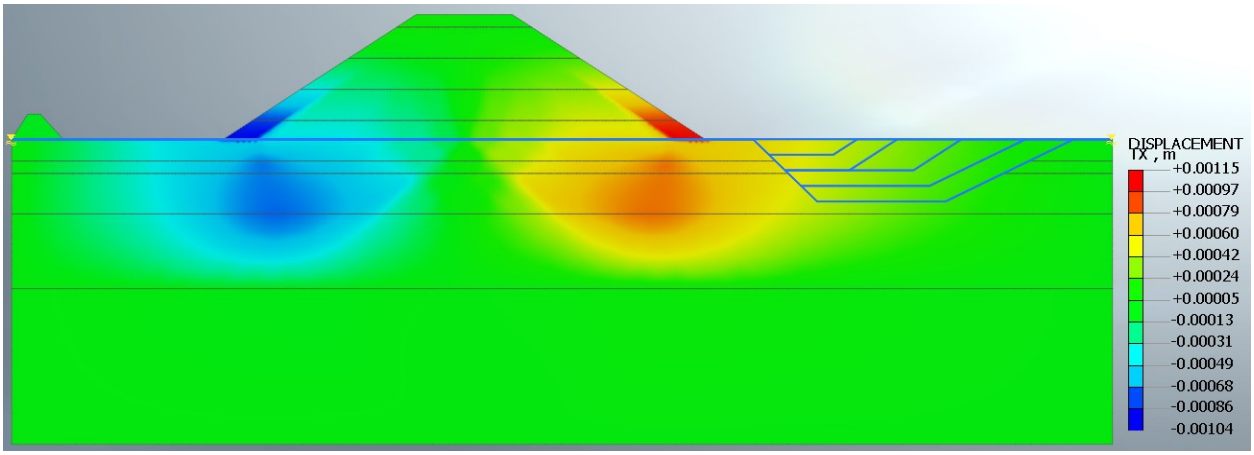

(b) Horizontal displacement, TX

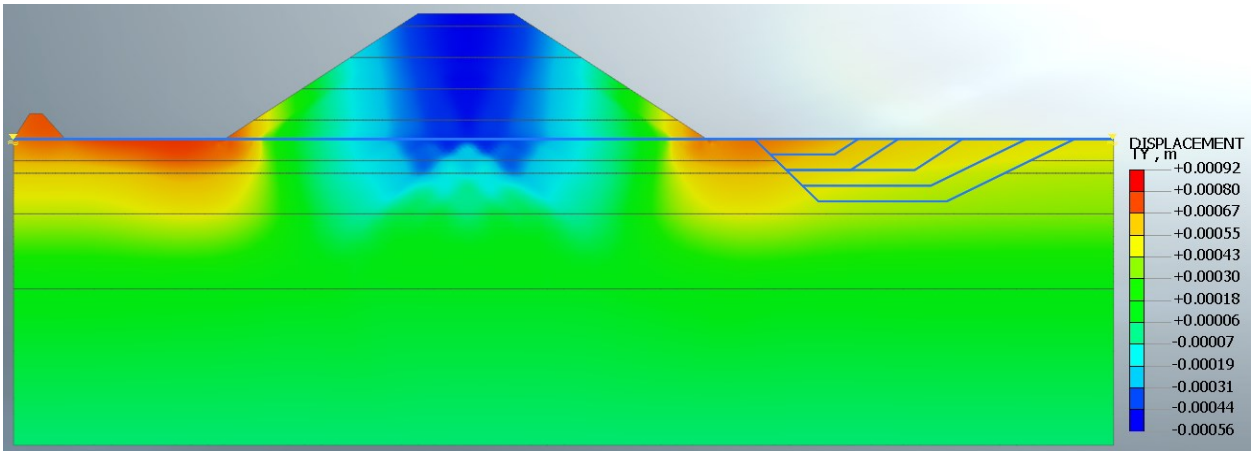

(c) Vertical displacement, TY

Figure D. 28. Displacements (m) when basin is filled.

Stage 13: First excavation transient seepage analysis

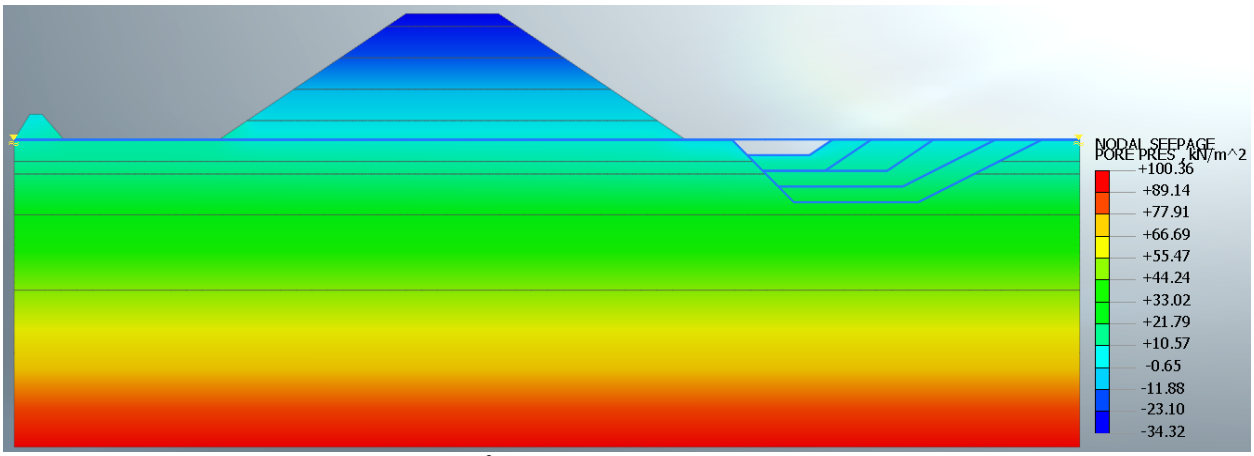

Figure D. 29. Pore stress (kN/m^2) from transient seepage analysis at first excavation stage.

Stage 14: First excavation stress analysis

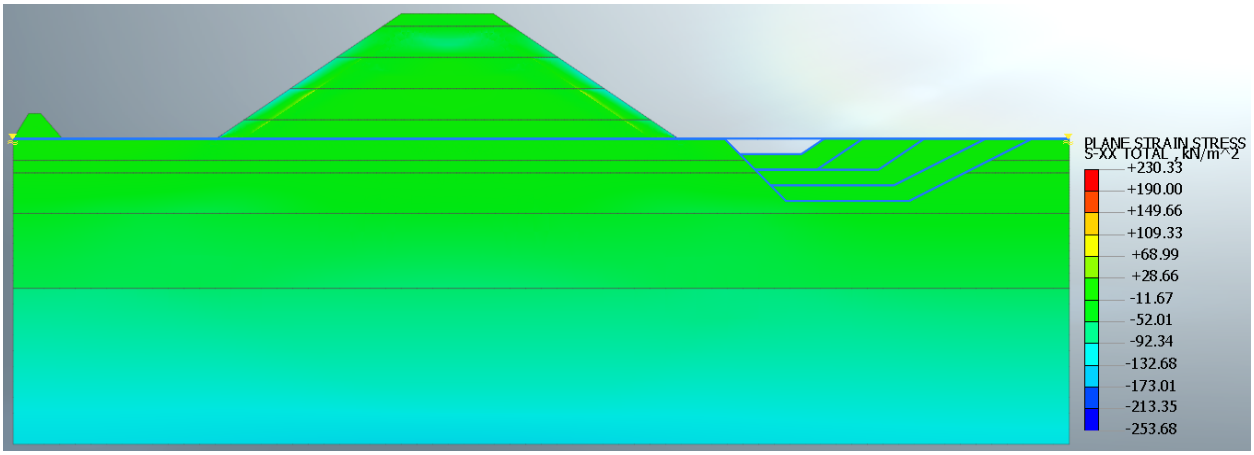

(a) Horizontal stress, S-XX

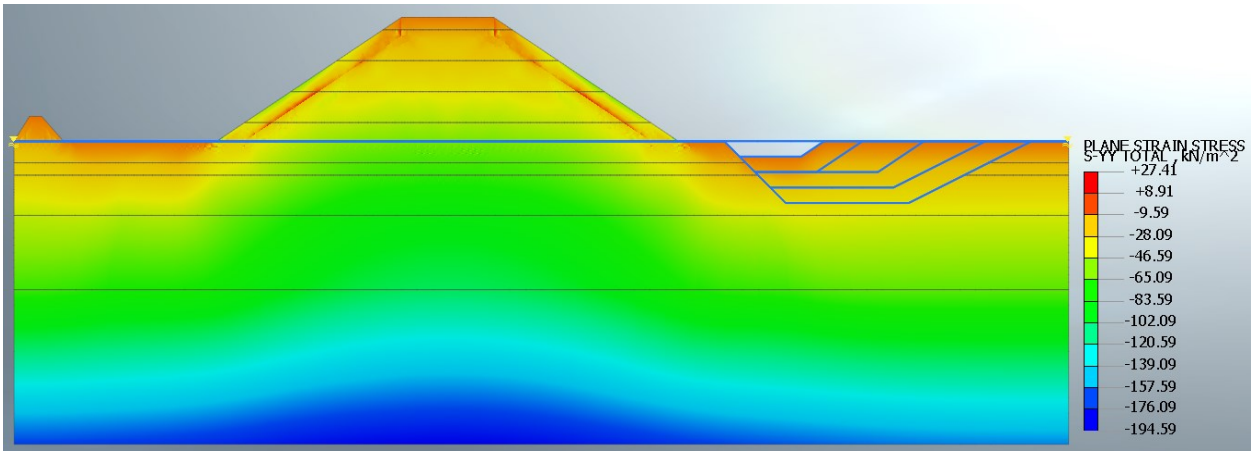

(b) Vertical stress, S-YY

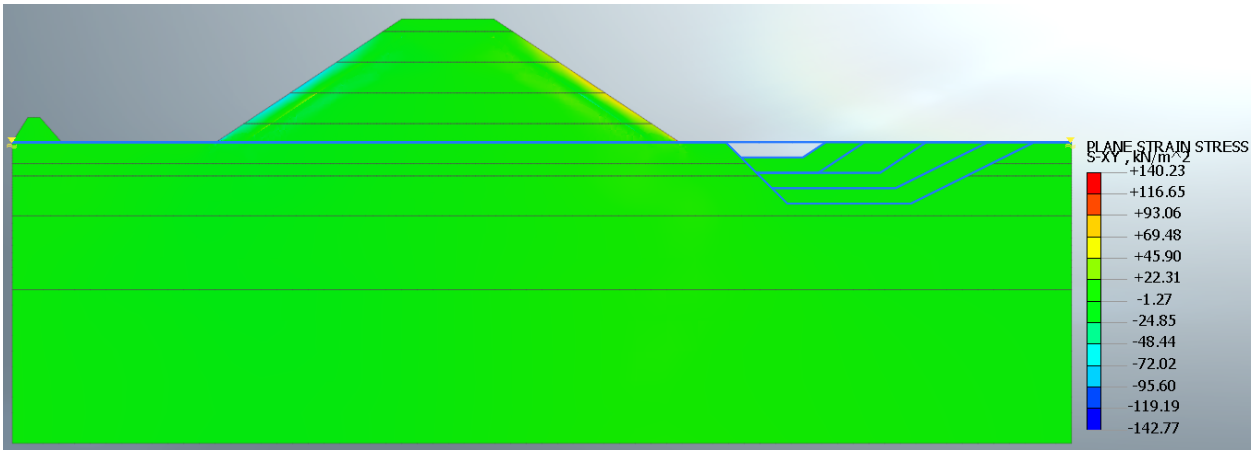

(c) Shear stress, S-XY

Figure D. 30. Total stresses and shear stress (kN/m^2) at first excavation stage.

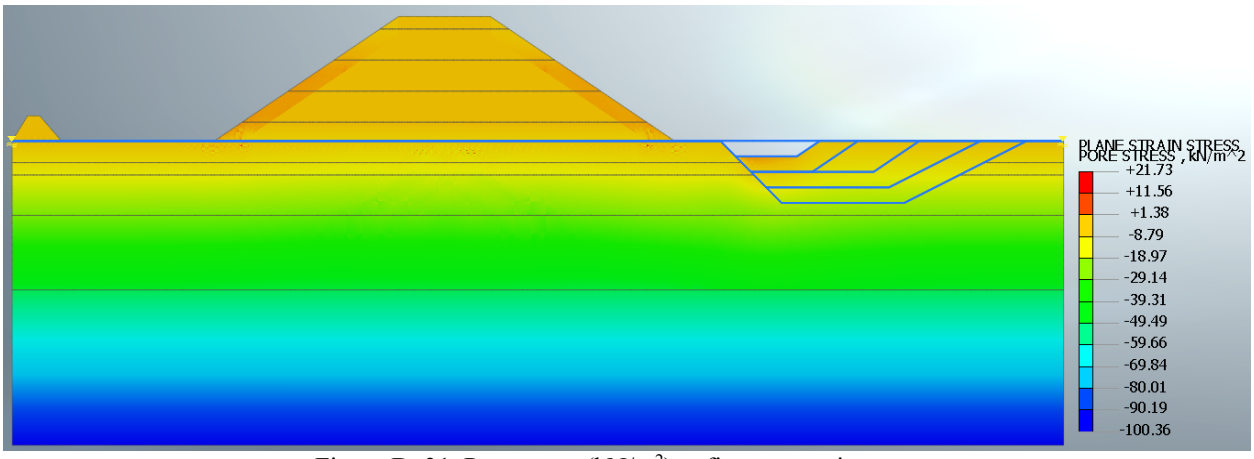

Figure D. 31. Pore stress (kN/m^2) at first excavation stage.

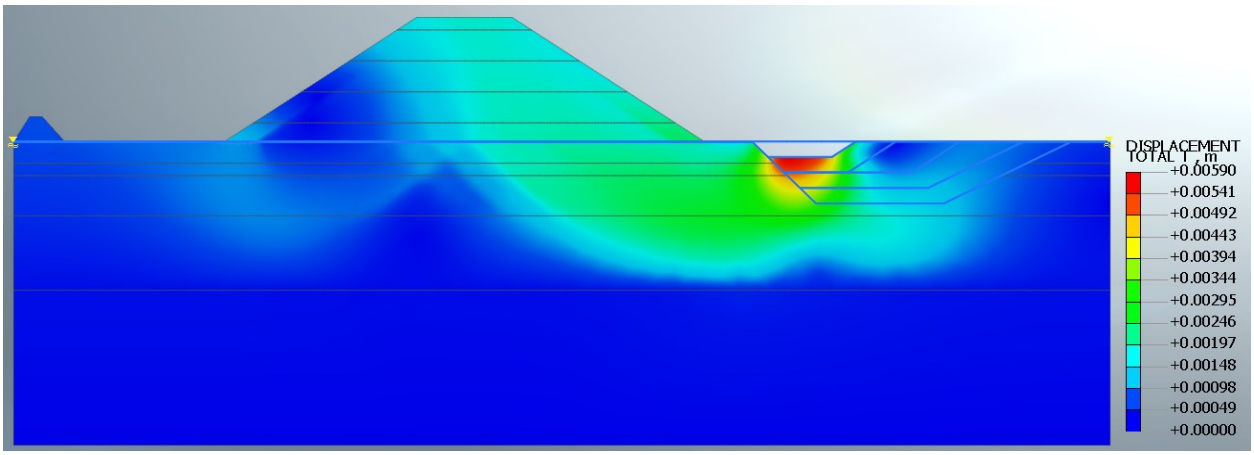

(a) Total displacement, T

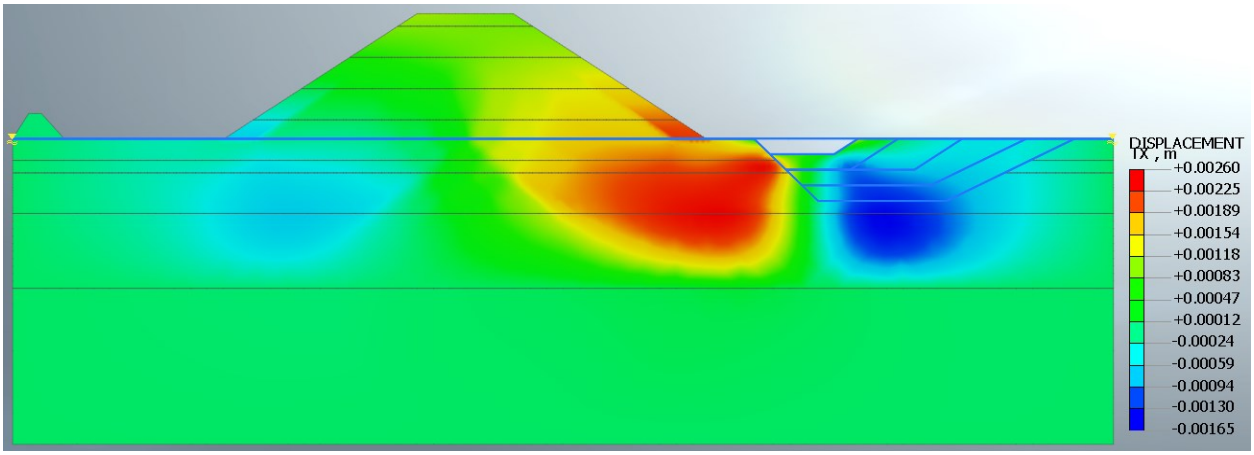

(b) Horizontal displacement, TX

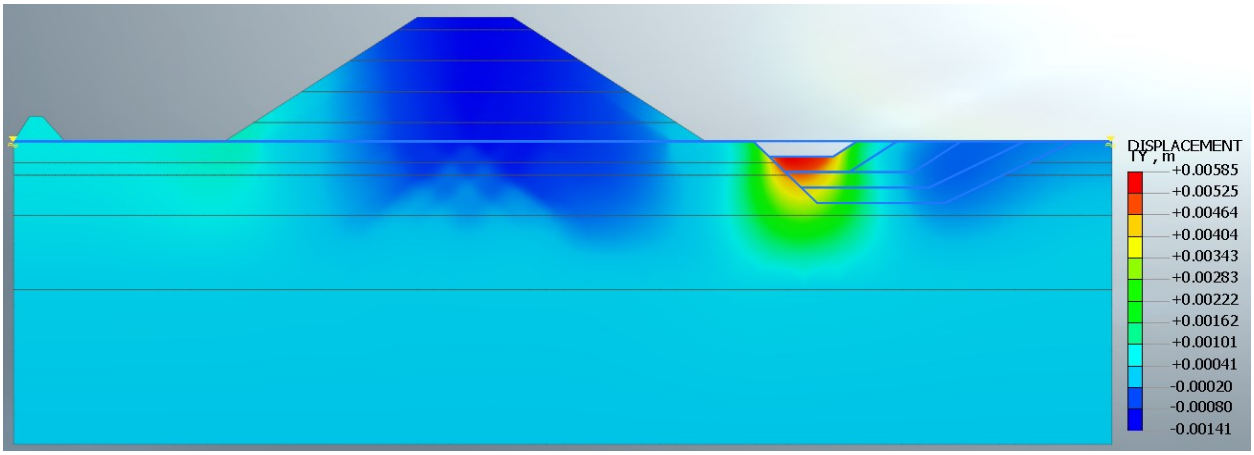

(C) Vertical displacement, TY

Figure D. 32. Displacements (m) at first excavation stage.

Stage 15: Second excavation transient seepage analysis

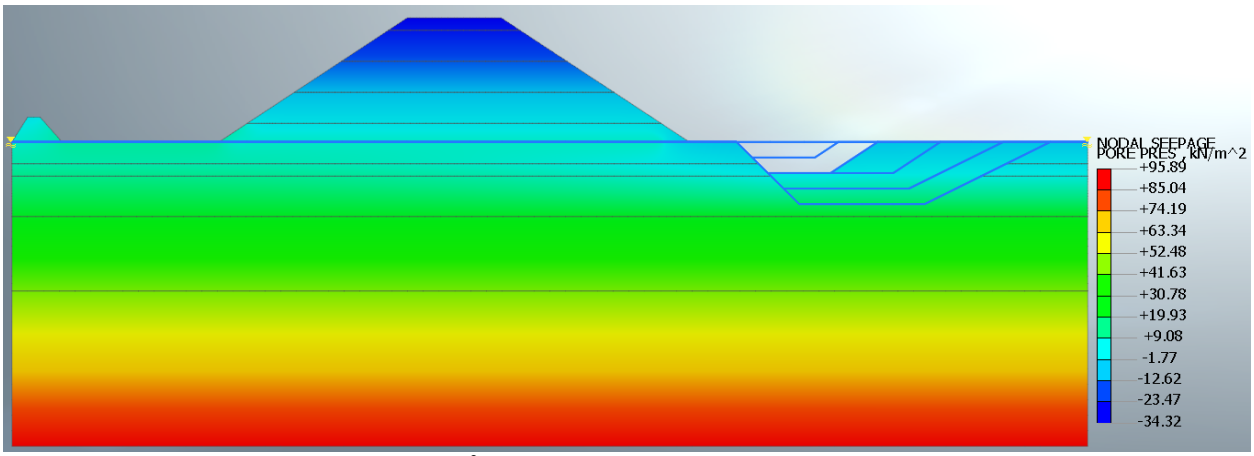

Figure D. 33. Pore stress (kN/m^2) from transient seepage analysis at second excavation stage.

Stage 16: Second excavation stress analysis

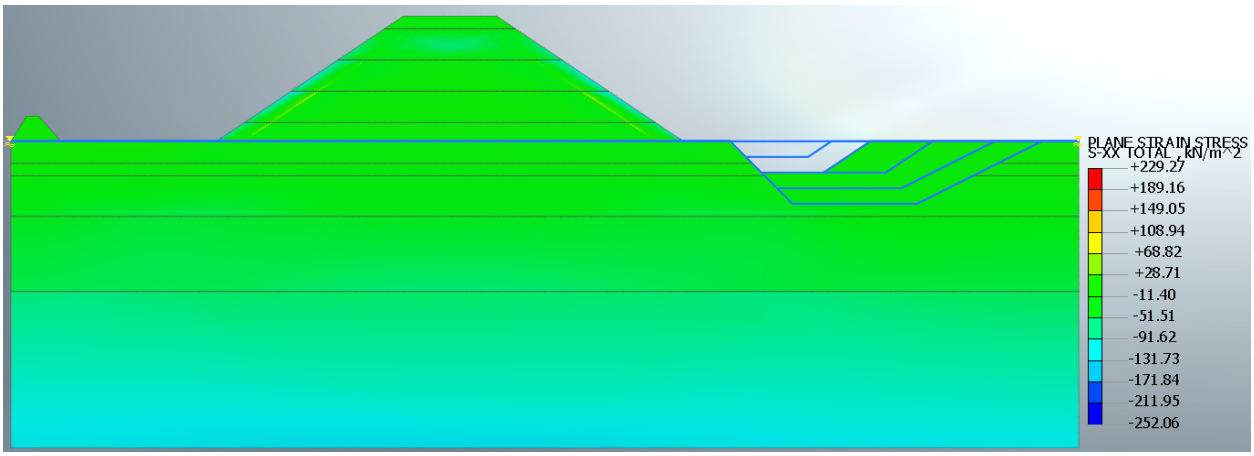

(a) Horizontal stress, S-XX

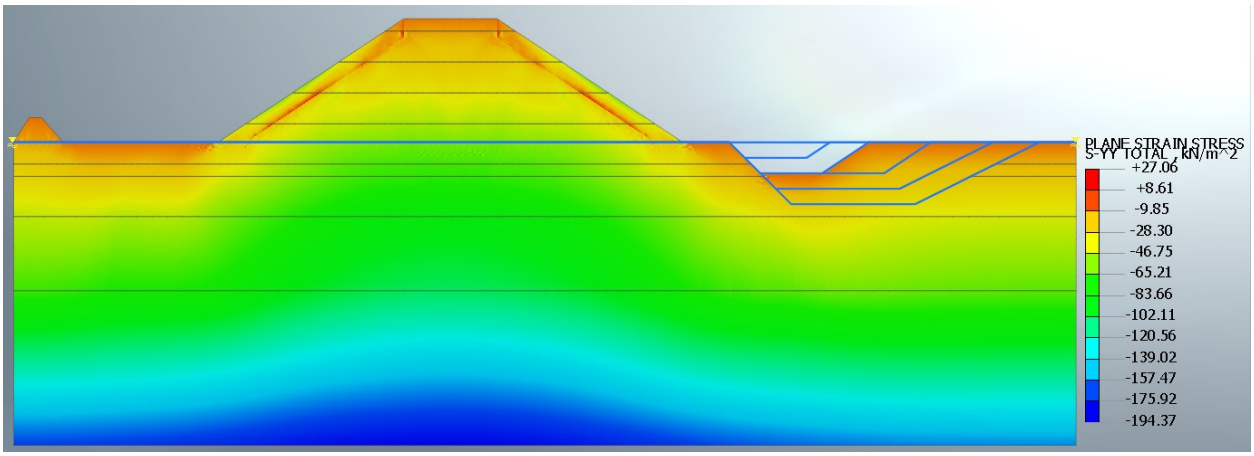

(b) Vertical stress, S-YY

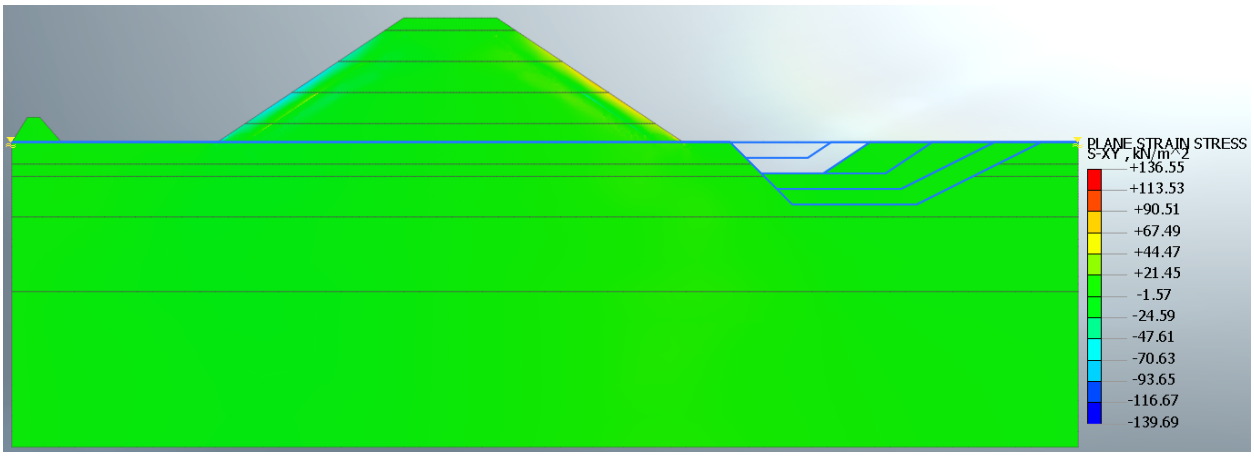

(c) Shear stress, S-XY

Figure D. 34. Total stresses and shear stress (kN/m^2) at second excavation stage.

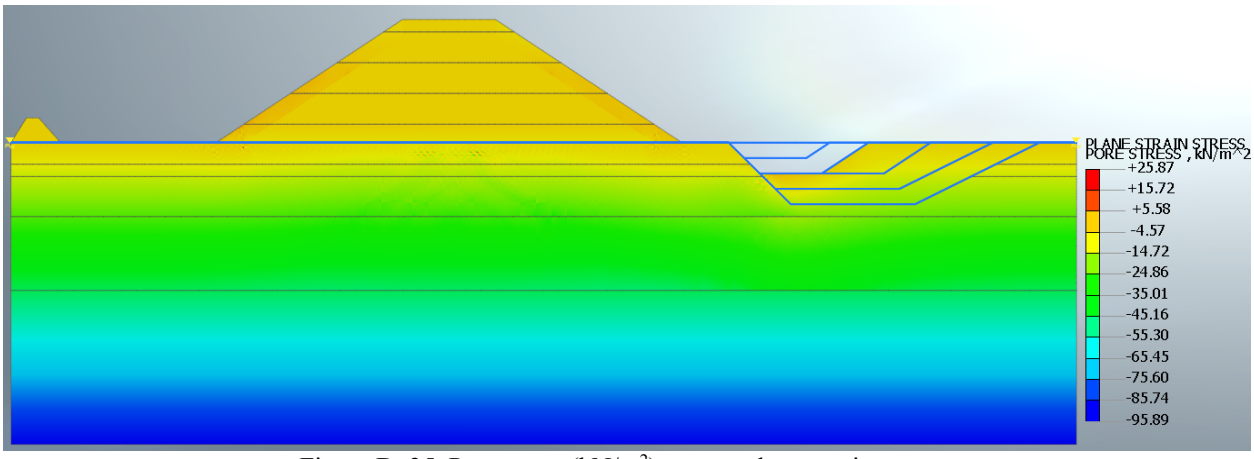

Figure D. 35. Pore stress (kN/m^2) at second excavation stage.

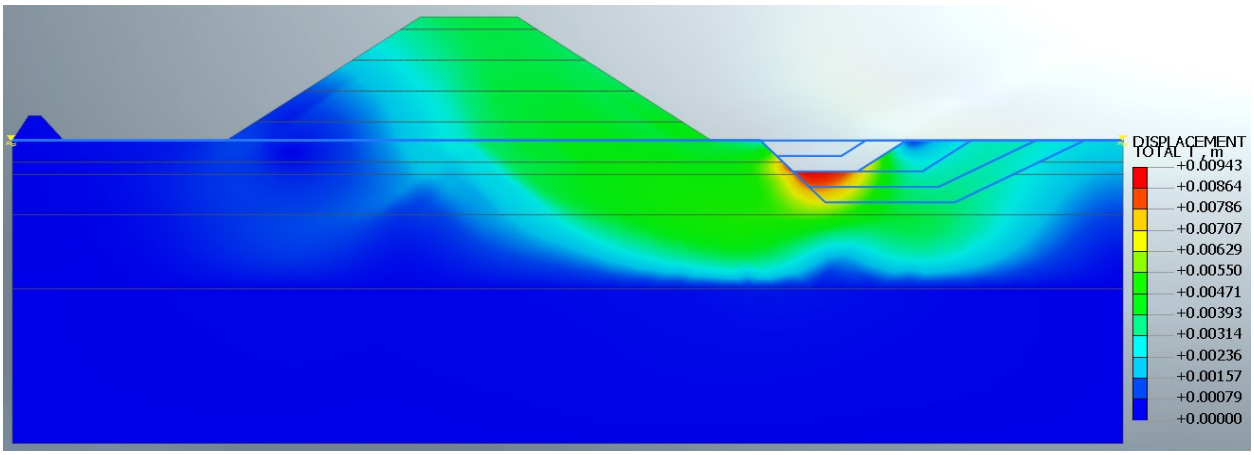

(a) Total displacement, T

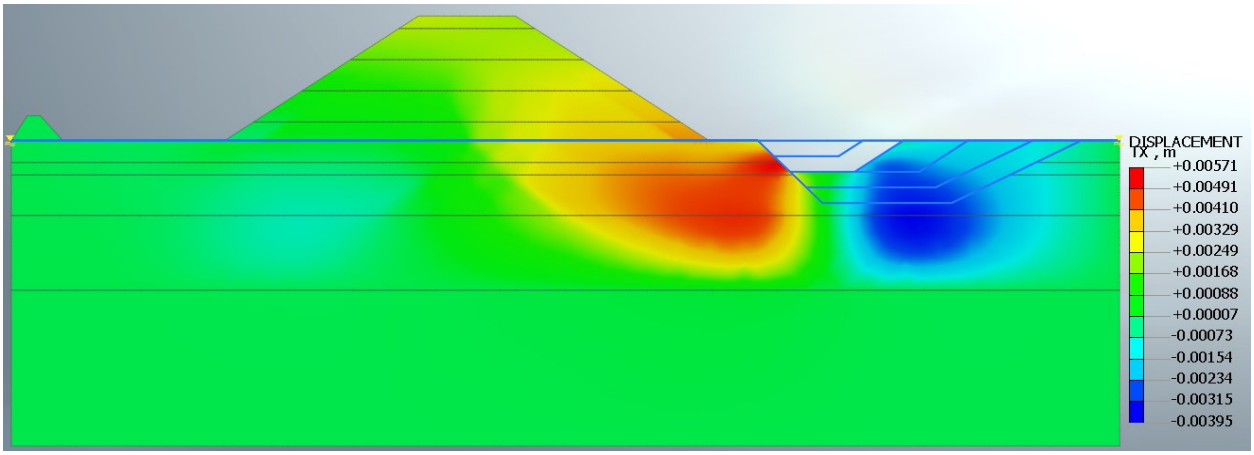

(b) Horizontal displacement, TX

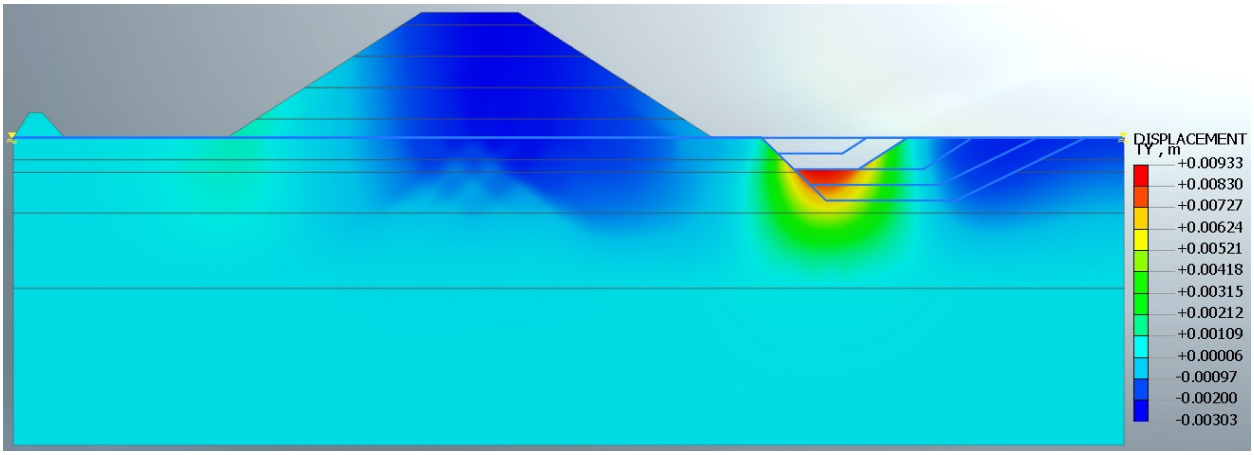

(c) Vertical displacement, TY

Figure D. 36. Displacements (m) at second excavation stage.

Stage 17: Third excavation transient seepage analysis

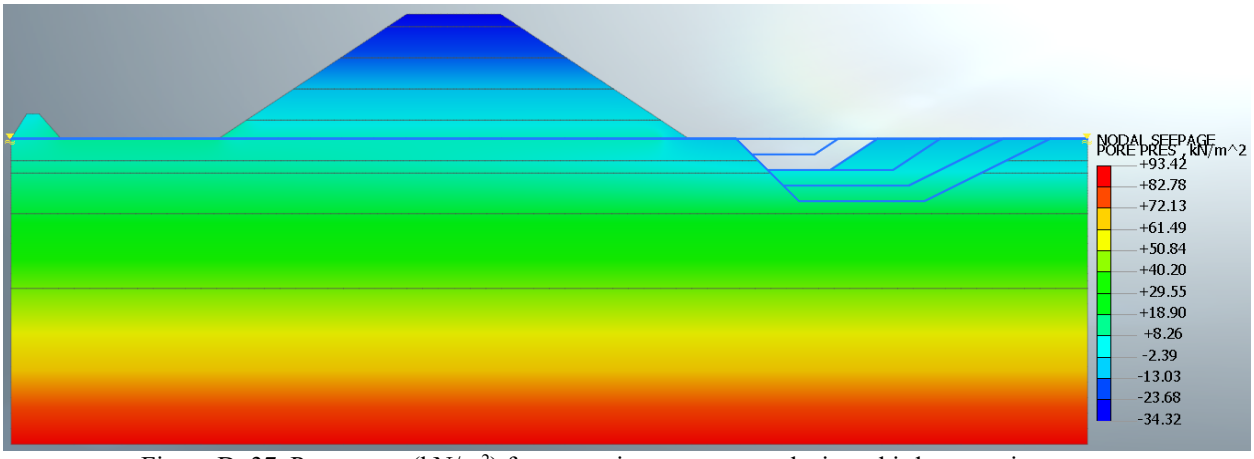

Figure D. 37. Pore stress (kN/m^2) from transient seepage analysis at third excavation stage.

Stage 18: Third excavation stress analysis

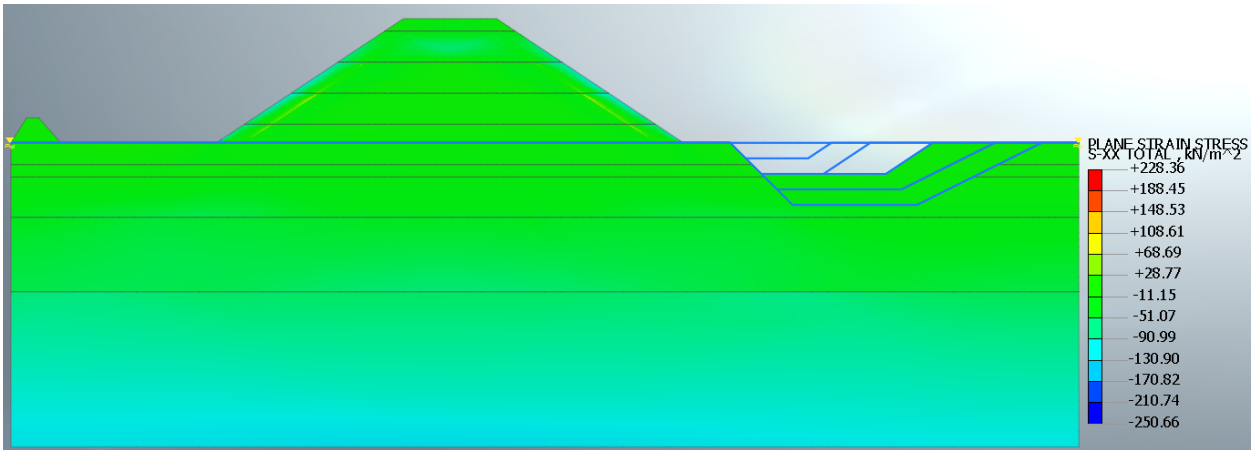

(a) Horizontal stress, S-XX

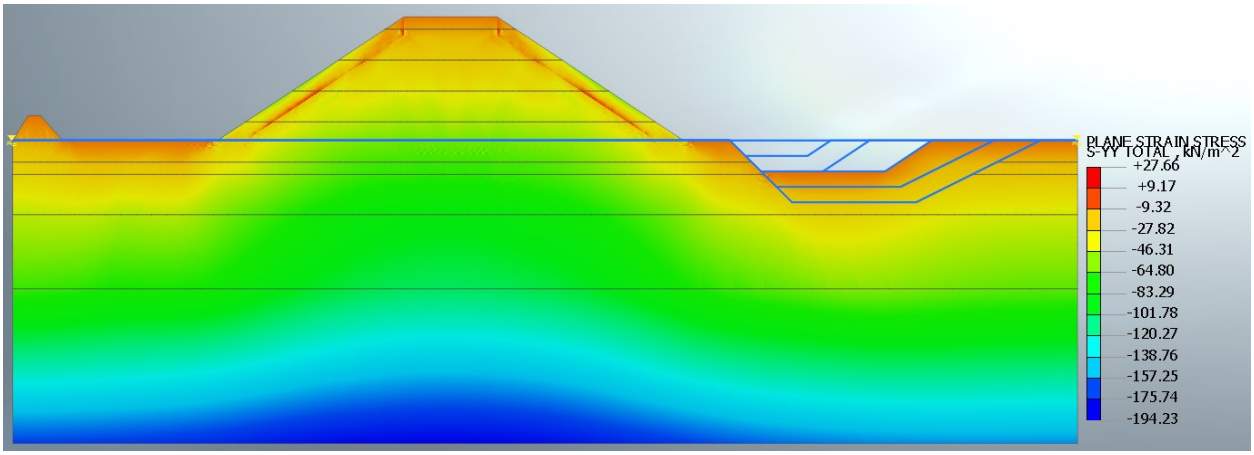

(b) Vertical stress, S-YY

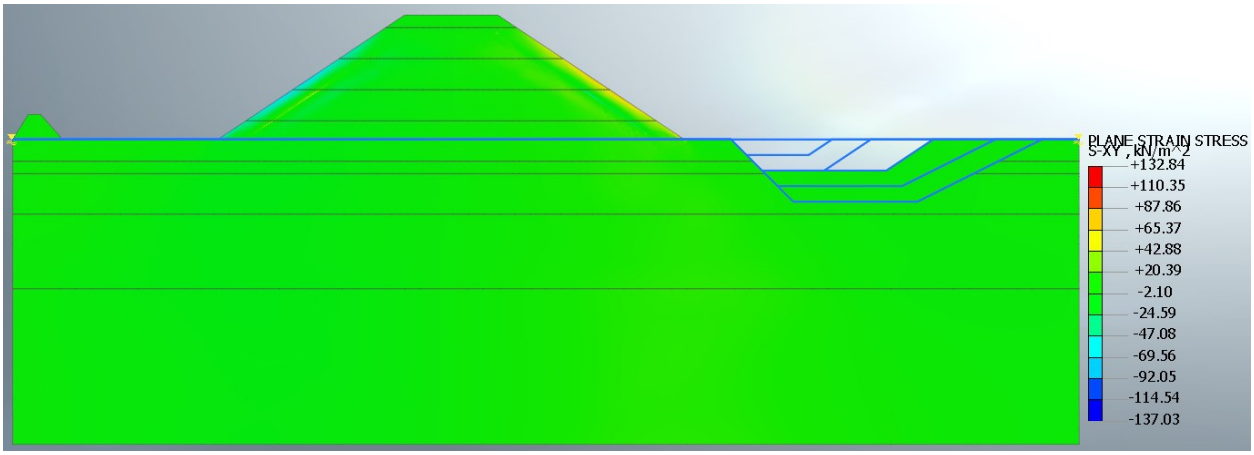

(c) Shear stress, S-XY

Figure D. 38. Total stresses and shear stress (kN/m^2) at third excavation stage.

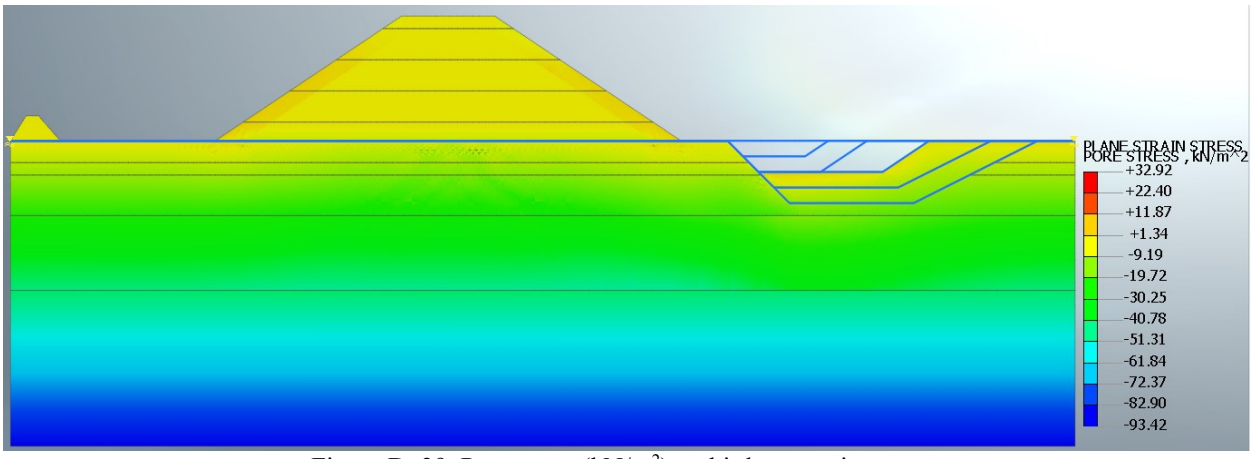

Figure D. 39. Pore stress (kN/m^2) at third excavation stage.

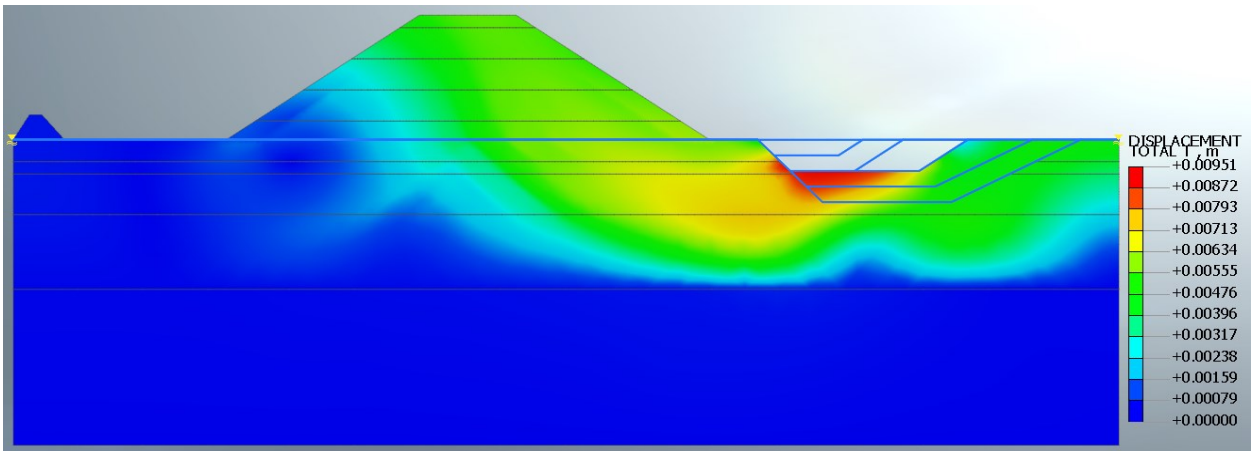

(a) Total displacement, T

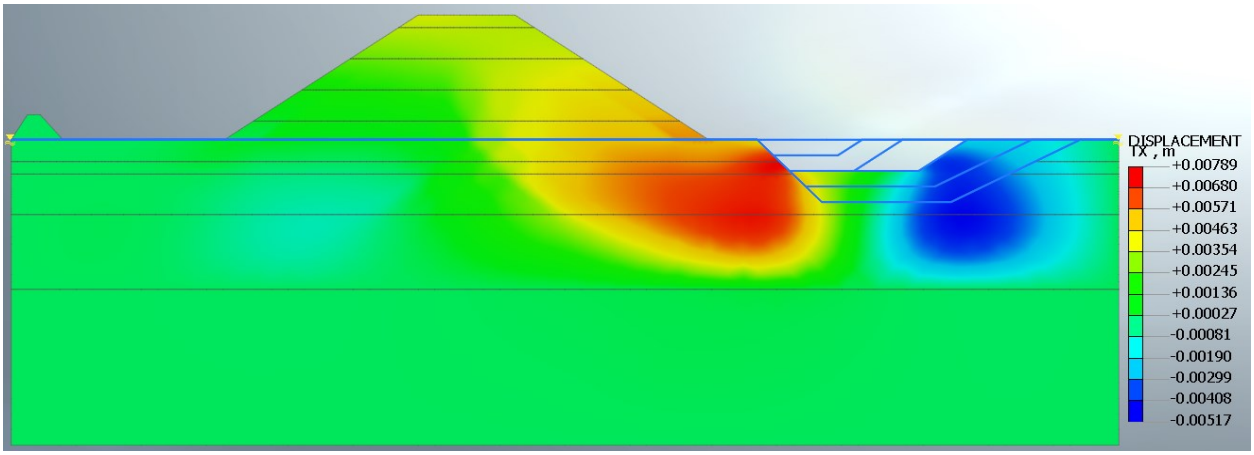

(b) Horizontal displacement, TX

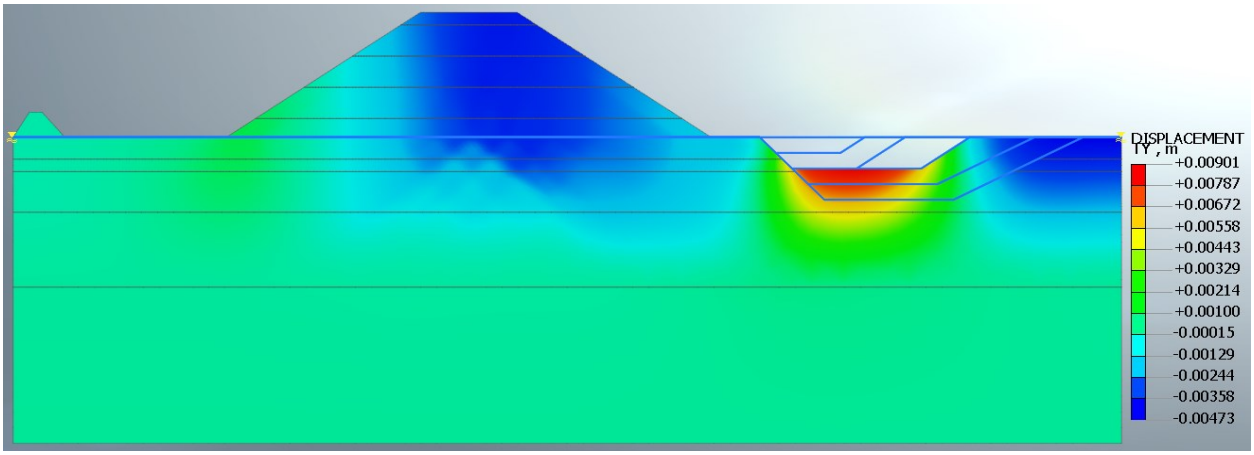

(c) Vertical displacement, TY

Figure D. 40. Displacements (m) at third excavation stage.

Stage 19: Consolidation (transient seepage analysis)

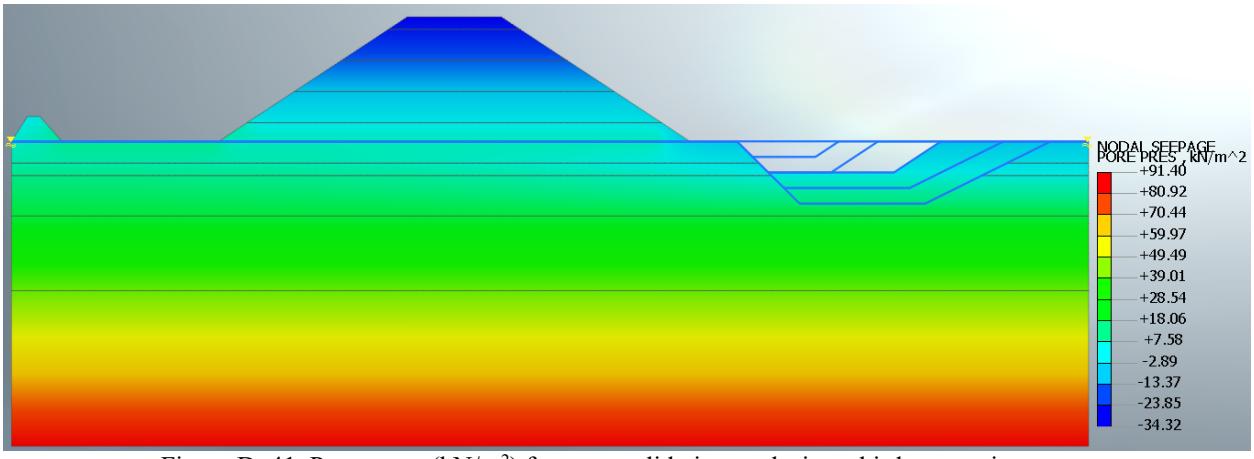

Figure D. 41. Pore stress (kN/m^2) from consolidation analysis at third excavation stage.

Stage 20: Fourth excavation transient seepage analysis

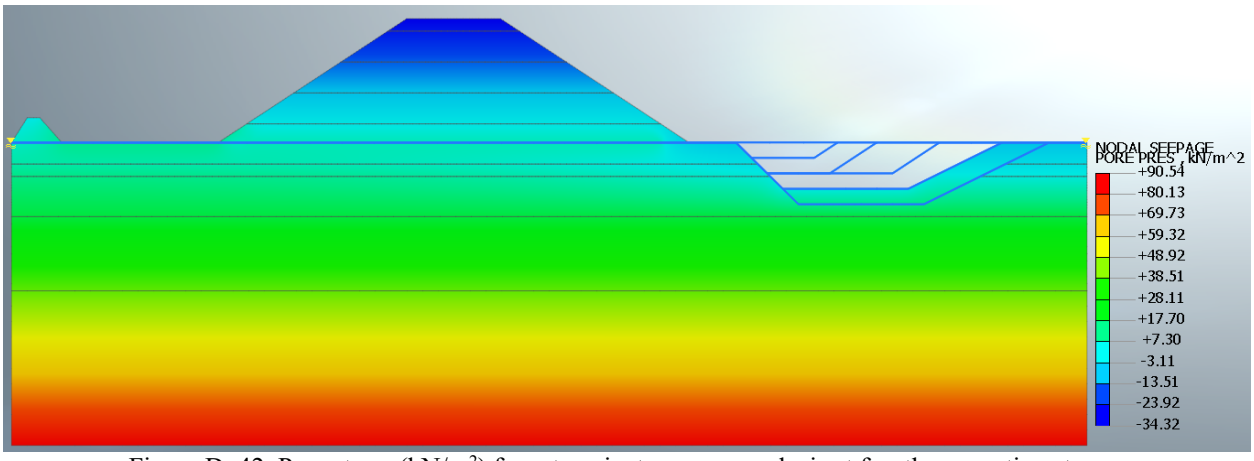

Figure D. 42. Pore stress (kN/m^2) from transient seepage analysis at fourth excavation stage.

Stage 21: Fourth excavation stress analysis

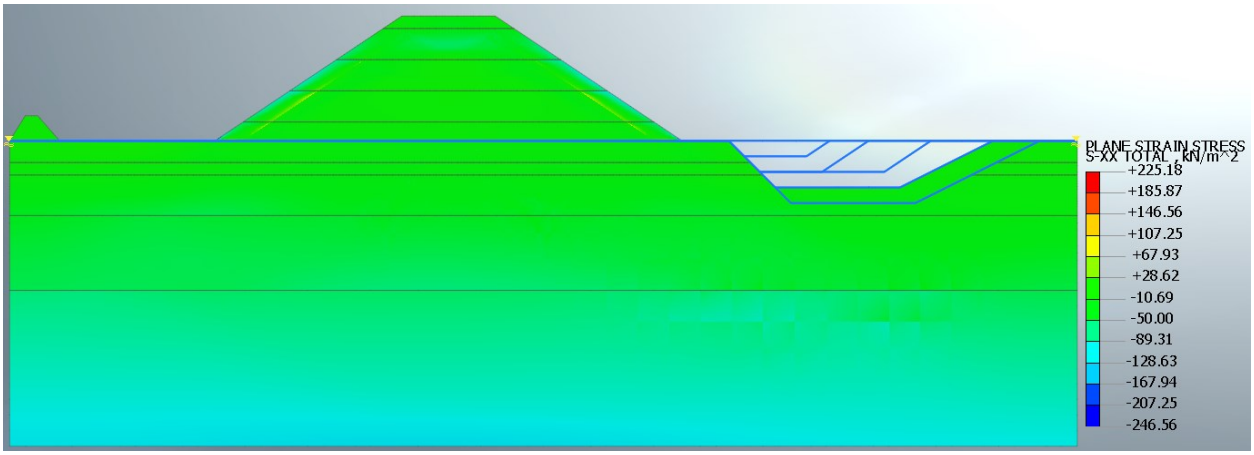

(a) Horizontal stress, S-XX

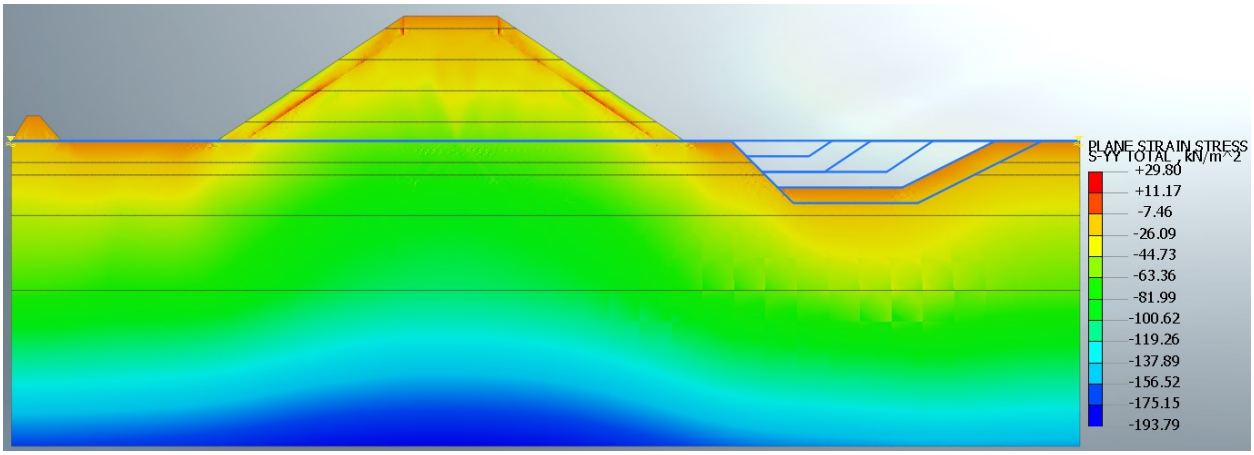

(b) Vertical stress, S-YY

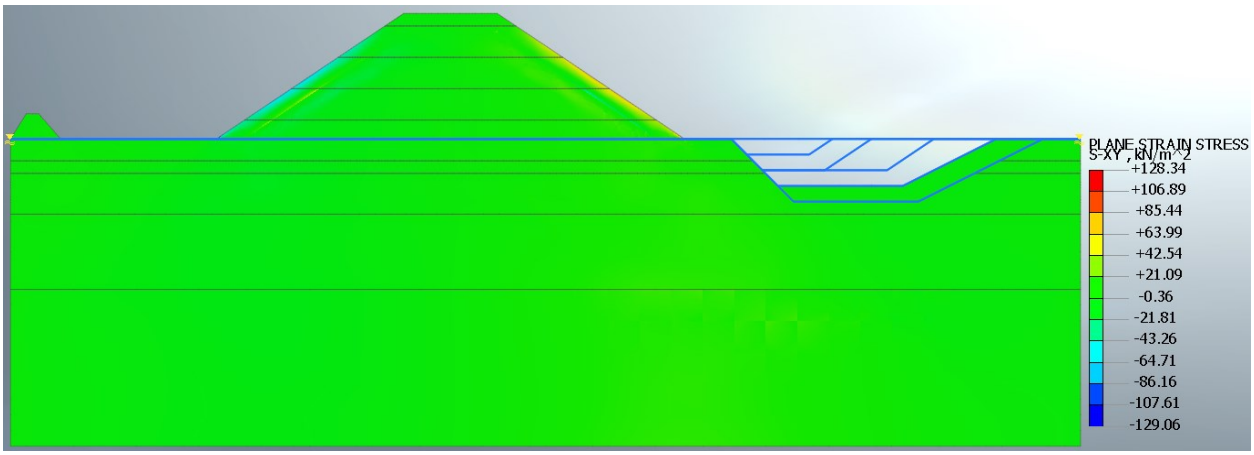

(c) Shear stress, S-XY

Figure D. 43. Total stresses and shear stress (kN/m^2) at fourth excavation stage.

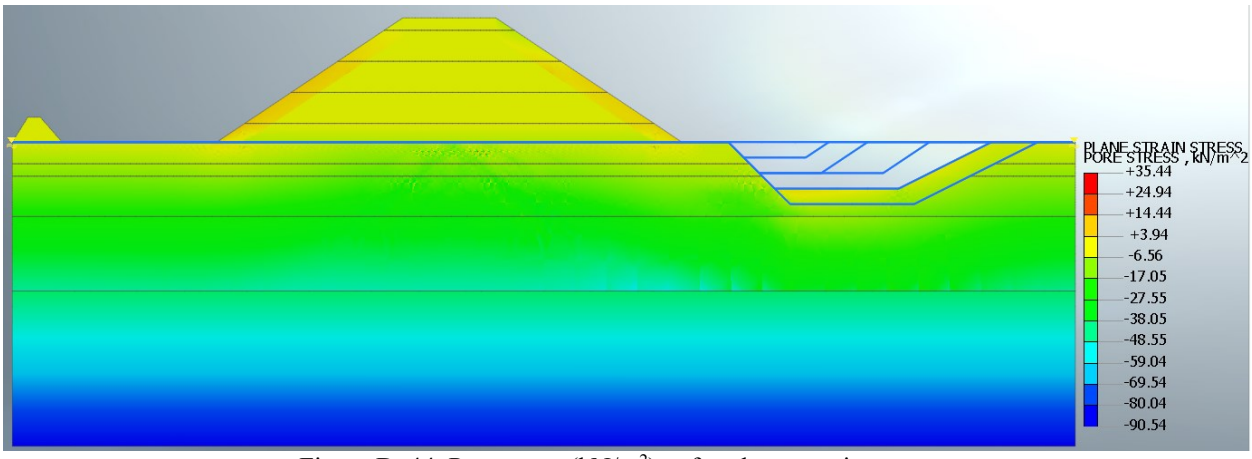

Figure D. 44. Pore stress (kN/m^2) at fourth excavation stage.

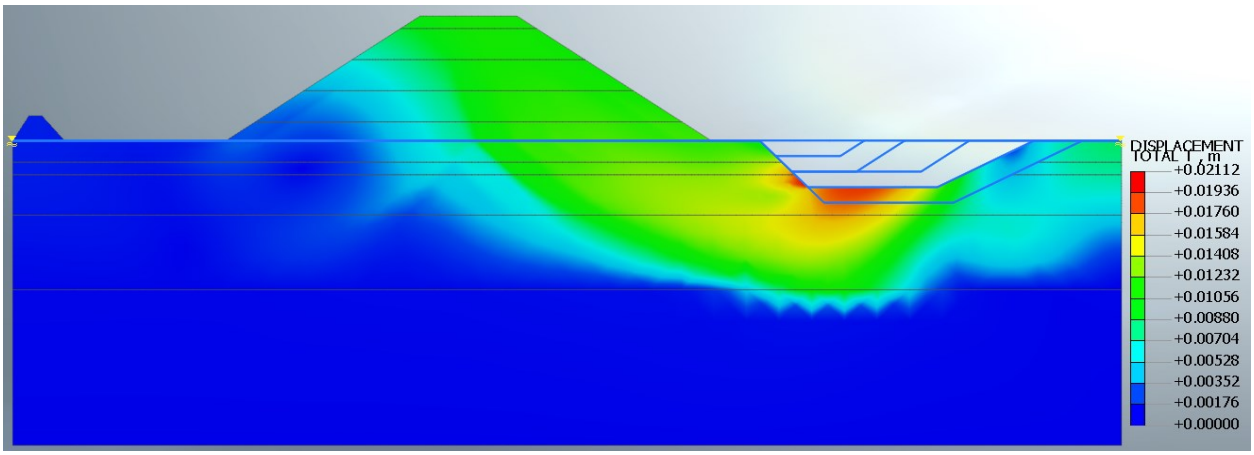

(a) Total displacement, T

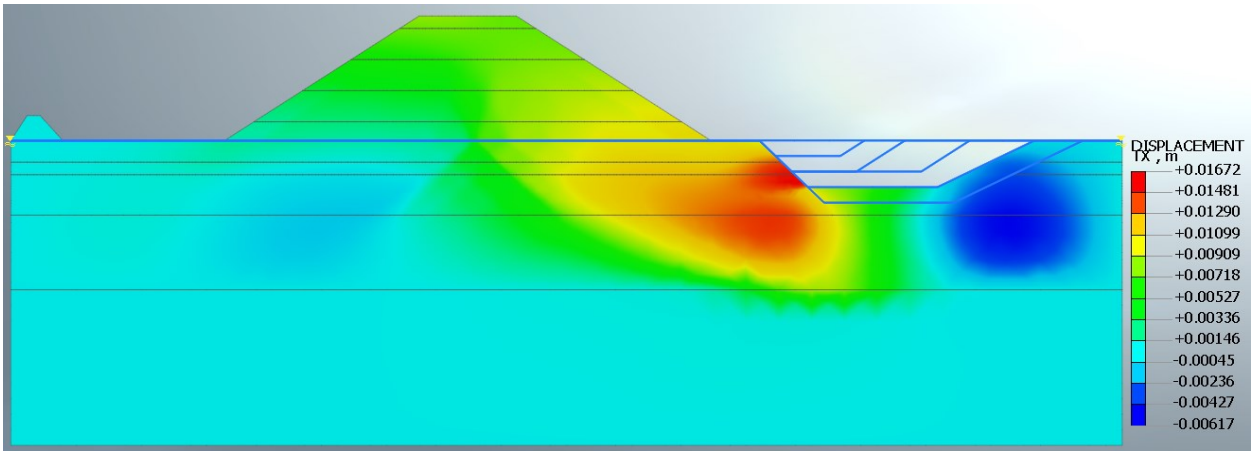

(b) Horizontal displacement, TX

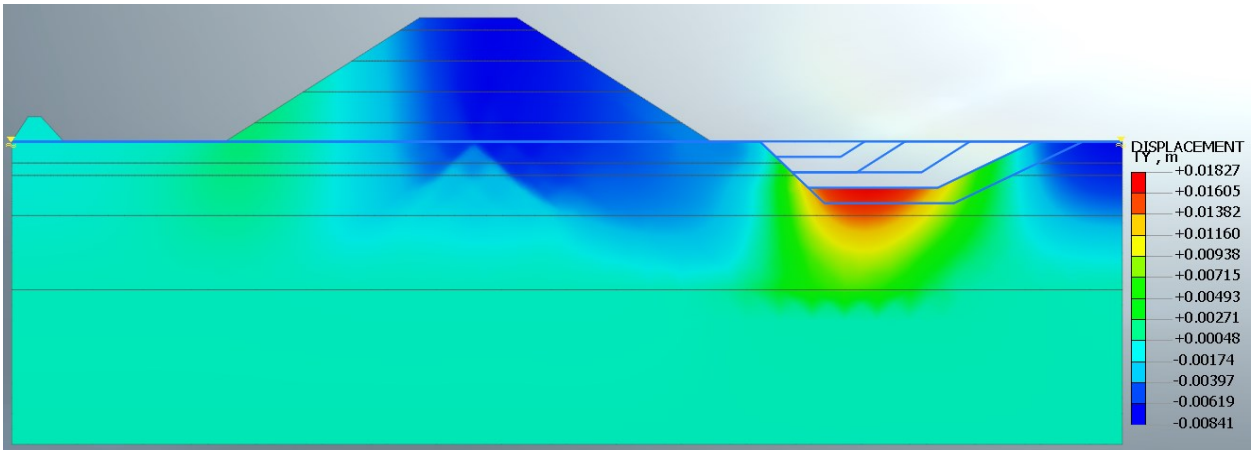

(c) Vertical displacement, TY

Figure D. 45. Displacements (m) at fourth excavation stage.

Stage 22: Fifth excavation transient seepage analysis

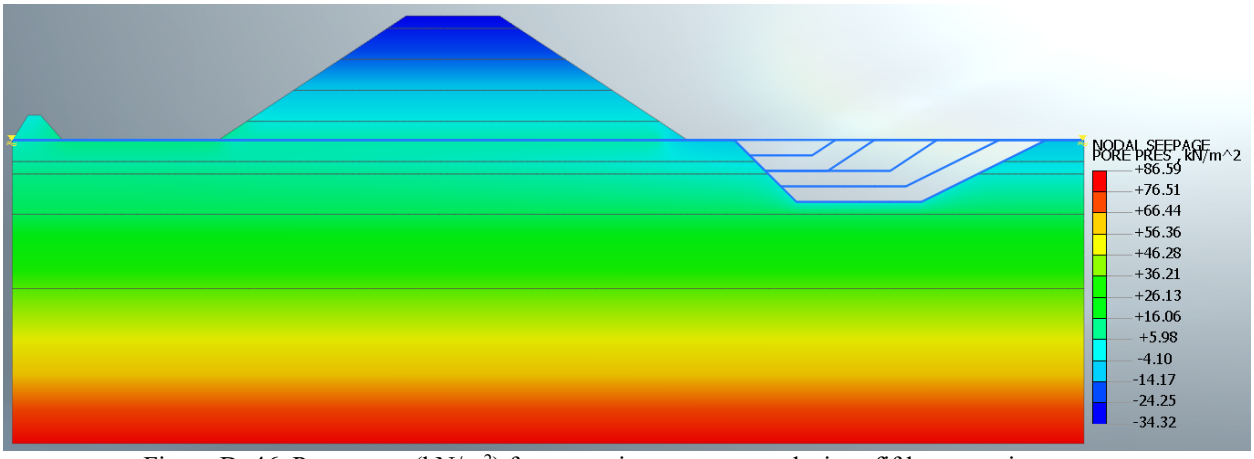

Figure D. 46. Pore stress (kN/m^2) from transient seepage analysis at fifth excavation stage.

Stage 23: Fifth excavation stress analysis

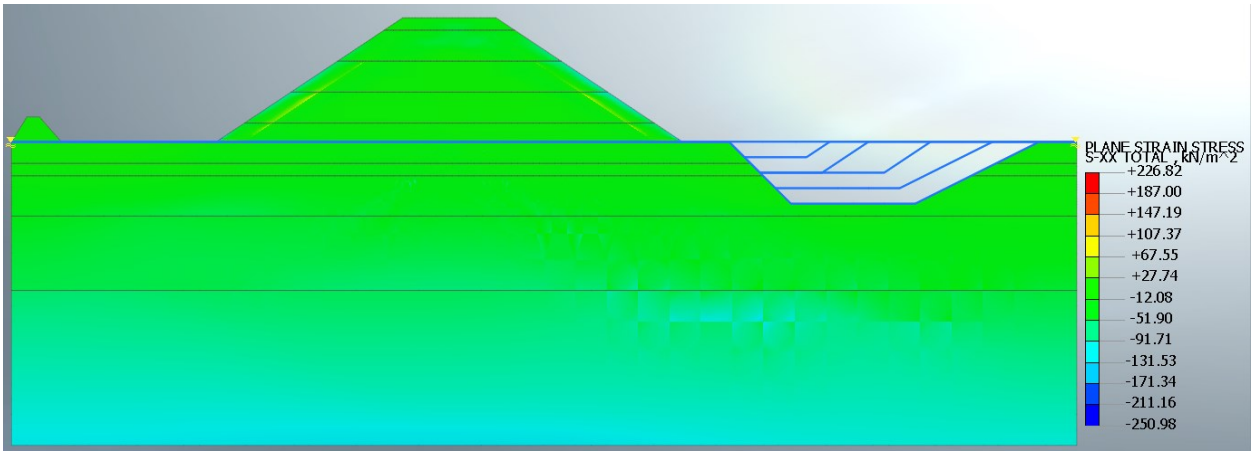

(a) Horizontal stress, S-XX

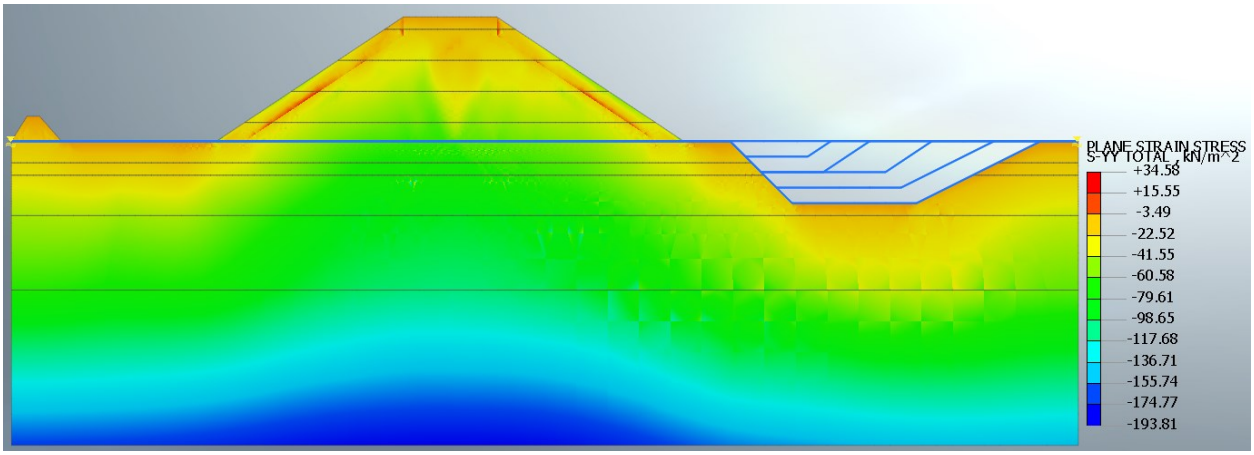

(b) Vertical stress, S-YY

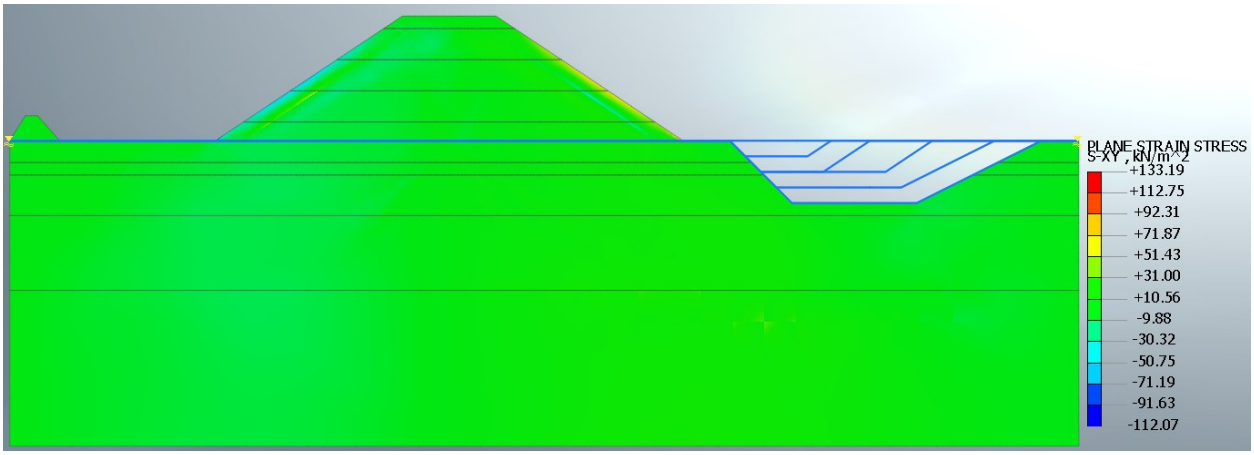

(c) Shear stress, S-XY

Figure D. 47. Total stresses and shear stress (kN/m^2) at fifth excavation stage.

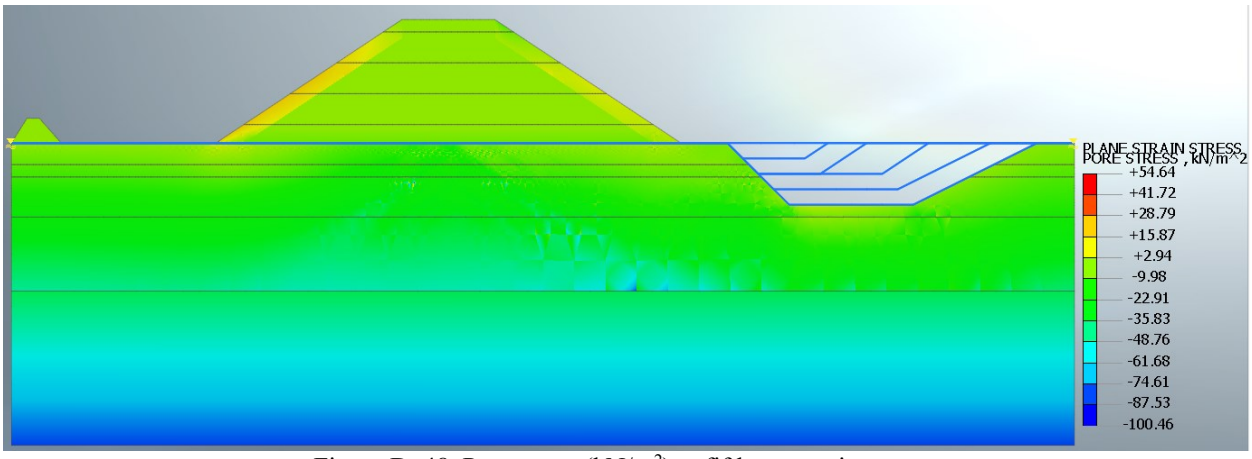

Figure D. 48. Pore stress (kN/m^2) at fifth excavation stage.

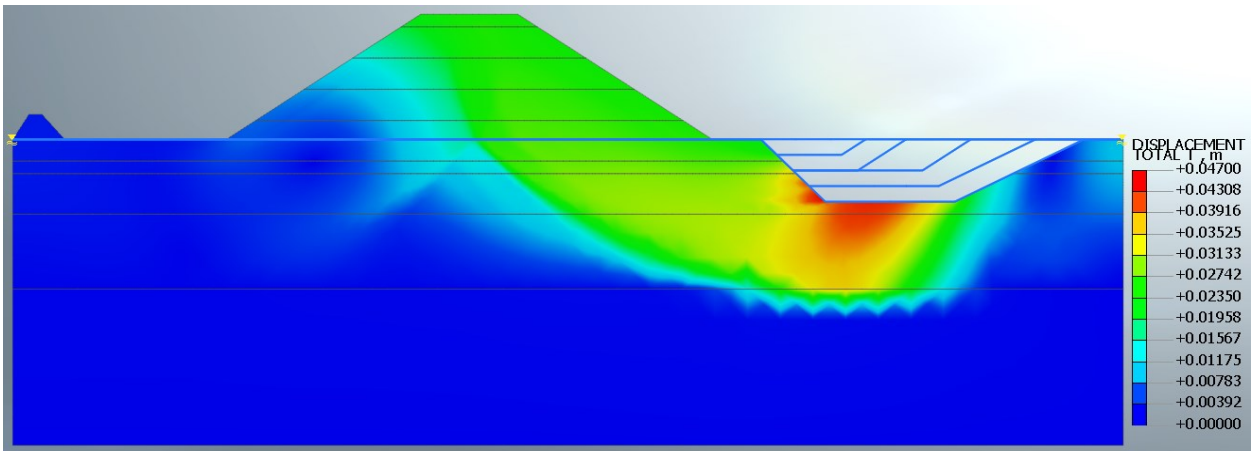

(a) Total displacement, T

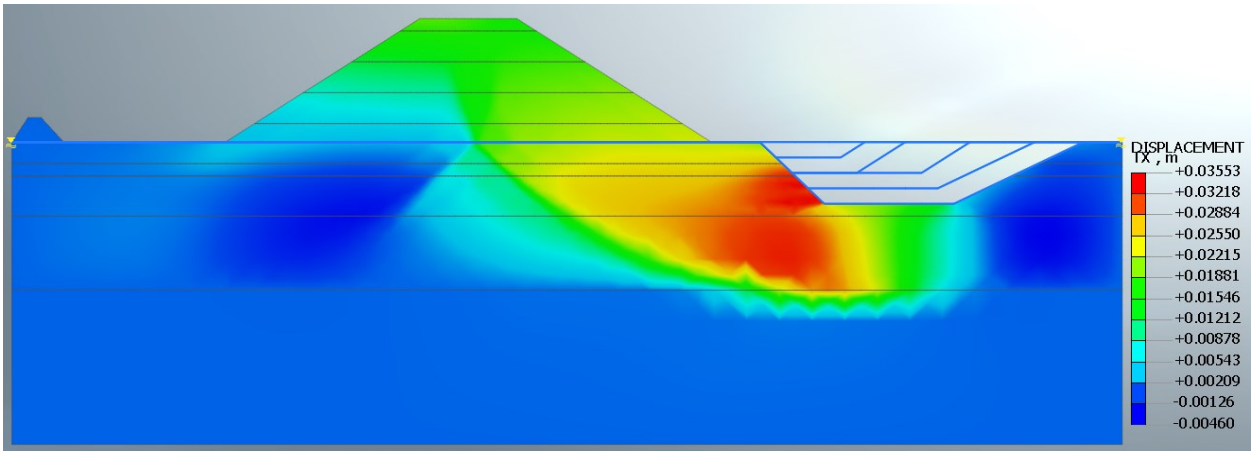

(b) Horizontal displacement, TX

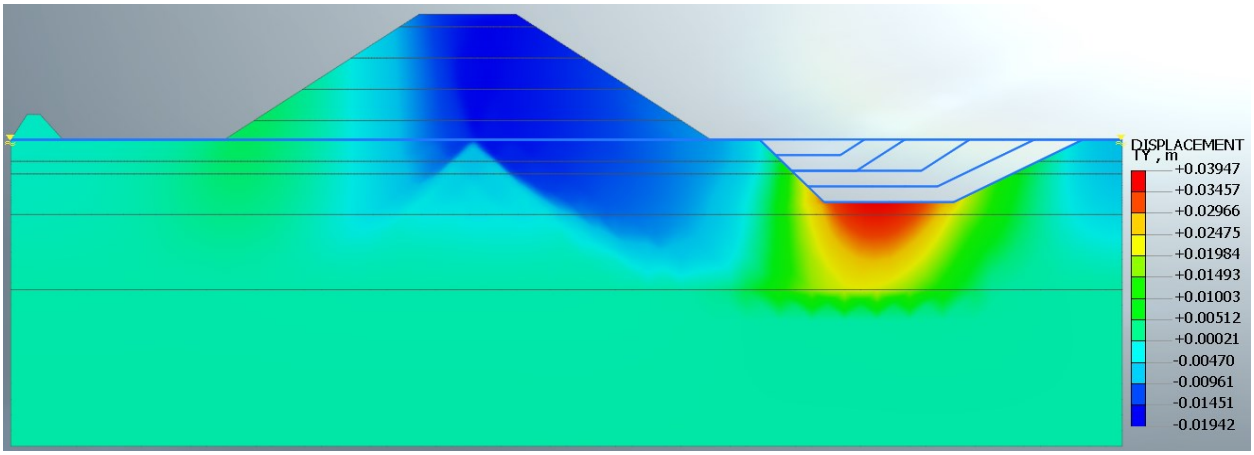

(c) Vertical displacement, TY

Figure D. 49. Displacements (m) at fifth excavation stage.

Stage 24: Second filling of sand core transient seepage analysis

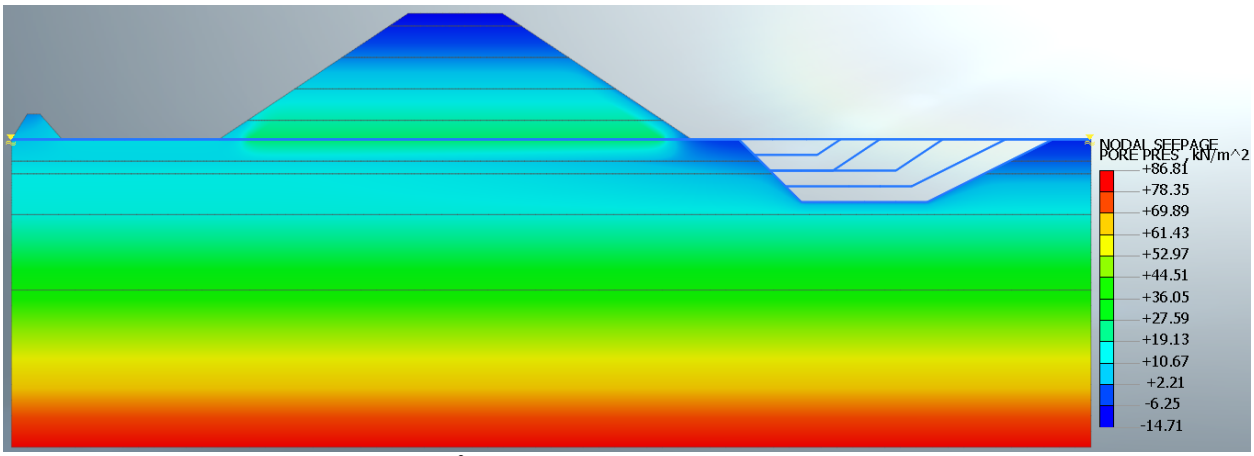

Figure D. 50. Pore stress (kN/m^2) from transient seepage analysis at second filling of sand core.

Stage 25: Second filling of sand core stress analysis

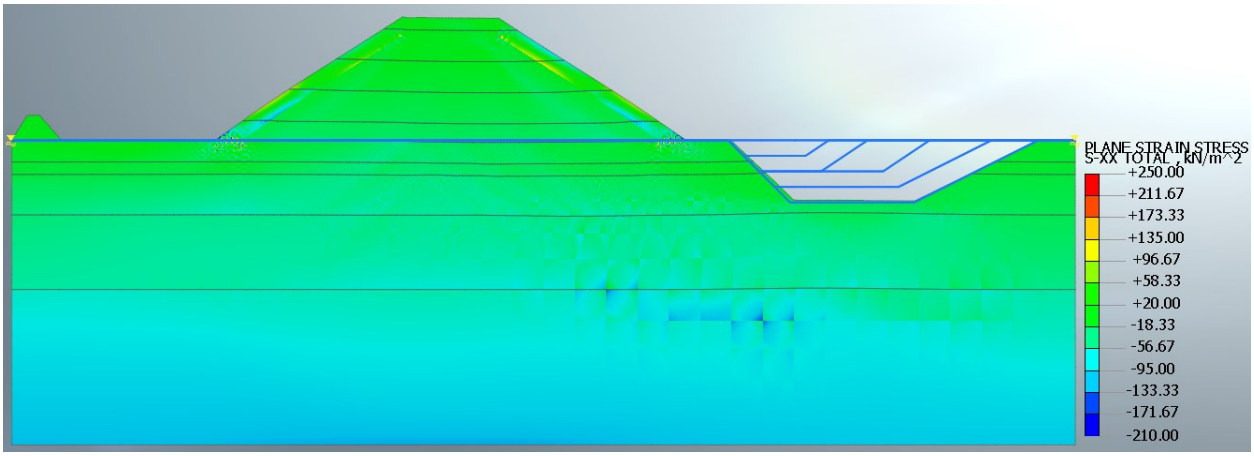

(a) Horizontal stress, S-XX

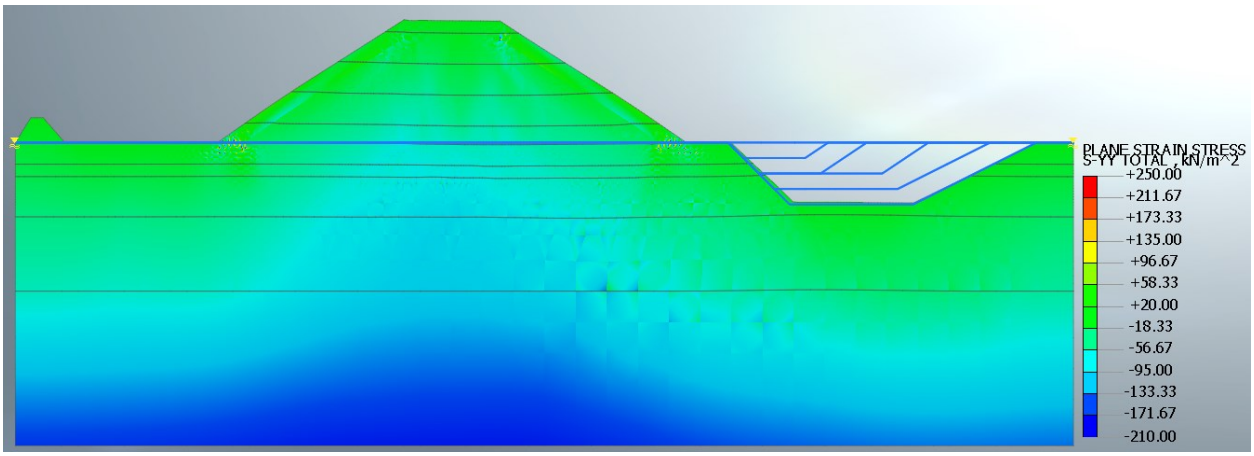

(b) Vertical stress, S-YY

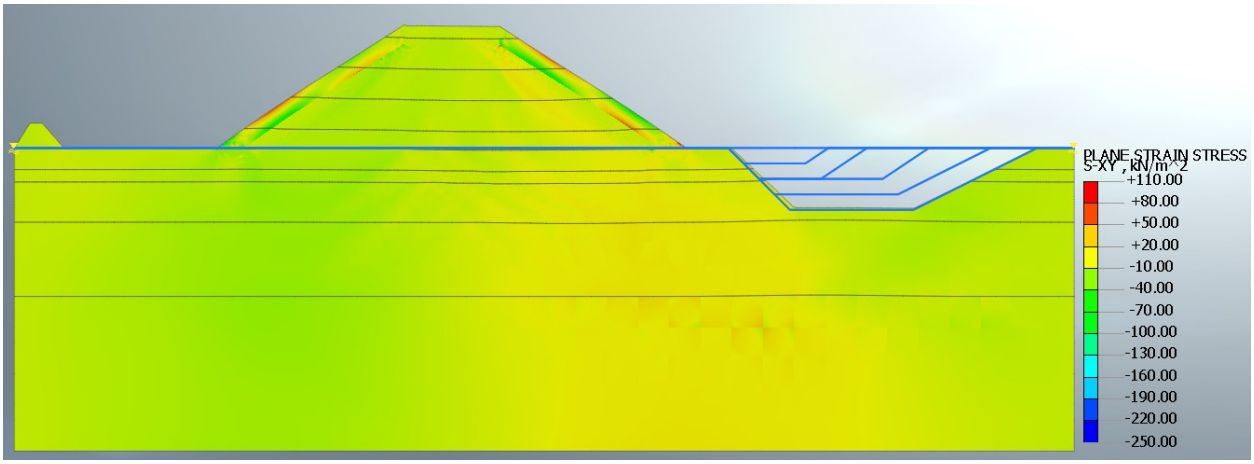

(c) Shear stress, S-XY

Figure D. 51. Total stresses and shear stress (kN/m^2) at second filling of sand core (scaled for better visualization).

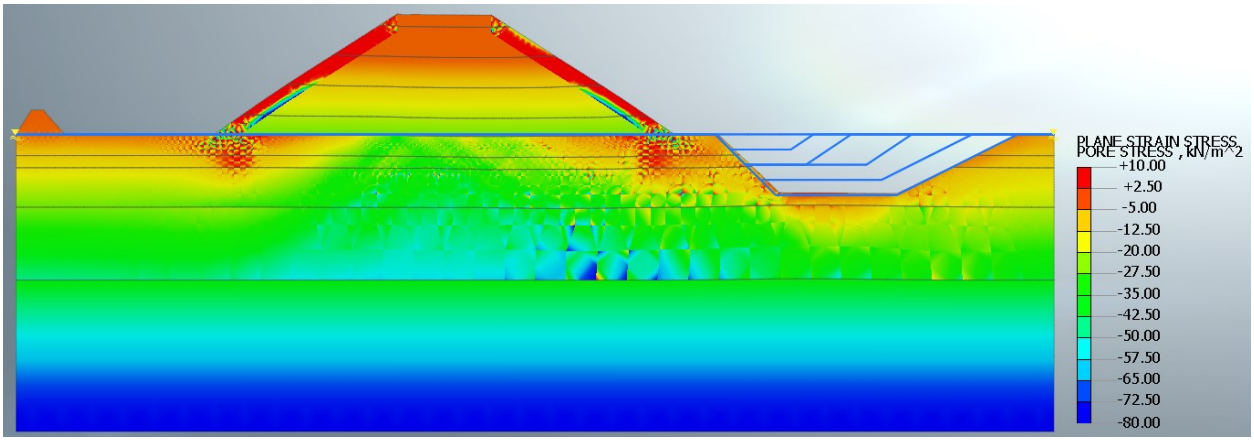

Figure D. 52. Pore stress (kN/m^2) at second filling of sand core (scaled for better visualization).

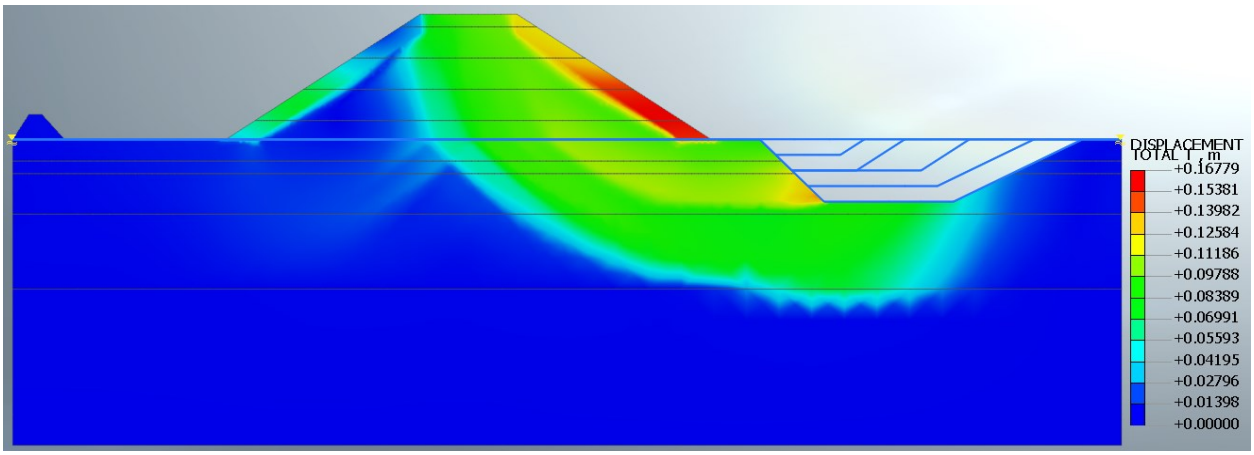

(a) Total displacement, T

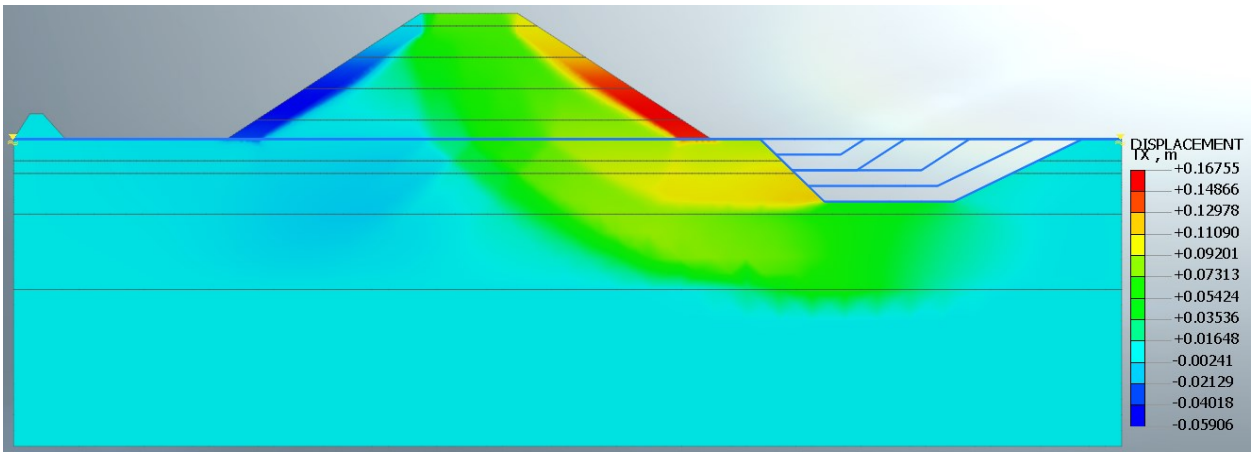

(b) Horizontal displacement, TX

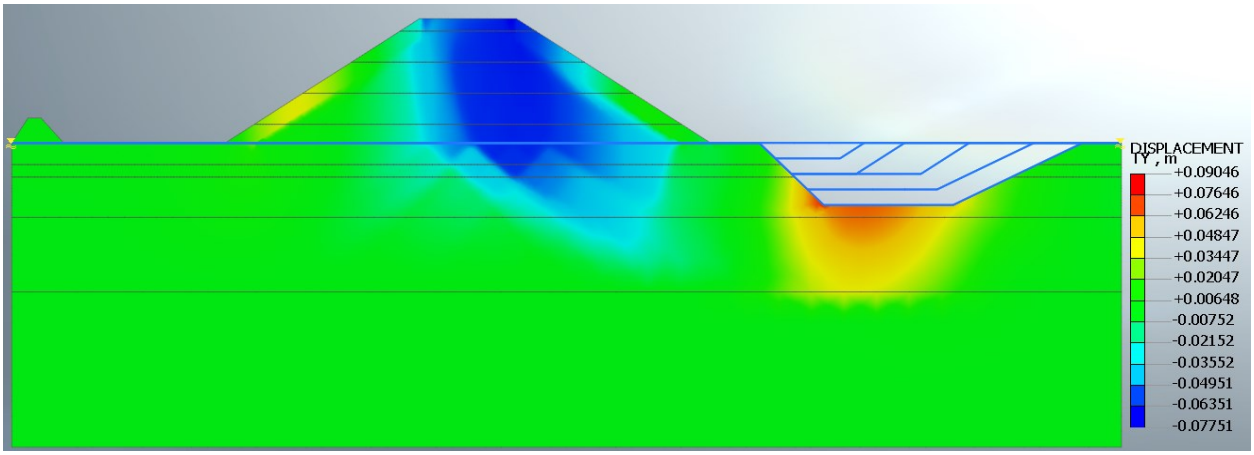

(c) Vertical displacement, TY

Figure D. 53. Displacements (m) at second filling of sand core.

APPENDIX E

The parametric analysis performed on the base peat property of the South Dike, and the corresponding changes made to each of the simulation runs are listed in Table E.1. As stated earlier, the first run serves as the reference.

Table E.2 provides the simulations and safety factors for each stage at which the simulation stopped. Their total displacement contour at the end of each of their SRM simulations is illustrated in Figures E.1 to E.6. All show that the failure mechanism developed is a deep sliding plane.

Regarding Figure E.7, it presents the settlement at the end of the levee construction step, with (a) representing the base run result, (b) representing the fifth run and, (c) representing the sixth run.

Table E. 1. Modified base peat properties and their respective simulation runs.

Base peat property	First run	Second run	Third run	Fourth run	Fifth run	Sixth run
Suction considered	no	**yes**	no	no	no	No
Effective friction angle [°]	27.5	27.5	27.5	**24**	27.5	27.5
Effective cohesion [kN/m^2]	9.7	9.7	**7**	9.7	9.7	9.7
Slope of consolidation line,	0.278	0.278	0.278	0.278	**0.265**	0.278
Slope of over consolidation line, κ	0.03	0.03	0.03	0.03	0.03	**0.0261**

Table E. 2. Factor of safety of each run and their respective final simulation stages.

Run	Final seepage simulation stage	Final stress simulation stage	Safety Factor (FS)
First	Sand core filled	Containers filled	1.050
Second	Sand core filled	Containers filled	1.064
Third	Second sand core filling	Excavation 5	1.138
Fourth	Second sand core filling	Excavation 5	1.739
Fifth	Sand core filled	Containers filled	1.031
Sixth	Sand core filled	Containers filled	1.031

First run:

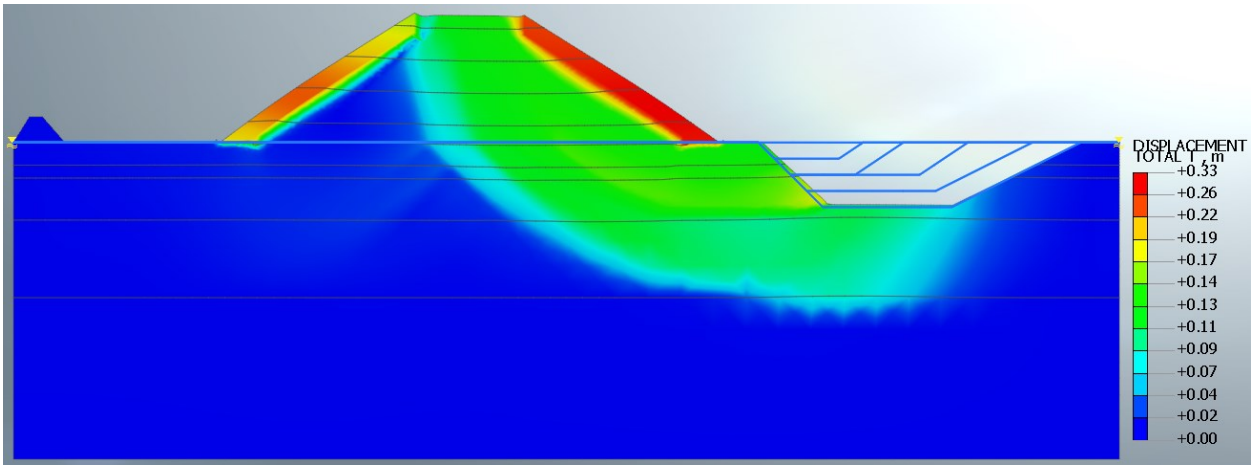

Figure E. 1. Total displacement (m) contour of the first run at its final stage (Containers filled).

Second run

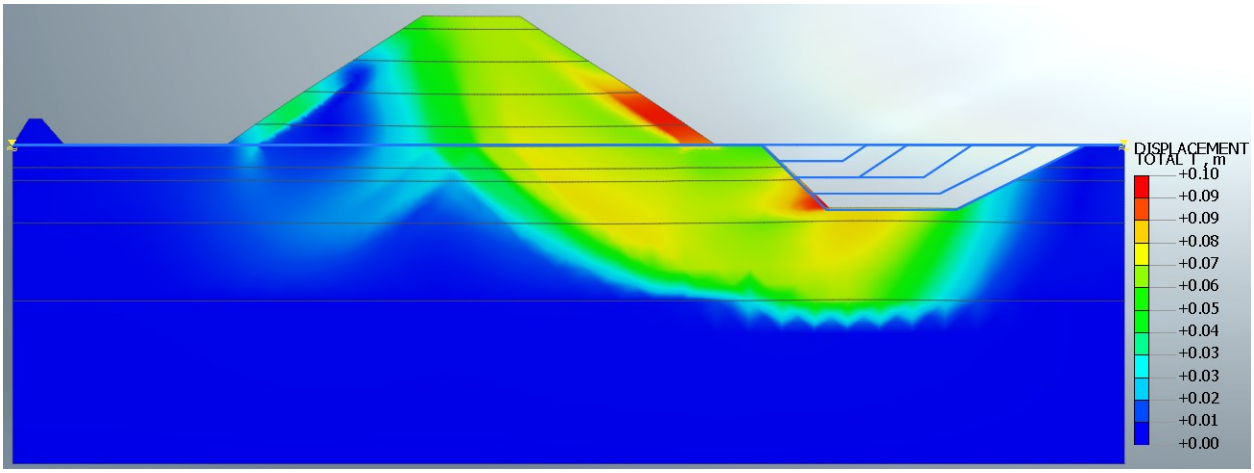

Figure E. 2. Total displacement (m) contour of the second run at its final stage (Containers filled).

Third run

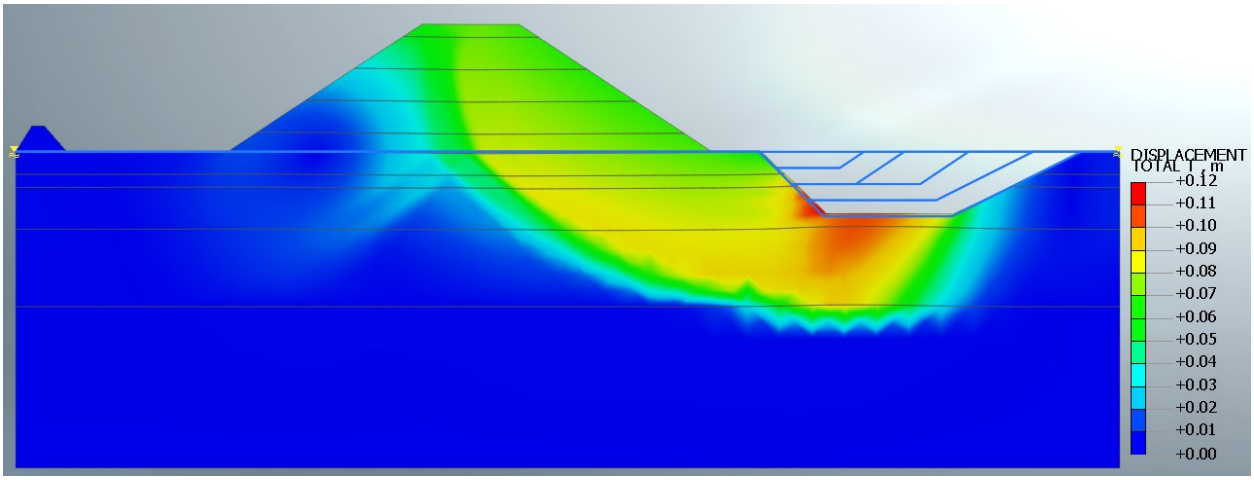

Figure E. 3. Total displacement (m) contour of the third run at its final stage (Excavation 5).

Fourth run

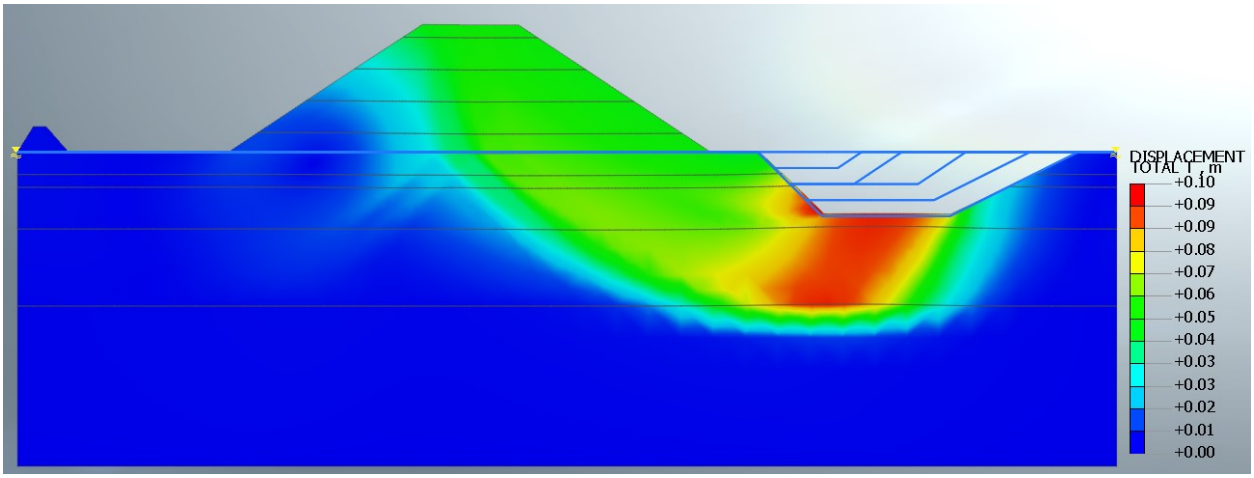

Figure E. 4. Total displacement (m) contour of the fourth run at its final stage (Excavation 5).

Fifth run

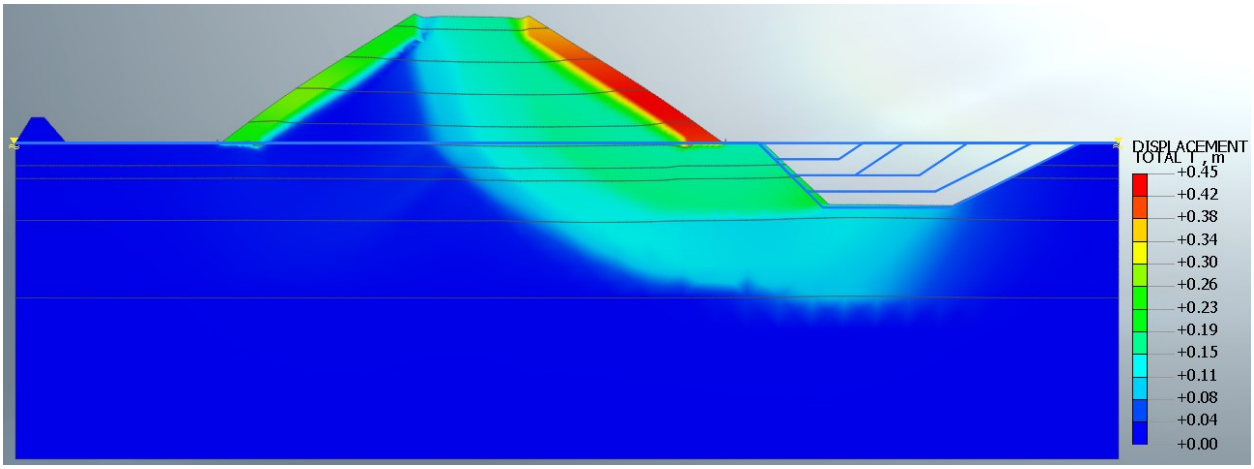

Figure E. 5. Total displacement (m) contour of the fifth run at its final stage (Containes filled).

Sixth run

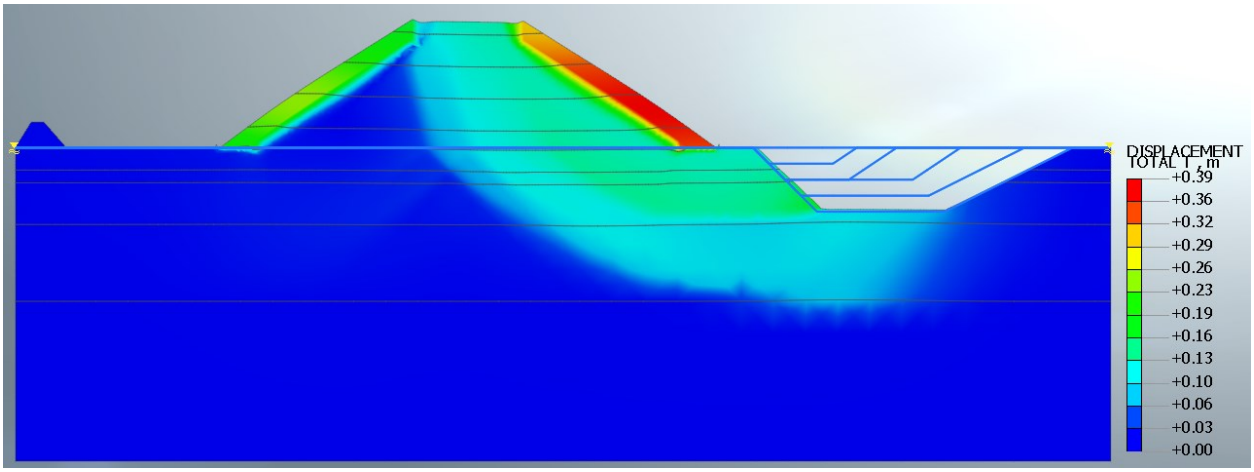

Figure E. 6. Total displacement (m) contour of the sixth run at its final stage (Containers filled).

Stage 7: Levee construction step 5

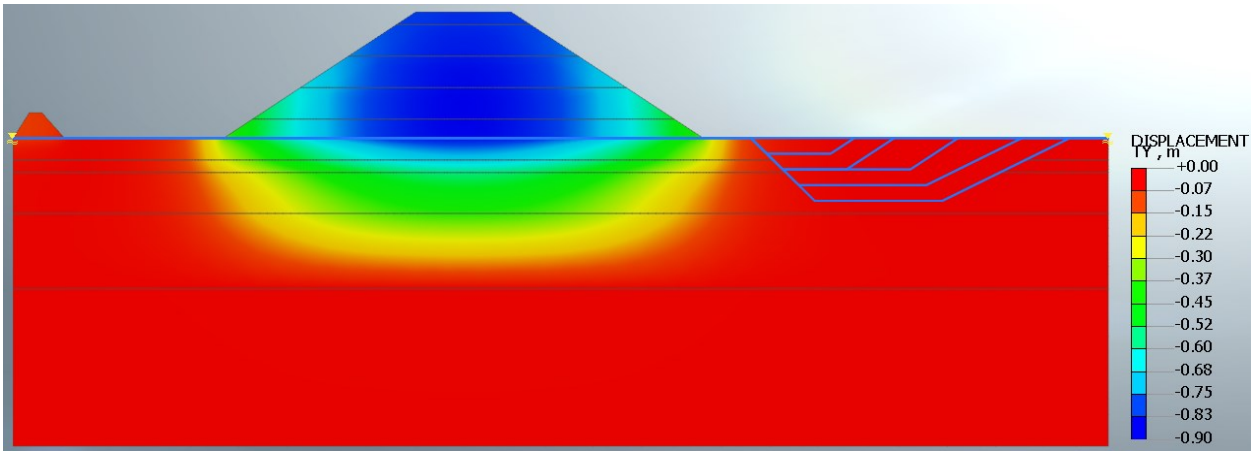

(b) Reference run

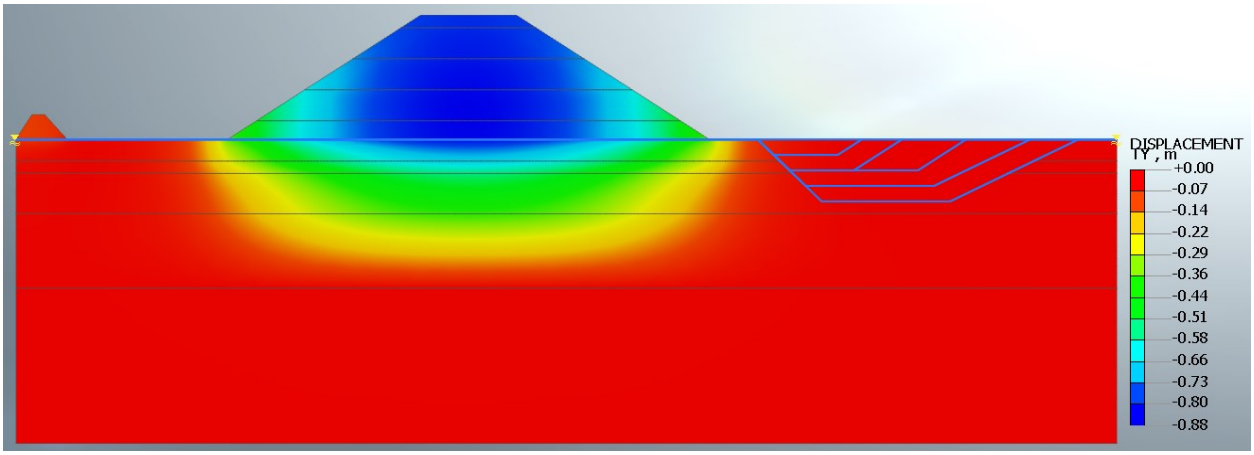

Run 5

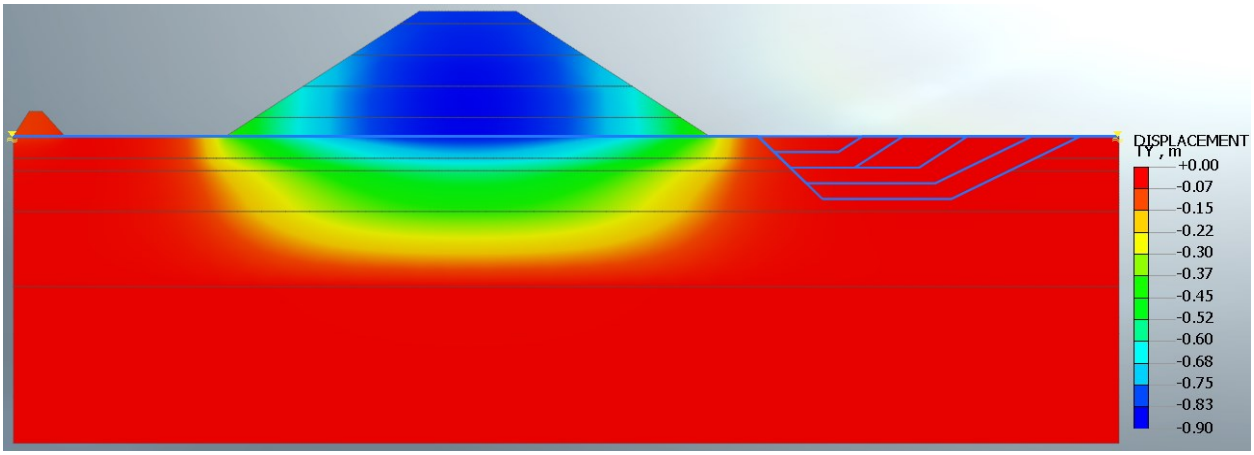

(c) Run 6

Figure E. 7. Settlement (m) results of the reference run, run 5 and run 6.

APPENDIX F

This Appendix presents the post-failure analysis results of the South Dike generated using Anura3D.

Tables F.1 and F.2 present the development of the vertical stress and pore pressure respectively. The total number of load steps is 125 with each step lasting 0.1s. Overall, the simulation took 12.5s to complete. Note that the results are scaled for the best visualization.

Moreover, three MPs have been selected to plot their displacements over the 12.5s period. Figure F.1(a) illustrates their locations, the first at the crest, the second at the toe while the third is at the ditch. Their corresponding horizontal and vertical displacements are given in Figure F.1(b).

Observing the initial phase up to around 1.4s, a significant increase in the horizontal movement of the MPs becomes evident at the toe, ditch and crest, reaching approximately 0.63m, 0.50m and 0.24m respectively. Afterwards, the displacement steadily rises until the simulation stops at 12.5s. At this point, the largest horizontal displacement is recorded at the toe, with a value of about 1.45m, and the smallest at the crest at 0.66m. During the experiment, the inclinometer measured a horizontal displacement of 0.83m at the toe, in the west cross section of the levee, and 1.65m in front of the toe, at the middle cross-section (see Table 7.1 in Chapter 7). Thus, the result of the simulation falls within the measurement of the inclinometer.

Furthermore, while the vertical movement of the of the MPs at the ditch and crest steadily drop throughout the simulation, the MP at the crest experiences a sharp decrease up to 1.4s, reaching a value of -0.79m, and then steadily decreases to -1.4m by the end of the simulation at 12.5s. This is the maximum vertical displacement, which is not very far from the experimental result that saw a drop of roughly -0.9m at the crest in the west cross section, as seen in Figure 7.1 in Chapter 7.

In addition, the plot of kinetic energy of the levee failure throughout the simulation is provided in Figure F.2. Several peaks are evident, with the highest being nearly 125kJ at about 1.5s. The first three peaks seen are due to the initial movement of the large deformation process. After the third peak at 2.5s, the kinetic energy drops, indicating that the slope's attempt to seek a new stable configuration. During this phase, at around 5s, a minor peak emerges due to numerical instability. Subsequently, starting from t = 7s, there is a notable rise in kinetic energy and a number of peaks produced with the highest having a value of approximately 16.4kJ. This corresponds to the reactivation of the levee movement, further advancing the sliding plane failure mechanism, causing bulking of the left ditch slope and uplift at the bottom of the ditch. By t = 9s, the kinetic energy falls to nearly 0 and remains constant till the end of the plot, although extremely small peaks can be noticed at around 11s due to numerical instabilities. Nevertheless, the constant values at the last part of the plot infer that the deformation of the levee has stopped.

Table F. 1. South Dike post-failure vertical stress evolution (0.0s to 12.5s).

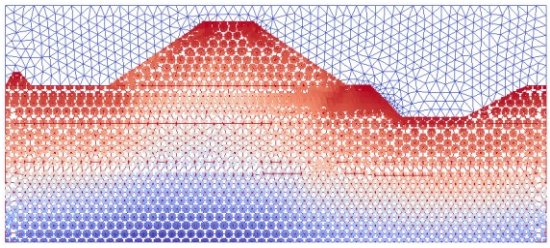

0.0s

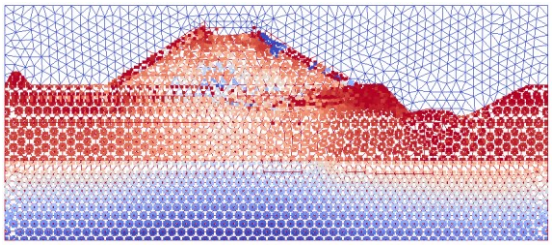

2.5s

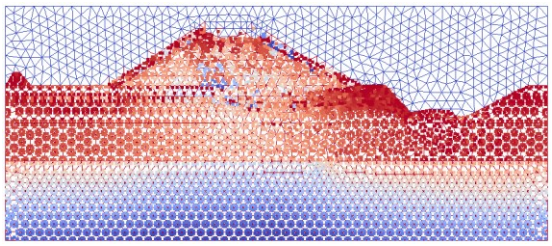

5.0s

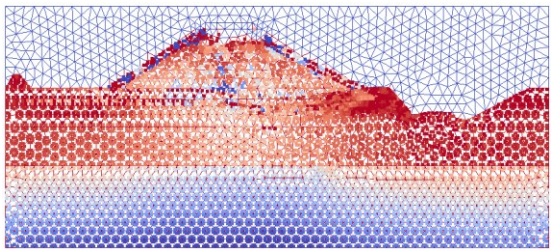

7.5s

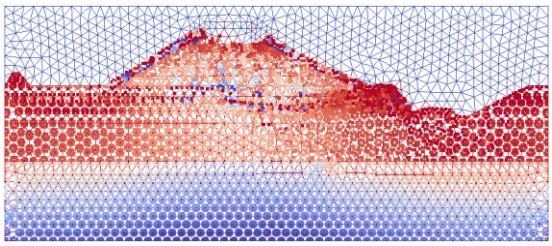

10.0s

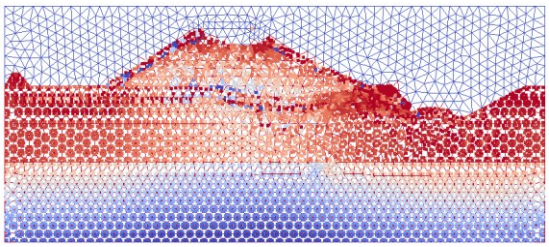

12.5s

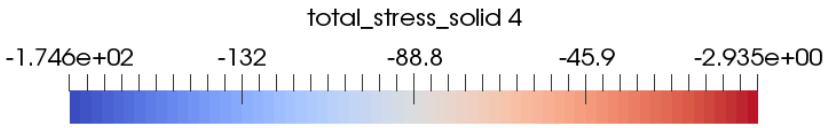

Table F. 2. South Dike post-failure pressure evolution (0.0s to 12.5s).

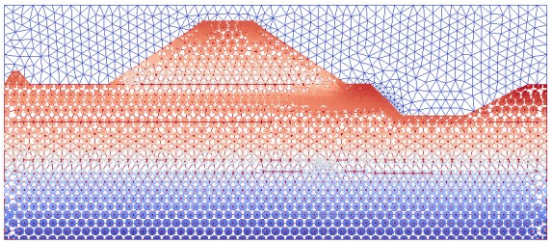

0.0s

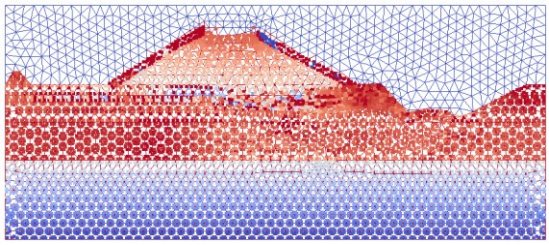

2.5s

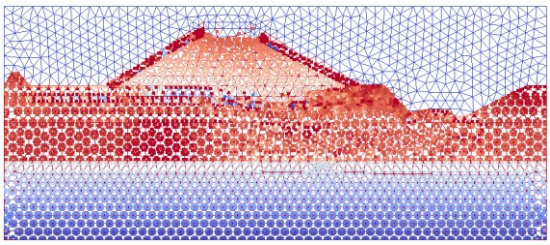

5.0s

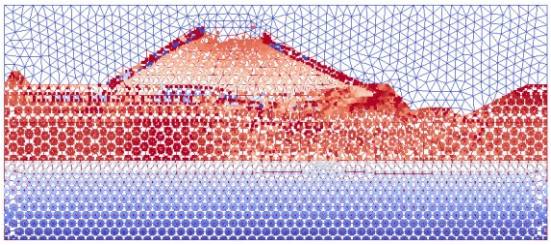

7.5s

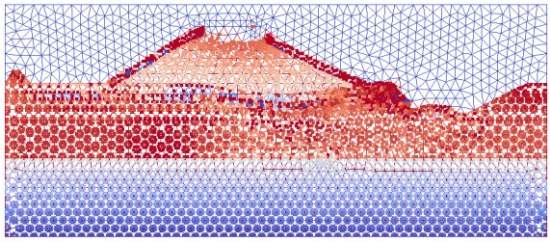

10.0s

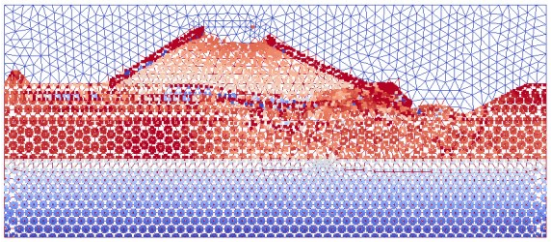

12.5s

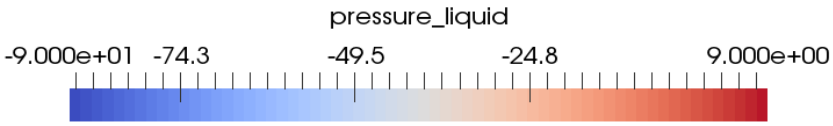

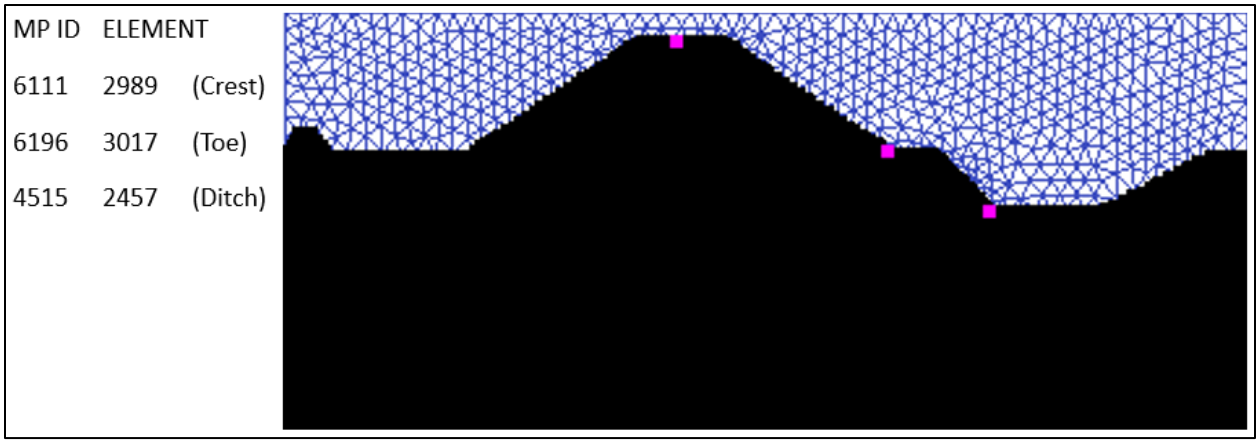

(a) MP location

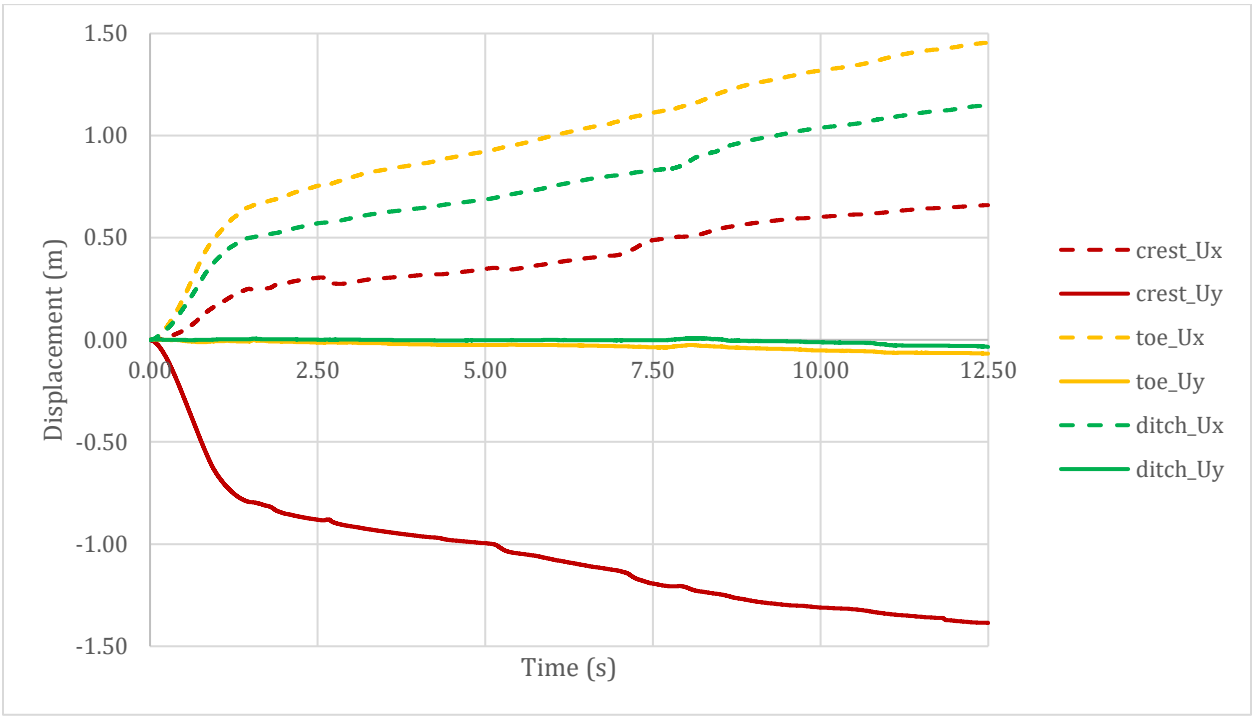

(b) Horizontal (Ux) and vertical (Uy) displacement plots

Figure F. 1. Location of MPs (a) and their respective displacements in m (b).

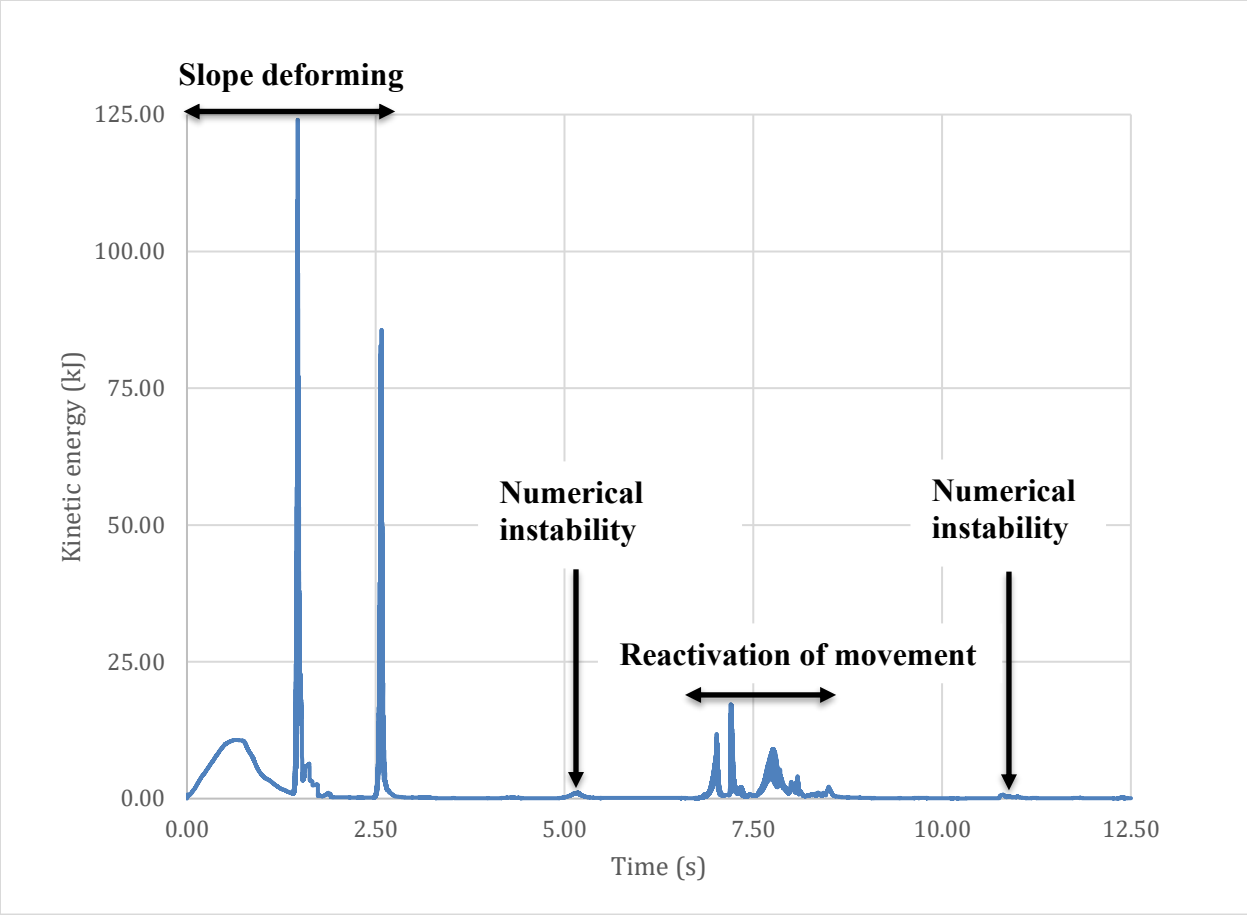

Figure F. 2. South Dike kinetic energy (kJ) plot.

APPENDIX G

Information about the distribution of MPs resulting from the parametric analysis performed for the post-failure analysis of the South Dike is provided in this appendix. Figures G.1 to G.4 display the distribution of the MPs during the final step of each of the runs, where the time per load step set is 0.1 s, along with the magnified location of the cross-cell and numerical instability issues.

Run 1: Final load-step = 125, duration = 12.5s

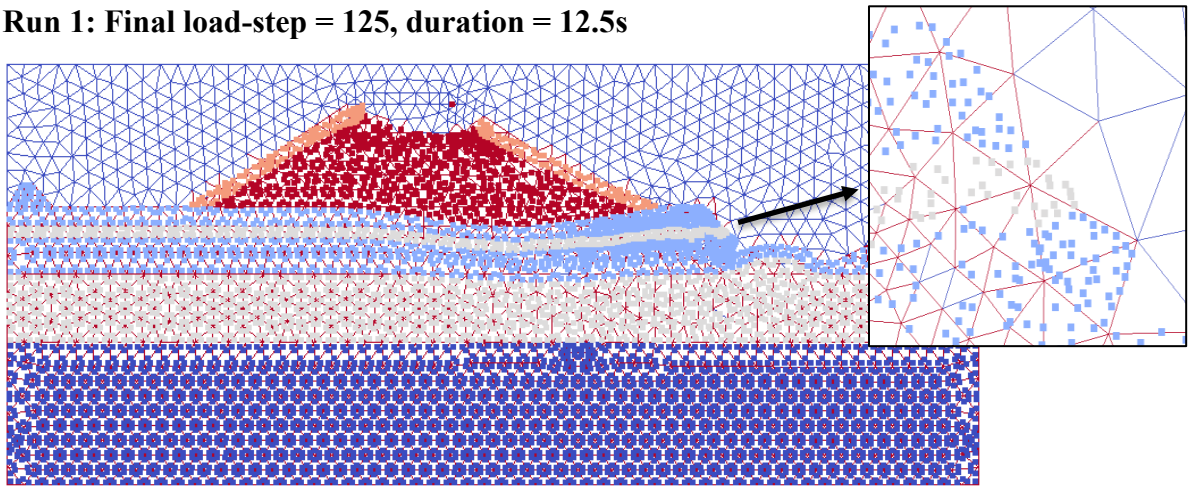

Figure G. 1. Final MP distribution of the first run.

Run 2: Final load-step = 1, duration = 0s

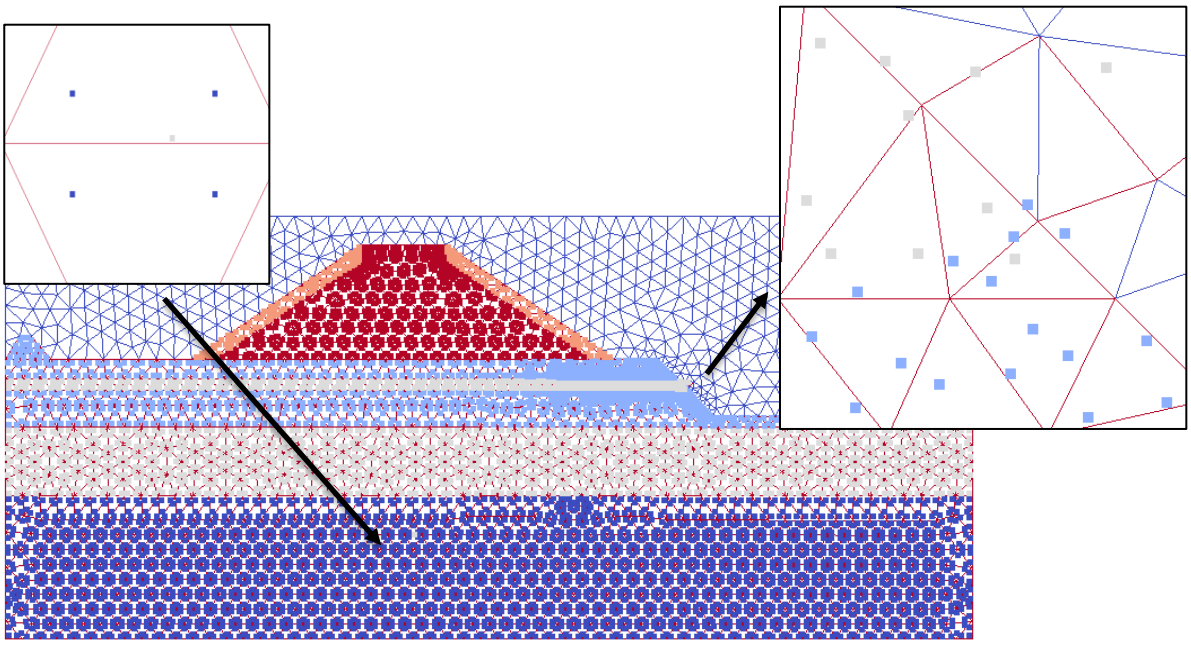

Figure G. 2. Final MP distribution of the second run.

Run 3: Final load-step = 10, duration = 0.9s

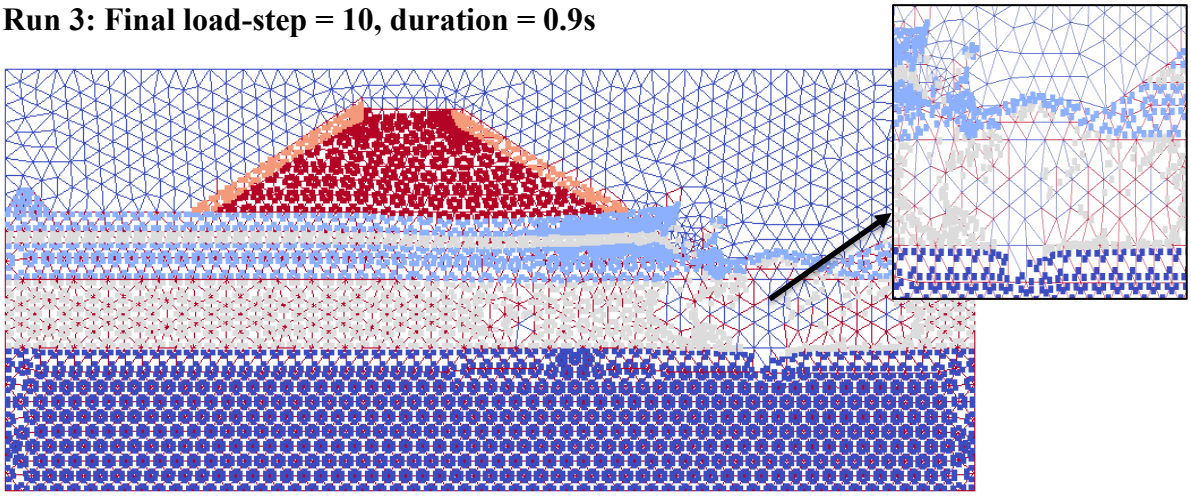

Figure G. 3. Final MP distribution of the third run.

Run 4: Final load-step = 13, duration = 1.2s

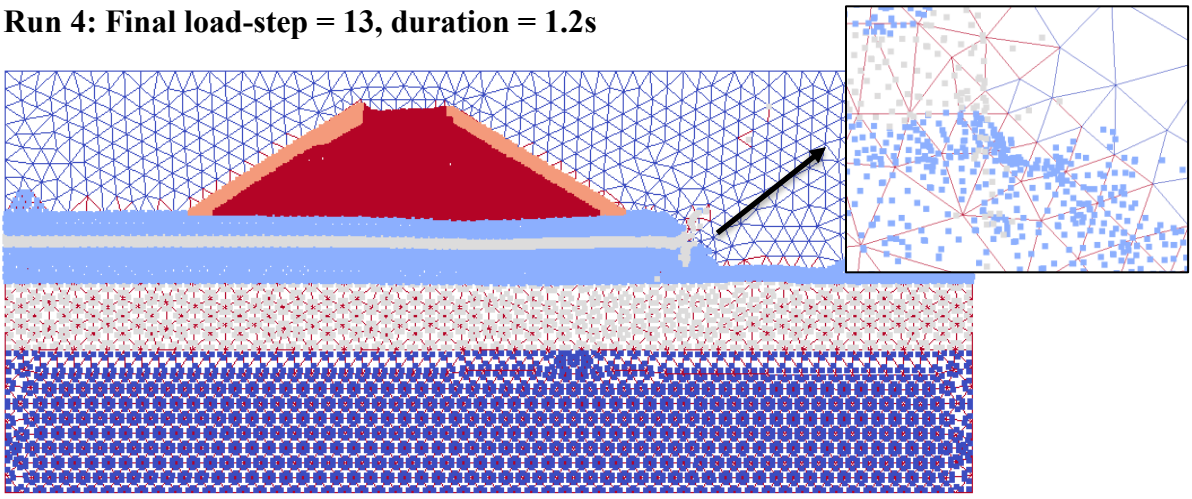

Figure G. 4. Final MP distribution of the fourth run.

9 BIBLIOGRAPHY

Anura3D. (2023). *ANURA3D version 2023 source code* (2023). Anura3D MPM Research Community. https://github.com/Anura3D/Anura3D_OpenSource

Anura3D MPM Research Community. (2022). *Anura3D Scientific Manual version 2022*.

Beuth, L., Więckowski, Z., & Vermeer, P. A. (2010). Solution of quasi-static large-strain problems by the material point method. *International Journal for Numerical and Analytical Methods in Geomechanics*, n/a-n/a. https://doi.org/10.1002/nag.965

Borja, R. I., Sama, K. M., & Sanz, P. F. (2003). On the numerical integration of three-invariant elastoplastic constitutive models. *Computer Methods in Applied Mechanics and Engineering*, *192*(9–10), 1227–1258. https://doi.org/10.1016/S0045-7825(02)00620-5

Ceccato, F. (2015). Study of large deformation geomechanical problems with the material point method. https://doi.org/10.13140/RG.2.1.2601.0080

Girardi, V., Ceccato, F., Rohe, A., Simonini, P., & Gabrieli, F. (2022). Failure of levees induced by toe uplift: Investigation of post-failure behavior using material point method. *Journal of Rock Mechanics and Geotechnical Engineering*. https://doi.org/10.1016/j.jrmge.2022.07.015

Girardi, V., Ceccato, F., Yerro, A., Simonini, P., & Gabrieli, F. (2023). *Large Strain Analysis of Unsaturated Heterogeneous Slopes with MPM* (pp. 229–236). https://doi.org/10.1007/978-3-031-12851-6_28

Girardi, V., Yerro, A., Ceccato, F., & Simonini, P. (2021). Modelling deformations in water retention structures with unsaturated material point method. *Proceedings of the Institution of Civil Engineers: Geotechnical Engineering*, *174*(5), 577–592. https://doi.org/10.1680/jgeen.21.00059

Griffth, D. V., & Lane, P. A. (1999). Slope stability analysis by finite elements. *Géotechnique*, *49*(3), 387–403. https://doi.org/10.1680/geot.1999.49.3.387

Hong, W.-K. (2020). The investigation of the structural performance of the hybrid composite precast frames with mechanical joints based on nonlinear finite element analysis. In *Hybrid Composite Precast Systems* (pp. 89–177). Elsevier. https://doi.org/10.1016/B978-0-08-102721-9.00003-0

Kim, J., Sonnenthal, E. L., & Rutqvist, J. (2012). Formulation and sequential numerical algorithms of coupled fluid/heat flow and geomechanics for multiple porosity materials. *International Journal for Numerical Methods in Engineering*, *92*(5), 425–456. https://doi.org/10.1002/nme.4340

Koelewijn, A. R. (2012). *MANAGEMENT SUMMARY THE ALL-IN-ONE SENSOR VALIDATION TEST OF THE IJKDIJK*.

Koelewijn, A. R., & Peters, D. J. (2012). *Design of IJkdijk All-in-One/Sensor Validation Test 1206242-000 Design of IJkdijk All-in-One/Sensor Validation Test*.

López-Acosta, N. P., & Tarantino, A. (2018). *Lessons Learned from Dike Failures in Recent Decades*. https://doi.org/10.4417/IJGCH-04-03-04

Melnikova, N., Jordan, D., Krzhizhanovskaya, V., & Sloot, P. (2015). Numerical prediction of the IJkDijk trial embankment failure. *Proceedings of the Institution of Civil Engineers: Geotechnical Engineering*, *168*(2), 158–171. https://doi.org/10.1680/geng.14.00040

Midas FEA, N. X. (2023). *Midas FEA NX-computer software, v.1.1*. Retrieved May 20, 2023, from https://globalsupport.midasuser.com/helpdesk/KB/View/32636105-midas-fea-nx-manuals-and-tutorials

Mississippi Valley Division, U. S. A. C. of E. (n.d.). *Levee Systems*. Retrieved May 2, 2023, from https://www.mvd.usace.army.mil/About/Mississippi-River-Commission-MRC/Mississippi-River-Tributaries-Project-MR-T/Levee-Systems/

Rohe, A., & Vermeer, P. A. (2014, July). *Multiphase modelling of large deformations using mpm: Applications in geotechnics and soil-water transition*.

Silva, W., Dijkman, J. P. M., & Loucks, D. P. (2004). Flood management options for The Netherlands. In *Intl. J. River Basin Management* (Vol. 2, Issue 2).

Sulsky, D., Chen, Z., & Schreyer, H. L. (1994). A particle method for history-dependent materials. *Computer Methods in Applied Mechanics and Engineering*, *118*(1–2), 179–196. https://doi.org/10.1016/0045-7825(94)90112-0

Wang, X., Wang, L. B., & Xu, L. M. (2004). Formulation of the return mapping algorithm for elastoplastic soil models. *Computers and Geotechnics*, *31*(4), 315–338. https://doi.org/10.1016/j.compgeo.2004.03.002

Zomer, W. (2012, September 13). *New tests IJkdijk: dike breaches predictable with new sensor systems*. https://www.dutchwatersector.com/news/new-tests-ijkdijk-dike-breaches-predictable-with-new-sensor-systems